8-9-2006

Permeability and Flammability Study of Composite Sandwich Structures for Cryogenic Applications

Monika Bubacz
University of New Orleans

PERMEABILITY AND FLAMMABILITY STUDY OF COMPOSITE SANDWICH STRUCTURES FOR CRYOGENIC APPLICATIONS

A Dissertation

Submitted to the Graduate Faculty of the
University of New Orleans
in partial fulfillment of the
requirements for the degree of

Doctor of Philosophy
in
The Engineering and Applied Science Program

by

Monika Bubacz

M.Sc. Poznan University of Technology, 1998

August, 2006

ACKNOWLEDGEMENTS

The writing of a dissertation can be a lonely and isolating experience, yet it is obviously not possible without the personal and practical support of numerous people. Thus my sincere gratitude goes to my parents and family, all my old friends in Poland, all new fiends and classmates for their love, support, and patience over the last few years. Big appreciation goes to my best friend since ever Arika Ligmann-Zielinska for always being there for me and an unconditional support.

I am appreciative and thankful for the support of my dissertation chair and supervisor, Professor David Hui, and the Members of my Committee, Professors Paul Herrington, Ting Wang, Bhaskar Kura, and Dongming Wei. Without their support this dissertation would not have been written. I would like to thank Prof. Hui for offering me graduate research assistantship and the possibility to travel and visit other research centers and facilities and attend the ICCE conference. The warmest thanks go to his wife, Ms. Shun-Ying Hui for her care and deep involvement in our lifes.

Many people on the faculty and staff of the Mechanical Engineering Department at the University of New Orleans assisted and encouraged me in various ways during my course of studies. I am especially grateful to Professors Kazim M. Akyuzlu, Paul Schilling, Robert H. Lipp, Melody Verges, Salvadore Guccione, Jr., Ram V. Mohan, Leo Daniel, and Ms. Deborah B. Duzac for all that they have taught me and all the help they offered.

My special thanks go to Professor Carl A. Ventrice, Jr. from the Department of Physics for expert help with setting up the test and designing and machining the sample holder.

This dissertation would not have been possible without the guidance of my esteemed advisor, Dr. Andrey Beyle from Pittsburg State University. I want to thank him especially for the many thought-provoking conversations we have had concerning every aspect of my research and the detailed comments and suggestions on this and other work.

The completing of this research would not have been possible without support of the faculty, staff, and students of the Engineering Technology Department at Pittsburg State University. Prof. Chris C. Ibeh offered me a research associate position at the Center for NanoComposites and Multifunctional Materials and his help after unexpected relocation caused by Hurricane Katrina.

Again, I thank my parents, Ewa and Andrzej Bubacz, and brother, Tomasz, to whom I dedicate this work, for their unflagging belief that despite their incomprehension about what I do, I must be saving the world. I am indebted to my parents for continuous support, trust, and inculcating in me the dedication and discipline to do whatever I undertake well no matter what happens.

Finally, I am thankful for the many diversions I have enjoyed during my sojourn in the United States. Without them, crossing over to the realms of insanity would have been entirely within reach. My dear friends, my beloved dog Roxie, my various hobbies, and beautiful, beautiful New Orleans, with its unique culture and spirit, have connived to ensure that the road to my goal was not as bumpy as it could have been.

TABLE OF CONTENTS

LIST OF FIGURES

LIST OF TABLES

LIST OF ACRONYMS, ABBREVIATIONS, AND SYMBOLS

2-D	Two Dimensional
3-D	Three Dimensional
C	Concentration of Diffusing Substance
CFRP	Carbon Fiber Reinforced Plastic
COD	Crack Opening Displacement
CTE	Coefficients of Thermal Expansion
D	Diffusion Coefficient
DCOD	Delaminated Crack Opening Displacement
EHC	Effective Heat of Combustion
ERR	Energy Release Rate
f	Heat Flux
FEA	Finite Element Analysis
FEM	Finite Element Method
GHe	Gaseous Helium
h	Film Thickness
HRR	Heat Release Rate
J	Gas Flux
K	Permeability Coefficient
L	Maximal Value of Flow Density Derivative
LH2	Liquid Hydrogen
LN2	Liquid Nitrogen
LOX	Liquid Oxygen
M	Mass
MEKPO	Methyl Ethyl Ketone Peroxide
q	Flow Density or Permeation Rate
Q	Flow Rate or Leak Rate
p	Gas Pressure
PC	Polycarbonate
PEEK	Poly Ether Ether Ketone
PEHC	Peak of Effective Heat of Combustion
PHRR	Peak of Heat Release Rate
PMC	Polymeric Matrix Composite
PUF	Poly Urethane Foam
r	Thermal Load
R	Universal Gas Constant
RLV	Reusable Launch Vehicle
S	Solubility Coefficient
SERR	Strain Energy Release Rate
t	Time
T	Temperature
THR	Total Heat Release
V	Volume
W	Capacitance
Z	Time Integral of Flow Density
α	Aspect Ratio
ϕ	Volume Fraction
λ	Conductivity
ψ	Volume Concentration of Pores
ζ	Volume Concentration of Inclusions

ABSTRACT

Fiber reinforced plastics offer advantageous specific strength and stiffness compared to metals and has been identified as candidates for the reusable space transportation systems primary structures including cryogenic tanks. A number of carbon and aramid fiber reinforced plastics have been considered for the liquid hydrogen tanks. Materials selection is based upon mechanical properties and containment performance (long and short term) and upon manufacturing considerations. The liquid hydrogen tank carries shear, torque, end load, and bending moment due to gusts, maneuver, take-off, landing, lift, drag, and fuel sloshing. The tank is pressurized to about 1.5 atmosphere (14.6psi or 0.1MPa) differential pressure and on ascent maintains the liquid hydrogen at a temperature of 20K.

The objective of the research effort is to lay the foundation for developing the technology required for reliable prediction of the effects of various design, manufacturing, and service parameters on the susceptibility of composite tanks to develop excessive permeability to cryogenic fuels.

Efforts will be expended on developing the materials and structural concepts for the cryogenic tanks that can meet the functional requirements. This will include consideration for double wall composite sandwich structures, with inner wall to meet the cryogenic requirements. The structure will incorporate nanoparticles for properties modifications and developing barriers.

The main effort will be extended to tank wall's internal skin design. The main requirements for internal composite stack are:

- introduction of barrier film (e.g. honeycomb material paper sheet) to reduce the wall permeability to hydrogen,
- introduction of nanoparticles into laminate resin to prevent micro-cracking or crack propagation.

There is a need to characterize and analyze composite sandwich structural damage due to burning and explosion. Better understanding of the flammability and blast resistance of the composite structures needs to be evaluated.

Chapter 1

INTRODUCTION

1.1. Background

For aerospace application there is a continued drive to improve the efficiency of structural designs not least in area of weights. This has increasingly led to the use of fiber reinforced composite materials to augment metallic as the primary structural materials. Those composites with a wide level of acceptance are carbon and aramid fiber reinforced epoxy resins [1].

Reusable launch vehicle (RLV) uses cryogenic hydrogen and oxygen as fuel. The fuel will be stored in tanks at cryogenic temperatures. Numerous designs have been evaluated for the liquid hydrogen (LH2) and liquid oxygen (LOX) tanks. The designs include sandwich panels with foam or honeycomb core between two facesheets. The core serves as a portion of the cryogenic insulation and as a structural member [2].

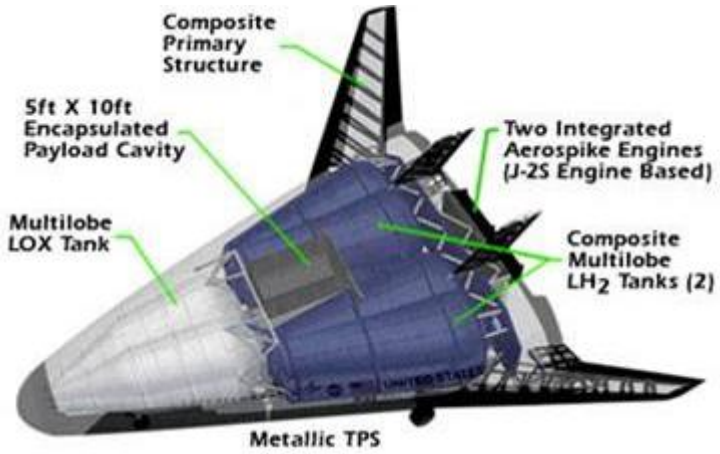

Fig. 1.1.1. Reusable launch vehicle design

Sandwich constructions provide an efficient solution to increase bending stiffness without significant increase in structural weight. The sandwich for aerospace application is generally made by bonding carbon fiber reinforced plastic (CFRP) facesheets to aramid paper honeycomb or foam cores. These structures can carry both in-plane and out-of-plane loads and remain stable under compression without a significant weight penalty [3].

A critical issue for the sandwich structure is environmental durability. Fuselage sandwich structure will be exposed to pressurized gases from both the interior and exterior of the RLV in service. Exposure to these agents in combination with thermal and mechanical loads can result in degradation of some composite structures. Sandwich structures have been observed to absorb gases and other fluids to

the point of saturation, resulting in weight gain, degradation of core and facesheet materials, and degradation of the core-to-facesheet bond [4].

The fuel tanks, which originally are at temperature of 20K due to the cryogenic fuel, can quickly reach above 400K during re-entry while the vehicle is re-entering the atmosphere at mach 15 with empty tanks. Theoretically, this large change in temperature will result in cracks initiating through the tank walls. This is expected of composite laminates since they are composed of several ply layers that expand in a dominant direction, producing a high amount of strain energy that can easily be relieved with the formation of cracks [5]. When the problem is coupled with cyclic switching of operating temperatures, dramatic changes in structure and properties of composite material can occur.

Cryogenic cycling efforts to date have focused on many of the factors contributing to damage initiation and development such as the number of cycles and the temperature profile of the applied cycle. The research proved that increased fiber modulus, increased matrix coefficient of thermal expansion, and lower matrix glass transition temperature (and subsequent lower matrix strength) corresponded to greater micro-crack densities and longer microcracks. The term ‘microcrack’ refers to a transverse crack in one or more plies with the length through the laminate thickness of the order of one ply thickness [6]. The immediate effect of microcracks is degradation in the thermomechanical properties of the laminate including changes in all effective moduli, Poisson ratios, and thermal expansion coefficients. A secondary effect of microcracks is that they nucleate other forms of damage. For example, microcracks can induce delamination, cause fiber breaks, or provide pathways for the entry of corrosive liquids or gases. Such damage modes may subsequently lead to laminate failure [7].

Honeycomb or foam sandwich structure has many advantages over typical stiffened wall concepts, not the least of which is reduced weight. However, sandwich construction has a number of potential problems because the presence of multiple interfaces serves as a source for failure initiation and growth. Debonding of the facesheet can occur due to high pressure inside the core material and is facilitated by the occurrence of cryopumping. Cryopumping can occur in closed cells during repeated cryogenic fluid fill and drain cycles and is simply the condensation of the gas on a cryogenically cooled surface that results in a vacuum or greatly decreased pressure inside the cells. For a cryotank with polymeric matrix composite (PMC) sandwich materials in the tank walls, this cryopumping will occur when the tank wall facesheet(s) develop leaks and allow the cryogen to permeate into the core. The most likely initial failure mode due to cryopumping is facesheet-to-core debonding that can lead to crack growth and a total separation of the facesheet [8]. That kind of failure mode occurred in the NASA X-33 reusable flight demonstration vehicle. The X-33 was designed with a large conformal tank made from a sandwich construction of graphite/epoxy laminate skin and phenolic honeycomb core. The failure or debonding location occurred almost exclusively at the core-to-adhesive surface on the inner facesheet side.

There is one approach to solve the problems associated with sandwich structure debonding which involves introducing a layer or layers of polymeric or metal film into (interleaving) or onto (coating) the composite inner skin that will act as a barrier or will arrest microcracks. Though addition of film

interleaves into composite laminates increases the fatigue properties and impact damage resistance of the composite, they also reduce the specific strength of the material due to increased part weight, which is unacceptable in weight-critical applications such as RLV. Currently under development for barrier film are novel nanocomposite materials made from organo-clay materials. Such materials form lamellar structures that both increase the modulus of the polymer and provide additional barrier properties. The use of these materials may actually increase the overall specific strength of the material, while providing the permeation resistance needed in cryogenic fuel tank application. These materials may be used as barrier film or matrix resin systems. Additionally, some studies indicate that thermoplastic interleaving materials may be superior to thermosetting materials in low-temperature, cryogenic applications.

Nanocomposites seem to be a new class of flame retardant systems. In recent years they have attracted great interest because they frequently exhibit remarkable improvements in mechanical and material properties. These improvements include a higher modulus, optical transparency, increased strength and keeping biodegradability of biodegradable polymers, furthermore increased heat resistance and decreased gas permeability and flammability [9]. The interface at the surface of particle inclusions plays a key role in the structure property relationship.

1.2. Objective, Scope, and Approach of Research

The objective of this work is to design a new sandwich structure for RLV fuel tank wall. The structure should remain based on facesheet-core-facesheet model and introduce new gas leakage protection concepts. Low cost and easy mass manufacturing stay a very important issue. The goal is to obtain good quality sandwich panels for cyclic usage, resistible to liquid agents and cryogenic temperature, and predict the damage within sandwich structure subjected to burning.

Several intermediate objectives have to be met in order to complete the primary objective. The main problem in designing of sandwich panel is selection of material for facesheets and core, and also proper adhesive, which will bond different materials and sustain mechanical, chemical and thermal load. The idea is to introduce an additional ply made from core material to the facesheet laminate and to use the same polymeric resin for both, skin and core, to make them more compatible to each other. The resin will be also altered by introduction of nanoparticles with the purpose of preventing gas leakage. Samples of core material with different resin systems will be tested for helium gas permeability using helium mass spectrometer and specially designed and manufactured sample fixture. The same samples will be also tested for damage caused by burning using state-of-the-art cone calorimeter.

Simultaneously, the permeability tests will be simulated using finite element method (FEM) software MSC.Nastran and the test results compared and discussed.

1.3. Organization of Dissertation

This dissertation is essentially divided into three sections. The second chapter of this dissertation is a literature review of microcracking in CFRP, sandwich structures for fuel tanks in RLV, gas permeability, mechanical impact properties, adhesives for composite sandwich application, nanotechnology, and flammability. Chapter 3 provides a detailed explanation of the experimental techniques and materials used in this research. Finally, Chapters 4 and 5 contain results of mathematical and computer simulations and laboratory tests, respectively. The results discussion, conclusions, and future recommendations for this research study are addressed in Chapter 6 of this dissertation.

References

[1] Daniel L., Tumino G., Henriksen T., Dujarric C. Survey of Advanced Materials in Reusable Launch Vehicle (RLV)

[2] Glass D.E. Bonding and Sealing Evaluation for Cryogenic Tanks NASA Contractor Report 201734 August 1997

[3] Meo M., Morris A.J., Vignjevic R., Marengo G. Composite Structures 62 (2003) 353-360

[4] Glass D.E., Raman V.V., Venkat V.S., Sankaran S.N. Honeycomb Core Permeability Under Mechanical Loads. NASA / CR-97-206263, December 1997

[5] Kessler S.S., Matuszeski T., McManus H., Cryocycling and Mechanical Testing of CFRP for X-33 Liquid H2 Fuel Tank Structure

[6] Bechel V.T., Fredin M.B., Donaldson S.L., Kim R.Y., Camping J.D. Composites: Part A 34 (2003) 663-672

[7] Nairn J.A. Comprehensive Composite Materials Vol. 2 403-432

[8] Gates T.S., Odegard G.M., Herring H.M. Facesheet Delamination of Composite Sandwich Materials at Cryogenic Temperatures

[9] Camino G., Tartaglione G., Frache A., Manferti C., Costa G. Polymer Degradation and Stability 90 (2005) 354-362

Chapter 2

LITERATURE REVIEW

2.1. Microcracking in Fiber Reinforced Plastics

Fiber reinforced polymer matrix composite materials offer significant advantages over metals in aerospace and other applications. Properties such as high strength-to-weight ratio, low thermal expansion coefficient, excellent fatigue behavior, and solvent resistance make these materials attractive alternatives to more conventional materials in both structural and non-structural applications. Additionally, these materials may be highly tailored to maximize their mechanical properties.

The enhancement of the mechanical properties of composite materials through various methods has been investigated in some detail over the past several years. Most of these studies have focused on improving the damage tolerance, interlaminar fracture toughness, and fatigue life of these materials. Design approaches for optimization of composite material mechanical properties include laminate stacking sequence, z-axis stitching, modifications to the matrix resins, and hybrid laminate concepts including resin and material interleaves.

Graphite fiber reinforced polymers are contenders for use in RLV components such as cryogenic fuel tanks, cryogenic fuel delivery lines, and parts of the cryogenic side of turbo-pumps. In addition to the requirements for the materials to be compatible with cryogenic temperatures, interior components of the vehicle may be subjected to significantly elevated temperatures due to heat conduction from the vehicle surfaces during and after atmospheric re-entry. For the RLV components, the focus is on preventing microcrack distributions that produce continuous through-thickness gas leakage paths rather than micro-cracks densities that alter ply coefficients of thermal expansion (CTE). Consequently, fundamental studies that document the microcrack densities in every ply and techniques for arresting microcracks and maximizing the number of microcrack free plies are of the greater interest [1].

Term microcrack is used to refer to a transverse crack in one or more plies with a length through the laminate thickness of the order of one ply thickness. Microcracks can be observed during tensile or fatigue loading, changing in temperature, and thermocycling. Microcracks can form in any plies, but they form predominantly in plies off-axis to loading directions.

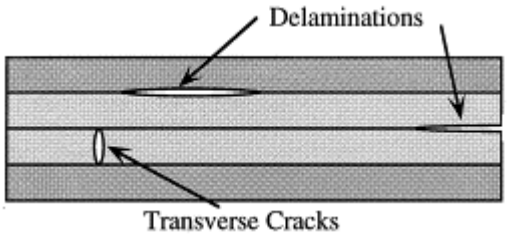

Fig. 2.1.1. Typical ply-level damage modes [10]

Microcracking affects the composite structure in two ways. First of all, it causes degradation in the thermomechanical properties of the laminate including changes in all effective moduli, Poisson ratios, and thermal expansion coefficients. Secondary, it damages the structure and induces delamination, fiber breaking, or provides pathways for the entry of corrosive liquids or gases. Such damage modes may subsequently lead to laminate failure.

Transverse matrix cracks in conjunction with inter-ply delamination originating from the tips of these cracks result in an intersecting network of passages that could allow fuel to penetrate. As depicted by the schematic in Fig. 2.1.2, the crack opening displacements associated with the delaminated transverse matrix cracks, when subjected to thermal and/or mechanical loading, form a path through the entire thickness of the cross-ply laminate, thereby allowing cryogenic fuel to permeate [2].

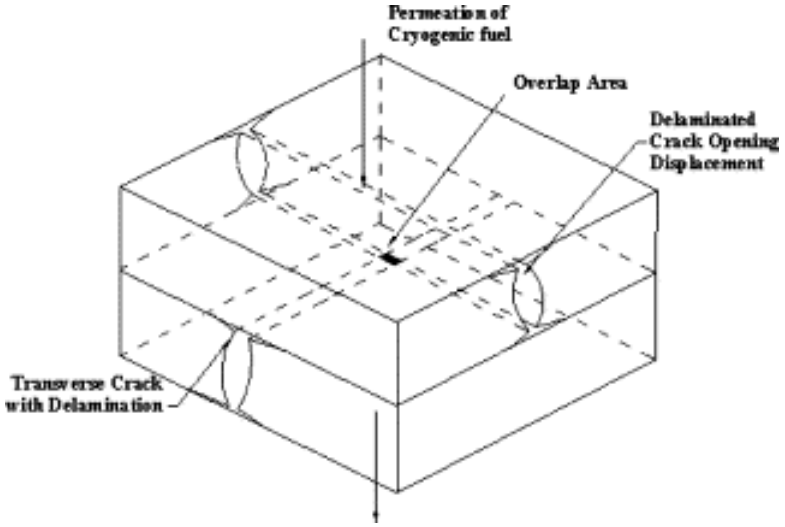

Fig. 2.1.2. Permeation path at overlap of two transverse cracks with delaminations [2]

Microcracking studies began in the 1970s with observation of the initiation of cracking. Since then there have been numerous papers on microcracking process under a variety of loading and environmental conditions. A major interest in studying microcracking is to be able to predict the microcracking process and to be able to design laminates that are resistant to microcracking [3].

The fatigue damage process in advanced high performance composite structures is very complex because it consists of a variety of damage modes due to the heterogeneity of the system, such as: microcracking, debonding between fiber and resin, fiber fracture, delamination between plies within facesheet laminate or between skin and core in sandwich structure. Variances in the geometry of the composite laminate and material properties of sandwich components make it difficult to determine how these damage modes interact with one another for all possible designs.

Numerous approaches and analytical models have been developed to study the initiation, constraint and propagation of transverse cracks in cross-ply laminates. Early work used classical laminated plate theory to calculate stresses and transverse strength failure criteria. Stress and strain field

predictions for microcracking have been accomplished using shear lag model, finite element methods and approximate solutions. The most prevalent approach to crack prediction is fracture mechanics.

Fracture mechanics tools have often been used to predict progressive transverse ply cracking in cross-ply laminates under quasistatic and fatigue loading. The non-dimensional damage parameter $\frac{d}{t}$ (where *d* is crack density, *t* is the cracked layer thickness) is often used. A two-dimensional shear-lag analysis, associated with an energy release rate criterion, was used to predict cracking development in each cross-ply (0^o and 90^o) laminate subjected to any fatigue loading. Stress distribution, elastic constants of the damaged layers and laminate, strain energy release rate in mode I, mode II, and mixed-mode were then obtained as functions of the crack densities in the 0^o and 90^o layers of the laminate [4]. In case of thermal cycling, no stresses were directly applied to the laminate, but each layer is in a biaxial stress state [5]. Moreover, the widthwise growth of the fatigue cracks was modeled by a non-linear wave equation [6].

In another publication [7] shear-lag model was used but no consideration was given to the origin of the microcrack and the way it propagates through the layer thickness. The analysis predicted the conditions under which a crack can exist in the matrix by considering the energy state of the body just before the crack is formed.

Shear-lag equations for analysis of stresses in a multilayered composite were derived using a series of approximations to exact two-dimensional elasticity methods [8]. A solution method for shear-lag equations for planar problems in composites was outlined based on eigen-analysis of a matrix of shear-lag parameters. The optimal, shear-lag analysis differs from most prior shear-lag methods in the literature. By adding more assumptions, the optimal analysis was reduced to two common, prior shear-lag methods. Because these interlayer methods required more assumptions than the optimal method, they were less accurate than that method. Several examples illustrated the types of problems that could be accurately solved by shear-lag analysis and the differences in accuracy between the various shear lag methods.

A limitation of shear-lag analysis is that the constraining layers are assumed as a homogenous medium without taking into account the stacking sequence effects. Also, the increase in crack opening displacement (COD) due to delamination plays an important role in determining the amount of permeation of cryogenic fuel, which is not included in a standard shear-lag model.

A fracture mechanics approach used the concept of an effective flaw distribution or critical flaw size [9]. The basic mechanisms of 90^o ply transverse cracking under monotonic tension have been explained and predicted by an application of the energy release rate method. Multiple cracks in the 90^o ply have been described by a stochastic procedure incorporating the concept of effective flaw distribution as an inherent ply material property. The usefulness of the same approach to predict the growth behavior of free-edge delamination under both static and fatigue load has also been established. Using a 2-D or 3-D finite elements sequential analysis in thickness direction the order of failure events within a laminate can be predicted, i.e. cracking in 90^o layers, 0^o layers, delamination, and ultimate failure, in which certain

assumptions regarding the size of the fracture zones, crack spacing, and inherent flaws are made. X-ray, acoustic emission and edge microscopy are used for detailed observation and comparison with analytical and numerical methods [10].

A reasonable hypothesis is that all plies contain multitudes of initial flaws of various sizes and orientations, and at random locations, which develop during the manufacturing process. At sufficiently high stresses the energy release rates (ERR) will reach their critical value for initiation of growth usually at the largest flaws, which will be activated first. These flaws may grow stably or unstably and can be expected to subsequently span the entire thickness of the ply group (several plies of the same angle stacked together). This cracking process redistributes the stress field in the laminate, and all subsequent cracking must reflect couplings between any newly activated flaws and the increasingly complex, non-uniform stress field. Thermal exposure is likely to enhance the coupling [11].

ERR release rate method [3] assumes that the next microcrack forms when the total energy released by the formation of the microcrack reaches a critical value called material microcracking fracture toughness. By measuring changes of this value in various aging environments, it is possible to study degradation of laminates and make predictions about durability. Another advantage of the energy analysis is that it can be extended to explain microcracking during fatigue loading either by cyclic mechanical loads or cyclic changes in temperature. In static loading, microcrack propagation is governed by the thickness of the 90^{o} plies. When the 90^{o} plies are thick, the microcrack propagation is instantaneous; when the 90^{o} plies are thin, the microcrack propagation is controlled or perhaps even suppressed. That can be explained by taking into consideration a significant effect of 90^{o} ply thickness on the strain to microcrack initiation. For 90^{o} plies greater than around 0.5mm thick, microcracks form as instantaneous fracture events. For thicknesses between 0.1 and 0.5mm, individual microcracks can sometimes be observed to initiate on the edges and propagate across the width of the laminate. For thicknesses less than 0.1mm, the microcracks are suppressed entirely and the laminate fails before initiation of microcracking. During fatigue loading, microcrack propagation depends also on the amplitude of the fatigue stress. Also, the stress intensity factor or energy release rate for the propagating microcrack is independent of the length of the microcrack and only a function of the space between existing microcracks where the microcrack is growing. Thermal cycling induces biaxial loading while mechanical cycling is predominantly axial loading. Temperature effects such as physical aging or thermal degradation at high temperature, embrittlement at low temperature, and other temperature-dependent mechanical properties normally cause the thermal cycling results to differ from the corresponding mechanical fatigue results.

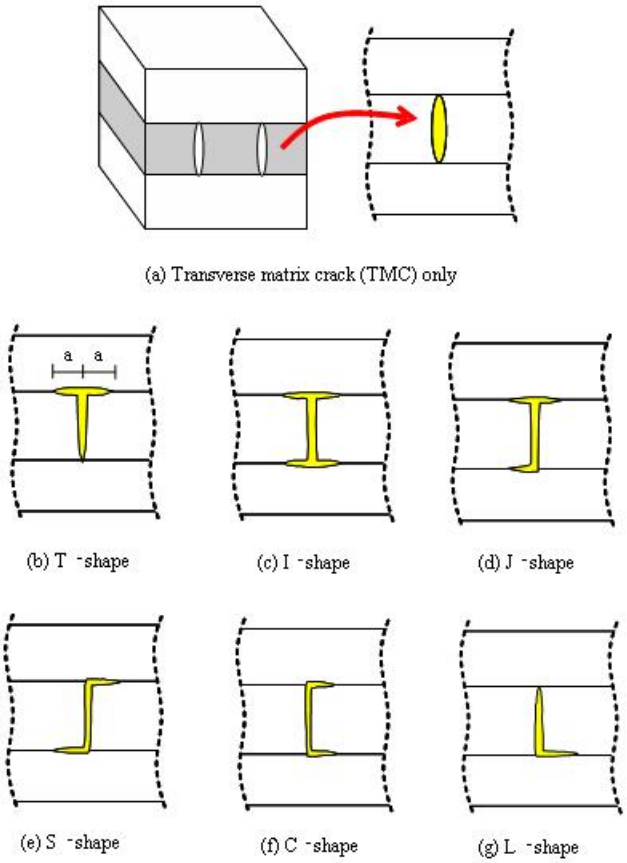

Fig. 2.1.3. Various damage configurations [12]

Strain energy release rate (SERR) was used for a delamination at the intersection of matrix cracking. SERR available for driving delamination growth varies along the delamination front and is very sensitive to a variety of geometric and load parameters. As the ply thickness decreases, the SERR decreases, but has no adverse effect on sensitivity to microcrack density. The result indicates that the delamination would grow with a certain width along the microcracks. The size of the width depends on the critical SERR and the loadings. The opening displacement was calculated for various damage configurations with transverse matrix cracking and delaminations. Effect of crack junction area (in that case assumed to be simple intersection of the cracks) on the effective permeability of a two-ply composite was studied by altering the relative orientation of two plies. Characterization of effective permeability of a composite mainly involved three steps. The first was damage characterization, which involved estimation of ply level damage using non-destructive techniques such as X-ray scanning, ultrasonic, and edge optical inspection. The second was estimation of matrix microcracking and crack junction openings for a given ply crack density. The third step was estimation of the effective permeability of the composite by analyzing flow through microcracking and their junctions that made up leakage paths. Due to the large size of microcracking compared to crack junction, resistance offered by transverse matrix cracking to

cryogen flow was taken to be small when compared to resistance offered by crack junction. Thus, the permeability of a composite was proved to be greatly dependent on the number and distribution of crack junctions. Due to varying crack density in each ply it was difficult to choose a representative volume element that includes representative cracks in all plies. Hence, the problem was bifurcated into series/parallel combinations of crack junctions for permeability estimation [12].

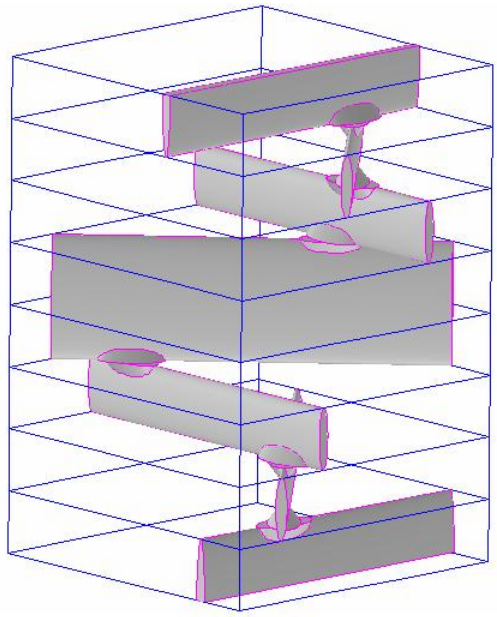

Fig. 2.1.4. 3-D schematic of leakage path [12]

It has been claimed that the rate of energy released in the formation of a new full-width microcrack is consistent with fracture mechanics based on microcrack growth. The theoretical basis of using such an energy release rate criterion for the transverse cracking was shown by deriving a steady-state cracking model for a laminate use of a path-independent surface integral. Solutions for steady-state microcracking of cross-ply laminates were determined using energy calculations based on a variational model that had demonstrated accuracy. As demonstrated, in general steady-state cracking is not expected to occur because of the free-edge effects. The influence of this effect on the initiation of layer transverse cracking and potential microcracking that may develop at the fiber/matrix interface was investigated using the average macroscopic stress field predictions within a single cell in a micromechanics model [10].

A new method called the crack-tip force method was derived for computing ERR in delaminated beams and plates. In this method the delaminated plate was divided into two laminates on either side of the plane of delamination. The interaction forces, called crack-tip forces, between the sub-laminates at the crack-tip were computed. The ERR was expressed as a quadratic function of the crack-tip forces and the plate compliance coefficients. The crack-tip force method was compared to the virtual crack closure

technique as well as to the strain energy density method using double cantilevered beam specimens as examples [13].

In order to study the permeation problem, it is necessary to predict the COD in every layer that forms a path through the entire thickness of the laminate by finding an analytical solution for delaminated crack opening displacement (DCOD). The main factors influencing the permeability of cryogenic fuel are the DCOD and the crack density in each ply. An analytical methodology based on first-order shear laminate theory was applied to predict opening displacement associated with delamination in a cross-ply laminate system subject to thermal and mechanical loading conditions. A comparison mathematical model was developed using Darcy's law for isothermal, viscous flow of gases through porous media [2].

Both energy release rate and average ply stress calculated using damage mechanics analysis were used to evaluate matrix microcracking under thermal fatigue loading. Constrain effects on the matrix cracking can be explained by the energy criterion, but these effects are not observed in thick plies experimentally. So both the energy release rate and ply stress should be considered for the matrix cracking under fatigue loading. Modified Paris law approach was used and proved effective in thin plies and average stress approach was effective for thick plies [14].

Another analytical method for thermally loaded laminates was also developed. Microcrack density in one ply group, and reduced laminate properties resulting from these cracks, were predicted as functions of monotonically decreasing temperature. The effects of thermal cycling were included in the analysis by using a material degradation fatigue model. However, the method was severely limited in its practical use by the ability to predict crack density in only one ply group and microcracking is predicted in all but the surface plies of any symmetric laminate [15].

Ply cracking behavior of quasi-isotropic laminates has been investigated in constant-amplitude tension-tension and tension-compression fatigue. Block loading tests were also performed to assess the load sequence effect on ply microcracking. The results revealed that low/high sequence is more deleterious than high/low sequence. A cumulative damage model was introduced to describe the ply cracking under a variety of fatigue loadings and approach of ply stress-life relation was proposed. According to the model, the initial microcracking of constituent plies can be represented by a stress-life curve using a polynomial failure function. The stress redistribution resulting from ply cracking is described by stiffness reduction coefficients [16].

Variations such as fiber orientation, laminate stacking sequence, and modification of the composite matrix resin component can yield a desired variety of material and structural properties. The type of fibers and the polymeric matrix used in the composite play a large role in determining the propensity for microcracking as well as the microcrack morphology. Higher fiber tensile moduli result in increased microcrack density and larger cracks. Increased backbone flexibility causes an increase in microcrack density and decreases the glass transition temperatures of the laminates. The curing agent used in the matrix formulation also plays a key role in the response of the resulting material to cryogenic cycling. The presence of a rubber toughener prevents the formation of microcracks and the fibers and the

matrix used play an important role in determining the response to cryogenic cycling by altering the thermal stresses present in material as well as the ability of the material to resist thermal stresses.

Many studies were based on testing the whole variety of samples in different loading and cycling conditions. Cryogenic cycling efforts to date have focused on many of the factors contributing to damage initiation and development such as the number of cycles and the temperature profile of the applied cycle. Microcrack formation in composites is typically observed on the exposed edge of a sample. While the measurement of the location and density of matrix cracks observed on the laminate edge is important, the distance that the cracks grow away from the edge of the sample (span) is also needed to determine whether the accumulated microcrack will significantly affect structural permeability or mechanical properties. Several researchers using X-radiography, die-enhancing penetrant, and visual observation on the laminate edge or through partially transparent composites have shown that under mechanical static loading, mechanical fatigue loading, or thermal cycling, a consistent pattern of microcrack formation and growth occurs in cross-ply and angle-ply laminates.

Large thermal stresses may develop in CFRP laminates due to the mismatch in CTE of the fibers and the matrix, at a microscopic level, and consequently of adjacent plies stacked with different orientations. So, in cross-ply laminate for example, cyclic temperature variations induce cyclic biaxial in-plane stresses in every layer. In that case, cyclic thermal exposure is likely to enhance damage similar to that observed under mechanical fatigue. Fatigue tests at room temperature and thermal cycling experiments have been performed on carbon/epoxy laminates of cross-ply $(0_3/90_3)_S$ and $(90_3/0_3)_S$ made from T300/914 and complex stacking sequences $((0/\pm45/0/90)_3)_S$ made from IM7/997-2 in temperature range (-50/150^{o}C) and (-50/180^{o}C) respectively in up to 500 cycles [17]. The subscript *s* signifies that the laminate is symmetric with respect to its mid-plane, and the numerical subscripts denote the number of similar plies. A $(90_4/0_4)_S$ cross-ply laminate has been tested in four different temperature ranges: (-200/20^{o}C), (-200/50^{o}C), (-200/90^{o}C), and (-200/130^{o}C) in 30 or 40 cycles. Microcracks were found to initiate in both 0 and 90^o plies, followed by delamination along the cracks, at the 0/90 interface. The influence of the temperature amplitude has been clearly shown [5].

Different epoxy resins like EPON 828, 836, and 871 with two curing agents and carbon fibers Toray T3000, T800H, and M35J in the form of unidirectional pre-pregs and $(0_3/90_3)_S$ configuration laminates were tested. Dynamic mechanical analysis and cryogenic cycling (-195.8/22^{o}C) for 5 times was performed. It was observed that the laminates with lower glass transition temperatures displayed greater microcrack densities. Increased backbone flexibility altered the response of the matrix to temperature changes. Variations in the matrix chemistry and the incorporation of a rubber toughening agent could have altered the degree of adhesion between the fiber/matrix interface, and any change in the strength of adhesion in this area could have significantly altered the response of the composite materials to cryogenic cycling. The tensile modulus of the fibers influenced the microcrack morphology as well as the crack density. The cracks typically became wider and more convoluted when higher modulus fibers were used [18].

Test of aerospace grade composites were performed in NASA laboratories. Three graphite fiber systems, IM7/5250-4, IM6/950-1, IM7/T24 with $(90_2/0_2)_S$ and $(90/45/0/-45)_S$ lay-ups were considered for permeability estimation. 4-point bending and uniaxial tension testing under thermo-mechanical load took place [12].

Transverse cracking behavior of cross-ply and quasi-isotropic CRRP laminates under cyclic loading was studied for IM7/133 intermediate modulus carbon fiber combined with toughened epoxy resin. Four types of stacking sequence of $(45/0/-45/90)_S$, $(45/0/-45/90/-45/0/45)_S$, $(0/90)_S$, and (0/90/0) were prepared. Detailed observations of both crack density and crack length in coupon specimens suggested there was a three-stage process comprising of edge crack initiation, edge crack growth, and crack propagation across the width in quasi-isotropic laminates, whereas simultaneous transverse crack initiation and propagation in width direction takes place in cross-ply laminates. ERRs associated with crack propagation were derived using the 2-D analytical model [19].

A new test method was presented for mode I delamination fracture toughness testing of laminated composites containing a high density of stitches or translaminar reinforcements. The test set-up induced an axial tension in the specimen in addition to the transverse forces responsible for propagation of delamination. The tensile stresses reduced the compressive stresses in the vicinity of the crack tip caused by the large bending moments required for crack propagation. The nonlinear differential equations of equilibrium were solved using an iterative procedure to obtain the strain energy release rate as a function of load and crack length. Results conducted using carbon/epoxy included mode I fracture toughness, crack tip bending moment, transverse deflection and slope as a function of crack length [20].

Effects of through-thickness stitching on mode II delamination toughness of graphite/epoxy uniweave textile laminates have been investigated by performing end-notched flexure tests. Different stitch yarns and stitch densities were considered. The crack propagation in stitched laminates was observed to be gradual and steady, unlike in the unstitched laminates where it was sudden. New methods of evaluating the effective or apparent critical strain-energy release rate for stitched laminates were presented [21]. There appeared to be an optimum stitch density at which the toughness had maximum value. The critical strain-energy release rate increased with increase in crack length as more and more stitches bridged the delamination.

Through-thickness reinforcement in the form of transverse stitching can significantly improve resistance to delamination of composite laminates in low-velocity impact [22]. The paper revealed that the analytical predictions of the area of delamination of stitched laminates is about 15% less than that of unstitched ones, and the numerical results are comparable with the test results. The resistance to low-velocity impact delamination can be better achieved by increasing stitch density.

Comparison of two different resin systems, epoxy 977-2 and 977-3, and bismaleimide 5250-4 with the same carbon fiber IM7 was made in cycling 1000 times with an elevated temperature/LN2 (-196/120^{o}C) or (-196/177^{o}C) and room temperature/LN2 cycle. Laminate sequence had the following orientation: $(0/90)_{2S}$ and $(0/\pm45/90)_S$. Microcracks were counted after 0, 1, 5, 15, 30, 75, 125, 175, 250,

325, 400, 500, 650, 800, and 1000 cycles. The combined cryogenic and elevated temperature thermal cycle produced substantially greater amounts of damage in the material systems tested than LN2/room temperature cycle [23]. Similar tests were performed for another resin, epoxy 3K, and compared to previous results. The thinner-ply laminates had significantly greater microcrack densities in some of the inner plies. Sectioning showed crack densities in sample interiors that were equal to or greater than those measured on the sample edges once damage became relatively pervasive in a ply. In addition, the 977-2 epoxy samples had in the order of magnitude fewer cracks in each ply as a function of cycling compared to the 5250-4 bismaleimide. Despite the severe damage build-up in 5250-4, 977-2 would not necessarily be preferred in all cases, because each material system had at least 2 damage free plies, which would help prevent leakage in fluid containment applications. Higher 5250-4 maximum service temperature could be also necessary in some structures [24].

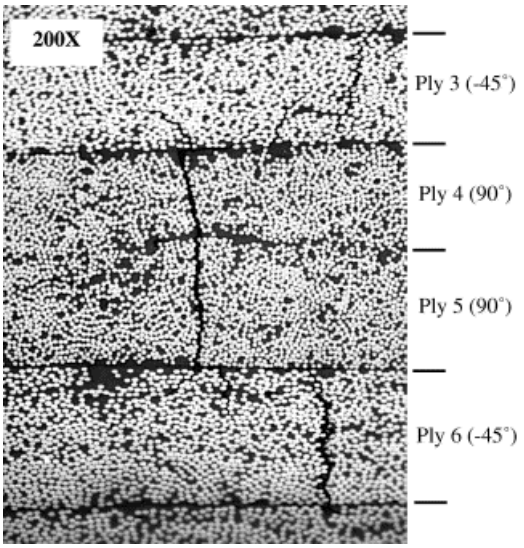

Fig. 2.1.5. Micro-crack locations in IM7/5250-4 ($[0/\pm45/90]_S$) [23]

The success of IM7/5250-4 graphite/bismaleimide in high performance aircraft applications and its expected application to aerospace cryogenic applications has prompted a number of studies of its response to various combined cryogenic and mechanical loadings. The amount, location, and span of microcracks produced by hundreds of cryogenic temperature cycles were documented as a function of lay-up sequence. Two cross-ply lay-ups, $(0/90)_{2S}$ and (90/0/90/0/90/0/90/0/90), and a quasi-isotropic laminate $(0/\pm45/90)_S$ of IM7/5250-4 were cycled 400 times between -196^{o}C and ambient temperature to determine whether blocking plies affected thermal fatigue resistance, laminate modulus or laminate 0^{o} tensile strength after conditioning. The samples were sectioned to determine whether cracks observed on the edges spanned the full width of the sample, leading to conclusions about the effect of cycling full sized panels versus relatively small samples with edges exposed to cryogen. $(0/90)_{2S}$ and $(0/\pm45/90)_S$ have adjacent (blocked) 90^{o} plies midway through the thickness, while (90/0/90/0/90/0/90/0/90) is a laminate without blocked plies, and the effect of blocked lay-ups could be observed. An un-blocked

laminate with relatively thin plies is most desirable since the microcracks may be trapped in the surface plies, allowing the inner plies to remain as a barrier to fluid leakage. A stacking sequence with the ply adjacent to the surface ply 90^o out of phase with the surface ply is more desirable than one with an adjacent ply only 45^o out of phase because the interface between plies 90^o out of phase is more effective in arresting the many surface ply microcracks due to thermal stresses [25].

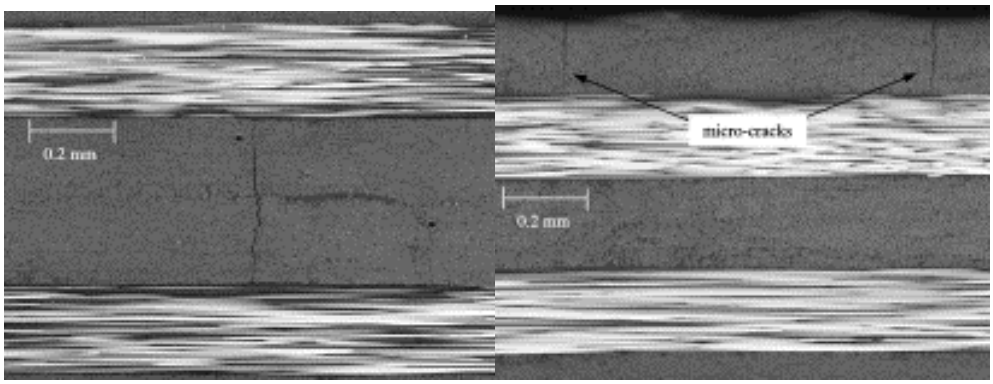

Fig. 2.1.6. Micro-cracks in 90° ply block of a $[0/90]_{2S}$ on the left and in surface ply of [90/0/90/0/90/0/90/0/90] on the right [25]

Four different cross-ply laminate IM7/5250-4 panels (0/90/0), $(0/90_2/0)$, $(0/90_3/0)$, and $(0/90_4/0)$ were fabricated in an autoclave from pre-preg form. Evidence for steady-state cracking has been shown for $(0/90_3/0)$ and $(0/90_4/0)$ laminates whereas the (0/90/0) and $(0/90_2/0)$ laminates exhibited partial edge cracks, i.e. stable ply-level transverse cracking [10].

Microscopic damage behavior of carbon/bismaleimide G40-800/5260 under tensile loading for 10 kinds of laminate configuration was investigated for two temperatures: 25 and 180^oC. G40-800/5260 is a candidate for structural material because of the high heat-proof quality of bismaleimide resin. Resin rich layers were located between layers to improve the interlaminar fracture toughness. Matrix cracks and delamination initiated at both room and high temperatures. The difference of the microscopic damage was that matrix cracks in 90^o plies went through the width at room temperature, however, cracks grew only up to the delamination front at high temperatures. There was no effect of adjacent ply modulus of 90^o plies on matrix microcracking behavior. First cracking strains were independent of the ply thickness; however, matrix crack density growth rates became larger as the ply became thinner. Matrix crack resistance of G40-800/5260 was larger than epoxy-based CFRP [26].

A carbon fiber reinforced polyimide PMR-15 system with two laminate stacking sequences, $(0/90)_6$ and $(\pm45)_6$, was investigated to evaluate fiber and matrix dominated laminate properties. The samples were thermally cycled using a simulated component cycle between -18 and 232^oC increasing at 43^oC/min and decreasing at 10^oC/min with a 10min dwell at each temperature. No evidence of microcrack intensity plateau was observed at 5000 thermal cycles. Microcracking of the inner plies gave rise to reduction in matrix-dominated (compression and shear) residual strengths at both room and 232^oC temperatures, although the effects were less pronounced at 232^oC. No significant effects on moduli at

either temperature were exhibited. Microcracking had no effect on fiber-dominated properties. Isothermal ageing after thermal cycling produced further reduction in matrix-dominated residual strengths. Compressive fatigue loading (1000 cycles) had little additional microcracking effect on thermally cycled samples. Thermal cycling of cracked samples having 1% moisture content gave no significant increase in microcracking compared to relatively dry samples [27].

Two thermoplastic resin systems, a semicrystalline polyetheretherketone (PEEK) reinforced with high tensile AS4 carbon fibers and an amorphous polycarbonate (PC) reinforced with high tensile HTA 7 carbon fibers, were selected for other experiments. Unidirectional and cross-ply laminates were tested in cryogenic, high frequency test equipment in temperature cycles from room to liquid nitrogen temperature with stable cooling and heating rate. Carbon reinforced thermoplastics at low temperature showed a higher sensitivity against tension-tension fatigue loads than epoxy matrix composites. The fatigue endurance limit was significantly lower than predicted from the durability of carbon fiber. Due to local fiber buckling the fatigue endurance limit decreased in tension-compression tests to less than 30% of the initial strength [28]. The tensile tests were performed with 'dog bone' specimens, necked in the thickness (for unidirectional composites, tested parallel) or necked in the width. The interlaminar shear strengths were examined in series of short beam shear tests with a span to thickness ratio of 5:1. All tests were performed in liquid nitrogen, liquid helium and room temperature. From examination it was concluded that in general the high cryogenic fracture strength of some advanced thermoplastics is beneficial for the tensile fracture strength of CFRPs. The comparatively high production temperatures of the thermoplastics are problematic, because they result in thermal pre-stresses within the unidirectional layers and within angle-ply composites due to the expansion mismatch and due to the expansion anisotropy, respectively. This especially holds true with respect to the mechanical response to long term and fatigue loads [29].

Influence of manufacturing process was also investigated. Three types of high tensile carbon fibers, G30-500, AS-4, HTA 7, and two resin systems, epoxy EP Rigidite R5212 and a modification of the thermoplastic, semicrystalline PEEK were chosen as matrix systems. The following manufacturing processes were used: pressing of unidirectional layers, filament winding, and pressing in autoclave [30].

Other types of fibers were studied, and at least one should be mentioned here. Laminates with 3M type 1003 E-glass/epoxy with a cross-ply $(0_2/90_3)_S$ and multi-directional $(\pm 45/90_3)_S$ sequence were examined in quasi-static and cyclic tests. These laminates were chosen because the $(0_2/90_3)_S$ laminate displays an ultimate failure mode that is dominated by the 0^o fibers, while $(\pm 45/90_3)_S$ laminate exhibits an ultimate failure mode that is dominated by matrix in the 45^o constraining plies. The response of the laminates was investigated by examining parameters such as crack density, stiffness reduction, the achievement of a characteristic damage state, damage growth, as well as damage life curves for the different lay-ups. The $(0_2/90_3)_S$ specimens were found to require larger loads before damage initiated . This was due to the much higher stiffness associated with the outer constraining plies. Both the $(0_2/90_3)_S$ and $(\pm 45/90_3)_S$ laminates experienced similar drops in the magnitude of the stiffness due to the matrix cracking. However, in terms of percentage with respect to the undamaged stiffness, the reduction for the

$(\pm 45/90_3)_S$ laminates was 60% compared to 20% for the $(0_2/90_3)_S$ laminates. In comparison to the quasi-static results microcracks under cyclic loading initiated at lower stresses [31].

Low temperature influence on E-glass and S2-glass reinforced polyester composites was studied by subjecting the samples to flexural tests. A commercially produced E-glass fiber reinforced plastic composite produced cracks on prolonged thermal cycling between 50^{o}C and -60^{o}C temperature for 100 times, but a specially manufactured S2-glass woven laminate did not produce any visual cracks for two and a half times more thermal cycling in the same temperature range. The polyester resin matrix of E-glass composites appeared to have a higher rate of modulus increase than the one with S2-glass. Low temperature thermal cycling has shown degradation of both the Young's modulus and shear modulus of the plain-weave glass composites [32].

Carbon fiber/bismaleimide composite has recently been developed for high temperature applications. It offers hot/wet service temperatures up to 230^{o}C. Such materials are invariably used in aerospace industry, and so knowledge of thermal stability and corresponding ageing behavior is essential if such materials are to be used with any confidence. Of all polyimides, bismaleimides are the easiest to fabricate and can be processed using similar conditions to epoxy resins. Early bismaleimides were extremely brittle due to their high crosslink density, and would often crack during the post-curing cooling-down phase. More recent developments have largely reduced this effect by chemically modifying the resin constituents. The results showed that different degradation mechanisms are at work at different ageing temperatures [33].

For graphite/bismaleimide composites, the bismaleimide cure reactions are incomplete after standard composite fabrication and post-cure procedures and further cure can occur in service environment conditions resulting in increases in glass transition temperature and associated composite mechanical property deteriorations. The studies were carried out in order to ascertain the sequence and relative rates of the cure reactions and the nature of chemical reactions that are capable of further reactions, with associated thermal and mechanical property modifications, in future aerospace service environmental conditions [34].

Above carbon fiber reinforced bismaleimide composite was also evaluated to determine the effect of fiber type and exposure to a high temperature environment on its interlaminar-shear strength and impact performance. The laminates were manufactured using Cytec 5250-4 bismaleimide pre-preg system and two different types of carbon fibers, T300 and T650-35. Thermal aging of specimens at temperatures of 210, 230, and 250^{o}C for up to 2000h resulted in progressively increased matrix loss and fiber-matrix interface degradation. The degradation manifested itself mainly as a gradual reduction in interlaminar shear strength and variations in impact failure modes. Higher values of peak force and total impact fracture energy were obtained with the composites containing T650-35 carbon fibers, and the associated specimens exhibited hinging due to fiber bridging at the higher levels of aging [35].

Two polyimide matrix systems (Avimid and PETI with IM7) were subjected to a series of hygrothermal aging experiments at various temperatures and relative humidities. For each aging

condition, the water absorption rate and the microcracking toughness were measured as a function of aging time. The toughness increased with time and the rate of decrease increased with temperature and relative humidity [36].

Five different laminate configurations of carbon fiber polymeric composite IM7/PETI-5 that were evaluated for tensile and compressive strength and stiffness at room and two cryogenic temperatures (-196°C and -296°C) have been examined respectively. The effects of laminate configuration, test temperature, and preconditioning or aging were investigated. The measured properties [37,38,39] indicated that temperature, aging, and loading mode can all have significant influence on performance, which influence is a strong function of laminate stacking sequence. Aging consisted of 576 hours of exposure in a -184°C environment, both with and without constant-strain mechanical load. Microscopic examination of the surface morphology showed evidence of degradation along the exposed edges of the material because of aging at cryogenic temperatures. Examination of the basic laminate properties such as strength and stiffness, in the longitudinal and transverse directions, indicates that cryogenic temperatures can have an appreciable influence on behavior, as expected, but unexpected trends can occur. For example, the tension test data show that the longitudinal and transverse stiffness and strength decreased as the test temperature decreased. Conversely, the tensile shear modulus and strength increased as the temperature decreased. For tension loading, some of the laminate stacking sequences, such as $[45/90_3/-45/0_3]_S$ and $[\pm 25]_{3S}$, were less influenced by a reduction in temperature, than the other laminates. However, the $[45/90_3/-45/0_3]_S$ laminate was more sensitive to cryogenic temperatures than the $[\pm 25]_{3S}$ laminate. For compression loads, exposure to cryogenic temperatures produced an increase in both the modulus and strength of all the laminates. The greatest increase in compressive strength occurred for the $[90]_{12}$ laminates and the greatest increase in modulus occurred for the $[\pm 45]_{3S}$ laminates. Based on lamination theory, residual-stress calculations indicate that the transverse tensile ply stresses, associated with matrix cracking, can be quite high at cryogenic test temperatures. The $[\pm 25]_{3S}$ and $[45/90_3/-45/0_3]_S$ laminates were predicted to have the highest values of residual stress, which is important because these transverse residual stresses may reduce the strength and stiffness of the laminates by accelerating the initiation, growth, and accumulation of transverse microcracks in a ply. The aging did not influence the fracture surface characteristics. Cryogenic temperatures affected the fracture surfaces of only the tensile specimens. In general, the fracture surfaces from the room-temperature tensile tests appeared catastrophic, having irregular breaks, whereas the specimens tested at cryogenic temperatures exhibited clean breaks with a more regular appearance. The differences in the fracture surfaces of the tensile specimens were attributed to the ductility of the matrix material at room temperature versus the brittle nature of the matrix at low temperatures.

The efficiency of load transfer through the interface between the fiber and the matrix plays a critical role in the performance and behavior of fiber reinforced composite materials, such as pull-out, push-out, microbond, and fragmentation tests, have been extensively used in recent decades. Single fiber pull-out tests were used for investigation of interfacial bond strength or toughness and load transfer

between polymeric matrices and glass fibers having different diameters. The interfacial bond strength was well characterized by an ultimate interfacial shear strength whose values were nearly independent of fiber diameter. The same experiments were also analyzed by fracture mechanics methods to determine the interfacial toughness [40].

2.2. Sandwich Structure for Liquid Gas Storage

The aerospace community has long recognized the necessity of strong, lightweight, damage-tolerant structures. Composite materials or materials generally comprised of two or more constituents with combined properties that are superior to the individual components, which have been touted as the future for engineering materials, are still considered prototypical and largely used in only military and experimental craft. One concept that has a long history in aerospace structures and has received considerable attention is sandwich structure. A sandwich structure consists of thin high-strength facesheets (skins) bonded to a relatively thick, low-density, low-strength, lightweight core. This type of construction was first used in aircraft in the 1920s and has been used in some form in nearly every aircraft and spacecraft since.

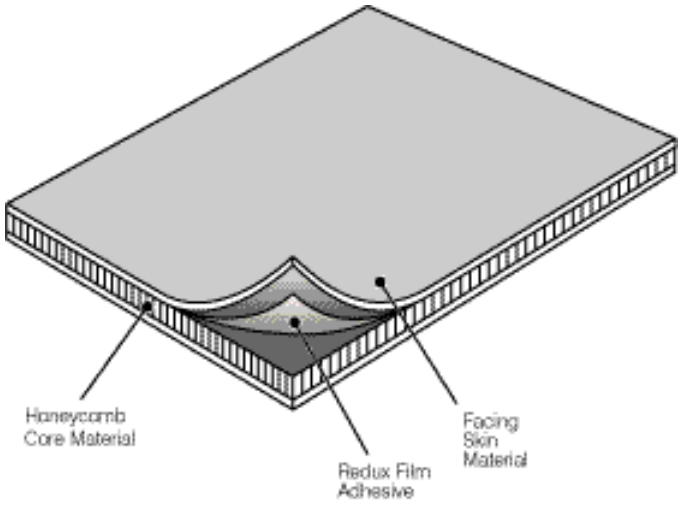

Fig. 2.2.1. Sandwich structure

Cores of sandwich structures typically can be divided into four types according to geometry and shape as follows [41]:

- honeycomb core,
- solid of foam core,
- corrugated core or truss core,
- web core.

However, several approaches to design new types of core component have lately been presented. Examples include:

- star shaped repeated pattern core,
- cellular core formed by the progressive corrugation of a single continuous sheet of material,
- new honeycomb core and tube-core,
- foam-reinforced web core of foam-filled core (sometimes referred to as Rohacell sandwich construction).

In Fig. 2.2.2. a sandwich structure and a monolithic structure are shown and the efficiency of the sandwich concept is demonstrated. The sandwich panel has facesheets that are 1/10 the thickness of the core, while the monolithic panel has a thickness twice that of a facesheet. The same amount of facesheet material is present in both panels, but the sandwich panel has a bending stiffness 75 times that of the monolithic structure. Hence, for a given weight the stiffness of a sandwich structure can far exceed that of traditional monolithic design. This efficiency makes it very attractive for use in any vehicle structure. In addition, sandwich structures offer superior acoustic damping and provide an excellent thermal barrier.

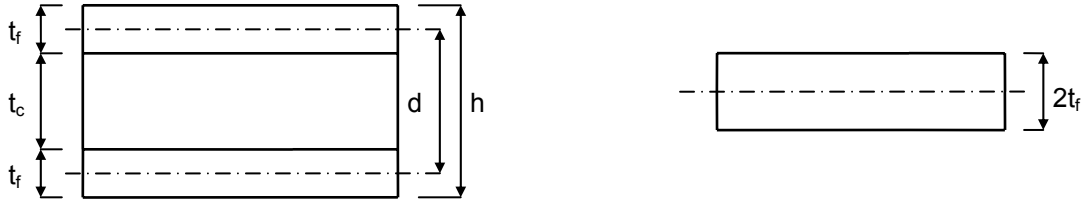

sandwich construction

monolithic construction

$$D_{sand} = \frac{E_f t_f t_c^2}{2\left(1-\nu_f^2\right)}$$

$$D_{mon} = \frac{E_f t_f^3}{3\left(1-\nu_f^2\right)}$$

$$\frac{D_{sand}}{D_{mon}} = \frac{3}{4}\left(\frac{t_c}{t_f}\right)^2 ; \frac{t_c}{t_f} = 10 \Rightarrow \frac{D_{sand}}{D_{mon}} = 75$$

Fig. 2.2.2. Comparison of sandwich and monolithic construction

The typical failure modes of sandwich structures include:

- tensile or compressive failure (generally of the facesheets),
- transverse shear fatigue (typically within the core),
- buckling of the entire structure,
- core shear instability,
- face wrinkling instability,
- face dimpling.

Furthermore, it has been shown that adhesively bonded sandwich structures are susceptible to damage from low velocity impact. Impact generally leads to debonding of the facesheets from the core. Once debonded, under certain loading conditions, catastrophic failure may occur due to this weakening of the structure. Microcracking of the facesheet during manufacturing or resulting from thermocycling, load,

fatigue or impact leaves the sandwich structure vulnerable to moisture or gas penetration. With increased pressure within the opened cell core, both core failure and facesheet/core debonding are more critical.

The next generation of space transportation vehicles will require advances in lightweight structural materials and related design concepts to meet the increased demands on performance. One potential source for significant structural weight reduction is the replacement of traditional metallic cryogenic fuel tanks with new designs for PMC tanks. These new tank designs may take the form of thin-walled sandwich constructed with lightweight core and composite facesheets. Life-time durability requirements for cryogenic fuel tanks imply that the materials must safely carry pressure loads, external structural loads, resist leakage, and operate over an extremely wide temperature range.

One of the first demonstrations of a PMC cryogenic fuel tank occurred in 1996 when the DC-XA suborbital demonstration vehicle was build with an all-composite liquid hydrogen fuel tank. The DC-XA tank was designed as an unlined and unstiffened cylinder measuring approximately 2.4m in diameter. The tank performed as expected in both ground and flight tests.

One possible failure mechanism, associated with the use of sandwich materials for an integrated cryogenic tank (i.e. one that is integral to the airframe structure), is debonding of the facesheet. This mechanism can occur due to high pressure inside the core material and is facilitated by the occurrence of cryopumping [42]. The most extensively used sandwich structure in aerospace technology is the honeycomb-core sandwich structure. Because the honeycomb cell generatrix (a line whose motion generates a honeycomb cell wall) is perpendicular to the facesheets, only line contact endures proper bonding between the facesheets and the honeycomb core. Cryopumping can occur in closed cells during repeated cryogenic fluid fill and drain cycles and is simply the condensation of a gas on a cryogenically cooled surface that results in a vacuum and greatly decreased pressure inside the cells. For a cryotank with PMC sandwich materials in the tank walls, this cryopumping will occur when the tank wall facesheet(s) develop leaks and allow the cryogen to permeate into the core. Subsequent warming of the cryogen causes a transition from a liquid to a gas phase and results in a substantial increase in core pressure. Without proper venting of this pressure, the core, facesheet, and bondline must sustain the resultant pressure loads without failure. The most likely initial failure mode due to cryopumping is facesheet-to-core debonding that can lead to crack growth and a total separation of the facesheet.

Most notably of such failure mode is the NASA X-33 reusable flight demonstration vehicle. The X-33 was designed with a large (8.7 x 6.1 x 4.3m), conformal tank made from a sandwich construction of polymeric composite skins and phenolic core. After successful completion of the first protoflight pressure and loads test, the tank was drained of its liquid hydrogen fluid, and a purge of the tank began. Approximately 15 minutes after the tank was drained, the outer facesheet and core separated from the inner facesheet along part of the tank wall. It was subsequently determined that many factors contributed to the tank failure. Considering the mechanics of the failure, it was found that the inner tank wall allowed permeation (and hence cryopumping) by way of microcracks in the facesheet. As pressure and strain decreased below the required level to sustain the microcrack paths, the leak paths closed. As the tank

warmed, the remaining trapped cryogens proceeded to vaporization, creating high pressure. This pressure, coupled with bondline defects, likely caused the failure. The failure or debonding location occurred almost exclusively at the core-to-adhesive surface on the inner facesheet side.

A team from NASA and Lockheed Martin and several independent consultants investigated the incident. The team followed a fault tree approach with a combination of analyses, tests, and data evaluations to determine potential causes of the failure. The Korex-3/16-3.0 (1.5in thick) core used on the LH2 tank was a combination of light and dark material. During the cryopumping tests, the dark core communicated the GHe purge gas quicker than did the light core. The basic light Korex was made from 2.6mil Kevlar paper, while the dark core was made from 1.8mil paper. The 1.8mil core required more phenolic dips to obtain the required weight. There was some evidence that the region of the failed core (dark core) had a better bond than the light colored core over most of the acreage. The outer facesheet was a 7-ply, IM7/977-2 laminate (0.034in thick) with stacking sequence (65/0/-65/90/-65/0/65). The inner facesheet was a 13-ply laminate (0.066in thick) with stacking sequence ($45/90_3/-45/0_3/-45/90_3/45$). Several tests and analyses were used to determine the most likely cause of failure. Microstructural analysis showed the potential for microcracking under combined thermal and mechanical loads. Inner facesheet coupon tests with cryogenic and bi-axial mechanical loads demonstrated the same phenomenon. The specimen permeability test confirmed that the inner facesheet microcracked and that the leakage rates were a function of tank pressure. Thermal analysis correlation with measured temperatures demonstrated that both hydrogen and nitrogen must be present in the core to achieve the high cryopumping loads observed. Additional tests on different sandwich structure materials were performed. The two core materials used for the test specimens were Hexcel HRP-3.16-8.0 (fiberglass reinforced phenolic honeycomb) and DuPont Korex-1/8-4.5 (aramid fiber reinforced phenolic honeycomb); these were nominally 0.5in thick. The facesheets were made of Hercules AS4/8552 graphite/epoxy composites and were nominally 0.059in thick. The permeability of the sandwich specimens was measured during both static (tension) and dynamic (reversed and non-reversed) shear loads [43].

Above mentioned tests were followed by many researchers searching for the optimal sandwich structure solution for cryogenic tanks. IM7/977-2 and Kevlar honeycomb were chosen as the most prospective and reliable materials. Sandwich structure with 15-ply quasi-orthotropic facesheet (45/90/-45/0/-45/90/45/0/45/90/-45/0/-45/90/45) fabricated with per-ply thickness of 0.132mm, 3/16-6.0 non-perforated Kevlar core, adhesive, and aluminum foil as a permeability barrier was tested in three-point bending at room temperature, -196^{o}C, and -269^{o}C. The in-plane stiffness of the composite facesheets was a strong and week function of laminate orientation and a test temperature respectively. It was determined that critical SERR increased with a decrease in temperature and simultaneously decreased with an increase in crack length [42].

Thin polymer films were considered as candidate materials to augment the permeation resistance of cryogenic hydrogen fuel tanks. To evaluate performance of candidate films after environmental

exposure, the experimental study was performed to measure the thermal/mechanical and permeation performance of six commercial-grade materials: polyimide Kapton, metallized polyester Mylar, polyvinyl fluoride Tedlar, Eval-F, which is an ethylene vinyl alcohol bonded to a polyester substrate, polyurethane 3M PUR, and fluoro-polymer Paint Replacement film [44]. Preconditioning consisted of specific combination of elevated temperature, cryogenic temperature, and moisture for extended periods of time. Polyimides are known to absorb moisture, influencing their mechanical properties. Metallized Mylar and Tedlar were not affected by hygrothermal exposure because polyesters and polyvinyl fluoride materials do not readily absorb moisture. The permeability data of three of the films, 3M PUR, Kapton, and Tedlar, showed no evidence that pre-conditioning had any significant effect, and Tedlar possessed the best barrier properties overall as it showed the lowest rate of helium gas permeation. The other three films, Eval-F, Mylar, and Paint Replacement, were not amenable to permeability testing.

Groups of IM7/977-2 laminate samples were thermally cycled under pre-specified numbers of times in a custom-built cryogenic Dewar, and then tested for strength and stiffness. An optical microcrack analysis and permeability tests were performed to help detail the underlying mechanisms behind these material property degradations [45].

A thermal evaluation of a composite tank wall design for a liquid hydrogen tank was performed. The basic tank wall configuration consisted of IM7/977-2 carbon/epoxy facesheets and a Korex honeycomb core sandwich that was insulated with Airex cryogenic foam and an Alumina Enhanced Thermal Barrier AETB-12. Tank wall models at a windward side location on the fuel tank were analyzed for three basic flight conditions: cold-soak (ground-hold), ascent (launch), and re-entry. Wall through-the-thickness temperature gradients as a function of flight time were obtained for future incorporation into a full-scale thermostructural analysis to evaluate the adhesive bondlines [46].

A Finite Element Analysis (FEA) based micromechanics method was developed to investigate microcracking in a graphite/epoxy composite liquid hydrogen tank at cryogenic temperatures. The unit cell of the fiber composite was modeled using solid elements. Periodic boundary conditions were applied to the surfaces of the unit cell. The analysis took the variable CTE of the matrix material into account. The thermo-elastic properties of the graphite/epoxy composites were evaluated by using the micromechanics model. The components of macro-strain at the desired location in the composite were computed from global analysis. Then the strains and temperatures were applied to obtain the micro-stresses in the fiber and matrix media, which are used to predict failure such as microcracking of the matrix phase [47]. The stress singularity at the tip of a transverse crack touching a ply-interface was determined using an analytical procedure. The results were also verified by performing a FEA of four-point bending and uniaxial tensile specimens containing a transverse crack. The fracture tests were performed under cryogenic conditions in liquid nitrogen [48].

Sandwich structure with Toray graphite/epoxy pre-preg and stacking sequence (65/0/-65/90/-65/0/65) and 1in thick Nomex honeycomb core 1/8-4.0 was used in cryogenic temperature cycling and compression-after-impact tests. Test with the cryo-cycled panels showed that the exposure to cryogenic

temperature significantly decreased the compressive strength due to the formation of micro-cracks. The laminate was impacted with a cylindrical projectile with a hemispherical nose using a gas gun at different velocities. The leakage after impact was measured using change in pressure in the pressure chamber. The autoclave-cured laminates performed better than vacuum-oven-cured ones and cryo-cycling reduced the threshold impact velocity for damage [49].

Several polymer films were introduced between layers in the composite to form an interleaved, or hybrid composite to determine the effects on permeability. The effects of the interleaved layer thickness, number, and location on the mechanical properties of composite laminate were investigated. It involved introducing a layer or layers of polymeric film into (interleaving) or onto (coating) the composite inner skin that will act as a barrier and contain LH2 fuel in presence of microcracks. The following materials were taken into consideration: aluminized Mylar, self-metallized polyimide, Vectra, inorganic-organic films, polyimide/nanoclay interleaf, and phenylethynyl-containing imide silanes. Based on the results of the permeability tests, the phenylethynyl-containing imide silanes and the aluminized Mylar films showed the greatest promise as barriers to argon gas at room temperature. Mechanical tests of the interleaved composite panels showed that failure was delamination caused by a weak aluminum to Mylar bond [50].

Current autoclave methods for manufacturing reusable aerospace structures are time-consuming, expensive and unreliable. Additionally, these methods are not conducive to manufacturing of new smart composite materials with embedded sensors due to damage that is caused to the sensor material during curing. The overall objectives of another project were to investigate the use of cost effective, non-autoclave manufacturing techniques for the fabrication of large, reusable composite structures. The program focused on the advanced fiber placement composite manufacturing technique that has shown potential to produce cost effective structures. Composite fabrication is a complex process with numerous physical phenomena occurring simultaneously. These phenomena include heat transfer, resin flow ply compaction, resin cure kinetics, and void growth and collapse. Advanced fiber placement uses a computer controlled placement head to lay the pre-preg tape in a precise geometric pattern on the surface of the mandrel. Once the lay-up procedure is completed, the part still must be cured in an autoclave. Combining the lay-up procedure with cure-on-the-fly technologies would be particularly attractive because the pre-preg tape is laid down, consolidated, and cured in a single step. Also a new concept for hydrogen gas detection has been developed based on a piezoelectric-sound-resonance-cavity and included in new tank design [51].

Though different tank concepts are being considered, many require that the cryogenic insulation will be evacuated and bonded to a structure. An attempt was made to evaluate the effectiveness of maintaining a vacuum on a specimen when they were cycled down to liquid nitrogen temperatures. Foam of honeycomb core was encased within graphite/epoxy laminate skins and that involved fabricating ravioli shaped specimens. In addition to these tests, flatwise adhesion pull-off tests were performed at room temperature on several combinations of materials with different adhesives. The materials bonded included graphite/epoxy, graphite/bismaleimide, aluminum, and stainless steel facesheets, and titanium

and Hexel honeycomb or Rohacell foam core materials. Two types of tests were performed in support of cryotank development efforts [52].

Many space structures require not only high stiffness but precision alignment and dimensional stability as well, which makes the low CTE of carbon fiber composites attractive. Composite laminates can be tailored to obtain a near-zero CTE, however, laminate CTE can change in service as a result of physical damage or material property changes associated with thermal cycling, outgassing, and exposure to atomic oxygen, radiation, etc. Strain gages provide an inexpensive yet accurate means of measuring very low CTEs (and CTE changes) of composite laminates, provided care is taken to minimize extraneous sources of error. Lamina thermal strains of the composite materials studied, AS4/3501-6 and XN-70/RS3, varied nearly linearly with temperature over the range explored [53].

Structural optimization capabilities in MSC.NASTRAN were used to size substructures and reduce the weight of honeycomb sandwich conformal cryogenic tank structures. The facesheet and honeycomb core thickness of the sandwich structures were used as design variables to be optimized. The thickness of the outer facesheet was assumed to be equal to the inner facesheet to avoid coupling between bending and extension. Geometrical nonlinear analysis results confirmed that final LOX and LH2 tank-wall designs met the strain constrains [54].

A composite dome was designed and manufactured to be used for experimental permeability characterization and leakage validation of composite vessels pressurized using LH2 and LN2. The preliminary design of the dome was completed using membrane shell analysis. Due to the configuration of the test setup, the dome would experience some flexural stresses and stress concentration in addition to membrane stresses. Also, a potential buckling condition exists for the dome due to external pressure during the leak testing. The dome design includes a circular opening in the center for the installation of a polar boss, which introduces a geometric discontinuity that causes high stresses in the region near the hole. The test article was a one-piece carbon/epoxy composite hemispherical dome cap and flange. In regions where stress concentration or gradients occur, rather than increasing the thickness of the entire dome, additional layers of carbon/epoxy cloth were used to attenuate these stress concentration. A complete numerical investigation of the critical load cases for CFRP dome have provided analytical results which showed the test article remained below required stress levels [55].

Over the years, many researchers have studied sandwich structures with special emphasis on the facesheets and it is generally agreed that the behavior of facesheet materials is well known. The same, however, cannot be said about sandwich core materials, especially those made from foam cores. It is clear that the delamination at the sub-interface region and the shear strength of the core in essence dictate the performance of the sandwich composites under flexure.

The unconstrained mode of deformation of the honeycomb core consists of slight stretching of the cell walls oriented within the loading direction and considerable bending of the cell walls perpendicular to the macroscopic loading direction. Especially the bending deformation of the cell walls is incompatible with the unconstrained mode of deformation associated with the facesheets. This incompatibility results in

the development of transition zones with increased strain energy density in the vicinity of the adhesive bond. At the intersections of multiple cell walls, singular stress fields have to be expected [56].

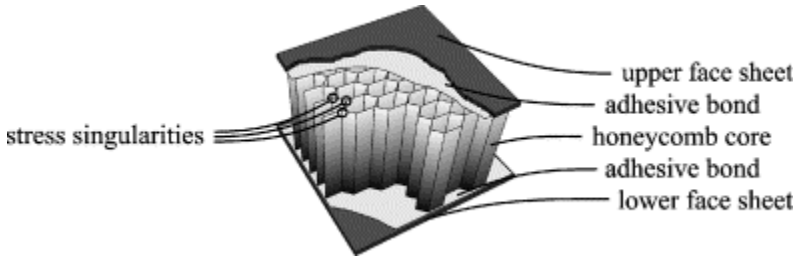

Fig. 2.2.3. Structural sandwich panel [56]

The research on microcracking of PMC laminates as sandwich skins was performed taking into consideration the interaction between core and facesheets. The shear-lag model was used to predict transverse crack initiation, propagation, and blocking mechanisms in facesheets. Different core types, very compliant and very stiff, and the interface between them and the last ply were considered. For a given elastic moduli ratio in the transverse and fiber direction in skin laminate, there exists a critical facesheet thickness above which the crack blocking is ensured and crack growth is prevented. Equivalently, for a given facesheet thickness, there exists a critical elastic moduli ratio below which the crack blocking is ensured [57].

Increasing use of curved sandwich panels as aerospace structure components makes it vital to fully understand their thermostructural behavior and identify key factors affecting the open-mode debonding failure. Open-mode debonding analysis was performed on a family of curved honeycomb core sandwich panels with different radii of curvature. The curved sandwich panels were either simply supported or clamped, and were subjected to uniform heating on the convex side and uniform cryogenic cooling on the concave side. The critical stress point, where potential debonding failure could initiate, was found to be at the midspan (or outer span) of the inner bonding interface between the sandwich core and facesheet on the concave side, depending on the boundary condition and panel curvature. Open-mode (radial tensile) stress increases with increasing panel curvature, reaching a maximum value at certain high curvature, and then decreases slightly as the panel curvature continues to increase and approach that of quarter circle. Changing the boundary conditions from simply supported to clamped reduces the magnitudes of open-mode stresses and the associated sandwich core depth stretching [58].

The fatigue characteristics of polyurethane foam (PUF) core composite sandwich structures were investigated using three-point bending tests. Three types of PUF core sandwich specimens with facesheets made from epoxy/glass or polyester/glass laminates, and mixed skins were investigated. Experimental results indicated that degradation of stiffness occurred due to debonding and sliding between the facesheet and foam core during fatigue cycles. Epoxy/glass sandwich structures exhibited higher bending strength along with higher stiffness degradation than the other two types of sandwich panels, due to higher initial fatigue loading. The lowest fatigue properties have been obtained for the

polyester/glass sandwich panel specimens. Most of the specimens failed within the foam region and not at the skin level [59].

The effects of PUF density and skin materials (epoxy/glass or polyester/glass) on the damping behavior of PUF sandwich structures were investigated in the temperature range -20 to 100^{o}C. The damping capacity of a material refers to its ability to convert mechanical vibration energy into thermal energy. Three types of specimens, like above, with three foam densities (0.6, 0.65, and 0.7gm/cc) were considered and the effects of the skin material, the density of foam, the interface bonding between the skin, and the foam, and the operating temperature on the damping mechanism of the sandwich structure were discussed. The viscoelastic PUF absorbs mechanical energy by means of converting the vibration energy into heat energy. The vibration waves induce compression and expansion of the foam cells, which causes continuous movement of gas present in the foam cells. The damping coefficient of sandwich panels is influenced by the skin strength and thickness, as the skin elasticity is an important phenomenon. The experimental results showed the maximum peak damping capacity at 0^{o}C in case of sandwich with polyester facesheets and foam density 0.6gm/cc. The damping capacity initially increased in the temperature range -20 to 0^{o}C, attained peak value at 0^{o}C, further decreased marginally up to 60^{o}C and finally, drastically decreased in the temperature range 60 to 100^{o}C [60].

Low velocity instrumented impact tests were carried out on sandwich panels made of glass fiber reinforced plastic facesheets and PUF core. Sandwich structures exhibit potentially good damage-tolerance, since the core can absorb impact energy by local plastic deformation whilst still offering enough overall support to prevent high local bending strains in composites. The failure modes commonly observed in composite sandwich plates subjected to low-velocity impact are: fiber failure, matrix cracking, delamination, debonding, and core crushing. Four different types of sandwich samples using polyester and epoxy skin materials were considered for investigation. Glass/epoxy facesheets sandwich specimens have shown superior performance in terms of energy absorbing properties and strength due to the higher stiffness of skins. Facesheet failures were due to flexural and shear stress at the point of impact, when core failure was due to shear strain and delamination between the facesheet and the core. Backsheet failed mainly due to bending stresses caused by the delamination between the core and the backsheet [61].

The properties of PUFs can be modified within wide limits depending on the raw material used. The density, flowability, compressive, tensile or shearing strength, the thermal and dimensional stability, combustibility and other properties can be adjusted to suit the requirements of a given application. The polyols and isocyanates have a major impact on the properties of the foams. Also blowing agents and other additives, like flame retardants, are important. Rigid PUF performs well in most areas of low-temperature insulations. Products in density ranging from approximately 30 to 200kg/m^{3} withstand temperatures down to -196^{o}C [62].

Similar three-point bending tests were performed to compare properties of different cores. One type of sandwich had facesheets made of aluminum alloy 1145-O and core made of Rohacell 31, a

closed-cell polymethacrylimide rigid foam. The other type of composite structure was made of aluminum alloy 5052-H19 and fuzzy carbon core, a proprietary material made by Energy Science Laboratories, Inc. When compared with the theoretical values, the measured load and displacement at yield and the modulus of elasticity indicated that the samples were not stiff as expected [63].

Similarly, the fracture properties of a big number of sandwich structures have been investigated using simple three point bending test geometry [64]. The center notch flexure sandwich test involved loading the lower skin of the sandwich structure and propagating a central crack along the lower skin-core interface. A finite element analysis agreed well with strain energy release rate data obtained via experiment on several foam, balsa, and honeycomb-based sandwich structures. The sandwich panels comprised of Nomex honeycomb core exhibited load-displacement responses where specimen loading was linear and crack growth stable. Tests on a range of sandwich panels have shown that structures based on Nomex honeycomb cores offer high fracture energies, whereas those manufactured from cross-linked foams offer relatively low values of critical strain energy release rate.

An analytical and experimental comparison of Kevlar/epoxy panels and Kevlar/epoxy sandwich structures with polymethacrylimide foam core loaded by in-plane shear was presented [65]. The static strength of the sandwich panels was approximately five percent lower than the strength of the solid panels. The fatigue life of the sandwich panels was shorter than that for the solid panel. In addition, the influence of ground-based environments on long-term (10 years) durability of Kevlar/epoxy systems has been studied [66].

Due to the low flexural stiffness of sandwich structures, the geometrical nonlinear deformation effects tend to appear earlier in foam core sandwich plates than in other laminated and sandwich plates. An experimental and analytical study to investigate the nonlinear behavior of foam core sandwich plates subjected to in-plane shear loads was presented [67]. Based upon the assumption of large amplitude deflection, the in-plane shear strain is related to the in-plane normal stiffness in addition to the in-plane shear stiffness. The in-plane normal strains appear under laterally applied loads, which accounts for the difference between the diagonal compressive strains and tensile strains observed in experiments. The nonlinear deformation effects are significant for the plate structures having low flexural stiffness, and the analytical results can be applied to all plates experiencing large deflection subjected to the in-plane shear loads.

Due to large differences in stiffness between the face sheet and core, any load generates concentrated transverse shear stresses that contribute to the formation of delaminations at the facesheet-core interface and potentially lead to the eventual failure of the structure. One possible way to alleviate the large interfacial shear stress concentration is through the gradual variation of stiffness properties at the core-skin interface. It is thought that perhaps this objective can be realized through the incorporation of functionally graded materials, where the stiffness can be tailored to vary through the thickness. Although still largely in development, these materials are commonly foams and the variation of stiffness is most often accomplished through variations of the cell density. An analytical 3-D elasticity solution for the

stresses and displacements of a sandwich composite with a functionally graded core subjected to an arbitrary transverse pressure distribution has been presented [68]. The analyzed sandwich panel consisted of orthotropic facesheets bonded to an isotropic, functionally graded core with a Young's modulus that varies exponentially with respect to the transverse direction.

The problem of steady state heat conduction in a functionally graded open-cell metal foam thermal insulation was studied [69]. The mass was minimized by varying the solidity profile for a given thickness. An optimality condition was derived and the optimization problem was reduced to that of an ordinary, nonlinear differential equation, which was solved numerically. The results included optimum cell size variation through the thickness of the insulation for given aerodynamic heating and the corresponding temperature distribution. It was shown that for given thickness using a functionally graded material can reduce the mass of insulation panel.

The problem of contact between rigid cylindrical indentor and a sandwich beam with functionally graded core was studied [70]. The core Young's modulus was assumed to vary exponentially, but the Poisson radio was kept constant. Plane elasticity equations were used to analyze the core and the facesheet was modeled as an Euler-Bernoulli beam. The contact problem was solved using the assumed contact stress distribution method. Results indicated that the contact stiffness of the beam with functionally graded core increased causing the contact stresses and other stress components in the vicinity of contact to increase. However, values of maximum strains were reduced considerably due to grading of the core properties. The results indicated that functionally graded cores could be used effectively to mitigate or completely prevent impact damage in sandwich composites.

An elasticity solution was obtained for a sandwich beam with a functionally graded core subjected to transverse loads [71]. The sandwich was subdivided into four elements, the top and bottom facesheets, and top and bottom halves of the sandwich core. The equations of each element were expressed in terms of the surface tractions and displacements. By enforcing the compatibility of the tractions and displacement at the interfaces the complete solution for displacements and stresses in the beam were obtained. It was shown that the functionally graded core reduced the core/facesheet interface shear stress. The normal stress varied linearly through the thickness and was independent of the variation in core properties. The elasticity solution was verified using FEA. The developed method can be extended to any general variation of elastic modulus by using multiple elements of the core to approximate the required elastic modulus.

Sandwich constructions with reinforced cores by the way of 3-D Z-pins embedded into foam, honeycomb cells filled with foam, and hollow/space accessible Z-pins acting as core reinforcement were considered. A 3-D truss/network of pins is embedded in foam core in a predetermined array (geometry) that penetrates into the facesheets during the curing process. Reinforcing the foam with pins has the advantage that the transverse stiffness of the core is enhanced. Titanium, pultruded glass/epoxy tow rod and steel Z-pins were tailored to this task. A suitable alternative to closed-cell foam core is the concept of using foam-filled honeycomb as a core material. This concept optimizes the relationship between the

honeycomb and the foam, offering the benefits of both, while selectively eliminating the disadvantages of both. The increased surface area allows stress forces to dissipate over a larger area than that offered by the honeycomb alone. The core absorbs much greater impacts by transmitting forces to the adjacent cells. The effect is greater resistance to shear force perpendicular to the sandwich (fracture), increased moment resistance (less bending) and better dampening of shock waves along the surface (less vibrations). The Z-pin reinforcement of the core suppressed core crashing effectively under the high strain rate impact loading. The pins could conceivably be used to tailor transverse stiffness, electrical and/or thermal conduction, as vibration tailoring devices or as sensors. The polyurethane foam-filled kraft paper honeycomb suppressed the core crashing effectively as well [72].

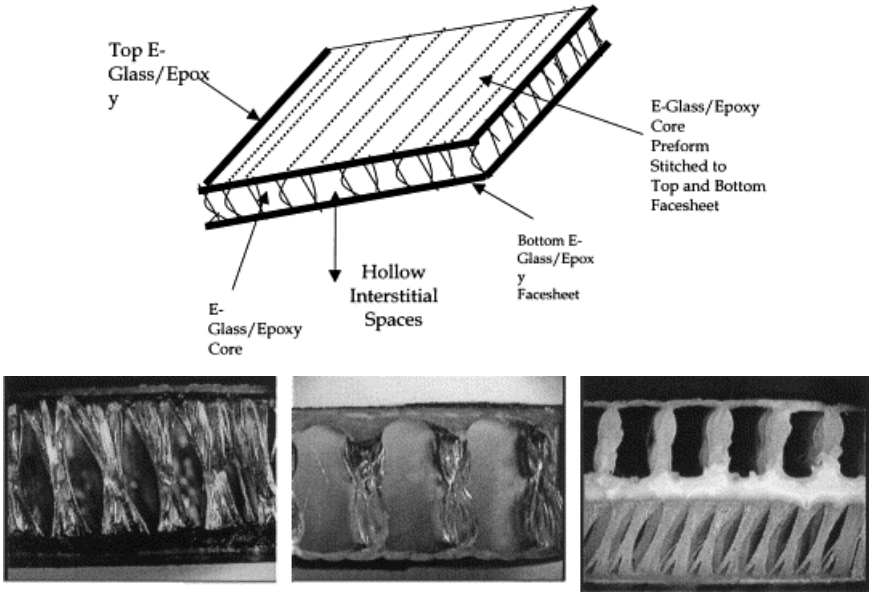

Fig. 2.2.4. Schematic (above) and microstructure in weft and warp direction (below) of integrated sandwich core [73]

An innovative integrated hollow (space) core sandwich composite construction is a by-product of advances in textile/preform technology. A 3D fabric preform consists of two bidirectional woven fabric surfaces, which are mechanically connected with vertical woven plies, as illustrated in Fig. 2.2.4. Such sandwich possesses several multi-functional benefits in addition to the providing lightweight and bending stiffness advantages. In comparison with traditional foam and honeycomb cores, the integrated space core provides means to route wires/rods, embedded electronic assemblies, and store fuel and fire-retardant foam, among other conceivable benefits. A low-velocity impact response was investigated for three thicknesses of integrated and functionality-embedded E-glass/epoxy sandwich cores: 6, 9 and 17 mm. The cores provided enhanced impact resistance due to energy additional energy absorption mechanisms. The delamination mode of failure between the facesheet to the core, which is often of concern for sandwich composites, was found to be effectively suppressed/absent using the integrated

core sandwich design. Damage was primarily by tearing of the top facesheet and microbuckling of a localized system of glass/epoxy core members [73].

An analysis and optimization of sandwich plates simply supported on all four edges with a foam-reinforced web core subjected to in-plane compressive loads were presented [41]. Due to many failure modes of this kind of sandwich structure such as overall instability of the sandwich as a whole, face plate instability, face wrinkling, and instability of the webs, the analysis of each mode was investigated and discussed in order to understand the physical behaviors of the whole structure and its components. The sandwich plate subjected to a uniaxial compressive load was optimized for the minimum weight by taking into account the above four failure criteria. Additionally, for any given set of materials, the optimum face thickness, web component thickness, web component spacing, core depth, and foam core modulus for any values of in-plane compressive loads was evaluated analytically.

Experimental results and 2-D numerical simulation are given for a progressive collapse of polymer composite sandwich beams. The skins consisted of a unidirectional glass epoxy pre-preg lay-up in a cross-ply form and the core was made from Divinycell foam. Standard foam models and a simplified method of inputting material damage were used, skin was modeled ply by ply and the core had 10 elements through its depth. Damage in the skin was controlled by the total strain in the direction along the beam and the multi-axial collapse of the core was described by critical state theory and continuum modeling [74].

A recent study made use of 3-D FEA with full meshing of the core for three geometries (pyramidal truss cores, folded (corrugated) plate cores and honeycombs) to explore the relative effectiveness of these cores under blast loads [75]. In the study analytic work has indicated that reasonably accurate predictions for sandwich plate responses can be obtained without detailed characterization of the core as long as its energy absorbing capacities are correctly represented for the relevant modes of deformation. An alternative approach to full meshing of core geometry is to model the core by a continuum constitutive law and fill the space between the faces with smeared out core material. The constitutive model falls within the framework of a compressible rate-independent, orthotropic elastic-plastic solid that is way it is sufficient for metallic sandwich cores. Selected examples have been analyzed and presented to demonstrate both the robustness of the new model in a computational setting and physical aspects for sandwich plates stemming from both anisotropy and plastic compressibility.

All previous studies have been focused mainly on stiffness, neglecting for the most part skin effects. The skin effect can significantly affect interfacial stress distribution, yielding a coupled stress state: a normal stress arises for transverse shear and a shear stress results from in-plane stretching. There is an apparent stress concentration at the panel corners, making this location potentially critical in design. An analytical model that permits the computation of stiffness as well as interfacial stresses, considering the skin effect for hexagonal honeycomb sandwich, subjected to in-plane and out-of-plane forces, was developed. An explicit analytical model was derived based on equilibrium equations, where boundary conditions imposed by the skin effect were appropriately considered. The accuracy of the

solution was verified through close correlations with existing stiffness formulations and finite element results [76].

Attempts have been made to improve the performance of the sandwich by strengthening the core but partially sacrificing the debond fracture toughness of the sandwich construction [77]. Strengthening of the core was accomplished by infusing nanoparticles into the parent polymer of the core material when it was in the liquid stage. The core material was PUF made from polymeric isocyanate and reacting with polyol. Spherical nanoparticles such as TiO_2 were infused into liquid foam and the amount varied from 1 to 3% by weight. When the nanoparticles are dispersed in a polymer they synergistically combined the properties of both the host polymer matrix and discrete nanoparticles therein. Extensive flexural tests were conducted on the foam materials and it was observed that 3% nanoparticle loading the gain in flexural strength and stiffness over the neat system is around 26 to 56% respectively. This gain is attributed to the enhanced cross-linking in the polymer due to the presence of nanoparticles which are acting as catalysts.

Sandwich structures with faces which differ in thickness, faces of different materials, or additional interleaves are asymmetric with respect to the mid-plane. Such differences may be incorporated for reasons other than purely structural. A design that can take advantage of this asymmetry can be utilized advantageously to minimize, if not negate, the bending stresses that are developed within bending boundary layer. In the bending boundary layer located adjacent to each and every structural, material, or load discontinuity, bending stresses are superimposed upon membrane stresses. Governing equations for mid-plane asymmetric sandwich cylindrical shell subjected to axially symmetric load were derived and solved [78]. The equations were based on previous work, in which sandwich beams with mid-plane asymmetry were analyzed, designed, and optimized. Both classical beam theory and a refined theory involving transverse shear deformation were utilized. Explicit solutions for the beam subjected to a uniform lateral load for the boundary conditions of both ends clamped, both ends simply supported, and a cantilevered beam were given. To obtain minimum face weight, the means to select each face thickness and the core depth were given for any given material system [79].

Cylindrical bending of a sandwich panel assembly consisting of straight and curved sections was considered in another research [80]. The sandwich assembly was statically determined, loaded by a uniform pressure and possibly by forces and moments at its edges. The influence of the change of geometry upon the stresses and displacements at the transition zone between the different panel sections was investigated and an exact asymptotic mathematical model based on a number of small parameters was derived. The model assumed the faces of the sandwich panels to be thin elastic beams obeying the Kirchhoff-Love assumptions, while the isotropic core was treated as a 2-D elastic medium.

Some interesting results were obtained as a part of a design study regarding a non-circular pressurized sandwich fuselage. The idea behind this design concept was to achieve a fuselage cross section providing a more efficient cargo space than the usual circular fuselage cross section. The modeling and analysis was conducted using a high-order sandwich theory formulation in which the elastic

response of each face laminate is accounted for, including bending-stretching coupling, and including the transverse flexibility of the core material. A high-order sandwich theory approach was adopted for the analysis of the fuselage section, including the formulations for flat and curved sandwich panels. Results of a parametric study, which included the effects on the structural response of varying the sandwich panel mid-plane asymmetry, the core properties, and the radius of curvature of the fuselage cross section corners, were assessed [81].

A bending behavior of unidirectional singly curved sandwich panels with a soft core and delaminated (debonded) zones or slipping layers was also described [82]. The delaminated zone was assumed to exist through the width of the panels and was in the form of an interfacial debonded zone at one of the face-core interfaces, thus subdividing the length of the panel into three zones, i.e. two fully bonded zones and one that is debonded (delaminated). The mathematical model was based on a high-order sandwich theory, and used equivalent shear and radial springs to simulate the effects of debonding or slip layers. The mathematical formulation used the equivalent spring approach, where the existence of continuously distributed shear and radial springs was assumed at the face–core interfaces, along with the principle of minimum energy. The field equations along with the boundary and continuity conditions have been derived through variational principles. The stress and displacement fields in the core have been derived analytically.

The performance of non-loss storage of liquefied gases, such as precious, high-purity, noxious and flammable, is affected by many factors: thermal insulation performance (heat load), storage pressure, the environmental pressure and fraction of liquid volume, liquid stratification, and liquid property. The insulation performance, fraction of liquid volume is the main factors that affect the non-loss storage under given pressure. The storage time can be calculated through non-dimensional criterion such as non-dimensional pressure, non-dimensional thermal load and primal liquid volume fraction. The mechanical mix, thermal mix, insulation short, condensation of the vapor to reduce the heat and adding fin can be used to reduce or eliminate the temperature stratification of the liquid and increase the non-loss storage time [83].

To test RLV tank designs, a cryogenic pressure box (cryobox) has been designed and fabricated to enable representative tank panel sections to be tested at actual operating conditions and loads (-253^{o}C (LH2 temperature) with an internal pressure up to 52psig) [84]. In the cryobox, which is located at the NASA Langley Research Center, curved stiffened panels are subjected to biaxial tensile loads by applying pneumatic pressure on the internal surface of the panel and tensile loads on the edges of the panel. The tensile load in the circumferential direction (hoop load) of the panel is reacted through rods with turnbuckles that are attached to the ring frames and skin of the panel. The tensile load in the axial direction of the panel is applied by means of four hydraulic actuators. The load introduction structure, consisting of four stainless steel load plates and numerous fingers attaching the load plates to the test panel, is designed to introduce loads into the test panel that represent stresses in the actual tank structure. Fingers are used to minimize load interactions between the panel and the load plates. The load

plates are trace cooled with LN2 to reduce thermal gradients that may produce bending in the load plates, and thus introduce additional stresses into the test panel.

2.3. Gas Permeability of Composite Structures

Fiber reinforced plastics are attractive alternatives to metals for cryogenic applications because of their specific strength and stiffness, and their low electrical and thermal conductivity. A disadvantage is the ease of permeability of gases with small molecular diameter through the material at room temperature, and after damage accumulation at cryogenic temperature. In order to reduce technical risk The 2nd Generation Reusable Launch Vehicle NASA Program identified high permeability in past composite cryotank material developments as a high interest technology area. It was duly noted how biaxial strain to a certain configuration specific minimum at cryogenic temperatures caused excessive microcracking in X-33 materials [85]. It is still somewhat speculative at the current time to describe and/or state the number of representative in-use environment cycles that NASA will deem necessary in order to qualify the material for flight. It has been reported that the requirement adopted by National Aerospace Plane Program is that the allowable permeation rate for the tanks is determined by allowing the entire tank surface area to permeate an amount equal to 10% of what will leak out of valves and fittings. This allowable permeation rate is then calculated to be in the range of 10^{-4} to 10^{-3}scc/s*in^2, at least two orders of magnitude greater than the discriminating value (currently minimum detectable or $2*10^{-6}$scc/s*in^2). Furthermore, depending upon the failure mode and representative vehicle configuration, realistic hydrogen permeability allowable ranges from $2.32*10^{-3}$ to 5.6 scc/s*in^2.

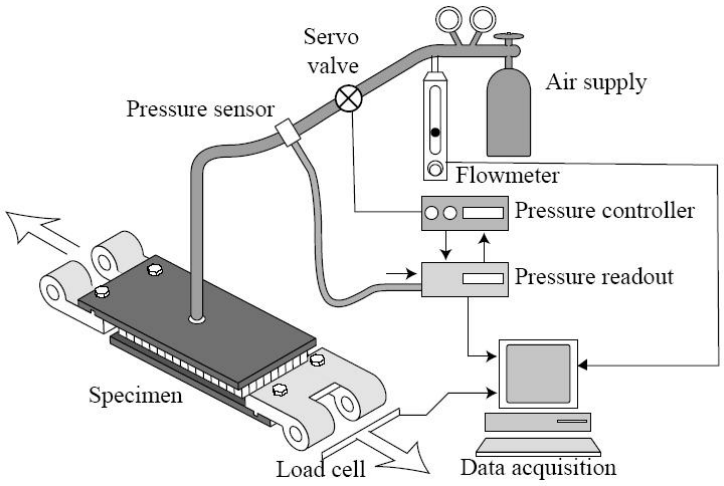

Fig. 2.3.1. Schematic diagram of test setup for permeability shear tests [86]

The environmental durability of the sandwich panels must be demonstrated prior to use in fuselage skin panels. The resistance of the core material to damage that would allow integral migration of fluids from local ingression points must also be understood. Characterizing the air permeability of

sandwich core materials as a function of applied transverse shear stress was an important step in understanding the usefulness of the sandwich panels [86,87]. The air permeability, defined as the flow rate divided by applied pressure, gave an indication of how fluids migrate into the structure. The Hexel HPR and Korex honeycomb cores were evaluated under both static and dynamic (reversed and non-reversed) loads. The Korex core specimens failed in the honeycomb core and the permeability increased almost instantaneously at failure. The HPR core failed at the bondline and the permeability gradually increased until the failure.

Many apparatus have been developed for measuring gas leakage rate. For one study, a special experimental leak detector was built based on a controlled gas (helium) flow through a diaphragm and mass spectroscopic measurement. A few of available glass/epoxy composite laminates were tested for permeation performance at room temperature before and after damage caused by thermal shock and tensile loading. Thermal shocks between room temperature and -196^{o}C had no effect on the helium permeability, solubility, and diffusion rates at room temperatures. Glass fiber composites have been shown to conserve their properties after 100 thermal shocks. The laminates showed different tensile behaviors at room temperature and -268^{o}C and developed different damage processes and gas permeation behavior [88].

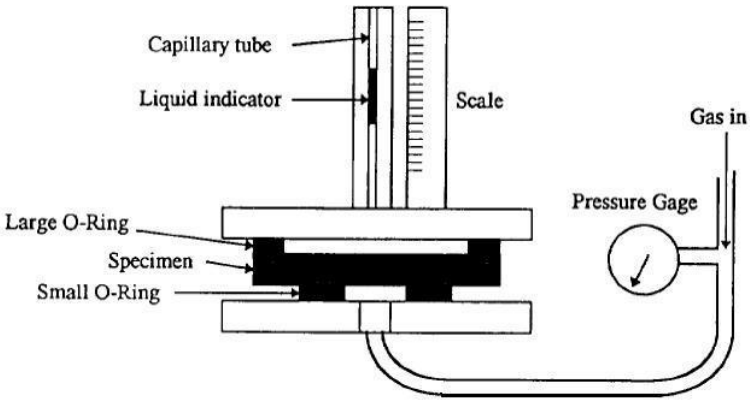

Fig. 2.3.2. Cross section of permeability apparatus [106]

The rate of hydrogen leakage can be a function of material, tank fabrication method, mechanical load to the tank, internal damage-state of the material, and the temperatures at which the tank must operate. A method for measuring leakage through a geometrically complex structure at cryogenic temperature and under mechanical load was developed, calibrated, and used to measure hydrogen leakage through complex X-33 liquid-hydrogen tank structure sections. The investigation has demonstrated the need for structures-level leak testing to validate composites and composite manufacturing process for LH2 tank applications. These tests should include thermal and thermo-mechanical conditioning and testing of structures under operational mechanical loads and temperatures [89].

A special apparatus was developed for cryo-biaxial permeability measurement. The intention was to be able to induce cyclic biaxial strains at cryogenic temperatures. In order to simulate the environment of a LH2 tank in a cyclic environment, a computer program was written to control the strain in the experimental sample by controlling pressure inside the fixture (upstream pressure). A great number of different IM7 carbon fiber/epoxy or bismaleimide in quasi-isotropic lay-up (0/45/-45/90/90/-45/45/0), tow-placed or hand-laid up, were tested. The IM7/977-2 laminates prepared from 2.6mil pre-preg by hand lay-up from tape showed very promising resistance to microcracking in cycling between liquid hydrogen and ambient temperature with biaxial loading. The aluminum barrier was the most effective barrier examined on laminates. Barrier/liner adhesion at -254^{o}C limited the performance of sandwich laminates [85].

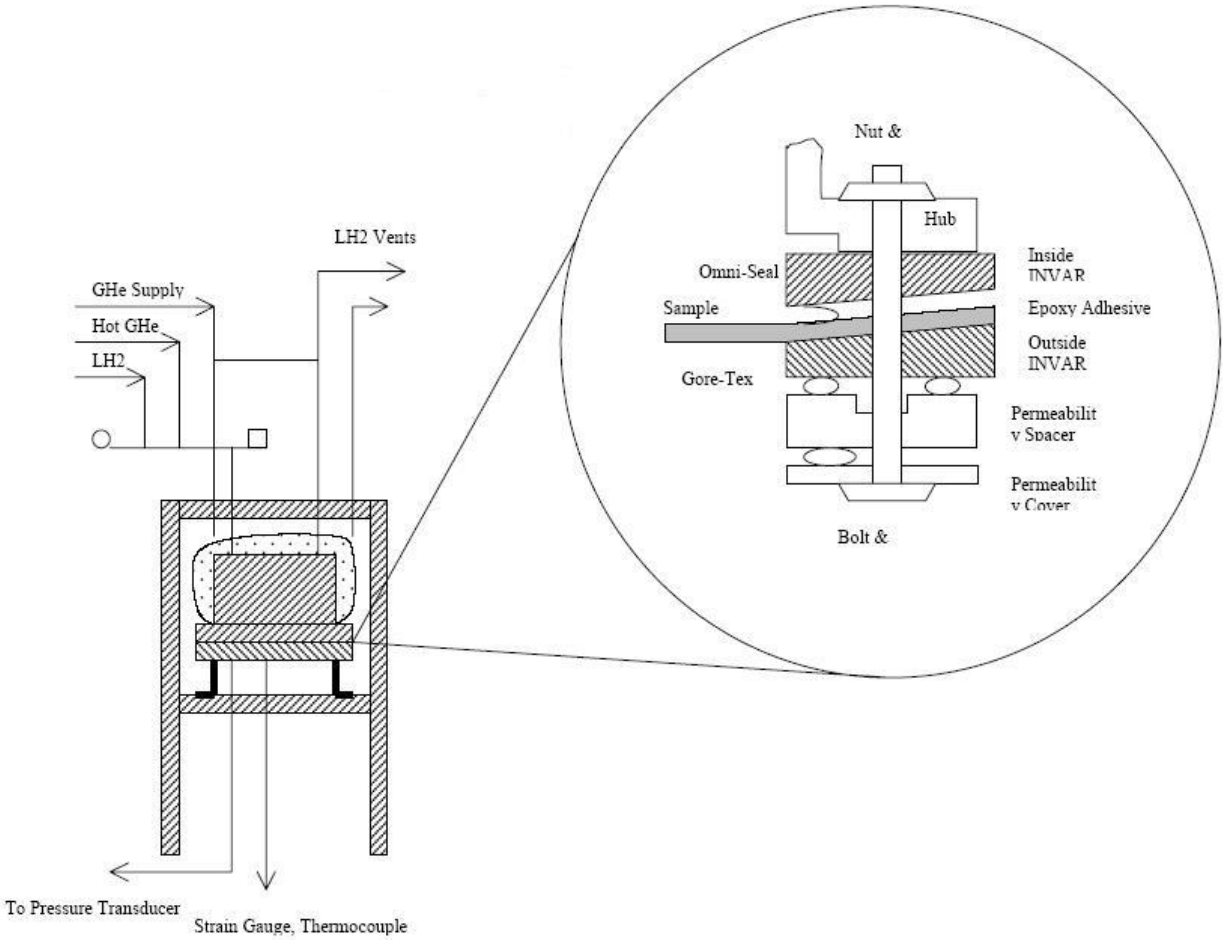

Fig. 2.3.3. Cryo-biaxial permeability apparatus [85]

The results of hydrogen permeability testing on bismaleimide based graphite fiber composite material were obtained under a variety of tetra-axial strain states. Laminates with stacking sequence $(90/60/90/-60/0)_S$, i.e. 10 plies, were cycled to liquid hydrogen temperatures and gas permeability was measured. There was evidence that localized failures may be occurring in surface plies of bismaleimide material as low as 1500micro-strain at room temperature with uniform tetra-axial in-plane strain.

Widespread microcracking of the surface plies began between 2500 and 3000micro-strain. A continuous through-thickness crack system began to form between 3500 and 4000micro-strain and catastrophic failure of the laminate occurred somewhere above 4600micro-strain. The as-processed bismaleimide material exhibited a time dependent sealing mechanism at room temperature after returning to an unstrained state from a series of microcrack inducing tetra-axial strain levels. A hysteresis effect between loading and unloading in load versus strain curves generally accompanied this phenomenon [90]. Microcracking in composite laminate can also occur due to foreign object impact. Prepregs composed of IM7 fiber in five-harness weave architecture impregnated with EX1522 epoxy resin were used to construct four ply laminates and impacted in drop-weight tester in varying levels of damage from almost nondetectable to near penetration. Then the specimens were tested for helium permeability using volumetric technique. All laminates showed leakage after impact, even when visible damage was detected with magnifying techniques [91].

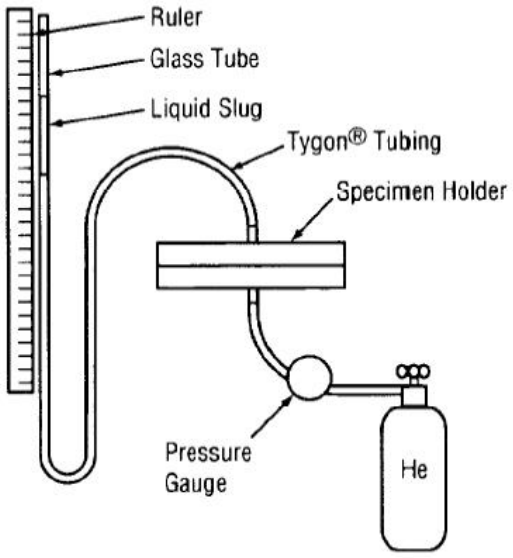

Fig. 2.3.4. Volumetric permeability apparatus [91]

2.4. Impact Properties of Sandwich Structures

Polymer composite sandwich panels are increasingly utilized as primary load-carrying components in air- and aerospace structures. Serving in this capacity, these structures are subjected to impacts such as tool drops, hail, bird strikes, and runway debris. When the duration of these impacts is much longer than the period of the lowest natural frequency of the structure, the impact is often loosely termed a low-velocity impact, or being more specific, a large mass impact, or a boundary condition controlled impact, as described by Olsson's mass criterion. These impacts have been found to create internal damage that is difficult or impossible to detect from the exterior surface of foam or honeycomb sandwich structures. Unlike their solid metallic counterparts, predictions of the effects of impact damage

of composite structures are difficult and are still relatively immature. For this reason, many analytical, computational, and experimental studies have been performed to predict and characterize the damage created by wave propagation and boundary conditions controlled impacts [92].

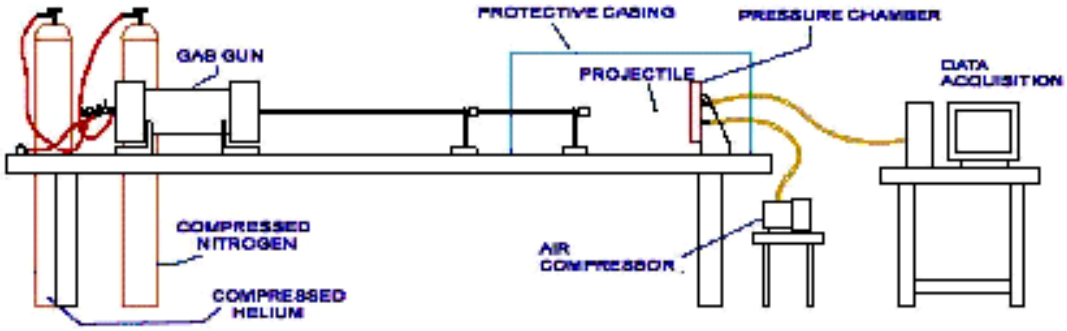

Fig. 2.4.1. High velocity impact test setup [49]

Most studies have been conducted with impact energy as the only factor that has the effect on impact damage, but varying mass while leaving the impact energy constant has a large affect on the delamination area of sandwich composites. It has been shown that small-mass impactors cause higher impact loads and earlier damage initiation than large-mass impactors with the same kinetic energy. At the same impact energy large mass impacts are governed by a quasi-static impact response while small mass impacts are governed by a wave-controlled response. Damage may consist of fiber breakage, matrix cracking, and delamination [93].

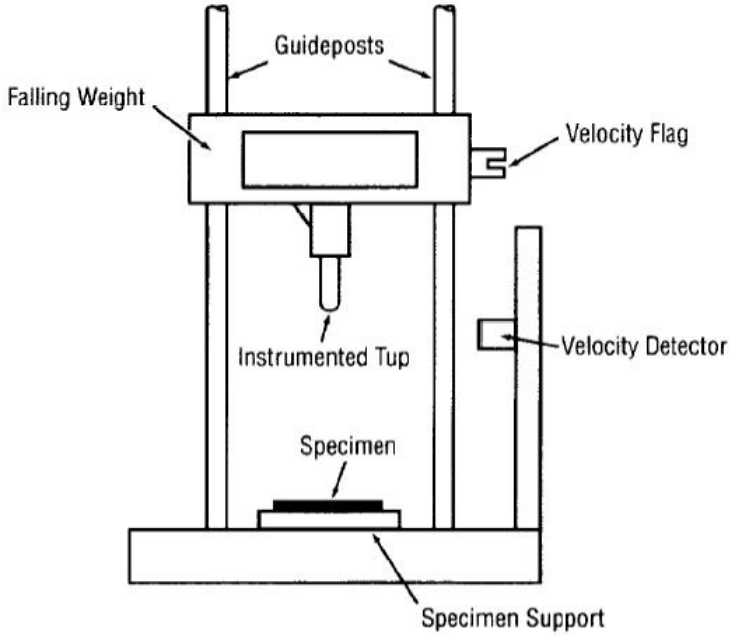

Fig. 2.4.2. Low velocity impact test setup [91]

The specific geometry of the core becomes critical in the core-to-facesheet bond strength in case of impact load. More specifically, the amount of surface area allowed for bonding between the core and skin dramatically effects the stress distribution throughout the composite. Cores made from honeycomb structures typically can exhibit difficulties in bond adhesion to the skin due to the lack of usable surface area for bonding. Filling the honeycomb structure with foam can alleviate many of the bonding issues associated with honeycomb structures by providing a more favorable stress distribution via increased bond surface area. In addition, by filling the structure with foam, the foam provides increased support to the honeycomb core. The core is then capable of increased impact resistance and can readily transfer higher loads to adjacent cells. The core also features increased fracture resistance in conjunction with increased moment resistance [94].

Experimental and numerical simulation studies on the impact and penetration damage of a sandwich panel by a solid, round-shaped impactor were performed for Nomex HRH core and carbon/epoxy AS4/8552 laminates in stacking sequence $(90/45)_S$ as facesheets. The main objective was to understand the load distribution in damaged sandwich structure and to study the failure mechanisms of such a structure in the presence of impact damage. The test was done by dropping a suitable tub and mass arrangement from a defined height onto the required impact location of the test panels, in order to achieve the required impact energy. Results from the impact-damage C-scan test indicated that significant internal damage occurred at relatively low-impact energy levels, which can significantly reduce the residual strength of the panel [95].

Two and four layer woven carbon fiber facesheet sandwich composite samples with polyurethane foam filled honeycomb core were impacted in a low velocity drop tester at 10, 20, and 30J with varying masses and velocities of the impactor [93]. Also two different foam densities were used for the two layer samples. The amount of damage to the sample increased as impactor mass increased for the same energy impact. Higher density foam absorbed more impact energy than a less dense one. The samples after impact were fatigued using a four point bending test. The failure mode of the two layer high density samples changed from shear at the contact point of the test fixture into bending. In bending failure a crack initiated next to the hole caused by the impact and propagated out from the center until it reached both ends of the sample at which time the sample failed. The fatigue life of the four layer samples and low density foam two layer samples were not affected by the impact.

An investigation of simplified dynamic (single degree of freedom) models incorporating energy dissipation for the low velocity impact behavior of foam and honeycomb sandwich laminates was performed [92]. The stiffness parameters of the models were derived from the results of 3-D quasi-static contact analyses of a rigid sphere indenting a multi-layer sandwich laminate. The validity of the models was examined through comparison with experimental force history results of impact on six different core and facesheet configurations. The skins were comprised of either (0/90/0) or $(0_2/90_2/0_2)$ carbon fiber fabric and the core was either Nomex HRH honeycomb or polymethacryimide WF foam, both in two different densities. Of the models examined, only a complex stiffness damping model and Maxwell

element model, which both initially required empirical estimations for their damping parameters, was found to be capable of accurately predicting the experimental contact force histories.

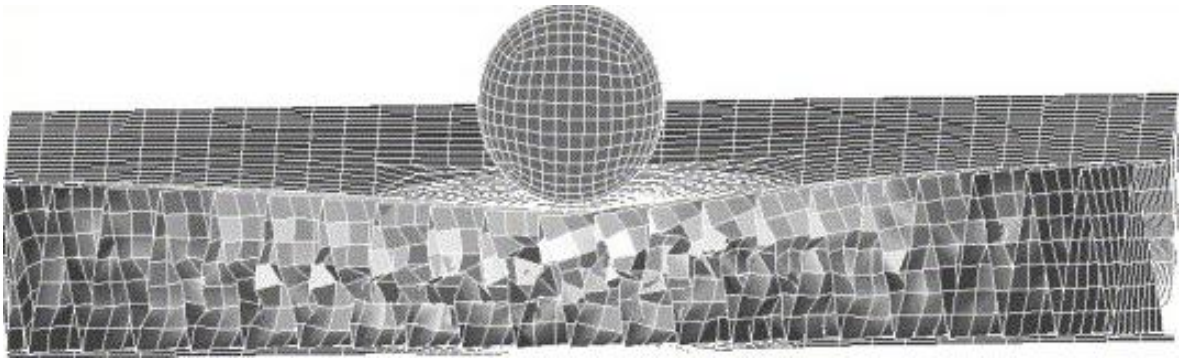

Fig. 2.4.3. Illustration depicting the extent of core buckling [96]

An explicit finite element based simulation tool has been developed to predict the damage within sandwich structures subjected to low velocity impact. The tool, Sandmesh, is capable of automatically generating 3-D shell models of both honeycomb and folded structure cores, as well as applying the necessary controls for solution generation. Sandmesh was validated via an experimental test program in which aluminum honeycomb sandwich panels were tested for impact resistance and damage. Comparison of the impact force-time history, maximum displacement, specimen damage area, core buckling behavior, and resulting indentation demonstrated that the modeling methodology accurately captured the impact characteristics. The program, developed using Ansys Parametric Design Language, requires nominal specimen dimensions as well as the core cell geometry, thicknesses and mesh density to be defined. The sandwich structure geometry and finite element model is then automatically generated using shell elements. Sandmesh can also incorporate a contact interface that represents a thin resin bond layer between the facesheet and the core [96].

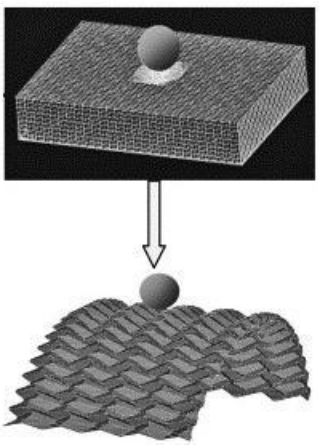

Fig. 2.4.4. Application of Sandmesh to folded core structures [96]

Traditional single layer sandwich structures consist of two facesheets and a core. With an additional sheet, called internal sheet, inserted into the core, a two-layer sandwich panel is formed. Two-layer panels with polymer matrix composite laminated facesheets and a thin internal sheet subjected to low velocity impact are studied. DYNA3D software was used to model and analyze the dynamic problem, and attention was focused on the local displacement of the honeycomb core under the point of impact in the conditions of various locations of the internal sheet and of different levels of impact energy. Simulated results revealed that the local displacement of the core along the direction of the impact decreased significantly by introducing the internal sheet into the traditional single sandwich structure and by reducing the space between the internal sheet and the impacted facesheet. The internal sheet had the tendency to spread the impact energy to the whole panels instead of concentrating the impact energy on a local area of the impact. No significant effects on the contact forces and the deflection of the sandwich structures ware detected, no matter what the locations of the internal sheet and the impact energy were. This result suggests a new sandwich structure to reduce the local crash/buckling of the core under the point of the impact [97].

For relatively low velocity projectiles, a sandwich panel may respond by bending and no damage will occur if the energy of the projectile can be accommodated by the elastic strain energy in the panel. At higher impact velocities a critical condition is reached when a local contact stress exceeds a local strength, core compression strength or interface delamination strength. The damage behavior of composite sandwich panels with Nomex honeycomb and polyetherimide foam cores under transverse impacts at high velocities was investigated. A numerical model was developed using the dynamic explicit finite element structure analysis program. For both sandwich structures numerical analysis reproduced physical behavior observed experimentally in impact tests [98].

A high strain rate response of polymer matrix composites undergoing high velocity, small mass impact was investigated by comparison of impact energies, absorbed energies, and residual compressive strength after impact. The absorbed energy was approximated in an effort to better understand the high strain rate behavior of sandwich composites. More specifically, the absorbed energy allowed insight into the damage induced courtesy of impact situations and the influence of each individual component. The samples were made from plain weave graphite/epoxy laminate and foam-filled honeycomb and impacted by the pneumatic gun with several different projectile velocities. Once the velocity approached a critical value, dependent upon sandwich material and geometry of the composite panel, the damage area induced by the impact situation was quite local until the impact energy approached and exceeded the critical energy value. In addition, the compression after impact tests indicated the increased presence of interlaminar cracking and delamination on samples for which the impact event has exceeded the critical energy value [94].

2.5. Adhesives

In the actual manufacture of sandwich panels, adhesives are used for:

- bonding the facesheets to core materials,
- bonding the core materials to one another,
- bonding of the interleaf to the structure.

Adhesive bonding offers many advantages over the classical fastening techniques such as welding, riveting, and mechanical fastening. It has a high resistance to fatigue and as a consequence the life-cycle maintenance costs are significantly reduced. The substantial reduction in weight that can be achieved by the use of adhesive bonding is an important advantage, especially for lightweight structures. In joining lightweight composites, adhesive bonding is the most appropriate joining technique. The adhesives also have disadvantages and the main is low durability when the structure is exposed to hostile environmental conditions. The effect of moisture on the strength of adhesively bonded joints is significant due to the deterioration of the adhesive layer and the interface. The strength of the joint is decreased dramatically when aged in hot/wet environments [99]. Adhesive bonding assembly can simplify the assembly process, increase production and quality, and reduce production cost. In spite of the increased usage of adhesive bonding in structural applications, the determination of adhesion strength and durability remains largely empirical in nature. This can result in over conservative design leading to structural redundancy or, conversely, to failure of adhesively bonded joints, typically due to the combined effects of complex modes of loading and environmental degradation [100].

A bonded adhesive structure consists of three components of different mechanical properties, namely the two adherents and the adhesive layer. Much attention has been paid to describing the mechanical response of such assembled systems, including their behavior under bending, tension, and shear [101]. The bending and tension tests of joints generally involve mixed modes of failures with unknown shear components. Adhesive failure is generally modeled by one of four approaches, namely:

- shear strength criterion,
- local shear strain criterion,
- fracture mechanics approach, using either the stress intensity factor, or the energy release rate.

Basically, the following types of joints are widely used in aerospace and automotive industries:

- single lap joints, see Fig. 2.5.1. a-c foe examples,
- double lap joints, see Fig. 2.5.1. d, e,
- T-type (T-peel) joints, see Fig. 2.5.1. f, g,
- stiffeners, see Fig. 2.5.1. h.

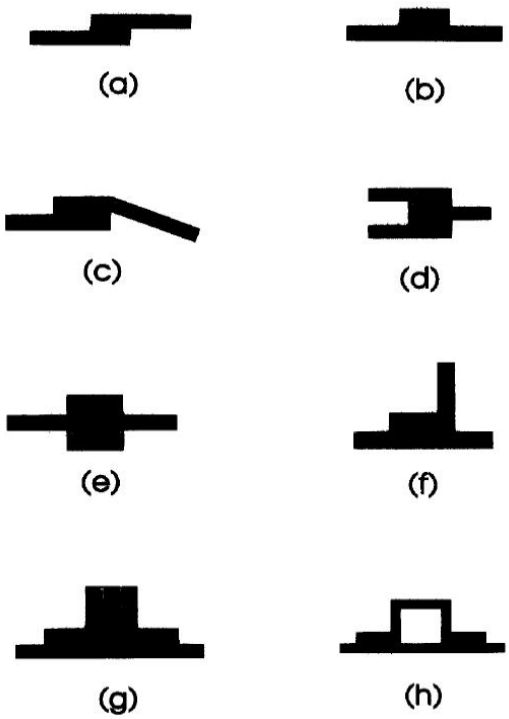

Fig.2.5.1. Typical structural adhesive joints [102]

For some considerable time, polyurethanes and polyurethane prepolymers have been used to give flexibility to epoxy resin formulations, especially those for use as sealants and mastics. Likewise, functional rubbers, particularly those based on butadiene and/or copolymers of acrylonitrile and butadiene, have been used to impart toughness and have lead to the relatively modern generations of toughened epoxy structural adhesives [103]. Required profile and possible applications of solvent-free two-component polyurethane adhesives and recently developed polyurethane hot-melt adhesives for manufacture and/or assembly of sandwich panels was described [104]. As practical experience shows, elastic bonding (and sealing) has been gaining increasing importance in many areas. Very often high adhesive force transmission like those created i.e. by phenolic-resin-based or epoxy-based adhesives are very disadvantageous. If their formulation is not explicitly elastic, they form very hard and consequently, very brittle adhesive joints. Since this behavior has an adverse effect at low temperatures, these pure adhesives play a minor role in the assembly of panels for low-temperature applications for liquid gas tanks.

Many years of research have been devoted to developing appropriate technology and formulating products that will satisfy the needs of the aerospace industry. Recently developed products, based on patented Permapol P3.1 technology, have made further advances in that they exhibit excellent cure profiles, and adhesion, and despite using little or no solvent, demonstrate outstanding tooling characteristics. Due to their chemical structure these liquid polymers have inherent resistance to fuel, water, high temperature, and in addition, exhibit high flexibility at temperatures as low as -60^{o}C. Sealants

based on this technology possess excellent physical properties and demonstrate adhesion to a wide range of substrates. The epoxy curing mechanism employed to vulcanize the sealant is ideal as assembly time can be shortened without loss of sealant performance and reliability. The cure profile meets both production and repair operations even at temperatures as low as 5^{o}C [105].

Epoxy resin based adhesive Hysol EA9394 was tested in NASA facilities for application in Composite Feedline Program. Nitrogen permeability tests were performed before and after thermal cycling. Bondline specimens were much more permeable than composite ones. Vacuum-mixed specimens tended to be less permeable before thermal cycling than air mixed or debulked ones. No major increase in permeability values was observed after 4 and 12 thermal cycles. Long term exposure to low level heat (100^{o}C) did not degrade the adhesive. The small mechanical shock waves set up in the specimens by dropping them into the oven while they were at cryogenic temperature also had no effect on the permeability [106].

Efficient epoxy-based adhesives for bonding of pultruded glass fiber/polyester composites were selected with respect to various environmental conditions. Successful adhesive testing depends on proper surface preparation of composite adherents, mixing and application of the tested adhesive, test specimen preparation, and final test execution. Single- and double-lap tensile shear tests were used since many adhesive bonded composite assemblies are designed to sustain shear stresses [107]. Three kinds of failure were distinguished:

- adhesive failure (rupture of the adhesive bond, such that the separation appears to be at the adhesive-adherent interface),
- cohesive failure (rupture of the adhesive bond, such that the separation appears to be within the adhesive),
- mixed failure (crack goes partly between adhesive and adherent and partly through adhesive and/or adherent).

The effect that test environment and pre-conditioning has on the fatigue behavior of CFRP/epoxy lap-strap joints was investigated. The lap-strap joint is representative of long overlap joints such as the bonding of stiffeners to wing skins. Features of the lap-strap joint are that the stresses at the crack tip are a mixture of modes I and II, and the crack growth is limited to a single bondline. It was shown that the fatigue resistance of the joints did not vary significantly until the glass transition temperature was approached, at which point a considerable reduction in fatigue threshold load was observed. It was also noted that absorbed moisture resulted in a significant reduction in the glass transition temperature of the adhesive. The joints with multidirectional adherents had lower fatigue initiation loads than those with unidirectional adherents, as predicted by the stress analysis. It was also seen that as the crack propagated along the lap-strap joint, the resolution of the forces at the crack tip tended to drive it into the strap adherent, which could result in complex mode fracture surfaces [108]. Fatigue strength of adhesively bonded joints was analyzed using stress analysis and fracture mechanics. The use of several criteria was investigated. Criteria based on the principal stress provided good threshold prediction for

small plastic deformation. The maximum principal strain, von Mises strain, shear stress and von Mises stress predicted with good accuracy the fatigue threshold of the joints that underwent large plasticity. Elastic and elasto-plastic fracture parameters were calculated for two different inherent cracks. The first one was initiated at the adhesive/adherent interface, while the second was in the center of the adhesive layer [109].

The bonding of similar and dissimilar materials was identified as being of primary importance to the automotive industry and a research was undertaken to give designers the freedom to choose from an expanded menu of low mass materials for component weight reduction. The research addressed the following areas of importance: bulk material characterization, structural fracture mechanics, modeling/characterization, process control and nondestructive evaluation, manufacturing demonstration, and advanced processing. Two adhesives were chosen for the fundamental, baseline work of the program: a tough urethane and a strong epoxy [110]. Tests explored fracture behavior with steel-steel, composite-composite and purely adhesive bonded joints (adhesive layer between two backing beams). The issues involved in bonding injected molded composites included: initial adhesion, bulk properties of substrates and adhesives (initial and over time), methods of dealing with mold release, production processing capability, joint performance, and environmental durability.

The effect of a fillet of a modified polyamide-epoxy adhesive at the end of an overlap region on the kinetics of moisture diffusion has been shown to be significant over considerable time scales. A simple analytical model was presented which enabled this effect to be assessed for those joints where the fillet size was large compared with the adhesive layer thickness [111]. It was shown that considerable degradation of the adhesive occurred, both in terms of initial stiffness and ultimate strengths. However, the strains to failure tended to increase with increasing water content. A procedure for coupled mechanical-diffusion analysis was developed which incorporates continuously varying adhesive material properties. This was applied to single-lap joints that were immersed in water for an extended period. The responses of exposed and dry joints to mechanical loading were found to be markedly different. It was suggested that joint failure occurs at the centre of the exposed joint, where the adhesive was dry and significantly less ductile than the adhesive at the overlap ends, and on this basis residual joint strengths were predicted to within a few percent.

A simplified FEM approach was used for the design analysis of structural adhesive joints, in which either all the substrates (the beam version) or most of the substrates (the hybrid version) were modeled by means of beam elements and the adhesive was modeled by using four-noded isoparametric elements. The joints investigated included a single lap joint, a double lap joint, and a T-type joint [102].

Coupled stress-diffusion FEAs, which were required to study the durability of adhesively bonded joints aged in hot/wet environment, were presented [99]. Two bonded joints have been considered: single lap joint and butt joint. The joints were immersed in water at 60^{o}C for up to 60 weeks. For both joints, transient finite element diffusion analyses were performed in order to determine the moisture distribution in the adhesive layer at different time intervals. The swelling strains were taken into account in the stress

analysis and were introduced to the adhesive layer according to the moisture distribution at a particular time. Cured epoxy adhesives with silane treatment were tested and the experimental results were compared with simulation.

The mixed mode flexure and notched coating adhesion tests have been carried out in order to characterize interfacial fracture for a range of environmental exposure conditions and to find a meaningful interfacial strength parameter using a fracture mechanics approach. Rubber toughened epoxy adhesive was used for bonding steel adherents. The moisture uptake of the adhesive was accelerated using an open-faced configuration. The critical loading to cause interfacial fracture was measured and was used in conjunction with FEA to determine the fracture energy under various exposure conditions. Moisture dependant material properties were incorporated in the FEA. Significant degradation of the fracture energy of the interface was found and this was matched by observed changes to the failure surface. The fracture energies were found to be largely independent of test method, exposure environment and time, and were primarily related only to the moisture concentration [100].

Normalized fatigue load-life data for four different structural configurations of the same adhesive-substrate system have been obtained through a large program of fatigue testing. Within these configurations, a lap strap, two single lap joints with different adhesion thickness, and T-type one made with hot cure rubber toughened epoxy adhesive, the effect of both the mean load and, to a lesser extent, the frequency of the fatigue cycle have been assessed. For the particular adhesive system being considered the effect of the frequency of the fatigue cycle was shown to be relatively unimportant. The mean load however has been found to have a significant effect on the fatigue response and a Goodman type curve has been shown to be a valid way of representing this effect. Load-life data has been plotted for all configurations. There was significant variation in initiation life fraction between configurations and with changing levels of load [112].

Double cantilever beam joints with epoxy adhesive were used to investigate cohesive and interlaminar crack growth in bonded composite joints under constant and variable amplitude loading. Numerical crack growth integration was used to predict the variable amplitude fatigue life using constant amplitude data. This underestimated the fatigue crack growth rate for interlaminar cracks, indicating crack growth acceleration due to load interactions. This was also the case for cohesive cracks subjected to a moderate initial strain energy release rate [113].

Double lap joints with epoxy adhesive were tested under constant and variable amplitude loading. Palmgren–Miner's rules were applied to predict the constant amplitude fatigue life using variable amplitude loading. These significantly overestimated the fatigue life, indicating high crack growth acceleration due to the load transitions in the variable amplitude fatigue spectrum. Crack growth acceleration was mainly attributed to mean stress variations in the spectrum but overloads were shown to be important in crack initiation. A model incorporating a cycle mix factor has been proposed as an improved method of predicting the fatigue life of bonded joints subjected to variable amplitude fatigue and this model has been shown to result in significantly improved fatigue lifetime predictions [114].

A generalized numerical procedure using FEA for prediction of the fatigue lifetime of adhesively bonded structures was proposed [115]. The number of cycles to failure was calculated by integrating a fatigue crack growth law between initial and final crack lengths. This crack growth law was formulated in terms of SERR, which was determined, at any crack length, from an FEA. This complete process was implemented within the finite element code, enabling automated calculation of the fatigue life for a given set of boundary conditions. The procedure was evaluated by application to a single-lap joint and good results were obtained in comparison with those using other methods.

Another generalized technique for prediction of fatigue crack propagation lifetime in bonded structures using FEA was presented [116]. The method was based on numerical integration of the fatigue crack growth law from an initial to a final crack size. The technique has been applied to carbon fiber composite joints bonded with an epoxy adhesive. A crack growth law was determined experimentally using double cantilever beam samples. Experimental load-life data were then generated for single and double lap joints manufactured from the same material. Good agreement was seen between the predicted and experimental load-life plots.

The mode I ERR including the effect of residual stresses was evaluated for both adhesive and laminate double cantilever beam specimens [117]. The energy release rate can be partitioned into a mechanical term and a residual-stress term in beam theory. The beam-theory mechanical term is not very accurate, but can be corrected by a slight modification to a previous correction factor. This correction factor accounts for crack tip rotation of the specimen arms. The beam-theory residual-stress term is very accurate for a wide range of specimen geometries; it can be used without correction.

A comparison of different methods used to calculate SERR in bonded double cantilever beam joints has been made. The standard beam theory method has been shown to be in error and models with a compliant crack front have been evaluated in search of a more reliable analytical model. It was found that in fatigue testing, a beam on elastic foundation model gives excellent results and a simple form of the beam on elastic foundation equation was proposed [118].

A new double-lap shear geometry testing was introduced, enhancing the traditional lap-shear test resolution [119]. This geometry was not only intended to control the thickness of the adhesive layers and obtain sharp edges, but also to limit to a considerable extent the occurrence of a peel stress. Using a modified shear-lag theory, the axial and shear stresses were determined in the adherents and adhesive, including the effects of internal stresses, using a simple formalism. It was further shown that internal stresses contribute to a great extent to reducing the strength of the joint and therefore must be accounted for. This analysis was further expanded to include effects of adhesive cohesive failure (microcracking) prior to interfacial debonding.

A new approach to adhesion tests by a compression-loaded, double lap shear specimen was introduced and stress analysis of that epoxy resin adhesive specimen presented. The geometry of conventional double lap shear tests was modified to minimize peel stresses and facilitate specimen fabrication, and thereby increase test reproducibility. The bonded part of the new specimen was identical

to a conventional double lap shear specimen, but the specimen was end-loaded in compression instead of in tension. The stress state was analyzed using a new shear-lag theory for multilayered systems that includes residual stresses and friction on debonded surfaces. Axial stresses, shear stresses, and axial displacements were calculated for specimens stressed in the elastic regime, or beyond where local damage or yielding of the adhesive were present. They all compared well with the results of FEA. Failure models of the specimen were derived using both strength and energy release rate methods. The model captured all the essential features of the energy release rate, including the effects of internal stresses and of friction at the debonded interface, within a certain range of debond length and friction stress [101]. The elements of joint design that minimize through thickness stresses in the composite adherents are well known. The use of an adhesive fillet at the ends of the overlap length greatly reduces the level of through-thickness stresses. The use of a reverse taper at the end of the adherents reduces this stress even further and joints designed in this way can give a reliably cohesive failure initiation. Even with well-designed joints, the quality of the laminate is important, as voidage and similar defects will greatly reduce the strength available in the through-thickness direction. Ideally, mechanisms that seek to control the cracking in adhesive bonded joints between composite adherents should be tunable so that propagating cracks can be maintained within the bond line even if the laminate through-thickness strength is low. In principle, if the growing crack can be maintained within the bondline, the possibility exists for developing crack-arrest mechanisms to limit crack growth. A hot cure epoxy adhesive was tested [120] and detailed FEA simulation of growing cracks in joints performed [121]. Adhesively bonded joints were modified using additional material, either continuous film or woven cloth placed along the center of the bondline, or discontinuous particulate material introduced along the interface below which delamination is expected to occur.

Development of rate-dependent constitutive models for polymeric adhesives is essential for carrying out meaningful stress analyses of bonded structures subject to sustained and fluctuating loads. A typical two-part epoxy adhesive system has been subjected to extensive testing, which includes constant strain rate, creep and recovery. The first two of these have been carried out in compression as well as tension. It was shown that the hydrostatic sensitive nature of the adhesive was manifest in creep, as well as constant strain rate loading. It was found that the constant strain rate and creep data were linked through a unique stress–strain rate relationship. It was found that current FEA material models have difficulty modeling both constant strain rate and creep data using the same material parameters. The rate-dependent elasto-plastic model was shown to be much better than power-law creep at this task [122]. Rate-dependent response of adhesively bonded structures was modeled and experimental study was undertaken to provide material data defining both tensile and shear response of the adhesive system. Three different rate-dependent material models have been assessed: von Mises, hydrostatic stress-sensitive and overstress-based visco-plastic. Two of these models were then used to simulate the various single lap joints tested and it appeared that the von Mises model gave closer predictions than the visco-

plastic one. It was also shown that a rate-dependent strain-based failure criterion appeared to give good predictions of joint strength in most of the configuration considered [123].

During crack growth of elastic-plastic materials, the total energy released can be partitioned into elastic work and plastic work. It was found that most prior methods for calculating the plastic work term during monotonic loading have led to results indistinguishable from elastic crack growth and thus simulations of stable crack growth are not possible [124]. To simulate stable crack growth, the fracture model must include extra irreversible energy effects. To get specific results, it was proposed that the irreversible energy can be assumed to be proportional to the plastic work in a plastic-flow analysis. This approach was used to develop a virtual material based on Dugdale yield zones at the crack tips. This virtual material was subjected to computer fracture experiments that showed it has many fracture properties in common with real ductile materials. A Dugdale material can serve as a model material for new simulations with the goal of studying the role of structure in the fracture properties of composites. One sample calculation showed that the toughness of a Dugdale material in an adhesive joint mimics the behavior or real adhesives.

A finite fracture mechanics model was used to predict the development of multiple cracks in the coating layer of coating/substrate systems. The stresses in a cracked coating were evaluated by a variational mechanics approach. These stresses were then used to calculate the total energy released due to the formation of a complete crack in the coating layer. The analysis handled tensile loads or bending loads and included the effect of residual thermal stresses. By assuming the next coating crack forms when the energy released due to the formation of a complete microcrack equals the in situ fracture toughness of coating, it was proposed that one can predict the number of coating cracks as a function of applied strain. Alternatively, it was proposed that experimental data for number of cracks versus strain could be fit to the fracture analysis and be used to determine in situ coating fracture toughness [125]. A series of coating/substrate systems, with typical automotive finishes as coatings, were loaded in four-point bending [126]. The coatings in these specimens usually failed as a result of multiple cracking. The density of coating cracks was recorded as a function of bending strain. These experimental results were fit to the fracture mechanics theory. This fitting procedure led to experimental results for coating fracture toughness. It was found that coating toughness continually dropped as the coatings were baked for longer times. There was also a profound substrate effect which meant that coating fracture toughness must be regarded as an in situ toughness property. The fracture toughness of polymeric coatings on steel substrates was more than an order of magnitude lower than the toughness of the same coating on polymeric substrates, and reached about 50-300J/m^2 for steel and 500-3000J/m^2 for polycarbonate. The in situ coating toughness was also weakly dependent on coating thickness; it increased as the coating got thicker.

2.6. Nanotechnology

The mechanical and thermal properties of polymers and composite structures can be altered through the use of various kinds of fillers. The dimensions of these fillers typically fall on a macroscopic (1 μm–1 mm) length scale. Fillers of this type increase the stiffness and heat distortion temperature of a polymer, primarily because the filler makes up a significant proportion of the total mass. However, macroscopic fillers usually cause decreases in strength, impact resistance, and processability. A new area of composites research has emerged in the last two decades that utilizes nanoparticle fillers to alter the properties of polymers. Definitive results have not yet been achieved, but trends show that when processed properly small amounts (≤5 wt.%) of nanoparticle fillers can increase the modulus, strength, toughness, resistance to chemical attack, gas impermeability, resistance to thermal degradation, and dimensional stability of polymeric materials. Inorganic nanoparticles have gained acceptance as possible reinforcing structures because of their low cost and ease of fabrication. Clays and inorganic reinforcements have been shown to be effective reinforcements in neat polymeric structures, but very little work has been done to examine advanced fiber-reinforced composites that utilize nanocomposite matrices [127].

Nanotechnology can be broadly defined as: the creation, processing, characterization, and utilization of materials, devices, and systems with dimensions on the order of 0.1–100 nm, exhibiting novel and significantly enhanced physical, chemical, and biological properties, functions, phenomena, and processes due to their nanoscale size. Current interests in nanotechnology encompass nano-biotechnology, nano-systems, nano-electronics, and nano-structured materials, of which nanocomposites are a significant part. A morphological characteristic that is of fundamental importance in the understanding of the structure–property relationship of nanocomposites is the surface area/volume ratio of the reinforcement materials. This paper discusses nanocomposites based upon the three categories of reinforcement materials: particles (silica, metal, and other organic and inorganic particles), layered materials (graphite, layered silicate, and other layered minerals), and fibrous materials (nanofibers and nanotubes). The change in particle diameter, layer thickness, or fibrous material diameter from micrometer to nanometer, changes the ratio by three orders in magnitude. At this scale, there is often distinct size dependence of the material properties. In addition, with the drastic increase in interfacial area, the properties of the composite become dominated more by the properties of the interface or interphase. Particulate composites reinforced with micron-sized particles of various materials are perhaps the most widely utilized composites in everyday materials. Particles are typically added to enhance the matrix elastic modulus and yield strength. By scaling the particle size down to the nanometer scale, it has been shown that novel material properties can be obtained [128].

The most distinct characteristic of nanotechnology is that the properties of nanomaterials are size-dependent. Due to the extremely small size of nanomaterials, the evaluation of their mechanical properties, such as elastic modulus, tensile/compressive strength and buckling resistance, presents significant challenges to researchers in nanomechanics. Among the many nanostructured materials,

carbon nanotubes have attracted considerable attention. They can be produced by an array of techniques, such as arc discharge, laser ablation and chemical vapor deposition. From the viewpoint of atomic arrangement, carbon nanotubes can be visualized as cylinders that rolled from sheets of graphite. They assume both single-walled or multi-walled structures and their helicity may also be different. It has been revealed that the conducting properties of carbon nanotubes depend dramatically on their helicity and diameter, and the stiffness, flexibility and strength of carbon nanotubes are much higher than those of conventional carbon fibers. The extraordinary properties of carbon nanotubes have motivated researchers worldwide to study the fundamentals of this novel material as well as to explore their applications in different fields [129].

Because of their small size, carbon nanotubes will tend to agglomerate when dispersed in a polymeric resin. To achieve good reinforcement in a composite, it is critical to have uniform dispersion within the polymer matrix. In addition to slipping of tubes that are not adhered to the matrix, aggregates of nanotube bundles effectively reduce the aspect ratio (length/diameter) of the reinforcement. In addition to uniform dispersion of nanotubes within the matrix, it is critical to process model systems with controlled structure and alignment so that the axial load-carrying efficiency of the nanotube can be utilized. A micro-scale twin-screw extruder was used to achieve dispersion of multi-walled carbon nanotubes in a polystyrene matrix. Highly aligned nanocomposite films were produced by extruding the polymer melt through a rectangular die and drawing the film prior to cooling. Randomly oriented nanocomposites were produced by achieving dispersion first with the twin-screw extruder followed by pressing a film using a hydraulic press. The tensile behavior of the aligned and random nanocomposite films with 5wt.% loading of nanotubes were characterized. Addition of nanotubes increased the tensile modulus, yield strength and ultimate strengths of the polymer films, and the improvement in elastic modulus with the aligned nanotube composite was five times greater than the improvement for the randomly oriented composite [130].

Structural mechanics approach to modeling the deformation of carbon nanotubes was presented [129]. Fundamental to the proposed concept was the notion that a carbon nanotube was a geometrical frame-like structure and the primary bonds between two nearest-neighboring atoms acted like load-bearing beam members, whereas an individual atom acted as the joint of the related load-bearing beam members. By establishing a linkage between structural mechanics and molecular mechanics, the sectional property parameters of these beam members were obtained. The accuracy and stability of the present method was verified by its application to graphite. Computations of the elastic deformation of single-walled carbon nanotubes revealed that the Young's moduli of carbon nanotubes varied with the tube diameter and were affected by their helicity. With increasing tube diameter, the Young's moduli of both armchair and zigzag carbon nanotubes increased monotonically and approach the Young's modulus of graphite.

The molecular structural mechanics approach originally developed for simulating single walled carbon nanotubes was extended to simulate the elastic behavior of multi-walled carbon nanotubes under tension and torsion. The individual tube layer was simulated as a frame-like structure. The van der Waals

forces between tube layers were taken into account by introducing a nonlinear truss rod model. Results indicated that the tube diameter, tube chirality and number of tube layers have some noticeable effects on the elastic properties of multi-walled carbon nanotubes. Furthermore, it has been demonstrated that the inner layers could be effectively deformed only through the direct application of tensile or shear forces, not through van der Waals interactions [131].

A critical review on the validity of different experimental and theoretical approaches to the mechanical properties of carbon nanotubes for advanced composite structures was presented [132]. Special attention has been paid to the measurement and modeling of tensile modulus, tensile strength, and torsional stiffness. Theoretical approaches such as molecular dynamic simulations, finite element analysis, and classical elastic shell theory were frequently used to analyze and interpret the mechanical features of carbon nanotubes. Due to the use of different fundamental assumptions and boundary conditions, inconsistent results were reported. Molecular dynamic simulation is a well-known technique that simulates accurately the chemical and physical properties of structures at atomic-scale level. However, it is limited by the time step, which is of the order of 10^{-15}s. The use of finite element modeling combined with molecular dynamic simulation can further decrease the processing time for calculating the mechanical properties of nanotubes. Since the aspect ratio of nanotubes is very large, the elastic rod or beam models can be adequately used to simulate their overall mechanical deformation.

Clays and inorganic reinforcements have been shown to be effective reinforcements in neat polymeric structures. The matrices of carbon fiber/epoxy composites were modified with layered nanoclays and the resulting changes in the mechanical properties and thermal cycling characteristics of these materials were determined [127]. Transverse cracking in symmetric carbon fiber/epoxy laminates as a response to cryogenic cycling was significantly reduced when nanoparticle fillers were used at concentrations much lower than those used for traditional fillers. The concentration of the particles and their distribution in the matrix was observed to be very important in maximizing the benefits of nanoparticle reinforcement. Large concentrations exhibited a typical, macro-scale filler effect and low concentrations showed little or no effect. Exfoliated and disordered intercalated structures provided the best reinforcement, with more ordered intercalated structures offering little benefit. The mechanical properties and processing characteristics of the laminates studied were not adversely influenced by the presence of the nanoparticles and the thermal expansion characteristics were improved.

High temperature thermoset polyimide was mixed with unmodified and modified montmorillonite (layered silicate) clay. Dynamic mechanical analysis results showed a significant increase in the thermomechanical properties of clay loaded nanocomposites in comparison with the neat polyimide. Also higher glass transition temperature was observed and flexural properties measurements showed a significant improvement in the modulus and strength, with no loss in elongation. Doubling the clay loading percentage resulted in degradation of nanocomposite flexural properties [133].

Nanocomposites can reduce the hydrogen permeability through the composite, without introducing a CTE mismatch, offering the potential for the development of linerless PMC tanks. Isothermal

aging in air results in a surface layer of oxidized polymer, which cracks with further aging. Cracking within the oxidation layer increases the surface area available for oxidation and allows permeation of oxygen into the bulk of the sample, furthering oxidative degradation. Dispersion of layered silicate nanoparticles in the polymer should decrease permeation of oxygen into the composite, thereby enhancing thermal stability. Montmorillonite clay was organically modified and dispersed into a thermoplastic and a thermosetting polyimide matrix [134]. The barrier properties of the neat resins and the nanocomposites were evaluated. Reductions in gas permeability and water absorption were observed in thermoplastic polyimide nanocomposites. The thermosetting polyimide showed a reduction in weight loss during isothermal aging at 288°C.

2.6. Flammability

Polymeric composites are widely used in the production of new engineering materials, due to their economic versatile applicability and good mechanical properties. The most important disadvantage of these materials concerns their low thermal resistance and fire behavior. For this reason, flame retardants are used. Flame retardants are defined as chemical compounds that modify pyrolysis reactions of polymers or oxidation reactions implied in the combustion by slowing down or by inhibiting them. They are mainly phosphorus, antimony, aluminum and boron-containing compounds, chlorides and bromides [135].

Thermoset polymers are widely used in applications where thermal insulation must be ensured at high working temperature because they do not melt. However, being organic materials they degrade to give volatile combustible products when they are heated above critical temperatures or involved in fires. Fire fatalities due to the evolved smoke and toxic gases create hazards to people and the environment. For these reasons it is fundamental to develop thermoset resins with good thermal stability and reduced flammability. This can be made by twofold modification: enhancement of crosslink density of the polymer and use of fire retardant additives [136].

Epoxy resins have been extensively used in many industrial applications such as coatings, adhesives, composites, laminates and encapsulants for electronic packaging because of their low cost, good chemical and electrical resistance, superior mechanical properties, low shrinkage upon curing, and outstanding adhesion properties. However, the flammability of epoxy resins is a serious limitation in areas requiring high flame retardance. Many different approaches have been reported for improving the flame retardance of epoxy resins and halogen-containing compounds have been reported to be effective. However, environmental concerns and legislation are driving the search of new, halogen-free flame retardant agents, like: phosphorus, nitrogen, and silicon compounds. And the combination of different types of these flame retardants can lead to a synergistic improvement in the fire retardance of epoxy systems [137]. Enhancement of flame retardancy of epoxy resins has been achieved by incorporation of phosphorus and silicon into epoxy resins with bringing a P-Si synergistic effect of flame retardation [138].

Brominated reactive compounds, like tetrabromo bisphenol A, are state of the art to achieve sufficient flame retardance for glass fabric based laminates. With the commencement of the directive 2002/95/EG (Official Journal of the European Union) the use of these well proven flame retardants will be prohibited from July 2006 on. From then there is a need to find an alternative, halogen-free flame retardant system which meets the demanding technical requirements for laminates. Flame retardants for epoxy resins, especially laminates, should be halogen free, non-volatile, not hygroscopic, harmless and should show excellent thermal stability. The thermal stability of the resin under load must not be affected as well [139].

Reactive organo-phosphorus compounds have been shown to have a powerful flame retardant effect and, in the case of epoxy resins, can be incorporated into the backbone of the network either through being part of the amine hardener or the epoxy itself. When compared to phosphorus-free epoxy resins, phosphorus-containing epoxy resins show a lower thermal stability, with a reduced initial decomposition temperature, but exhibit a multi-step degradation with a higher final char yield [140].

Currently no fire resistance requirements exist for exterior polymer composite structures on airplanes. However, the aircraft manufacturer will be required to demonstrate that polymer structural composites provide equivalent safety to the current material system (aluminum alloy). The primary hazards during aircraft fires are heat, smoke, and toxic gas. In a severe aircraft fire, life threatening levels of these hazards are produced by cabin flashover, the time to which is largely governed by the rate of heat release of the materials in the fire. Other concerns in a carbon fiber composite fire include the potential release of electrically conductive small carbon fibers that can cause damage to electrical equipment and health problems (from inhalation) [141].

Nanocomposites seem to be a new class of flame retardant systems. In recent years they have attracted great interest because they frequently exhibit remarkable improvements in mechanical and material properties. These improvements include a higher modulus, optical transparency, increased strength and keeping biodegradability of biodegradable polymers, furthermore increased heat resistance and decreased gas permeability and flammability [136]. The interface at the surface of particle inclusions plays a key role in the structure property relationship.

Work [142] presents use of layered double hydroxides, as an alternative to commonly used cationic clays, to formulate epoxy nanocomposites with high flame retardant properties. It is reported that layered double hydroxides contribute to the flame retardancy of the polymeric matrix, producing a refractory oxide residue on the surface of the material and releasing aqueous vapor and carbon dioxide during the decomposition. The endothermic nature of these processes and the dilution of combustible gases of pyrolysis increase the ignition time and reduce the heat release during the combustion. Concerning the flame retardant properties, epoxy nanocomposites based on the organic-modified layered double hydroxide exhibit:

- a unique self-extinguishing behavior in UL94HB test, never observed before in pure nanocomposites,

- a higher reduction in the PHRR (peak of heat release rate) compared to montmorillonite based nanocomposites,
- an increase in the reduction of PHRR for the thin sample compared to the thick sample,
- the formation of an intumescent compact char with an intercalated nanostructure,
- and a synergistic effect with ammonium polyphosphate.

The effect of combining the organo-phosphorus compounds with nanoparticles was studied [143]. There were two reasons for combining the synthesized phosphorous compounds with nanoparticles: (1) montmorillonite nanoplatelets were expected to compensate the softening effect of the flame retardants and (2) phosphorous flame retardants intercalated between the nanolayers were recently found to be very efficient in polypropylene and it was reasonable to try utilizing the same effect in epoxy resin. The incorporation of the nanoparticles did not create the desired flame retardant effect which can be explained by the increased heat conductivity and lower mobility of the nanoparticles due to the crosslinked structure.

Cone calorimeter is one of the most effective bench-scale methods for studying the fire retardant properties of polymeric materials. Fire-relevant properties such as the heat release rate (HRR), HRR peak, smoke production, and CO2 yield, are vital to the evaluation of the fire safety of materials. Various types of nanocomposite materials were found to have significant reductions in flammability. In general, the nanocomposites' flame retardant mechanism involves a high-performance carbonaceous-silicate char, which builds up on the surface during burning. This insulates the underlying material and slows the mass loss rate of decomposition products. Mechanism by which clay nanocomposites function involves the formation of a char that serves as a barrier to both mass and energy transport. As the fraction of clay increases, the amount of char that can be formed increases, and the rate at which heat is released decreases. In contrast, the decrease in the rate of heat release corresponds to (1) a decrease in mass loss rate and the amount of energy released by the time resin has ceased burning, and (2) a modest increase in the time at which the peak heat release is reached. The production of a char barrier must serve to retain some of the resin, and thus both the energy released and the mass loss rate decrease. The amount of smoke evolved and specific extinction area also decrease with the formation of the nanocomposites. There is some variability in the smoke production. Although it is observed that the formation of the nanocomposites reduces smoke production, the presence of additional clay does not continue this smoke reduction [144].

Recently, cone calorimetric experiments have demonstrated that the flame retardancy of many polymer/clay nanocomposites, including polyamide 6, polyamide 66, polypropylene, polystyrene, and polyethylene-co-vinyl acetate were improved; concretely, PHRR decreased significantly during the combustion. Studies of flammability of polyethylene/clay nanocomposites, which were prepared by melt intercalation using several organoclays, showed reduction in peak heat release rate of 30-40% by adding 3 wt% organoclay, but the mechanical properties were not reported [145].

References:

[1] Bechel V.T., Camping J.D., Kim R.Y. Composites: Part B 36B (2005) 171-182

[2] Roy S., Benjamin M. Composites Science and Technology 64 (2004) 2051-2065

[3] Nairn J.A. Comprehensive Composite Materials, Vol. 2 403-432

[4] Henaff-Gardin C., Lafarie-Frenot M.C., Gamby D. Composite Structures 36 (1996) 113-130

[5] Henaff-Gardin C., Lafarie-Frenot M.C., Gamby D. Composite Structures 36 (1996) 131-140

[6] Lafarie-Frenot M.C., Henaff-Gardin C., Gamby D. Composites Science and Technology 61 (2001) 2327-2336

[7] Huang X., Gillespie J.W.Jr, Eduljee R.F. Composites: Part B 28B (1997) 419-424

[8] Nairn J.A., Mendels D.A. Mechanics of Materials 33 (2001) 335-362

[9] Wang A.S.D., Kishore N.N., Li C.A. Composites Science and Technology 24 (1985) 1-31

[10] Pagano N.J., Schoeppner G.A., Kim R., Abrams F.L. Composites Science and Technology 58 (1998) 1811-1825

[11] Fang G.-P., Schapery R.A., Weitsman Y. Engineering Fracture Mechanics 33 (1989) 619-632

[12] Whitcomb J., Lagoudas D., Kinra V. NCAM Project No. 58404-S7

[13] Park O., Sankar B.V. Composite Structures 55 (2002) 429-434

[14] Kobayashi S., Terada K., Ogihara S., Takeda N. Composites Science and Technology 61 (2001) 1735-1742

[15] Park C.H., McManus H.L. Composites Science and Technology 56 (1996) 1209-1219

[16] Bartley-Cho J., Lim S.G., Hahn H.T., Shyprykevich P. Composites Science and Technology 58 (1998) 1535-1547

[17] Henaff-Gardin C., Lafarie-Frenot M.C. International Journal of Fatigue 24 (2002) 171-177

[18] Timmerman J.F., Tillman M.S., Hayes B.S., Seferis J.C. Composites: Part A 33 (2002) 323-329

[19] Yokozeki T., Aoki T., Ishikawa T. Composites Science and Technology 62 (2002) 1223-1229

[20] Chen L., Sankar B.V., Ifju P.G. Composites Science and Technology 62 (2002) 1407-1414

[21] Sankar B.V., Sharma S.K. Composites Science and Technology 57 (1997) 729-737

[22] Chen G., Li Z., Kou C., Gui L. Journal of Reinforced Plastics and Composites 23(9) (2004) 987-995

[23] Bechel V.T., Camping J.D., Kim R.Y. Composites: Part B 36 (2005) 171-182

[24] Bechel V.T., Kim R.Y. Composites Science and Technology 64 (2004) 1773-1784

[25] Bechel V.T., Fredin M.B., Donaldson S.L., Kim R.Y., Camping J.D. Composites: Part A 34 (2003) 663-672

[26] Kobayashi S., Takeda N. Composites: Part A 33 (2002) 1529-1538

[27] Owens G.A., Schofield S.E. Composites Science and Technology 33 (1988) 177-190

[28] Ahlborn K. Cryogenics 31 (1991) 257-260

[29] Ahlborn K. Cryogenics 31 (1991) 252-256

[30] Pannkoke K., Wagner H.J. Cryogenics 31 (1991) 248-251

[31] Wharmby A.W., Ellyin F., Wolodko J.D. International Journal of Fatigue 25 (2003) 437-446

[32] Dutta P.K., Hui D. Composites: Part B 27 (1996) 371-379

[33] Lowe A., Fox B., Otieno-Alego V. Composites: Part A 33 (2002) 1289-1292

[34] Morgan R.J., Shin E.E., Rosenberg B., Jurek A. Polymer 38(3) (1997) 639-646

[35] Akay M., Spratt G.R., Meenan B. Composites Science and Technology 63 (2003) 1053-1059

[36] Han M.H., Nairn J.A. Composites: Part A 34 (2003) 979-986

[37] Whitley K.S., Gates T.S. Mechanical Properties and Damage Mechanisms for Polymeric Matrix Composites Subjected to Cryogenic Environments ASC September 2001

[38] Gates T.S., Whitley K.S., Grenoble R.W., Bandorawalla T. Thermal/Mechanical Durability of Polymer Matrix Composites in Cryogenic Environments AIAA-2003-7408

[39] Whitley K.S., Gates T.S. NASA/TM-2003-212171

[40] Zhandarov S., Pisanova E., Mader E., Nairn J.A. Investigation of Load Transfer between the Fiber and the Matrix in Pull-out Tests with Fibers Having Different Diameters

[41] Aimmanee S., Vinson J.R. Journal of Sandwich Structures and Materials 4 (2002) April 115-139

[42] Gates T.S., Odegard G.M., Herring H.M. Facesheet Delamination of Composite Sandwich Materials at Cryogenic Temperatures, December 2003

[43] Final Report of the X-33 Liquid Hydrogen Tank Test Investigation Team. NASA May 2000

[44] Herring H.M. NASA/CR-2003-212422 June 2003

[45] Kessler S.S., Matuszeski T., McManus H. Cryocycling and Mechanical Testing of CFRP for X-33 Liquid H_2 Fuel Tank Structure ASC-2001 #093

[46] Smeltzer S.S., Waters W.A. Nonlinear Thermal Analyses of a Liquid Hydrogen Tank Wall

[47] Choi S., Sankar B.V. A Micromechanics Method to Predict the Microcracking of the LH2 Composite Tank at Cryogenic Temperature

[48] Choi S., Sankar B.V. Fracture Toughness of Transverse Cracks in Graphite/Epoxy Laminates at Cryogenic Conditions

[49] Ifju P., Sankar B.V. Fiber Composites for LH_2 Storage

[50] Grimsley B.W., Cano R.J., Johnston N.J., Loos A.C., McMahon W.M. Hybrid Composites for LH2 Fuel Tank Structure

[51] Loos A.C., Sturges R.H., Viehland D.D., Batra R.C. NCAM Project No. 58404-S8

[52] Glass D.E. NASA Contactor Report 201734 Contract NASI-96014 August 1997

[53] Kim R.Y., Crasto A.S., Schoeppner G.A. Composites Science and Technology 60 (2000) 2601-2608

[54] Wang J.T., Johnson T.F., Sleight D.W., Saether E. Cryogenic Tank Structure Sizing with Structural Optimization Method AIAA-2001-1599

[55] Estrada H., Smeltzer S.S. Design and Development of a Composite Dome for Experimental Characterization of Material Permeability

[56] Hohe J., Goswami S., Becker W. Computational Materials Science 26 (2003) 71-79

[57] Jiang H., Huang Y., Liu C. Composites: Part B 35 (2004) 551-556

[58] Ko W.L. NASA/TP-1999-206580 June 1999

[59] Sharma S.C., Krishna M., Narasimha Murthy H.N., Sathyamoorthy, Bhattacharya D. Journal of Materials Engineering and Performance 13(4) (2004) 1-5

[60] Sharma S.C., Narasimha Murthy H.N., Krishna M. Effect of Foam Density and Skin Material on the Damping Behaviour of Polyurethane Sandwich Structures

[61] Sharma S.C., Narasimha Murthy H.N., Krishna M. Low Velocity Impact Response of Polyurethane Foam Composite Sandwich Structures

[62] Demharter A. Cryogenics 38 (1998) 113-117

[63] Brown D., Butler D., Howell J., Lee A., Sizemore B., Wong M. Sandwich Composite – 3-Point Bending Test for Composites with Rohacell and Fuzzy Carbon Cores

[64] Ratcliffe J., Cantwell W.J. Journal of Reinforced Plastics and Composites 20 (2001) 945-970

[65] Baker D.J. Evaluation of Thin Kevlar-Epoxy Fabric Panels Subjected to Shear Loading, AIAA

[66] Baker D.J. NASA Technical Paper 3468 September 1994

[67] Wang J., Vinson J.R., Glancey J.L. Journal of Sandwich Structures and Materials 6 (2004) September 447-457

[68] Anderson T.A. Composite Structures 60 (2003) 265-274

[69] Zhu H., Sankar B.V., Haftka R.T., Venkataraman S., Blosser M. Minimum Mass Design of Insulation Made of Functionally Graded Material AIAA-2002-1425

[70] Apetre N.A., Sankar B.V., Venkataraman S. Indentation of a Sandwich Beam with Functionally Graded Core AIAA-2002-1683

[71] Venkataraman S., Sankar B.V. Analysis of Sandwich Beams with Functionally Graded Core

[72] Vaidya U.K., Nelson S., Sinn B., Mathew B. Composite Structures 52 (2001) 429-440

[73] Vaidya U.K., Hosur M.V., Earl D., Jeelani S. Composites: Part A 31 (2000) 761-772

[74] Mines R.A.W., Alias A. Composites: Part A 33 (2002) 11-26

[75] Xue Z., Hutchinson J.W. Constitutive Model for Metallic Sandwich Cores: I - Theory, II - Application

[76] Chen A., Davalos J.F. International Journal of Solids and Structures 42 (2005) 2711-2739

[77] Mahfuz H., Islam M.S., Rangari V.K., Saha M.C., Jeelani S. Composites: Part B 35 (2004) 543-550

[78] Preissner E.C., Vinson J.R. Journal of Sandwich Structures and Materials 5 (2003) July 233-251

[79] Satapathy N.R., Vinson J.R. Journal of Sandwich Structures and Materials 2 (2000) October 379-390

[80] Skvortsov V., Bozhevolnaya E., Thomsen O.T., Luckegaard A., Vinson J.R. Journal of Sandwich Structures and Materials 5 (2003) October 309-350

[81] Thomsen O.T., Vinson J.R. Journal of Sandwich Structures and Materials 3 (2001) July 220-250

[82] Frostig Y., Thomsen O.T., Vinson .R. Journal of Sandwich Structures and Materials 6 (2004) March 167-194

[83] Li Z., Xu L., Sun H., Xiao Y., Zhang J. Cryogenics 44 (2004) 357-362

[84] Glass D.E., Stevens J.C., Vause R.F., Winn P.M., Maguire J.F., Driscoll G.C., Blackburn C.L., Mason B.H. NASA/CR-1999-209822 December 1999

[85] Sparks S. Development of a Cryo-Biaxial Permeability Apparatus to Measure the Hydrogen Permeability Through Composite Cryotank Materials and the Generation of a Database to Aide in the Selection of Reusable Composite Cryotank Materials

[86] Glass D.E., Raman V.V., Venkat V.S., Sankaran S.N. NASA/CR-97-206263 December 1997

[87] Glass D.E., Raman V.V., Venkat V.S., Sankaran S.N. Composite Structures 44 (1999) 253-261

[88] Disdier S., Rey J.M., Pailler P., Bunsell A.R. Cryogenics 38 (1998) 135-142

[89] Rivers H.K., Sikora J.G., Sankaran S.N. Detection of Micro-Leaks through Complex Geometries under Mechanical Load and at Cryogenic Temperature AIAA-2001-1218

[90] Stokes E.H. Hydrogen Permeability of a Polymer Based Composite Tank Material under Tetra-Axial Strain

[91] Nettles A.T. NASA/TM-2001-210799 February 2001

[92] Anderson T.A. Composites: Part B 36 (2005) 135-142

[93] Freeman B., Schwingler E., Mahinfalah M., Kellogg K. Composite Structures 70 (2005) 374-381

[94] Christopherson J., Mahinfalah M., Jazar G.N., Aagaah M.R. Composite Structures 67 (2005) 299-306

[95] Meo M., Morris A.J., Vignjevic R., Marengo G. Composite Structures 62 (2003) 353-360

[96] Nguyen M.Q., Jacombs S.S., Thomson R.S., Hachenberg D., Scott M.L. Composite Structures 67 (2005) 217-227

[97] Jiang D., Shu D. Composite Structures 71 (2005) 53-60

[98] Aktay L., Johnson A.F., Holzapfel M. Computational Materials Science 32 (2005) 252-260

[99] Abdel Wahab M.M., Crocombe A.D., Beevers A., Ebtehaj K. International Journal of Adhesion & Adhesives 22 (2002) 61-73

[100] Loh W.K., Crocombe A.D., Abdel Wahab M.M., Ashcroft I.A. Engineering Fracture Mechanics 69 (2002) 2113-2128

[101] Mendels D.A., Page S.A., Manson J.A.E., Nairn J.A. A Compression-Loaded Double Lap Shear Tests: Part 1, Theory

[102] Wu G., Crocombe A.D. Computers & Structures 61(2) (1996) 385-391

[103] Bishopp J.A. International Journal of Adhesion & Adhesives 12(3) (1992) 178-184

[104] Karrer R. Cryogenics 38 (1998) 119-123

[105] Clark L.J., Cosman M.A. International Journal of Adhesion & Adhesives 23 (2003) 343-348

[106] Nettles A.T. NASA Technical Memorandum 108483 March 1995

[107] Balkova R., Holcnerova S., Cech V. International Journal of Adhesion & Adhesives 22 (2002) 291-295

[108] Ashcroft I.A., Abdel Wahab M.M., Crocombe A.D., Hughes D.J., Shaw S.J. Composites: Part A 32 (2001) 45-58

[109] Abdel Wahab M.M., Ashcroft I.A., Crocombe A.D., Hughes D.J., Shaw S.J. Composites: Part A 32 (2001) 59-69

[110] Adhesive Bonding Technologies for Automotive Structural Composites ORNL/TM-2001/2 February 2001

[111] Crocombe A.D. International Journal of Adhesion & Adhesives 17 (1997) 229-238

[112] Crocombe A.D., Richardson G. International Journal of Adhesion & Adhesives 19 (1999) 19-27

[113] Erpolat S., Ashcroft I.A., Crocombe A.D., Abdel Wahab M.M. Composites: Part A 35 (2004) 1175-1183

[114] Erpolat S., Ashcroft I.A., Crocombe A.D., Abdel Wahab M.M. International Journal of Adhesion & Adhesives 26 (2004) 1189-1196

[115] Abdel Wahab M.M., Ashcroft I.A., Crocombe A.D., Smith P.A. International Journal of Fatigue 24 (2002) 705-709

[116] Abdel Wahab M.M., Ashcroft I.A., Crocombe A.D., Smith P.A. Composites: Part A 35 (2004) 213-222

[117] Nairn J.A. International Journal of Adhesion & Adhesives 20 (2000) 59-70

[118] Erpolat S., Ashcroft I.A., Crocombe A.D., Abdel Wahab M.M. Engineering Fracture Mechanics 71 (2004) 1393-1401

[119] Mendels D.A., Page S.A., Leterrier Y., Manson J.A.E., Nairn J.A. A Modified Double Lap-Shear Test as a Mean to Measure Intrinsic Properties of Adhesive Joints ECCM-9 June 2000

[120] Potter K.D., Guild F.J., Harvey H.J., Wisnom M.R., Adams R.D. International Journal of Adhesion & Adhesives 21 (2001) 435-443

[121] Guild F.J., Potter K.D., Heinrich J., Adams R.D., Wisnom M.R. International Journal of Adhesion & Adhesives 21 (2001) 445-453

[122] Yu X.X., Crocombe A.D., Richardson G. International Journal of Adhesion & Adhesives 21 (2001) 197-210

[123] Zgoul M., Crocombe A.D. International Journal of Adhesion & Adhesives 24 (2004) 355-366

[124] Nairn J.A. Engineering Fracture Mechanics 72 (2005) 961–979

[125] Kim S.R., Nairn J.A. Engineering Fracture Mechanics 65 (2000) 573-593

[126] Kim S.R., Nairn J.A. Engineering Fracture Mechanics 65 (2000) 595-607

[127] Timmerman J.F., Hayes B.S., Seferis J.C. Composites Science and Technology 62 (2002) 1249-1258

[128] Thostenson E.T., Li C., Chou T.W. Composites Science and Technology 65 (2005) 491-516

[129] Li C., Chou T.W. International Journal of Solids and Structures 40 (2003) 2487-2499

[130] Thostenson E.T., Chou T.W. Journal of Physics D 35 (2002) L77-L80

[131] Li C., Chou T.W. Composites Science and Technology 63 (2003) 1517-1524

[132] Lau K.T., Chipara M., Ling H.Y., Hui D. Composites: Part B 35 (2004) 95-101

[133] Abdalla M.O., Dean D., Campbell S. Polymer 43 (2002) 5887-5893

[134] Campbell S., Johnston J.C., Inghram L., McCorkle L., Silverman E. NASA/TM-2003-212221 April 2003

[135] Demir H., Balkose D., Ulku S. Polymer Degradation and Stability 91 (2006) 1079-1085

[136] Camino G., Tartaglione G., Frache A., Manferti C., Costa G. Polymer Degradation and Stability 90 (2005) 354-362

[137] Wang Q., Shi W. Polymer Degradation and Stability, Article in Press

[138] Liu Y.L., Chou C.I. Polymer Degradation and Stability 90 (2005) 515-522

[139] Mauerer O. Polymer Degradation and Stability 88 (2005) 70-73

[140] Liu W., Russell J.V., Simon G.P. Polymer 47 (2006) 2091-2098

[141] Hergenrother P.M., Thompson C.M., Smith J.G. Jr., Connell J.W., Hinkley J.A., Lyon R.E., Moulton R. Polymer 46 (2005) 5012-5024

[142] Zammarano M., Franceschi M., Bellayer S., Gilman J.W., Meriani S. Polymer 46 (2005) 9314-9328

[143] Toldy A., Toth N., Anna P., Marosi G. Polymer Degradation and Stability 91 (2006) 585-592

[144] Ray S. S., Okamoto M. Progress in Polymer Science 28 (2003) 1539-1641

[145] Zhao C., Qin H., Gong F., Feng M., Zhang S., Yang M. Polymer Degradation and Stability 87 (2005) 183-189

Chapter 3

EXPERIMENTAL PROCEDURE

3.1. Materials

The tested sandwich structure will consist of graphite fiber/epoxy resin laminate skins and aramid paper honeycomb core with specially chosen adhesive. Nanoparticles will be added to the matrix to improve mechanical properties and decrease permeability. Particular materials will be tested and the best combination will be established.

Materials for composite sandwich structure:

- Facesheet laminate components:
  - Kevlar fabric,
- Core components:
  - Kevlar paper 2.8N636 and 3.9N636,
  - Nomex paper 3T412 and 2T412,
- Resins:
  - unsaturated polyester Bondo 7630800402 from Dynatron/Bondo Corp.,
  - fiberglass resin NAPA 765-1286 (polyester 26098-37-3 with styrene 100-42-5) from Balkamp, Inc.,
  - low viscosity epoxy MAS 30-002 with fast epoxy hardener MAS 30-012,
  - hot melt 977-2 epoxy from Cytec,
  - medium-low viscosity SilverTip Marine Epoxy laminating resin with fast hardener from System Three Resins, Inc.,
  - Kapton film HN,
- Nanoparticles:
  - Bentolite L-10 from Southern Clay Products, Inc.,
  - pretreated montmorillonite nanoclays I.30E from Nanocor, Inc.,
  - Pyrograf III carbon fibers HT grade from Pyrograf Products, Inc.,
- Additives:
  - Methyl Ethyl Ketone Peroxide (MEKPO),
  - Acetone,
  - Isopropyl alcohol.

Carbon Fibers - Fibers produced by the pyrolysis of organic precursor fibers such as rayon, polyacrylonitrile, and pitch in an inert atmosphere. The term is often used interchangeably with graphite; however, carbon fibers and graphite fibers differ in the temperature at which the fibers are made and

heat-treated, and the amount of carbon produced. Carbon fibers typically are carbonized at about 1300^{o}C and assay at 93 to 95% carbon, while graphite fibers are graphitized at 1900 to 3000^{o}C and assay at more than 99% elemental carbon.

Aramid - A manufactured fiber in which the fiber-forming substance consisting of a long-chain synthetic aromatic polyamide in which at least 85% of the amide (-CONH-) linkages are attached directly to two aromatic rings.

Epoxy Resin - Resins which may be of widely different structures but are characterized by the presence of the epoxy group. (The epoxy or epoxide group is usually present as glycidyl ether, glycidyl amine, or as part of an aliphatic ring system. The aromatic type epoxy resins are normally used in composites) [1].

Kapton - polyimide film by DuPont is an electrical insulation material with outstanding thermal, mechanical, chemical and electrical properties. Kapton has been used successfully in field applications where the environmental temperatures were as low as -269°C and as high as 400°C. Kapton can be easily fabricated by a wide variety of techniques, including die cutting, punching and thermoforming. It offers excellent adhesive bondability as well. Major application fields:

- flexible printed circuits (substrate material),
- semiconductor insulator pads,
- semiconductor radiation protection,
- aerospace-wire applications,
- magnet-wire applications,
- solder masks,
- fiber-optic cable protection,
- pressure-sensitive tape,
- high-performance parts,
- high-temperature diaphragms,
- pressure switches,
- aircraft shims,
- emergency escape smoke hood,
- motor slot liners,
- gaskets and diaphragms,
- belts,
- insulation blankets for the space program,
- military low-observables and electronic concealment,
- sensors,
- carrier film for tape automated bonding (TAB),
- bar code labels,
- voice coils.

MEKPO (Methyl Ethyl Ketone Peroxide) is a common name of peroxides produced by reacting methyl ethyl ketone with hydrogen peroxide, and is widely used in industry as a radical catalyst source for initiating and cross-linking polymerization.

Aramid paper honeycomb is manufactured from aramid fiber sheets. A thermosetting adhesive is used to bond these sheets at the nodes, and, after expanding to the hexagonal or OX-Core configuration, the block is dipped in resin. After curing the resin, slices are cut to the desired thickness. For special applications, such as air directionalizing, the honeycomb can be provided without the resin. Using this process, a wide range of cell sizes, paper thicknesses, and densities can be produced. The OX configuration is a hexagonal honeycomb that has been overexpanded in the W direction, providing a rectangular cell shape that facilitates curving or forming in the *L* direction.

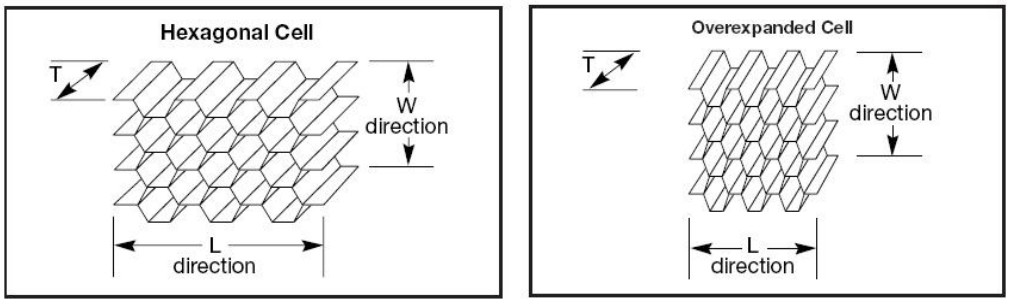

Fig 3.1.1. Honeycomb configuration [2]

The aramid honeycomb has been widely accepted throughout the aerospace industry and several commercial areas as a very tough, environmentally resistant core material in sandwich panels. It has been designed and used in flat and contoured shapes, with a wide variety of facing materials and adhesives, and it has extensive service in both structural and nonstructural parts [2].

Aramid honeycomb features:

- high strength at low densities,
- small cell sizes at low densities,
- damage resistant under normal shop use,
- formable,
- fire-resistant (self-extinguishing),
- water and fungus resistant,
- excellent dielectric properties,
- good bonding surfaces,
- good thermal and electrical insulator.

Nomex brand paper is produced from short meta-aramid fibers called floc and small binder meta-aramid particles called fibrids. The formed paper is calendared to add density and rigidity. Manufactured from Nomex aramid paper, Nomex honeycomb combines great strength with extremely light weight.

Korex and Kevlar are true composite (aramid/thermoset resin, e.g. phenolic or epoxy) honeycomb cores made from saturable paper containing para-aramid floc and meta-aramid fibrids. Their high modulus and strength, low moisture regain, and hot/wet property retention make them ideal for high-performance applications.

Characteristics of Nomex honeycomb [3]:

- thermal tolerance >200C (~400F) for short periods,
- available in wide density range, < 24 to >160 Kg/m3 (<1.5 to >10PCF),
- high specific shear strength, especially compared to foam cores,
- high toughness, especially compared to other honeycomb cores,
- meets stringent smoke, toxicity and flammability standards,
- excellent creep and fatigue performance,
- high wet strength, especially compared with cellulosic honeycomb,
- ease of fabrication,
- corrosion free and no galvanic action,
- thermally insulating.

Characteristics of Kevlar and Korex honeycomb:

- thermal stability similar to Nomex but with higher elevated temperature mechanical properties,
- available in wide density range (the lowest basis weight N636 sheet makes low density, small cell Kevlar honeycomb possible),
- improved shear strength and modulus,
- high toughness,
- meets stringent smoke, toxicity and flammability standards,
- improved creep and fatigue performance,
- hot/wet properties better than other composite honeycomb cores,
- established fabrication methods are suitable for Kevlar and Korex honeycombs, Kevlar has good thermal forming response,
- Kevlar, Korex and Nomex honeycombs share other aramid advantages.

Bentolite L-10 from Southern Clay Products, Inc. – is a white smectite powder produced from native, colloidal aluminum silicate materials found in South Central Texas. The high purity and consistency of Bentolite L-10 are made possible by selective mining and exhaustive assessment of the crude ore to thorough quality control of the finished product. Benefits from using Bentolite L-10: economical, shear tolerant, syneresis and settling control, wide pH range tolerance (6-12), excellent pigment extension properties, enzyme proof, substantially improved hiding.

Pretreated montmorillonite nanoclays I.30E from Nanocor, Inc. - Nanomer I.30E nanoclay is an onium ion surface modified montmorillonite mineral. It is designed to be easily dispersed into amine-cured epoxy resins to form nanocomposites. A number of properties are improved, including modulus, glass

transition temperature and chemical resistance. Amine-cured epoxy nanocomposites with 10-20% of Nanomer I.30E nanoclay exhibit significantly increased glass transition temperatures 10 to 20°C (DMA method). Nanocomposites with higher loadings demonstrate further increased modulus over a broad temperature range but nearly identical glass transition temperatures when compared to 10% loaded nanocomposites.

Pyrograf III carbon fibers HT grade from Pyrograf Products, Inc. - is a patented, very fine, highly graphitic, yet low cost, carbon nanofiber. Pyrograf III is available in diameters ranging from 70 and 200 nanometers and a length estimated to be 50-100 microns. Therefore, nanofibers are much smaller than conventional continuous or milled carbon fibers (5-10 microns) but significantly larger than carbon nanotubes (1-10 nanometers). Pyrograf III nanofiber is offered in two types and in four grades. Pyrograf III can simultaneously provide enhanced electrical conductivity over a broad range along with mechanical reinforcement of certain matrix materials. Other benefits provided by the nanofiber include improved heat distortion temperatures and increased electromagnetic shielding. Although direct measurement of many properties cannot be obtained by routine conventional methods, the physical properties of more graphitic forms of vapor grown carbon fiber are known to tend towards single crystal graphite.

Pyrograf III HT - heat treated carbon fiber:

- heated to temperatures up to 3,000°C,
- graphitizes chemically vapor deposited carbon present on the surface of Pyrograf,
- creates a highly electrically conductive carbon nanofiber,
- removes iron catalyst from carbon nanofiber.

3.2. Apparatus

Helium permeability tests will be performed on 4-8 samples (depending on repeatability) on a specially built set-up as shown in the Fig.3.2.1 with gaseous helium as a permeant. The helium was pumped with stable pressure 1 and 5 psi (6.9 and 34.5 MPa). The sample was a circular disk 1" (25.4 mm) in diameter and thickness measured in 4 points. The thickness differed for different trials and different coating processes.

The Alcatel ASM 142 is a universal helium leak detector with usable helium sensitivity in the 10^{-11}atm*cc/s range, comprehensive control panel with two distinct areas: one for the operation of the unit, the other for entering the test parameters. Special features include: auto-calibration, auto-zero, helium signal direct readout, full automation of the test cycle. The analyzer cell works on the principle of mass spectrometry and is set to the mass of helium (atomic mass =4).

Additionally samples were tested for flammability resistance. Heat release is the key measurement required to assess the fire resistance of materials and products. Traditionally it was very difficult to measure and more recently full scale testing of items was possible by burning these articles and measuring the evolved heat using a technique called oxygen depletion calorimetry.

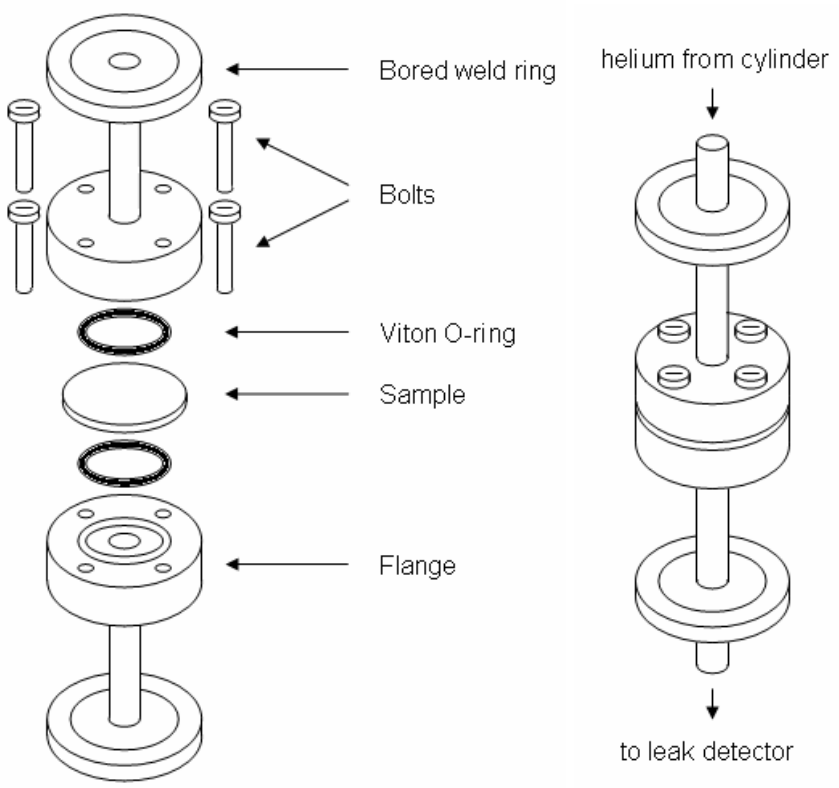

Fig.3.2.1. Sample fixture set-up

Fig.3.2.2. FTT Cone Calorimeter

Cone Calorimeter from Fire Testing Technology Ltd., United Kingdom is the most significant bench scale instrument in the field of fire testing (Fig.3.2.2). This name was derived from the shape of the

truncated conical heater that is used to irradiate the test specimen with fluxes up to 100 kW/m^2 in the test. The FTT Cone Calorimeter has been produced to meet all existing Standards (including ISO 5660, ASTM E 1354, ASTM E 1474, ASTM E 1740, ASTM F 1550, ASTM D 6113, NFPA 264, CAN ULC 135 and BS 476 Part 15). The cone calorimeter measures heat release rate, total heat released and effective heat of combustion by the oxygen consumption principle. The calorimeter also measures mass loss rate, time to ignition, specific extinction area, and, optionally, carbon monoxide and carbon dioxide production during the burning of material or product specimens exposed to radiant heat fluxes from a conical heater set at values from 0 to 100 kW/m^2.

Coated papers for flammability resistance tests were cut to size 100 mm x 100 mm and burned as stack of one, two, three, or six layers with heat flux set to 50kW/m^2 in horizontal position.

3.3. Procedures

3.3.1. Samples of Nomex and Kevlar papers coated with different resin systems obtained from Pittsburg State University

- Papers were coated with unsaturated polyester mixed with 1.5% of MEKPO, also 5% by wt. of acetone was added, as a diluent. Resin was brush and roller applied to both sides and samples were room temperature cured in press between sheets of nylon films and metal plates or in vacuum-bag between peel plies.
- Papers were coated with fiberglass polyester resin NAPA 765-1286 mixed with MEKPO and 91% alcohol. Resin was applied with brush then roller (iron) was used to impregnate paper pores and samples left to dry in 40ºC for several hours. Finally, samples were cured in vacuum-bag in oven.
- Papers were coated with epoxy resin MAS 30-002 mixed with fast epoxy hardener MAS 30-012 mixed in 2:1 ratio and with alcohol. Resin was applied with brush then roller (iron) was used to impregnate paper pores and samples left to dry in 40ºC for several hours. Finally, samples were cured in vacuum-bag in oven.
- Papers were coated with medium-low viscosity SilverTip Marine Epoxy laminating resin and fast hardener from System Three Resins, Inc. mixed in 2:1 ratio and with alcohol. Resin was poured on both sides of paper and gently distributed, placed between metal plates, and left to cure in room temperature overnight and than placed in oven for additional few hours in 50ºC.

3.3.2. Procedure of helium permeability tests of uncoated and coated aramid papers, and resin films

- Turn the helium leak detector on
- Start Hyperterminal, capture text
- Calibration (in case it is not automatic)

- Wait on stand-by for background reaching 10^{-11}mbar*l/s or approx. 15 min. for warm-up and stabilization
- Put the sample in the fixture
- Connect fixture to leak detector
- Cycle
- After 30-60 min. (depends on sample) start helium pumping setting at 1psi for uncoated paper samples and 5 or 10psi for coated ones
- Adjust the pressure
- Stop cycle after 12 or 24 hours
- On stand-by stop helium pumping
- Disconnect the fixture
- Take the sample of the fixture
- Leave the machine on stand-by in case of contamination for 6-12 hours
- Turn the machine of, stop Hyperterminal
- In order to convert leak detector leak rate unit in mbar*l/s into permeation rate unit in scc/s*in^2 values from machine must be divided by 0.112.

3.3.3. Addition of different nanoparticles to SilverTip Marine Epoxy laminating resin

- 2, 4, and 6% of Bentolite L-10 nanoclay and Pyrograf III carbon fibers HT grade were sonicated in 10 time bigger amount of acetone for 1 hour. Epoxy was added and mixed with stirring sticks for few minutes, and the mixture was placed in vacuum oven in temp. 60ºC for 1 to 3 hours depending on amount of acetone. After acetone was evaporated, epoxy was cooled, and hardener was added and mixed with stirring sticks for few minutes. The mixture was applied to aramid papers.
- 2, 4, and 6% of Nanocor I.30E nanoclay were sonicated in 10 time bigger amount of acetone for 2 minutes. Epoxy was added and mixed with stirring sticks for few minutes, and the mixture was placed in vacuum oven in temp. 60ºC for 1 to 3 hours depending on amount of acetone. After acetone was evaporated, epoxy was cooled; high speed mixed for 2 minutes, and hardener was added and mixed with stirring sticks for few minutes. The mixture was applied to aramid papers.

3.3.4. Flammability tests of uncoated and coated aramid papers and Kevlar fabric, and resin films using FTT Cone Calorimeter and based on FTT operational procedure.

References:

[1] Composite Materials Handbook Vol.2 Department of Defense Handbook May 1999

[2] Hexcel HRH-10 Product Data

[3] Loken H. Nomex, Kevlar, and Korex Honeycomb Cores Technical Tradeoffs February 2002

Chapter 4

MATHEMATICAL APPROACH AND MODELING

4.1. Permeability of Gases

Permeability of gases through polymer membranes or thin films, layers, coatings, etc. is determined by combination of different processes [1]:

- diffusion combined with sorption on one side and desorption on another side; this process is depending on the difference of concentrations of the gas on both sides as well as on properties of polymer;
- gas-dynamic flow through continuous system of defects: pores, microcracks, microchannels, zones of debonding in heterogeneous materials and so on; this process is depending on the difference of pressures (partial pressures) of the gas on both sides as well as on effective length, cross section and number per unit surface area of equivalent channels in polymer;
- thermal initiated flow through equivalent channels of defects; this process is similar to the flow in the chimney; it can be opposite to the gas-dynamic flow; this process is depending on difference of temperatures and on the same defect characteristics as the previous one;
- processes determined by differences of other potentials on two sides: chemical, electrical, magnetic; which are less probable in this particular case;
- combined processes, such as diffusion from one side of polymer layer to some pore inside the polymer, flow through this pore to another side of polymer layer, such as consequence of diffusion, flow, diffusion and so on.

All these processes can be in steady state or non-steady state but the beginning of each process is always non-steady.

Permeation of small gas molecules through a glassy polymer can be viewed as a jumping mechanism whereby a penetrant molecule spends most of the time in free-volume cavities and occasionally jumps into the neighboring cavity. Gas permeation depends on the number and size of cavities (static free volume) and the frequency of jumps (dynamic free volume) [2].

The permeability coefficient K is a product of solubility coefficient S, a thermodynamic parameter describing the ability of the polymer to dissolve the gas, and diffusivity coefficient D, a kinetic parameter describing the mobility of gas molecules in the polymer.

$$K = DS \tag{4.1}$$

Permeability equation can be formulated by applying analog to Fick's linear diffusion law for free gases and liquids:

$$q = K\frac{p_1 - p_2}{h} \tag{4.2}$$

where q is the amount of gas passing through unit area per second and p_1, p_2 are the partial pressures of the permeating gas at the two sides of the membrane of thickness h [3].

It is well known that molecular orientation and crystallinity improve the barrier properties of polymers. Qualitatively, this is understood in terms of free volume concepts because sorption and diffusion processes depend upon the availability of unoccupied volume in the polymer. In the lamellar crystals of a semicrystalline polymer and the extended chain structure of oriented polymers, chain packing is usually much more efficient than in the amorphous, isotropic state. The efficiency of chain packing in the crystalline phase reduces the free volume available for transport to such an extent that the crystalline phase may be regarded as impermeable relative to the amorphous phase. Alternatively, high aspect ratio flakes or platelets have been used to improve gas barrier properties. Typical polymer processing operations used in packaging lead to preferred orientation with platelets aligned parallel to the surface. It is imagined that the aligned, overlapping platelet particles greatly increase the diffusion distance by creating a tortuous path for the diffusing species [4].

The graph of gas flux through polymer film shows an initial increase of gas flux reflecting process of penetration of gas into the material as nonsteady-state diffusion. This part of the curve is determined mainly by the diffusion coefficient D. As the permeant concentration in the specimen reaches a constant distribution, the flux levels out and approaches the steady state value J. This value, normalized by the film thickness h and the permeant gas pressure p, defines the permeability coefficient K as:

$$K = \frac{Jh}{p} \tag{4.3}$$

An impermeable phase, such as crystallinity or particle reinforcements, have a strong effect on both the nonsteady-state and steady-state parts of the gas flux curve. The nonsteady-state region broadens (slower diffusion) while the steady-state permeability decreases with increasing content of the impermeable phase.

Permeability of complex structure is difficult to model accurately, but there exists a simple Nielsen approximation that operates with only a few parameters. This model leads to the following estimation of the permeability coefficient K in a system filled with randomly dispersed particles of an aspect ratio α:

$$K = K_0\frac{1-\phi}{1+\frac{\alpha\phi}{2}} \tag{4.4}$$

where ϕ is the volume fraction of filler, and K_0 is the permeability of the unfilled material.

4.2. Diffusion Equation

The mechanism by which gas molecules permeate through polymers is described as a solution-diffusion process. The permeability coefficient is a product of solubility coefficient, a thermodynamic parameter describing the ability of the polymer to dissolve the gas, and diffusivity coefficient, a kinetic parameter describing the mobility of gas molecules in the polymer. Permeation of small gas molecules through a glassy polymer can be viewed as a jumping mechanism whereby a penetrant molecule spends most of the time in free-volume cavities and occasionally jumps into the neighboring cavity. Gas permeation depends on the number and size of cavities (static free volume) and the frequency of jumps (dynamic free volume) [2].

The mathematical theory of diffusion in isotropic substances is based on the hypothesis that the rate of transfer of diffusing substance through unit area of a section is proportional to the concentration gradient measured normal to the section, i.e.

$$q = -D\frac{\partial C}{\partial x} \tag{4.5}$$

where q is the rate of transfer per unit area of section, C the concentration of diffusing substance, and x the space coordinate measured normal to the section [5].

We can also write:

$$C = Sp \tag{4.6}$$

where p is external gas pressure.

In case of diffusion through a plane sheet or membrane of thickness h and diffusion coefficient D, whose surfaces are maintained at constant concentrations, the diffusion equation in one dimension can be written as:

$$\frac{d}{dx}\left(D\frac{dC(x)}{dx}\right) = 0 \tag{4.7}$$

In case of laminates, in which the laminas are normal to the direction of flow, the above equation can be written for flow in the ith lamina as [3]:

$$\frac{d}{dx}\left(D_i\frac{dC_i(x)}{dx}\right) = 0 \tag{4.8}$$

Also, the dependence between overall permeability K of composite with thickness h and particular laminas, with K_i and h_i respectively, can be defined as follows:

$$\sum_{i=1}^{n}\frac{h_i}{K_i} = \frac{h}{K} \tag{4.9}$$

The effort of this research will be focused on proving equation 4.9 for new designed tank wall configuration.

Permeability through some medium is usually connected with a difference in one or more thermodynamic potentials or parameters describing the state of the penetrating medium [6]. When there

is a difference of pressure, the capillary flow of the gas or liquid through a porous medium is usually considered. When there is a difference of concentration, the diffusion process is observed. Difference of electrical potential/voltage gives electrical current and difference of temperatures results in heat flow. The last two are related to coupled effects such as electrodiffusion and thermodiffusion, when electrical charges or heat are transferred not only by exchange between membrane material and surrounding media on both sides of the membrane but also by passing some molecules (having electrical charges or elevated kinetic energy) through porous membrane. Typical linear law for combination of such phenomena used in membrane theory is:

$$q_M = -K_p \frac{\Delta p}{h} - K_c \frac{\Delta c}{h} - K_T \frac{\Delta T}{h} - K_U \frac{\Delta U}{h} \tag{4.10}$$

where q_M is the density of mass flow:

$$q_M = \frac{1}{A}\frac{dM}{dt} \tag{4.11}$$

Δp, Δc, ΔT, ΔU are differences in pressure, concentration, temperature, and voltage, respectively; K_p, K_c, K_T, K_U are coefficients of mass permeability, diffusion, thermodiffusion, and electrodiffusion, respectively; h, A, and M - are thickness, area, and mass of membrane. Taking thermodiffusion and electrodiffusion into consideration is not an abstract generalization: thermodiffusion of oxygen or electrodiffusion of ions into a hydrogen tank may create problems in some circumstances.

The permeability phenomenon in practice and laboratory study is employed usually when two or more parameters are different simultaneously. In the most typical case permeability is observed when both pressures and concentrations of penetrating medium on both sides of the membrane are different. It means that we can expect diffusion and capillary flow processes going parallel at the same time. Knowledge of the role of each individual penetration mechanism is important for correctly choosing the method of material and technology modification to achieve requirements on total permeability. Although in time these processes go parallel, but in space these processes can go parallel, consecutive, or in mixed mode (a molecule of penetrating medium can pass one part of the path by capillary flow; another part of the path can be passed by diffusion). In the case of individual gas, the concentration and pressure is interconnected and the linear law (equation 4.10) for the case of differences in pressure and concentration can be written as:

$$q_M = -K_{p;c} \frac{\Delta p}{h} \tag{4.12}$$

where $K_{p;c}$ is effective permeability coefficient (not to confuse it with K_p, which is determined at the condition $\Delta c = 0$). The same replacement of pressure and concentration by pressure is valid only in the case of solubility or sorption of penetrating medium in membrane material. The concentration of a penetrating medium in the membrane near the surface is dependent on pressure acting on this surface.

Integration of the expression 4.12 over area gives total mass flow:

$$Q_M = \iint_A q_M dA = -\iint_A K_{p;c}(x_i)\frac{\Delta p(x_i)}{h(x_i)}dA \tag{4.13}$$

where effective permeability coefficient, thickness, and difference of the pressures can be functions of the plane coordinates (x_i). Experimentally the average coefficient of permeability $\overline{K}_{p;c}$ is determined:

$$\left|Q_M\right| = \overline{K}_{p;c}\frac{\Delta\overline{p}}{\overline{h}}A \tag{4.14}$$

Usually there is a very wide distribution of local (not averaged) permeability coefficients. Very high permeability of some defect zones can give significant contribution into the average permeability coefficient despite their small contribution into the total area. For multilayered structure effective permeability coefficient $\left\langle K_Q \right\rangle$ can be calculated as:

$$\frac{1}{\left\langle K_Q \right\rangle} = \frac{1}{\sum_n h_n}\sum_n \frac{h_n}{K_{Q(n)}} \tag{4.15}$$

Here index *Q* replaces one of the following indices: *p, c, T, U, p;c.* Volume flow is convenient for liquids permeability because liquids are not very compressible. Mass flow is more convenient for gases permeability because the volume coming into membrane on one side under some pressure is not the same as volume going out of membrane under another pressure.

In experiments flow is not exactly proportional to the area, not exactly inversely proportional to the thickness and not exactly proportional to the pressure difference. The deviations are connected with non-uniformity of material structure; with scaling factor (probability of defects is higher in bigger volume); with different relative input of sorption–desorption processes in thin and thick membranes permeability; with non-linearity of the constitutive law instead of linear approximation (equations 4.10 and 4.12); with deformation of the membrane by pressure; etc. At the constant temperature, mass flow can be replaced by *pV* - flow (magnitude of the product *pV* is proportional to the mass passed through the membrane):

$$Q_{pV} = K_{pv}\frac{A}{h}\Delta p \tag{4.16}$$

4.3. Permeability Coefficient

In the case of gas permeability of a membrane or thin film, like in this case, unsteady state is described by mentioned before equations 4.11 and 4.12, which can also be written in special coordinates as:

$$\vec{q}_M = -K_M grad(p) = -K_M \nabla p \tag{4.17}$$

and equation of mass conservation:

$$div(\vec{q}_M) \equiv \nabla \cdot \vec{q}_M = -\frac{\partial}{\partial t}\left(\frac{M}{V}\right) \tag{4.18}$$

where V is volume of the membrane. After substitution of permeability law 4.12 into equation 4.18 the following equation can be obtained:

$$\nabla \cdot (K_M \nabla p) = \frac{\partial}{\partial t}\left(\frac{M}{V}\right) \tag{4.19}$$

For quasi-uniform media the following equation can be obtained:

$$K_M \nabla^2 p = \frac{\partial}{\partial t}\left(\frac{M}{V}\right) \tag{4.20}$$

Helium gas, as well as hydrogen, is very close in its thermo-mechanical behavior to the ideal gas, for which $pV = \frac{M}{\mu}RT$ and the following variation of equation 4.20 can be obtained:

$$K_M \nabla^2 p = \frac{\partial}{\partial t}\left(\frac{p\mu}{RT}\right) \tag{4.21}$$

or in case of isothermal process:

$$\frac{K_M RT}{\mu}\nabla^2 p = \frac{\partial p}{\partial t} \tag{4.22}$$

Since $K_{pV} = \frac{K_M RT}{\mu}$ the final equation can be written as:

$$K_{pV} \nabla^2 p = \frac{\partial p}{\partial t} \tag{4.23}$$

which is similar to the classical equations of unsteady diffusion or thermal conductivity. The same equation can be obtained from the combination of equation of diffusion and linear Henry's law for sorption. However, the mechanism of permeability of helium and hydrogen is different from activated diffusion and application of Henry's law can not be based on the physics of the process. Coefficient K_{pV} is connected to the density of pV flow through following equation:

$$q_{pV} = \frac{1}{A}\frac{d(pV)}{dt} = -K_{pV}\frac{\Delta p}{h} \tag{4.24}$$

Distribution of pressures through the membrane of thickness h, where on one side the pressure is constant and equal p_1, on the other the pressure p_2 is equal zero (p_1=Δp), and initial pressure is also equal zero, can be described by following equation:

$$\frac{p}{\Delta p} = 1 - \frac{x}{h} - \frac{2}{\pi}\sum_{n=1}^{\infty}\frac{1}{n}\sin\frac{n\pi x}{h}\exp\left(-\frac{K_{pV} n^2 \pi^2 t}{h^2}\right) \tag{4.25}$$

Flux (per unit area) in non-steady process can be obtained from:

$$q_{pV} = -K_{pV}\frac{dp}{dx} = K_{pV}\frac{\Delta p}{h}\left[1+2\sum_{n=1}^{\infty}\cos\frac{n\pi x}{h}\exp\left(-\frac{K_{pV}n^2\pi^2 t}{h^2}\right)\right] \tag{4.26}$$

At the opposite side of the membrane (at $x = h$) there is:

$$q_{pV} = K_{pV}\frac{\Delta p}{h}\left[1+2\sum_{n=1}^{\infty}(-1)^n\exp\left(-\frac{K_{pV}n^2\pi^2 t}{h^2}\right)\right] \tag{4.27}$$

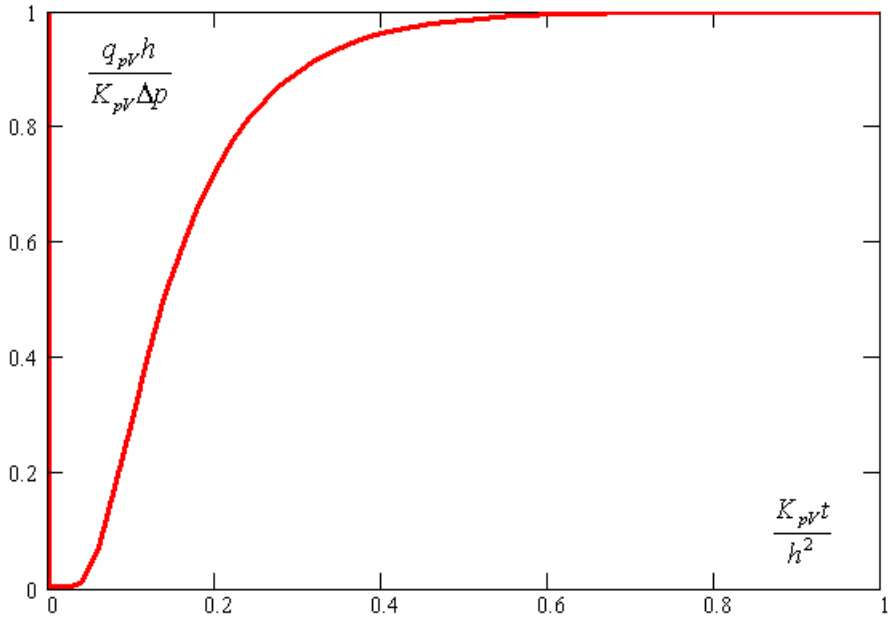

Fig. 4.3.1. Dimensionless graph of flow density calculated analytically

The results of calculations according this formula written in dimensionless form are plotted in Fig. 4.3.1. This graph can be used for finding permeability coefficient for both steady and unsteady state.

The first derivative of the flux is:

$$\frac{dq_{pV}}{dt} = -K_{pV}\frac{\Delta p}{h}2\left[\sum_{n=1}^{\infty}(-1)^n\frac{K_{pV}n^2\pi^2}{h^2}\exp\left(-\frac{K_{pV}n^2\pi^2 t}{h^2}\right)\right] \tag{4.28}$$

and the graph of this function in dimensionless form is shown in Fig. 4.3.2.

The second derivative is:

$$\frac{d^2q_{pV}}{dt^2} = K_{pV}\frac{\Delta p}{h}2\left[\sum_{n=1}^{\infty}(-1)^n\frac{K_{pV}^2n^4\pi^4}{h^4}\exp\left(-\frac{K_{pV}n^2\pi^2 t}{h^2}\right)\right] \tag{4.29}$$

and the graph of this function in dimensionless form is shown in Fig. 4.3.3.

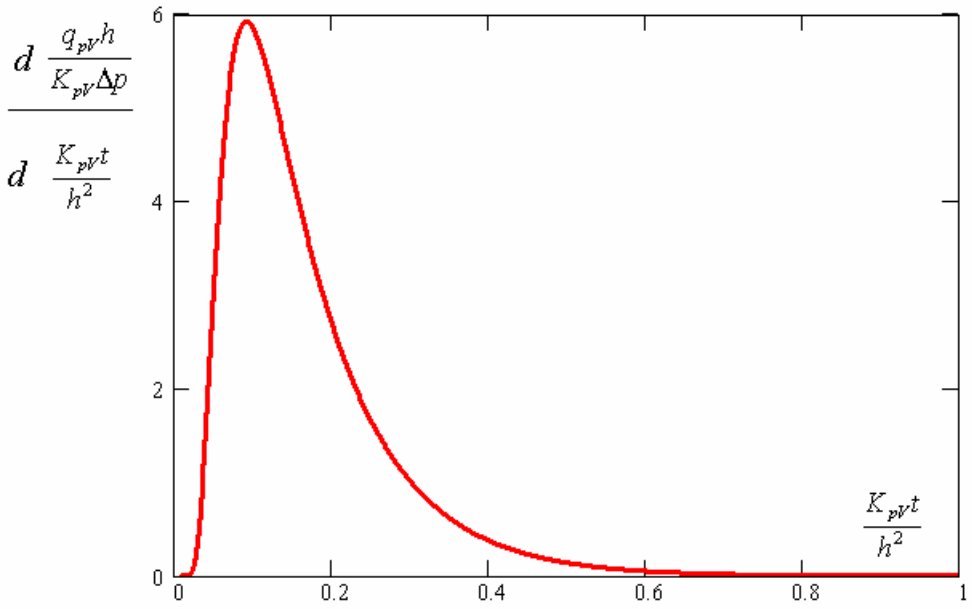

Fig. 4.3.2. Dimensionless graph of first derivative of flow density

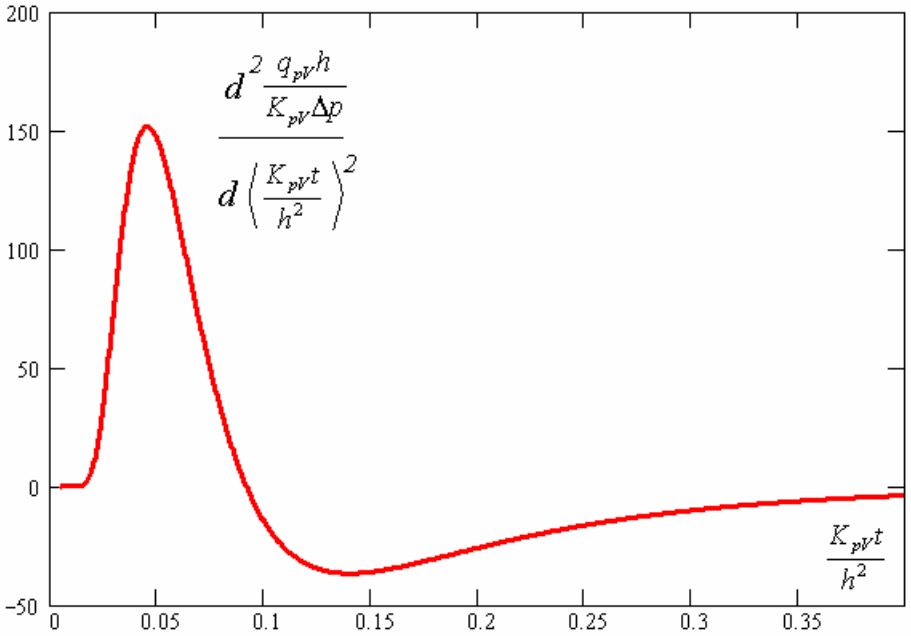

Fig. 4.3.3. Dimensionless graph of second derivative of flow density

The cusp point (point of maximum of the first derivative) can be used to determine the permeability coefficient in unsteady process. Let's denote the maximal value of the derivative as $L = \max\left(\frac{dq_{pV}}{dt}\right)$ and corresponding time as t^*. Then permeability coefficient can be calculated from:

$$K_{pV} = \sqrt{\frac{L}{5.922}\frac{h^3}{\Delta p}} \tag{4.30}$$

or from:

$$K_{pV} = 0.09175\frac{h^2}{t^*} \tag{4.31}$$

Total quantity of *pV* passed through unity of membrane area from the beginning up to current time *t* can be calculated from:

$$\begin{aligned} Z_{pV} &= \int_0^t q_{pV}\,dt = K_{pV}\frac{\Delta p}{h}\int_0^t\left[1+2\sum_{n=1}^{\infty}(-1)^n \exp\left(-\frac{K_{pV}n^2\pi^2 t}{h^2}\right)\right]dt = \\ &= K_{pV}\frac{\Delta p}{h}\left\{t-2\sum_{n=1}^{\infty}(-1)^n\frac{h^2}{K_{pV}n^2\pi^2}\left[\exp\left(-\frac{K_{pV}n^2\pi^2 t}{h^2}\right)-1\right]\right\} \end{aligned} \tag{4.32}$$

or, since $\sum_{n=1}^{\infty}(-1)^n\frac{1}{n^2} = -\frac{\pi^2}{12}$ [7], it can be obtained from:

$$\begin{aligned} Z_{pV} &= K_{pV}\frac{\Delta p}{h}\left[t-\frac{2h^2}{\pi^2 K_{pV}}\sum_{n=1}^{\infty}(-1)^n\frac{1}{n^2}\exp\left(-\frac{K_{pV}n^2\pi^2 t}{h^2}\right)-\frac{h^2}{6K_{pV}}\right] = \\ &= h\Delta p\left[-\frac{1}{6}+\frac{K_{pV}}{h^2}t-\frac{2}{\pi^2}\sum_{n=1}^{\infty}\frac{(-1)^n}{n^2}\exp\left(-\frac{K_{pV}n^2\pi^2 t}{h^2}\right)\right] \end{aligned} \tag{4.33}$$

and what matches well-known formula [5].

At the end of the process this dependence becomes an asymptotic straight line:

$$Z_{pV} = K_{pV}\frac{\Delta p}{h}\left[t-\frac{h^2}{6K_{pV}}\right] = h\Delta p\left[-\frac{1}{6}+\frac{K_{pV}}{h^2}t\right] \tag{4.34}$$

When this straight line intercepts the abscissa $Q_{pV}=0$, the time moment $t = t\text{^}$ is corresponding to:

$$t\text{^}-\frac{h^2}{6K_{pV}} = -\frac{1}{6}+\frac{K_{pV}}{h^2}t\text{^} = 0 \tag{4.35}$$

or:

$$K_{pV} = \frac{h^2}{6t\text{^}} \tag{4.36}$$

This intercept (time lag) can be used for permeability coefficient determination as well as the slope of the asymptotic straight line:

$$\frac{dZ_{pV}}{dt} = K_{pV}\frac{\Delta p}{h} \text{ at } t\to\infty \tag{4.37}$$

and:

$$K_{pV} = \frac{h}{\Delta p}\left(\frac{dZ_{pV}}{dt}\right)_{t\to\infty} \tag{4.38}$$

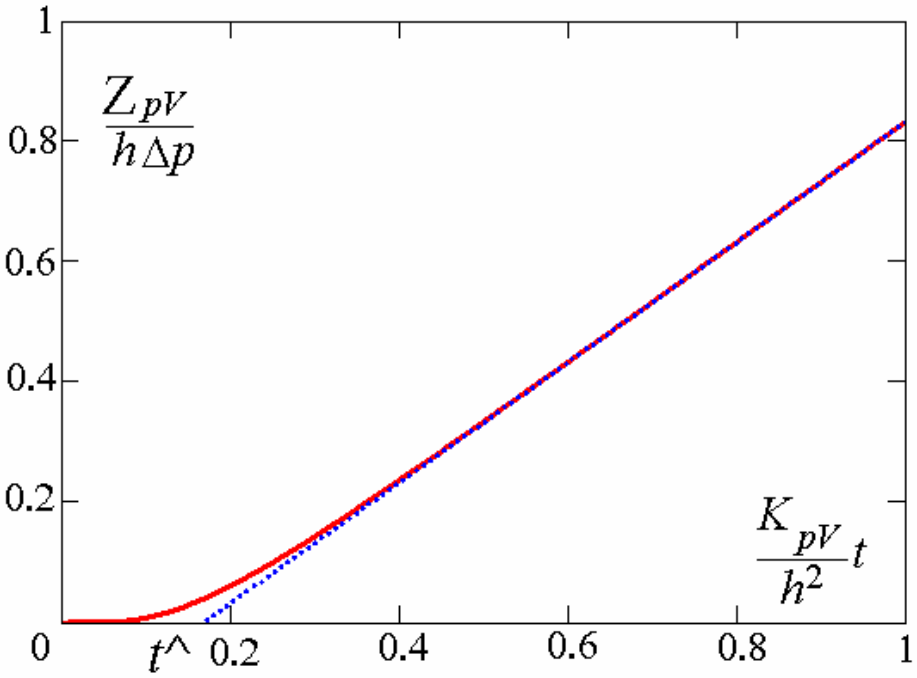

Fig. 4.3.4. Different approach to steady-state flow through a membrane

4.4. Role of Pores

Pores can be considered as ideally conducting media with respect to diffusion of light gases. In the case of spherical pores, the degenerated Maxwell's formula can be used:

$$\langle D\rangle = D_0\frac{1+2\psi}{1-\psi} \approx D_0(1+3\psi) \tag{4.39}$$

where $\langle D\rangle$ is effective diffusion coefficient of the porous medium, D_0 diffusion coefficient of polymer, ψ - volume concentration of spherical pores. In the case of non-spherical pores, more dangerous are pores elongated perpendicular to the layer's surface. Oblate pores parallel to the layers surface provide effective diffusion coefficient:

$$\langle D\rangle = D_0\frac{1}{1-\psi} \approx D_0(1+\psi) \tag{4.40}$$

which shows that this type of pores 3 times less dangerous than the spherical ones. Role of prolate pores oriented perpendicular to the layer's surface is much more significant, but it depends not only on the ratio

of the pore sizes but on the type of spatial lattice of pores also. In the worst case (Fig. 4.4.1.a) all pores are aligned along the single perpendicular to the layer surface:

$$\langle D \rangle = D_0 \left(1 + \frac{\psi}{1 - \chi} \right) \tag{4.41}$$

where $\chi = \frac{N d_{\max}}{h} < 1$ is linear concentration of the prolate pores along the perpendicular to the layer surface, N is the total number of pores, d_{max} is the size of the pore along its maximal diameter, h is thickness of the layer. In the case $\chi \geq 1$ the diffusion model is not valid and it is necessary to consider gas flow through the channels. Less dangerous situation (Fig. 4.4.1.b) is, when the pores are oriented by the same way and their axes are not coinciding but they are situated at maximal possible distance between neighbors. In this case:

$$\langle D \rangle = D_0 \left(1 + \frac{\psi}{1 - \frac{d_{\max}}{h}} \right) \tag{4.42}$$

Less dangerous situation (Fig. 4.4.1.c) when prolate pores are oriented parallel to the layer's surface and pores are mutually parallel. In this case:

$$\langle D \rangle = D_0 \left(\frac{1 + \psi}{1 - \psi} \right) \approx D_0 (1 + 2\psi) \tag{4.43}$$

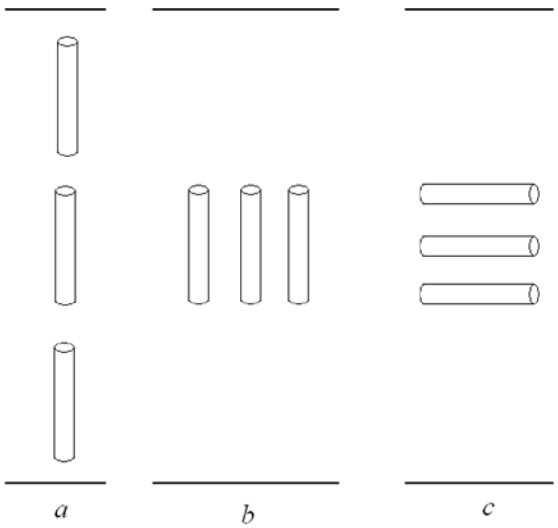

Fig. 4.4.1. Idealized prolate pores ensembles inside thin polymer layer

4.5. Role of Inclusions

Mineral fillers can be considered as ideally non-permeable ones. In the case of spherical particles, another degenerated form of Maxwell's formula can be used:

$$\langle D \rangle = D_0 \frac{1-\zeta}{1+\frac{1}{2}\zeta} \approx D_0\left(1-\frac{3}{2}\zeta\right) \tag{4.44}$$

where ζ is volume concentration of spherical inclusions. Role of the shape and orientation of inclusions is important also. Fibrous inclusions perpendicular to the layer surface are less effective than spherical ones because the effective diffusion coefficient is estimated as:

$$\langle D \rangle = D_0(1-\zeta) \tag{4.45}$$

Fibrous inclusions oriented parallel to the layer surface (similarly to the case shown in the Fig. 4.3.1.c) decrease effective permeability by two:

$$\langle D \rangle = D_0\left(\frac{1-\zeta}{1+\zeta}\right) \approx D_0(1-2\zeta) \tag{4.46}$$

Platelet inclusions parallel to the surface are much more effective, however prediction of the diffusion coefficient is more difficult because it is dependent not only on ratio of the sizes of inclusion but also on the type of the spatial lattice. We will consider these questions more detailed in separate publication.

4.6. Thermal Stresses and Cracking

There are two types of the stresses acting in filled polymer layer: effective averaged stresses and local micro-stresses. Averaged stresses calculated considering material as quasi-homogeneous one. When averaged stresses are equal to zero the local micro-stresses can be significant, but they must be self-equilibrated, for example, matrix polymer can be tensioned, but filler correspondingly compressed. Each of the types of stresses can be classified as initial/residual one and loading stress. Initial stress state created due to shrinkage of polymer matrix, due to difference of thermal expansion coefficients in the cooling process from the curing temperature to room temperature. Loading stresses are connected with mechanical load and thermal load from room temperature to cryogenic one. These stresses are connected with non-uniformity of temperature distribution, with anisotropy of thermal expansion, with difference of linear thermal expansion of constituents. As a result of these stresses, some local micro-fractures are possible as well as growing of the initial technological defects. These phenomena are critical for permeability as well as for applications of laboratory data obtained at one set of conditions to the predicting of structural permeability at real (different from laboratory) set of conditions. Cryogenic stress analysis is the big area of investigation.

4.7. Computer Modeling

NEiNastran is a powerful, general purpose finite element analysis tool with an integrated graphical user interface and model editor which is used to analyze linear and nonlinear stress, dynamics, and heat transfer characteristics of structures and mechanical components; created by Noran Engineering, Inc. (NEi), a world-wide leader in CAE software. It allows performing linear and nonlinear stress, dynamic, and heating transfer analysis. Steady State Heat Transfer and Transient Heat Transfer with linear or nonlinear conduction, convection, and radiation module are here used for modeling permeability.

Of principal interest in heat transfer analysis is the temperature distribution within a solid body. A byproduct of temperature calculation is information about the magnitude and direction of heat flow in the body. For a linear steady state (time independent) problem:

$$[\lambda]\{T\} = \{r\} \tag{4.47}$$

where *[λ]* is the global conductivity matrix, *{T}* is the global temperature vector, and *{r}* is the global thermal load vector. The global conductivity matrix depends on the conductivity of the material and is usually a function of temperature.

In case of gas permeability rate or gas mass flux through thin membrane Fourier heat conduction equation in one directional can be used:

$$f_x = -k\frac{\partial T}{\partial x} \tag{4.48}$$

where f_x is heat flux per unit area and k is the thermal conductivity. The negative sign means that heat flows in a direction opposite to the direction of temperature increase.

In the case of steady state heat transfer loads and boundary conditions do not vary with time. When steady state conditions do not prevail, temperature change in a unit volume of material is resisted by thermal mass that depends on the mass density of the material and its specific heat. The general heat transfer equation then becomes:

$$[\lambda]\{T\} + [W]\{\dot{T}\} = \{r\} \tag{4.49}$$

where *[W]* is the global capacitance matrix and $\{\dot{T}\}$ is $\partial T / \partial t$.

Nonlinear transient heat transfer analysis is implemented in NEiNastran using Newmark's method with adaptive time stepping. Convergence is achieved at each time step using the same Newton-Raphson iteration method used in nonlinear steady state heat transfer analysis.

In case of current gas permeability modeling equation 4.48 can be used as substitution for gas flow law, equation 4.12. Sample size has been rescaled to bigger size for easier meshing and pressures recalculated to be adequate to the dimensions. Nanoclays were modeled as small cylinders with aspect ration of 10 and 20. For transient analysis initial pressure was assumed to be atmospheric one.

References:

[1] Bubacz M., Hui D., Daniel L., Beyle A., Ibeh C., Susnik R. Different approaches to sandwich structure permeability problem using coated aramid papers SAMPE 37th International Technical Conference November 2005

[2] Baer E., Hu Y.S., Liu R.Y.F., Schiraldi D.A., Hiltner A. Polymeric Materials: Science and Engineering 89 (2003) 19-20

[3] Crank J., Park G.S. Diffusion in Polymers. Academic Press, New York, 1968

[4] Sekelik D.J., Stepanov E.V., Nazarenko S., Schiraldi D., Hiltner A., Baer E. Journal of Polymer Science: Part B 37 (1999) 847-857

[5] Crank J. The Mathematics of Diffusion. Clarendon Press, Oxford, 1974

[6] Bubacz M., Hui D., Beyle A., Santibhasker P., Ibeh C. Aramid Papers Coated with Different Resin Systems as Excellent Gas Permeability Barrier 47th AIAA/ASME/ASCE/AHS/ASC May 2006

[7] Gradshteyn I.S., Ryzhik I.M. Tables of integrals, series, and products. Academic Press, 1965

Chapter 5

TESTS RESULTS

5.1. Helium Permeability Tests

5.1.1. Nomex T412 and Kevlar N636 papers from DuPont

Table 5.1.1. Sample documentation for Nomex and Kevlar

Paper	Remarks Thickness T [in; mm]	Sample Nr	Sample thickness [in]
Nomex 3T412	White Inlet pressure, 1psi 0.003; 0.0762	N1.1	0.003
		N1.2	0.003
		N1.3	0.003
		N1.4	0.003
Kevlar 2.8N636	Yellow Vacuum leak 0.003; 0.0762	K1.1	0.003
		K1.2	0.003
		K1.3	0.003
		K1.4	0.003
Nomex 2T412	White Inlet pressure, 1psi 0.002; 0.0508	N2.1	0.002
		N2.2	0.002
		N2.3	0.002
		N2.4	0.002
Kevlar 3.9N636	Yellow Vacuum leak 0.004; 0.1016	K2.1	0.004

Two different grades of aramid papers were tested: Nomex T412 and Kevlar N636. Kevlar paper is very permeable to helium and any other gases and it was impossible to test it because the permeability machine was not able to create vacuum between sample and mass spectrometer. Nomex paper with two different thicknesses was tested under helium pressure of 1psi. First tests on Nomex 3T412 were performed under unstable inlet pressure due to big rate of gas flow through the sample and difficulties with keeping the inlet pressure at one level.

Fig. 5.1.1 and 5.1.2 show that thicker samples N1 have smaller permeability rate. That agrees with law which says that permeability depends and is inverse proportional to the thickness. Time of stabilization is also shown to depend on dimension of specimen. For thicker samples it takes more time to stabilize permeation rate because sorption process is longer and stabilization between sorption and desorption requires more time.

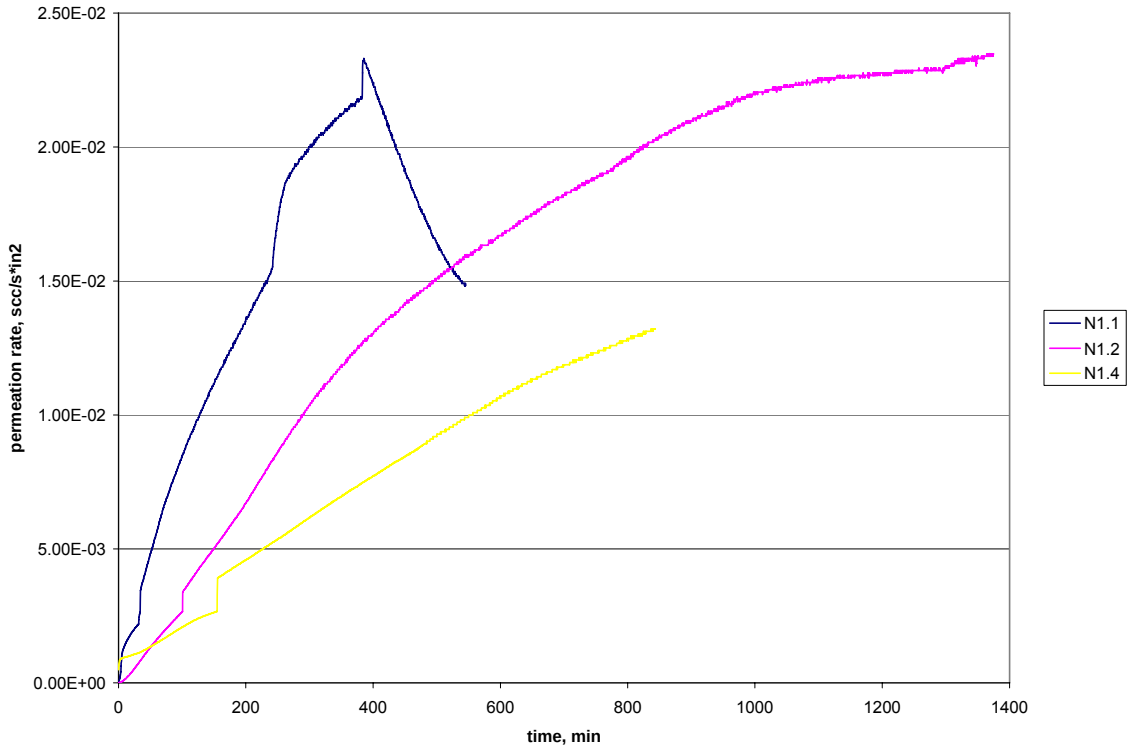

Fig. 5.1.1. Permeation rate of Nomex 3T412 uncoated

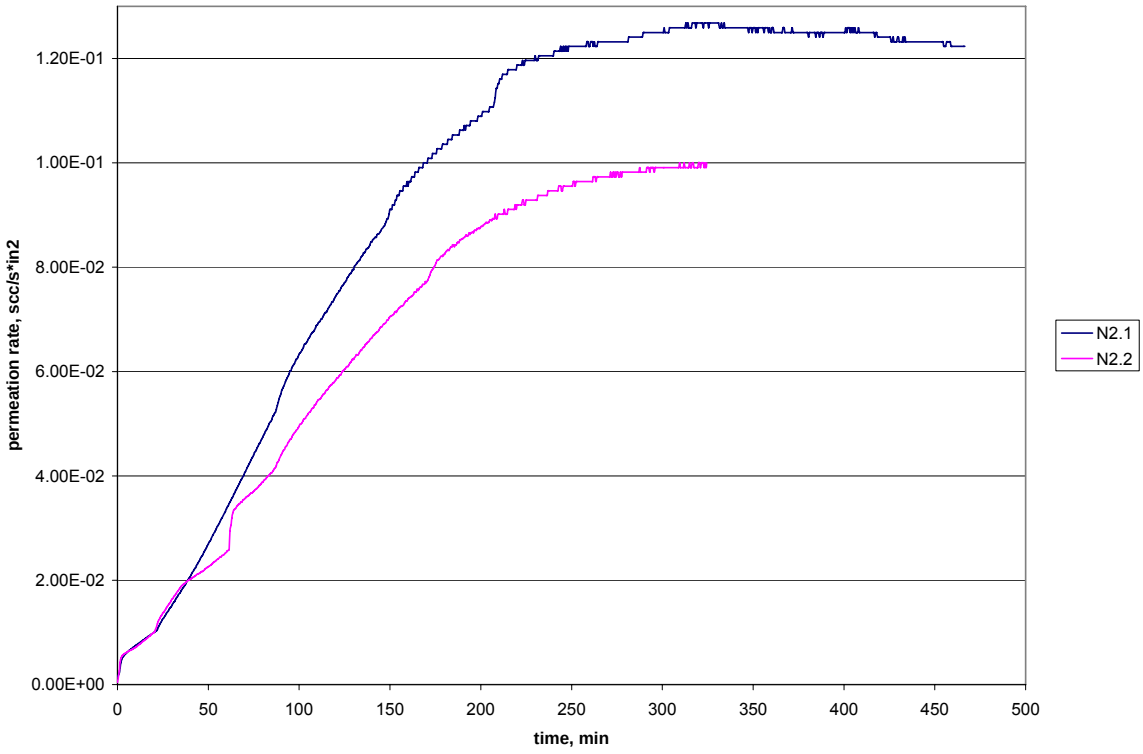

Fig. 5.1.2. Permeation rate of Nomex 2T412 uncoated

5.1.2. Nomex 3T412 and Kevlar 2.8N636 papers from DuPont coated with unsaturated polyester resin Bondo 7630800402 from Dynatron/Bondo Corp. mixed with 1.5% of MEKPO in 4 trials:

- Trial 1
  - resin applied with brush against both surfaces
  - placed between sheets of nylon film and metal plates and then in press to impregnate and cure
  - controlling the press load at low enough load was difficult, surged to high tonnage initially, then dropped-off
  - this, along with apparent non-permeability of resin/paper combination produced a thick coating on both surfaces
  - resin fell off Nomex paper
  - small bubbles on one side of Kevlar paper
- Trial 2
  - resin applied with brush against both surfaces
  - sandwiched between peel ply (to help remove air) and vacuum cured at room temperature in Boeing vacuum-bag assembly at 28inch Hg for 1 hr, metal plates were used between specimen assembly to apply pressure
  - the air was removed, but also much of the resin was bled into the peel ply (vacuum-bag is designed for fabrics)
  - almost no resin was observed on Nomex paper
  - Kevlar paper got stuck to nylon film, thin coat remained
- Trial 3
  - resin with 5% by weight of acetone as a diluent (to decrease viscosity) applied with brush against both surfaces
  - acetone was allowed to dry over a period of several hours
  - press pressure was applied to samples sandwiched between release film and metal plates
  - thick coatings with little permeation observed
  - Nomex paper partially coated, with air bubbles
  - uneven coat surface no Kevlar paper, wrinkles
- Trial 4
  - resin with 5% by weight of acetone applied with brush against both surfaces
  - roller (iron) used to impregnate pores
  - acetone was allowed to dry over a period of several hours
  - press pressure was applied to samples sandwiched between release film and metal plates

- very uneven coat on Nomex paper, cracked, falls off
- very thick coat on Kevlar paper with big air bubbles

Nomex T412 has low permeability without the resin coat, while Kevlar N635 paper is saturable and porous. As a consequence, resin will penetrate Kevlar paper, giving a non-porous material. Samples of Kevlar uncoated and coated in Trial 2 were very permeable to air and did not hold the vacuum during the test.

It was very difficult to coat Nomex paper with resin because of its smooth and non-adherent surface. Curing in vacuum-bag gave a coat which fell off, but traces of resin from Trial 2 remained on surface and improved helium permeability resistance. During testing samples of uncoated Nomex it was very difficult to keep the inlet pressure at 1psi. Sample N1.1 in Fig. 5.1.1 was left unattended after 6th hour of test resulting in helium pressure drop to almost 0psi. Test results for Nomex uncoated and coated in Trial 2 show a permeation rate jump at about 2.7*10^{-3}scc/sek*in^2 caused by machine automatic switching from normal to gross leak mode at 3*10^{-4}mbar*l/s of flow rate.

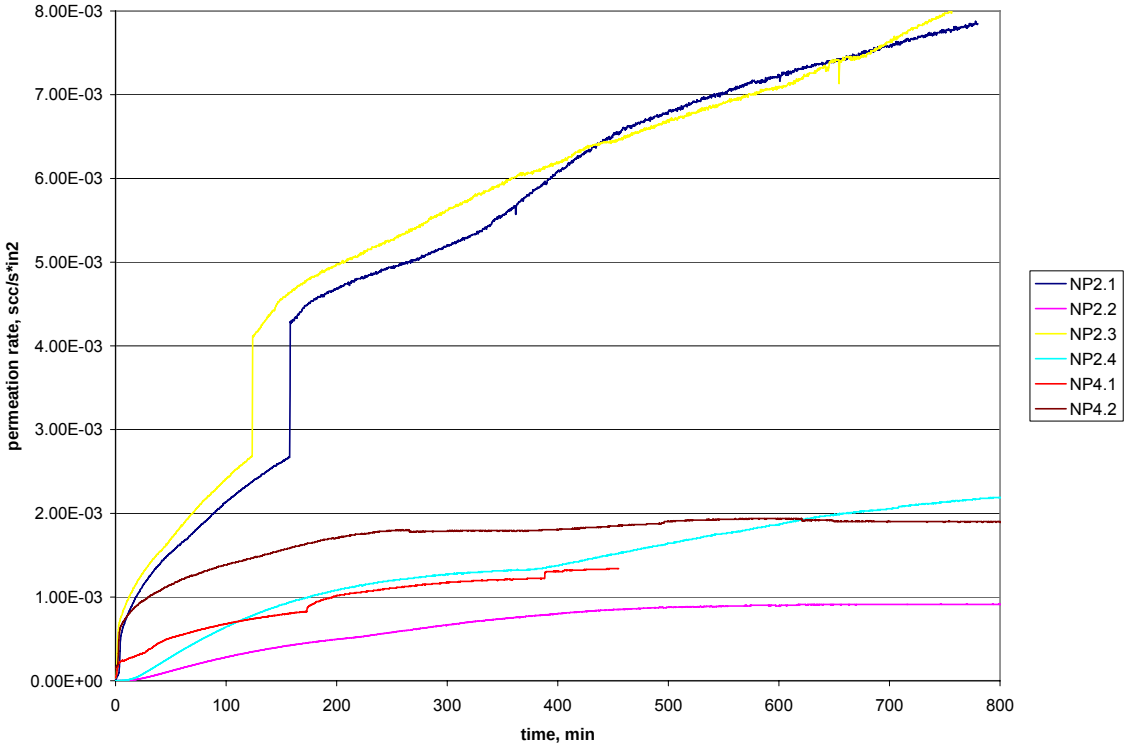

Fig. 5.1.3. Permeation rate of Nomex coated in Trials 2 and 4

Samples of Nomex coated with polyester diluted with acetone and cured in press at room temperature in Trial 3 maintained a relatively uniform thickness and smooth coating. Samples NP3.3 and NP3.5 have almost the same permeation rate values. Fig. 5.1.4 shows unexpected behavior of sample NP3.1, for which the permeation rate decreased with time instead of increasing. That sample has more small air bubbles than others and could exhibit different gas leakage behavior. However, the permeation

rate stabilized with time to value within a range similar to that of other samples. This behavior may be explained through understanding nature of permeability.

Samples of Nomex coated with polyester diluted with acetone and cured in press at room temperature in Trial 3 maintained a relatively uniform thickness and smooth coating. Samples NP3.3 and NP3.5 have almost the same permeation rate values. Fig. 5.1.4 shows unexpected behavior of sample NP3.1, for which the permeation rate decreased with time instead of increasing. That sample has more small air bubbles than others and could exhibit different gas leakage behavior. However, the permeation rate stabilized with time to value within a range similar to that of other samples. This behavior may be explained through understanding nature of permeability.

Table 5.1.2. Sample documentation for Nomex and Kevlar coated with polyester

Material		Remarks	Sample	Sample
Paper	Resin	Thickness T [in; mm]	Nr	thickness [in]
3T412	Trial 1	Resin fell off	-	
2.8N636		Small bubbles on one side Inlet pressure, 5psi 0.011; 0.2794	KP1.1	0.011
			KP1.2	0.013
			KP1.3	0.013
			KP1.4	0.011
			KP1.5	0.0105
3T412	Trial 2	Almost no resin observed Inlet pressure, 1psi 0.003; 0.0762	NP2.1	0.003
			NP2.2	0.0035
			NP2.3	0.003
			NP2.4	0.003
2.8N636		Paper stuck to nylon film, thin coat Inlet pressure, 5psi, vacuum leak 0.006; 0.1524	KP2.1	0.0055
			KP2.2	0.007
			KP2.3	0.006
3T412	Trial 3	Paper partially coated, with air bubbles, yellow Inlet pressure, 5psi 0.015; 0.381	NP3.1	0.013
			NP3.2	0.0125
			NP3.3	0.012
			NP3.4	0.013
			NP3.5	0.0165
2.8N636		Uneven coat surface, wrinkles Inlet pressure, 5psi 0.009; 0.2286	KP3.1	0.0055
			KP3.2	0.009
			KP3.3	0.013
			KP3.4	0.0075
			KP3.5	0.0115
			KP3.6	0.011
3T412	Trial 4	White coat, very uneven, cracked, falls off Inlet pressure, 1psi	NP4.1	0.003
			NP4.2	0.003
2.8N636		Very thick, big air bubbles Inlet pressure, 5psi 0.017; 0.4318	KP4.1	0.0155
			KP4.2	0.0135
			KP4.3	0.0125
			KP4.4	0.017
			KP4.5	0.0145
			KP4.6	0.014

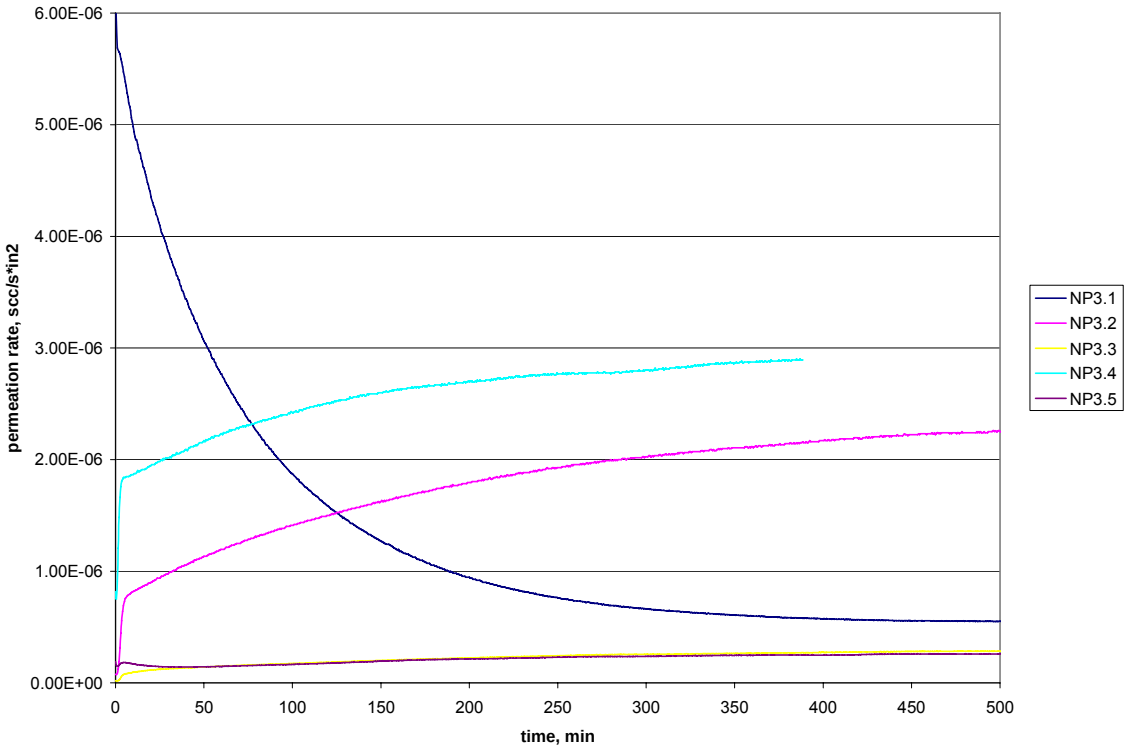

Fig. 5.1.4. Permeation rate of Nomex coated in Trial 3

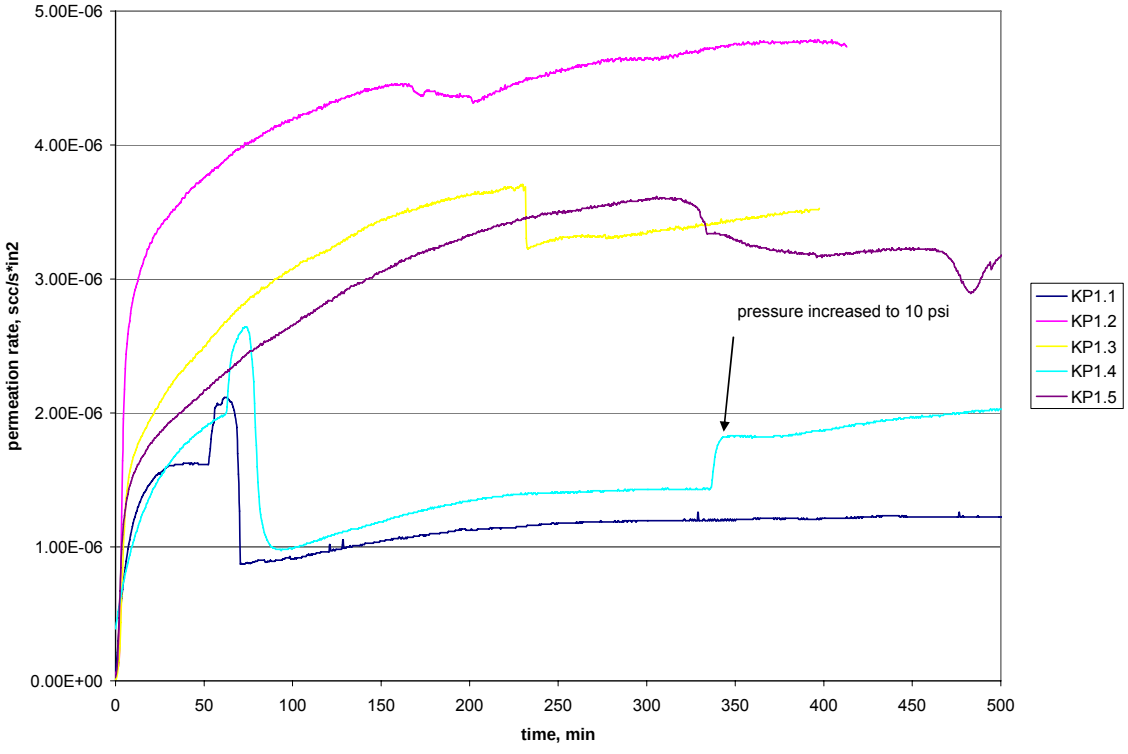

Fig. 5.1.5. Permeation rate of Kevlar coated in Trial 1

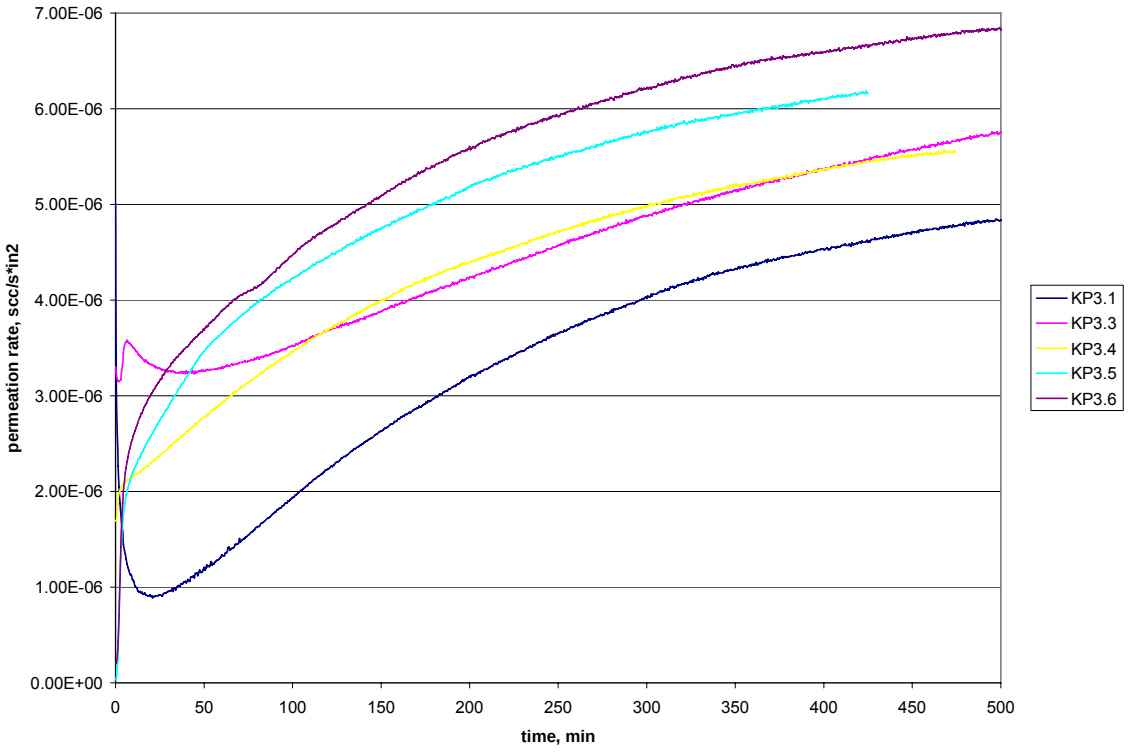

Fig. 5.1.6. Permeation rate of Kevlar coated in Trial 3

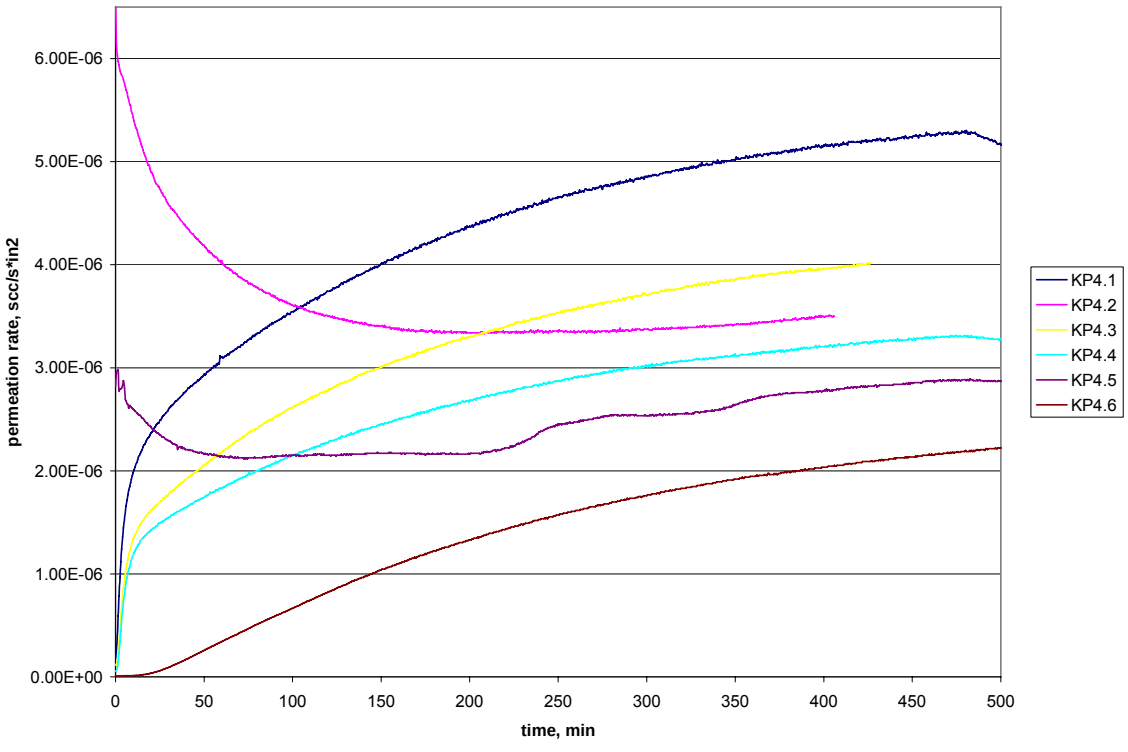

Fig. 5.1.7. Permeation rate of Kevlar coated in Trial 4

The mechanism by which gas molecules permeate through polymers is described as a solution-diffusion process. The permeability coefficient is a product of solubility coefficient, a thermodynamic parameter describing the ability of the polymer to dissolve the gas, and diffusivity coefficient, a kinetic parameter describing the mobility of gas molecules in the polymer. Permeation of small gas molecules through a glassy polymer can be viewed as a jumping mechanism whereby a penetrant molecule spends most of the time in free-volume cavities and occasionally jumps into the neighboring cavity. Gas permeation depends on the number and size of cavities (static free volume) and the frequency of jumps (dynamic free volume) [1].

Fig. 5.1.5 shows existence of permeation rate peaks for samples of Kevlar coated in Trial 1. The graph depicts an increase of helium leak rate to some amount and then immediate drop of this value and fast stabilization. It is especially visible for samples KP1.1 and KP1.4.

Test results for samples of Kevlar coated in Trial 3 are even more uneven. Sample KP3.1 with the most uneven coating and uncoated areas on one side shows in Fig. 5.1.6 a decreasing permeation rate behavior similar to that of sample NP3.1. There is a permeation rate peak at the beginning of sample KP3.3 test. However, the sample tests stabilize within first hour and show similar increasing rate.

A roller (iron) was used after applying resin with brush to better impregnate pores in trial 4, and very thick coat with rare big air bubbles was obtain. Samples of Kevlar coated in Trial 4 gave results depicted in Fig. 5.1.7. Samples KP4.2 and KP4.5 show different behavior, which is similar to that of samples NP3.1 and KP3.1. In general, the graphs have smooth slopes and stabilize within the same range of time and to similar value.

5.1.3. Nomex 3T412 and Kevlar 2.8N636 papers from DuPont coated with fiberglass polyester NAPA 765-1286 (polyester 26098-37-3 with styrene 100-42-5) from Balkamp, Inc. with 2% of MEKPO in following procedure:

- resin applied with brush against both surfaces
- roller (iron) used to impregnate pores
- left to dry in 40ºC for several hours
- vacuum-bag cured in oven

Results of tests of Nomex papers coated with polyester NAPA are depicted in Fig. 5.1.8 and 5.1.9. Both graphs show very unstable beginning of the process, especially for first 25min. After that permeation rate stabilizes and steadily increases. There is a permeation rate peak at the beginning of sample NF1.2 test, but the test stabilizes within first half an hour and shows similar increasing rate. Sample NF1.3 behaved in the most unusual way, showing steep steps, up and down, on the graph. There can be many explanations of such behavior, like rapid changes of vacuum pressure inside the machine caused by some leaks, or unusual sample material structure, like existing of big pores or air bubbles which stored amounts helium for some time. In the Fig. 5.1.9 sample NF2.4 was tested twice because first test was interrupted by power breakage. Nevertheless, the group of samples coated with polyester

NAPA diluted with alcohol gives the lowest permeation rate obtained so far. The permeability reaches values in the range of 4-7*10^{-7}scc/sek*in^2.

Table 5.1.3. Sample documentation for Nomex and Kevlar coated with fiberglass resin NAPA 765-1286

Paper	Remarks Thickness T [in; mm]	Sample Nr	Sample thickness [in]
None	1g of alcohol for 42g of resin Transparent foil Vacuum leak 0.003; 0.0762	F1.1	0.003
		F1.2	0.004
Nomex 3T412	Inlet pressure, 5psi 0.006; 0.1524	NF1.1	0.006
		NF1.2	0.007
		NF1.3	0.006
		NF1.4	0.006
		NF1.5	0.006
	1g of alcohol for 42g of resin Inlet pressure, 5psi 0.011; 0.2794	NF2.1	0.0065
		NF2.2	0.009
		NF2.3	0.007
		NF2.4	0.009
Kevlar 2.8N636	1.5g of alcohol for 64g of resin Inlet pressure, 5psi 0.005; 0.127	KF1.1	0.007
		KF1.2	0.0075
		KF1.3	0.005
		KF1.4	0.0055

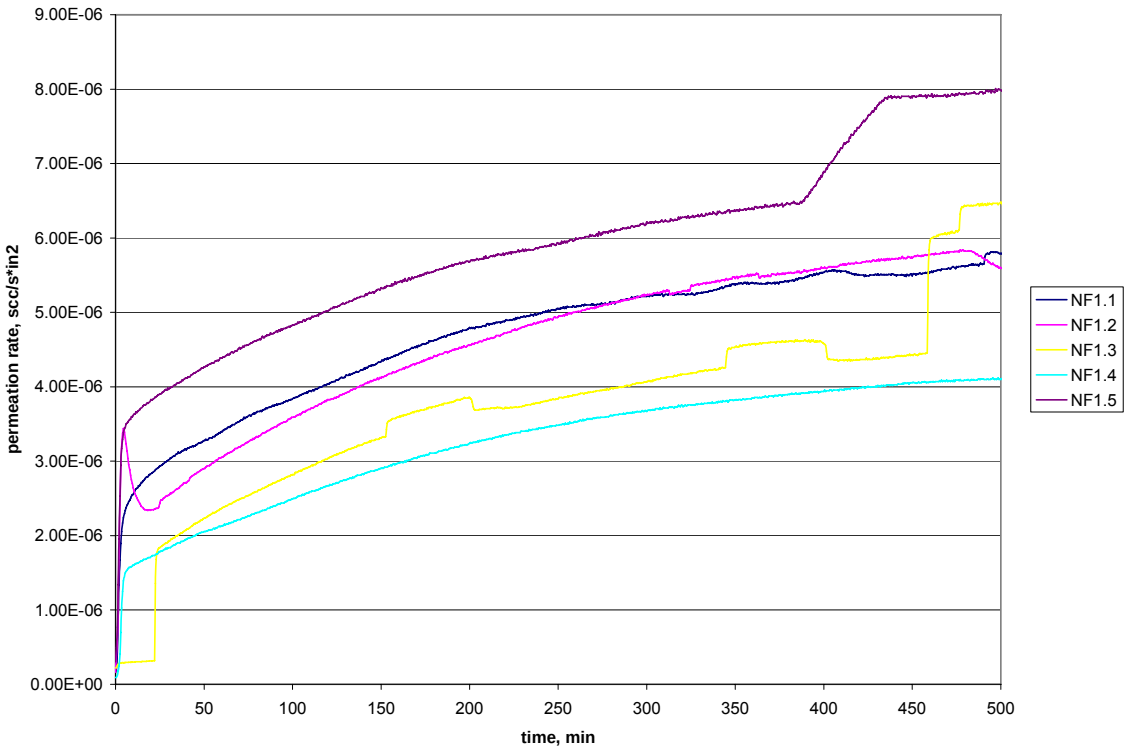

Fig. 5.1.8. Permeation rate of Nomex coated with NAPA 765-1286

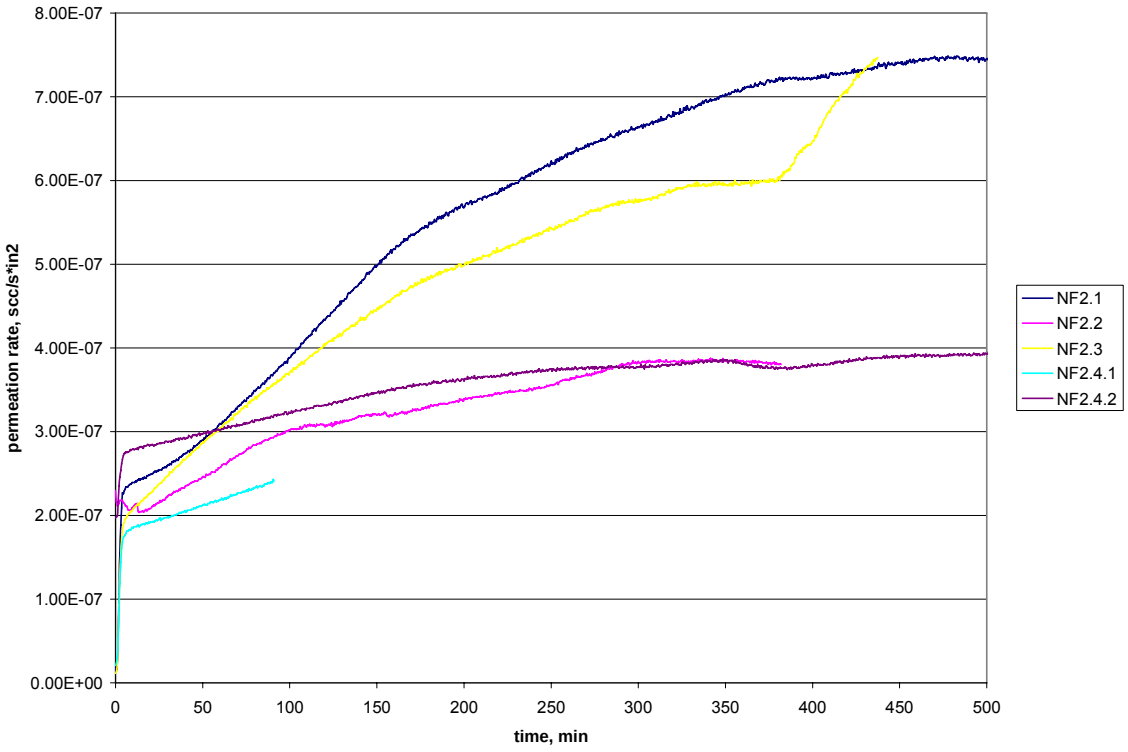

Fig. 5.1.9. Permeation rate of Nomex coated with NAPA 765-1286 diluted with alcohol

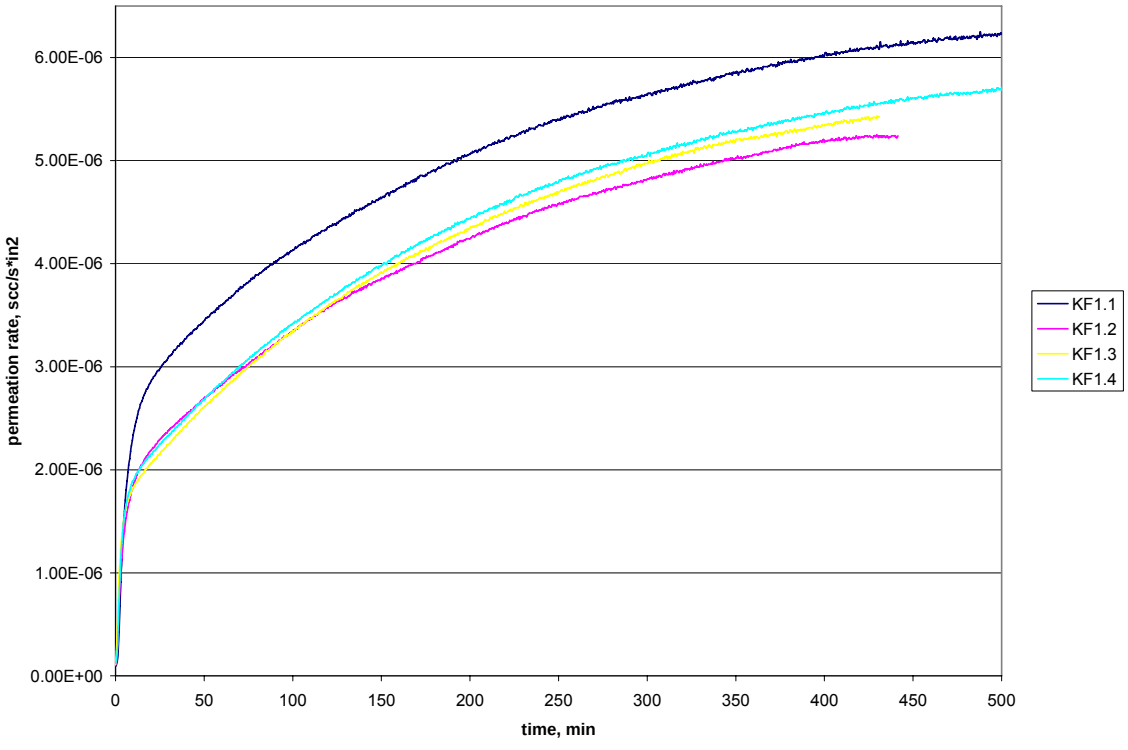

Fig. 5.1.10. Permeation rate of Kevlar coated with NAPA 765-1286 diluted with alcohol

Test results of Kevlar coated with NAPA are depicted in Fig. 5.1.10 and present very stable and comparable behavior of permeability rate.

5.1.4. Nomex 3T412 and Kevlar 2.8N636 papers from DuPont coated with low viscosity epoxy MAS 30-002 mixed with fast epoxy hardener MAS 30-012 in 2:1 proportion, with alcohol added, in following procedure:

- resin applied with brush against both surfaces
- roller (iron) used to impregnate pores
- left to dry in 40ºC for several hours
- vacuum-bag cured in oven

Fig. 5.1.11 depicts test results of Nomex paper coated with epoxy MAS while Fig. 5.1.12 and 5.1.13 show results for Kevlar samples. All three graphs illustrate very steady and similar permeation rate behavior with the best results for Nomex. Comparison of permeation rate for Kevlar paper coated with epoxy mixed with different alcohol contents shows similar behavior but calculated permeability coefficient is smaller for samples with bigger amount of alcohol, what is illustrated and discussed in next section.

Table 5.1.4. Sample documentation for Nomex and Kevlar coated with low viscosity epoxy MAS 30-002

Paper	Remarks Thickness T [in; mm]	Sample Nr	Sample thickness [in]
None	Transparent foil Vacuum leak 0.002; 0.0508	E1.1	0.002
		E1.2	0.0025
Nomex 3T412	Inlet pressure, 5psi 0.004; 0.1016	NE1.1	0.004
		NE1.2	0.004
		NE1.3	0.003
		NE1.4	0.0035
Kevlar 2.8N636	0.5g of alcohol for 36g of resin and 18g of hardener Inlet pressure, 5psi 0.011; 0.2794	KE1.1	0.007
		KE1.2	0.01
		KE1.3	0.011
		KE1.4	0.0105
	1g of alcohol for 36g of resin and 18g of hardener Inlet pressure, 5psi 0.005; 0.127	KE2.1	0.0045
		KE2.2	0.0045
		KE2.3	0.005
		KE2.4	0.005

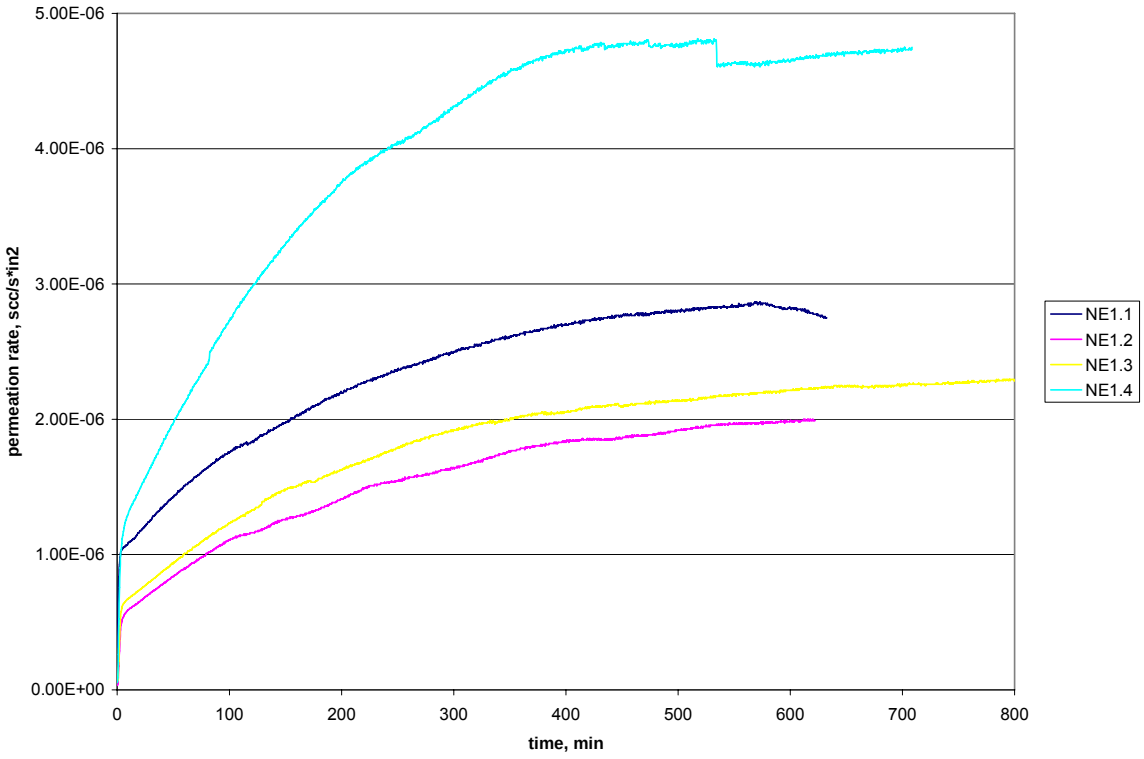

Fig. 5.1.11. Permeation rate of Nomex coated with epoxy MAS 30-002

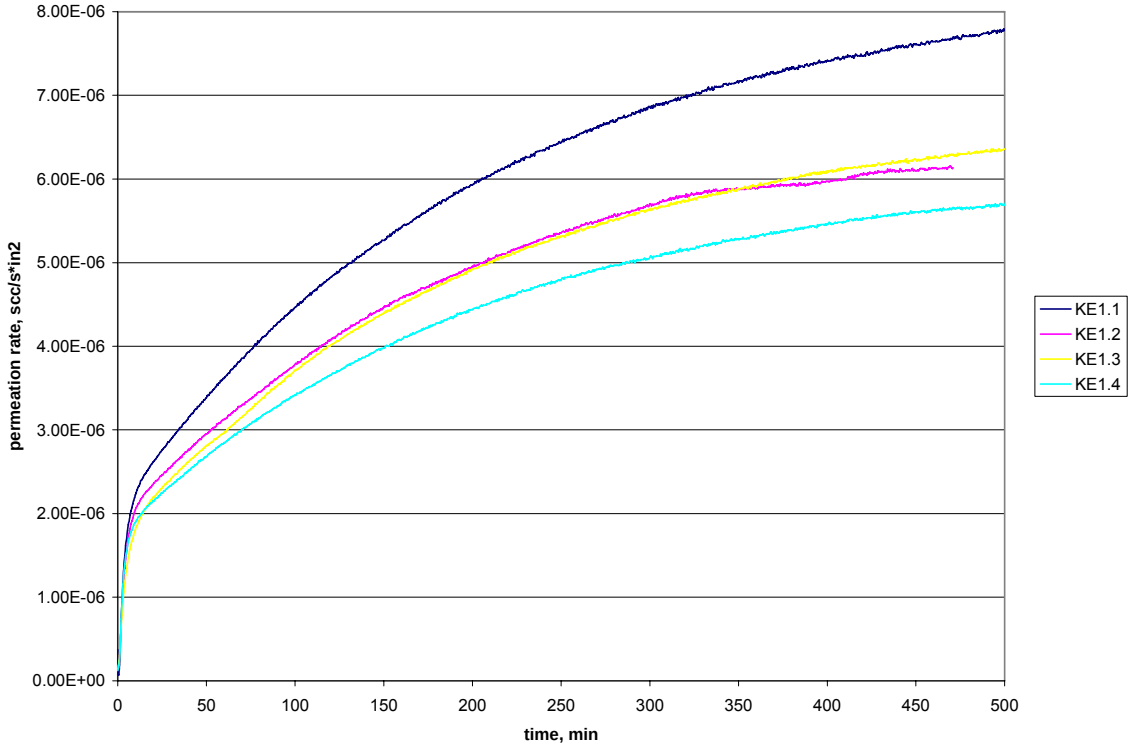

Fig. 5.1.12. Permeation rate of Kevlar coated with epoxy MAS 30-002 diluted with alcohol, 0.5g

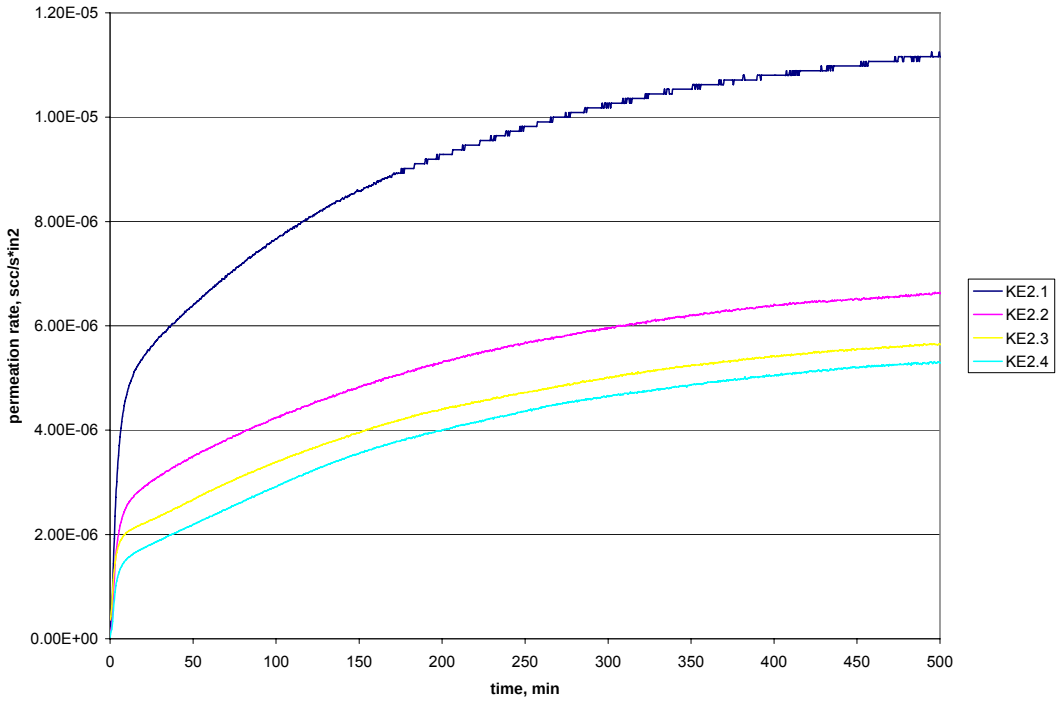

Fig. 5.1.13. Permeation rate of Kevlar coated with epoxy MAS 30-002 diluted with alcohol, 1g

5.1.5. Kapton films from DuPont

Table 5.1.5. Sample documentation for Kapton films

Film	Remarks Thickness T [in; mm]	Sample Nr	Sample thickness [in]
Kapton 50HN	Inlet pressure, 5psi 0.0005; 0.0127	K50.1	0.0005
		K50.2	0.0005
		K50.3	0.0005
		K50.4	0.0005
Kapton 100HN	Inlet pressure, 5psi 0.001; 0.0254	K100.1	0.001
		K100.2	0.001
		K100.3	0.001
		K100.4	0.001
Kapton 500HN	Inlet pressure, 5psi 0.005; 0.127	K500.1	0.005
		K500.2	0.005
		K500.3	0.005
		K500.4	0.005
	Inlet pressure, 10psi 0.005; 0.127	K500.5	0.005
		K500.6	0.005
		K500.7	0.005
		K500.8	0.005

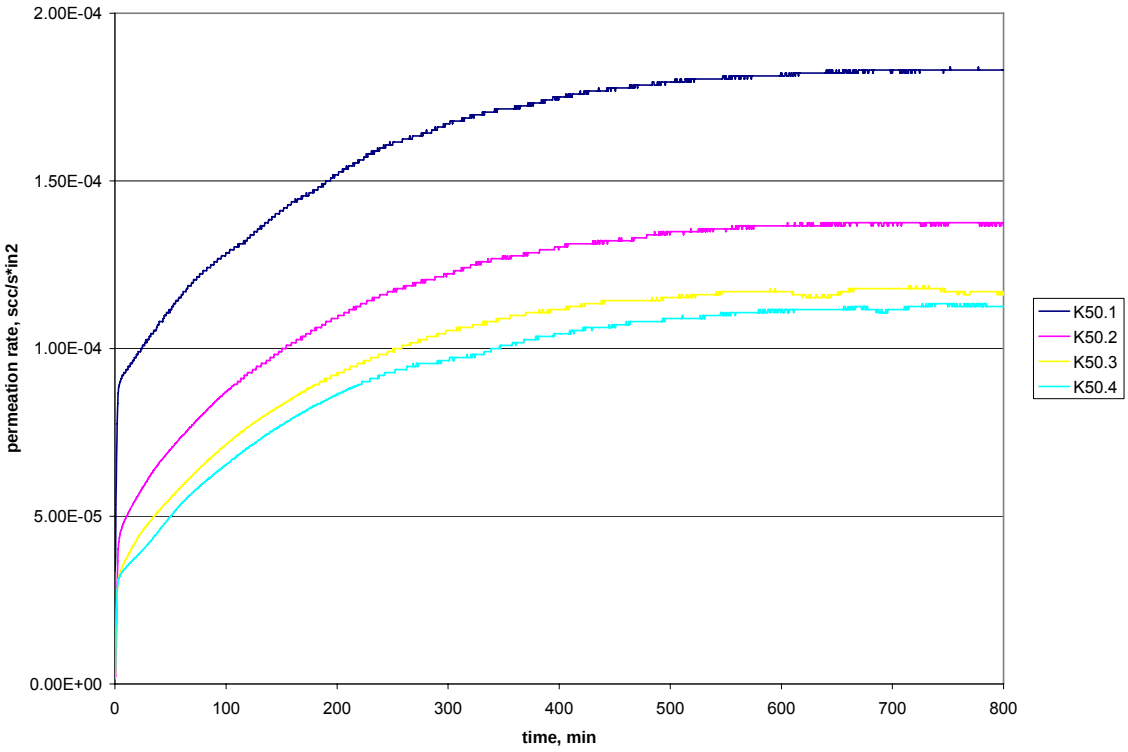

Fig. 5.1.14. Permeation rate of Kapton 50HN

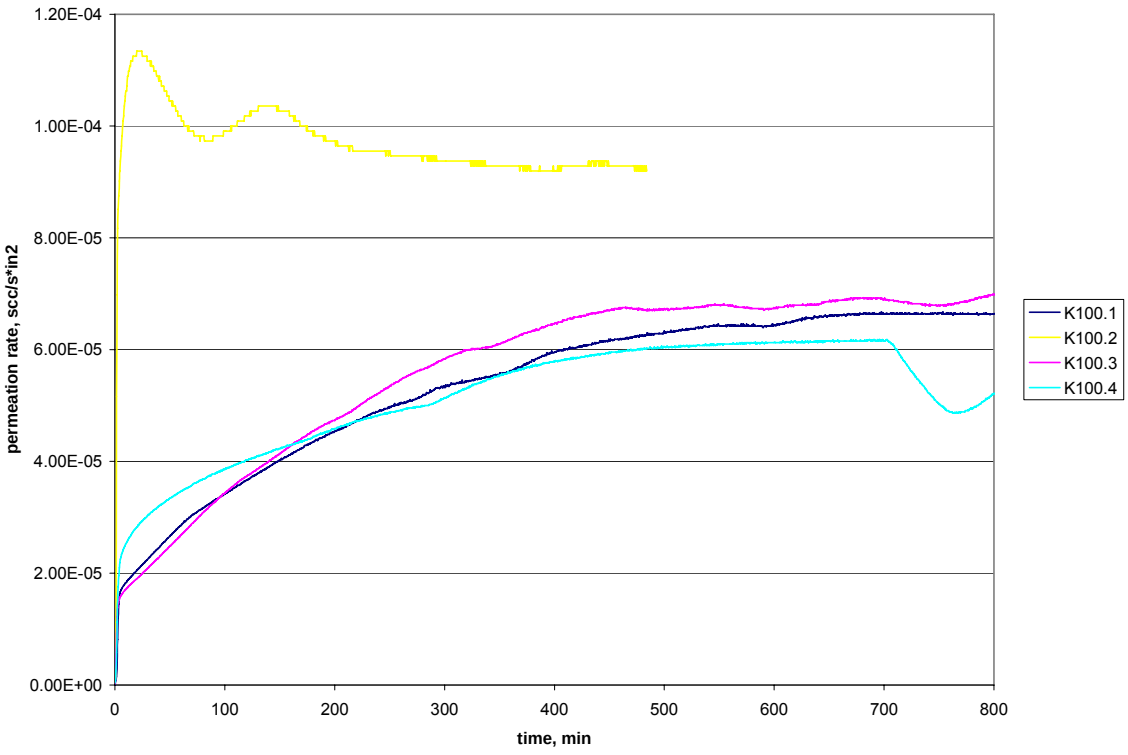

Fig. 5.1.15. Permeation rate of Kapton 100HN

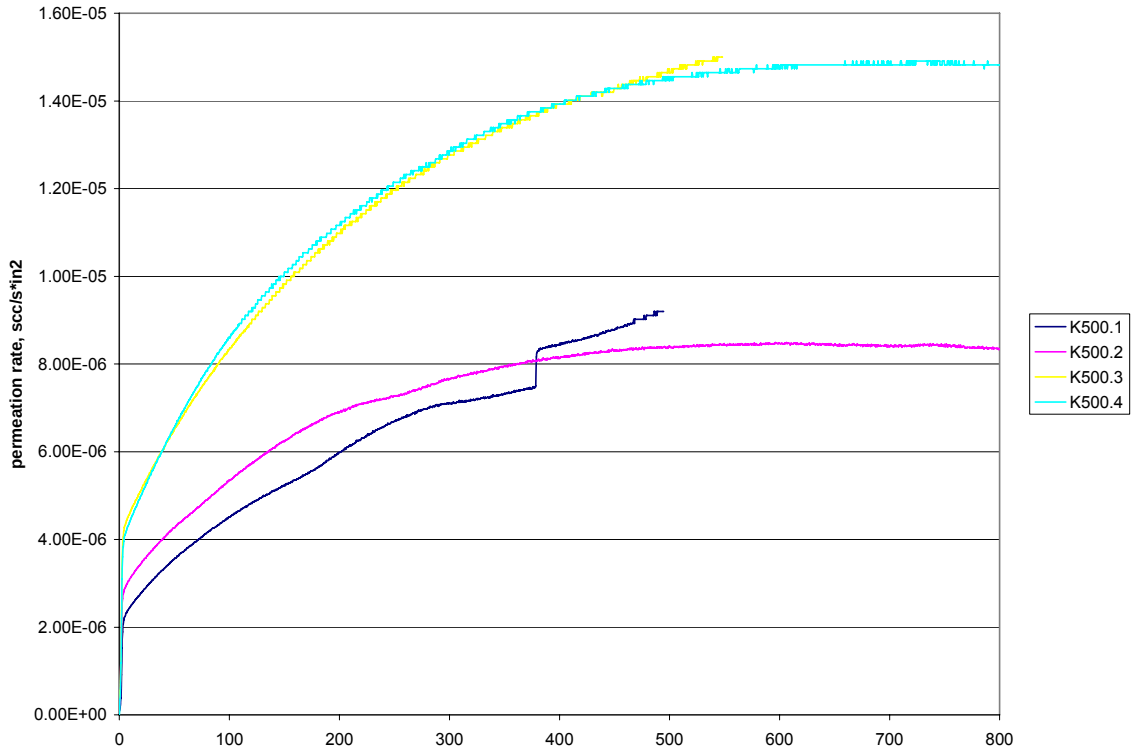

Fig. 5.1.16. Permeation rate of Kapton 500HN tested at 5psi

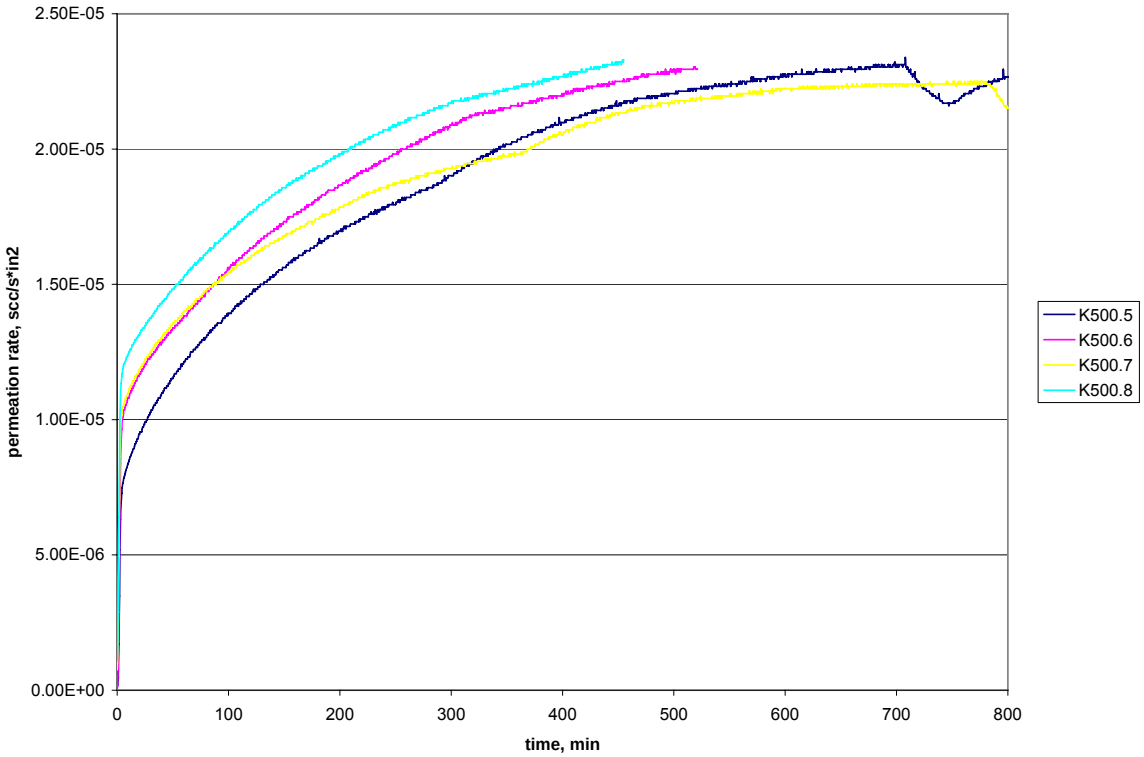

Fig. 5.1.17. Permeation rate of Kapton 500HN tested at 10psi

Permeability tests of industrial grade Kapton films gave very comparable results and similar permeability coefficients as will be showed later. Kapton 500HN has been chosen as reference material to investigate influence of pressure value on gas permeability. As it is showed in Fig. 5.1.17 for test pressure of 10psi the permeability curve is steeper and steady state is achieved slightly faster.

5.1.6. Nomex 2T412 and Kevlar 3.9N636 papers from DuPont coated with med-low viscosity SilverTip Marine Epoxy laminating resin mixed with fast hardener in 2:1 proportion, with 10% of acetone added, in following procedure:

- resin mixed with acetone
- left in the oven at 60ºC for few hours to evaporate acetone
- resin mixed with hardener
- mixture poured on both sides of papers
- placed between metal plates
- left to dry in room temperature overnight
- final cure in oven at 40ºC for few hours

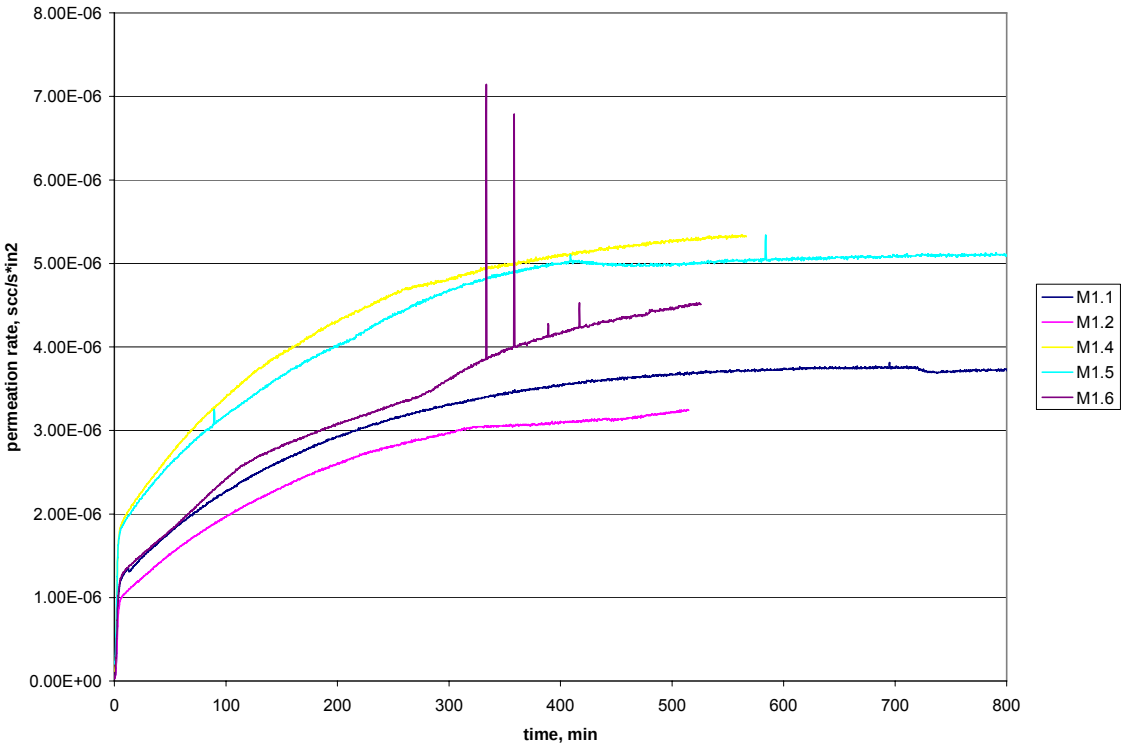

Fig. 5.1.18. Permeation rate of SilverTip marine epoxy films without acetone

All manufactured samples had very good coating without any gas bubbles or with few very small which did not influence steady state of permeability rate. That gave very comparable test results with mostly smooth curves. Thin films of epoxy were possible to test and Fig. 5.1.18 shows sample uniformity

and good quality excluding sample M1.6 which probably had some pores which accumulated helium. Only two samples of epoxy mixed with acetone had no through air bubbles and was possible to test and one of them showed worse permeation resistance and the other showed existence of some air pockets (See Figure 5.1.19). Addition of acetone increased permeability rate of all kinds of samples including coated papers. Curves of permeation rates for samples of Nomex and Kevlar coated with epoxy and acetone, showed in Fig. 5.1.21 and 5.1.23 respectively, depict existence of many rate peaks and more uneven behavior than for samples without acetone. Peaks in Fig. 5.1.23 could be explained by existence of many pores or gas bubbles inside samples which probably were created during curing through evaporating of acetone left in final mixture, which means that not all of acetone evaporated before mixing epoxy resin with hardener. Such gas pockets are more likely to exist in samples of coated Kevlar than coated Nomex since Kevlar is more porous and its surface is more uneven and fibrous.

Table 5.1.6. Sample documentation for Nomex and Kevlar coated with SilverTip marine epoxy

Paper	Remarks Thickness T [in; mm]	Sample Nr	Sample thickness [in]
None	No acetone Inlet pressure, 5psi 0.0136; 0.3454	M1.1	0.013
		M1.2	0.0133
		M1.3	0.013
	No acetone Inlet pressure, 5psi 0.0116; 0.2946	M1.4	0.0126
		M1.5	0.0114
		M1.6	0.0153
	Acetone added Inlet pressure, 5psi 0.008; 0.2032	M2.1	0.0055
		M2.2	0.0053
		M2.3	0.0091
		M2.4	0.0143
Nomex 2T412	No acetone Inlet pressure, 5psi 0.0161; 0.4089	NM1.1	0.0168
		NM1.2	0.0173
		NM1.3	0.0155
		NM1.4	0.016
	No acetone Inlet pressure, 5psi 0.0181; 0.4597	NM1.5	0.018
		NM1.6	0.0114
		NM1.7	0.0136
		NM1.8	0.0127
	Acetone added Inlet pressure, 5psi 0.086; 2.1844	NM2.1	0.0059
		NM2.2	0.0056
		NM2.3	0.0086
		NM2.4	0.0058
Kevlar 3.9N636	No acetone Inlet pressure, 5psi 0.019; 0.4826	KM1.1	0.0183
		KM1.2	0.0196
		KM1.3	0.0162
		KM1.4	0.0175
	Acetone added Inlet pressure, 5psi 0.0181; 0.4597	KM2.1	0.0207
		KM2.2	0.0189
		KM2.3	0.0188
		KM2.4	0.0183

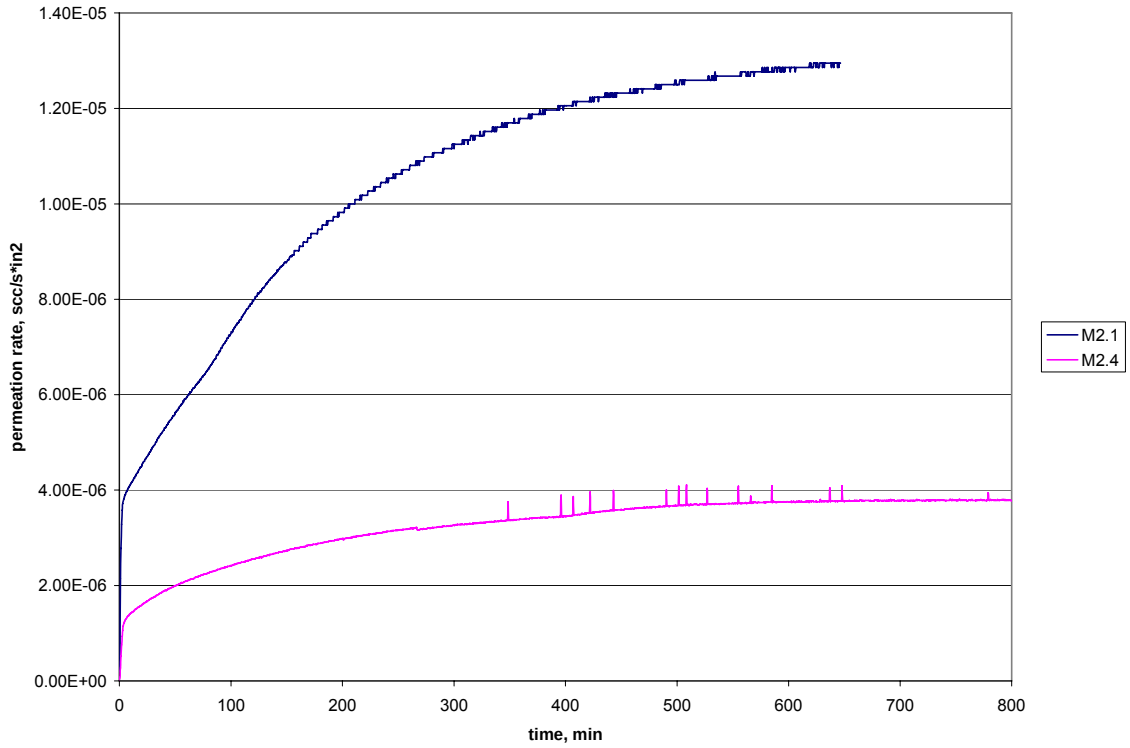

Fig. 5.1.19. Permeation rate of SilverTip marine epoxy films with acetone

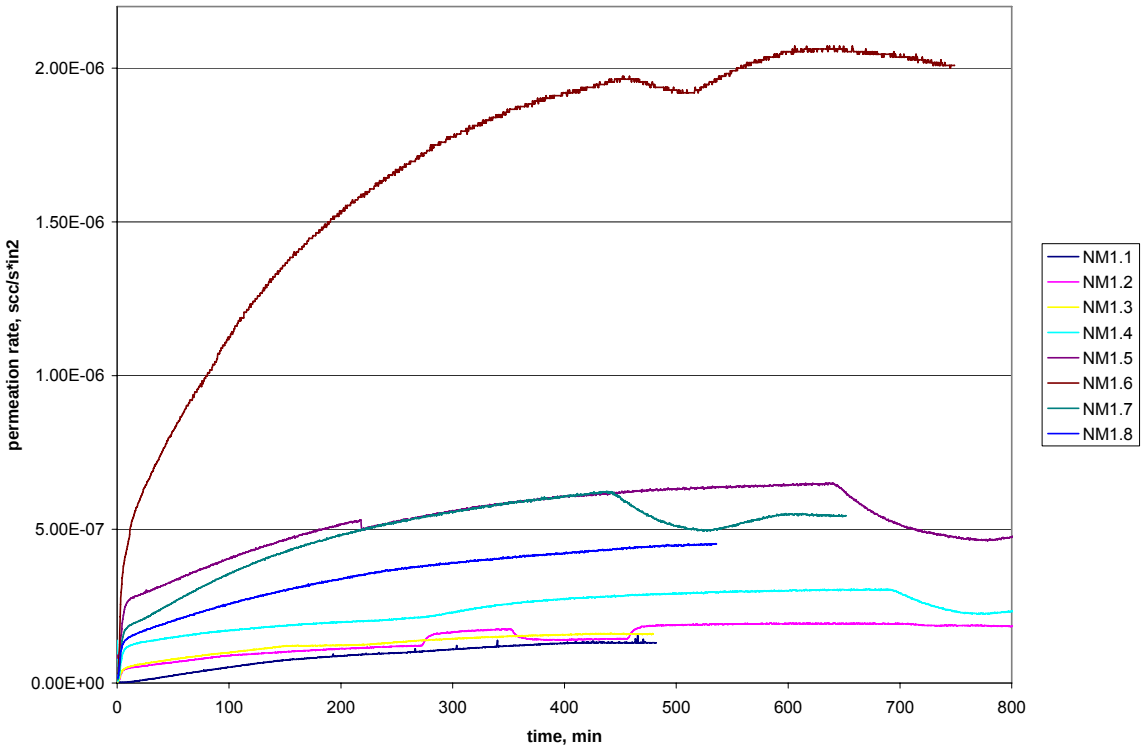

Fig. 5.1.20. Permeation rate of Nomex coated with SilverTip marine epoxy

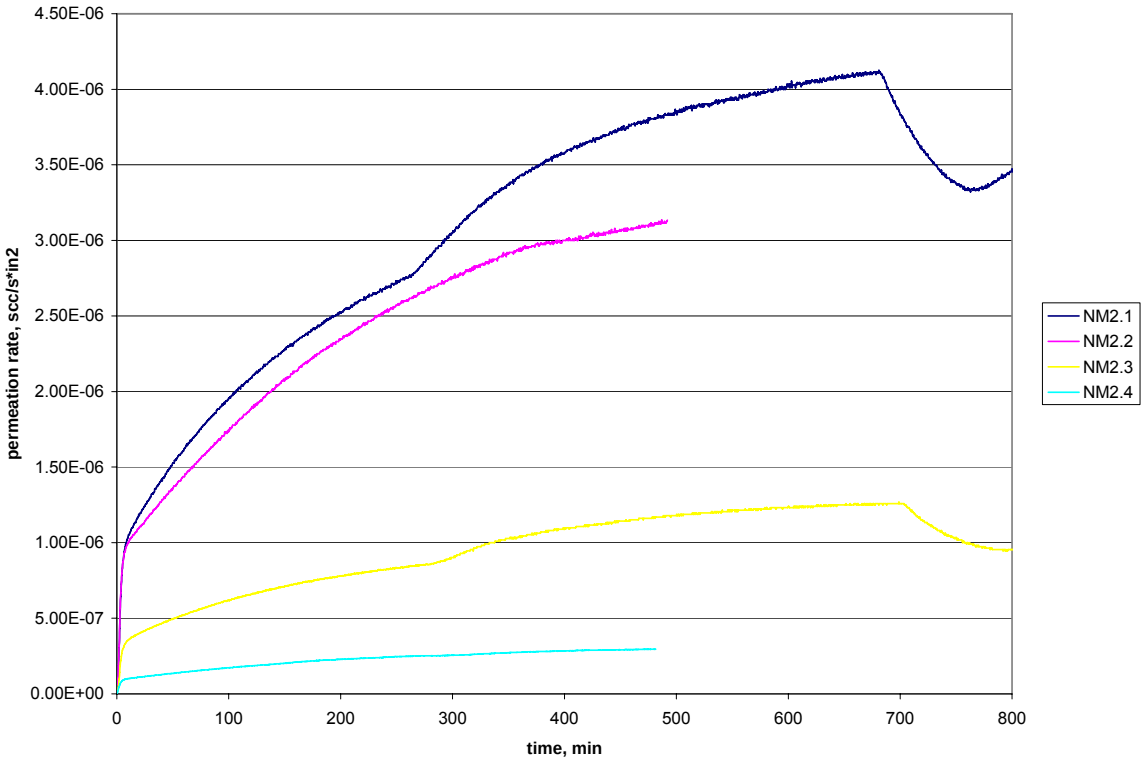

Fig. 5.1.21. Permeation rate of Nomex coated with SilverTip marine epoxy with acetone

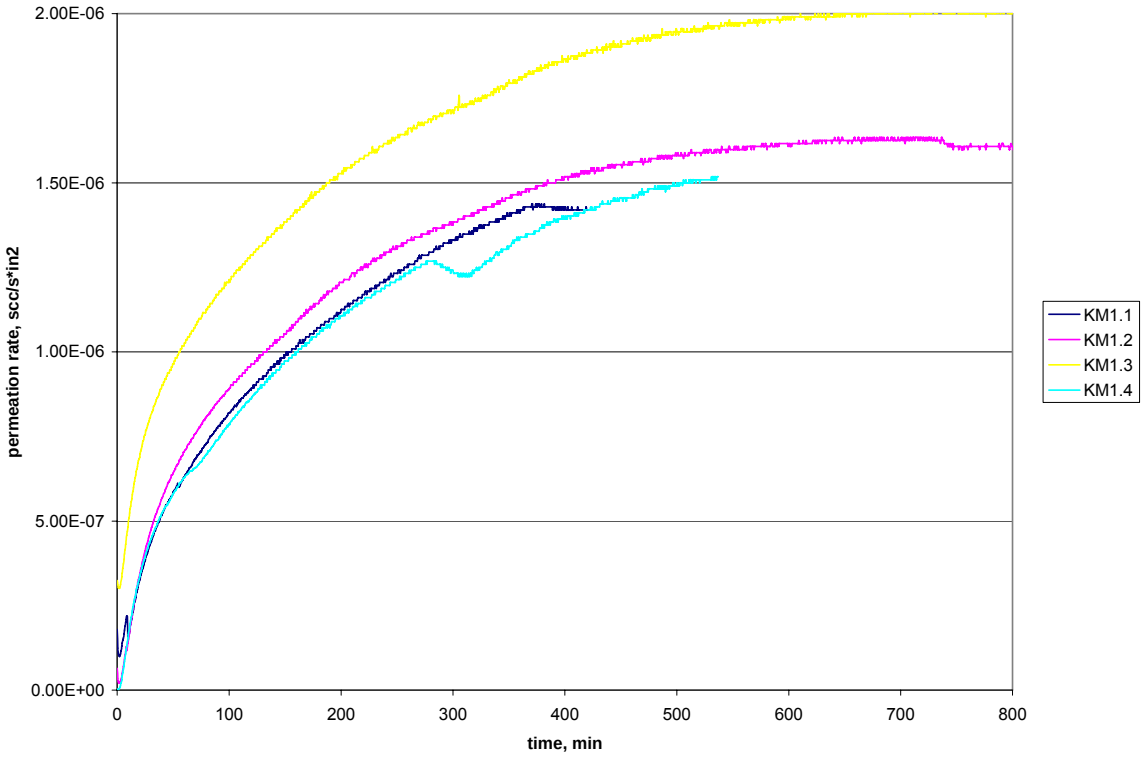

Fig. 5.1.22. Permeation rate of Kevlar coated with SilverTip marine epoxy

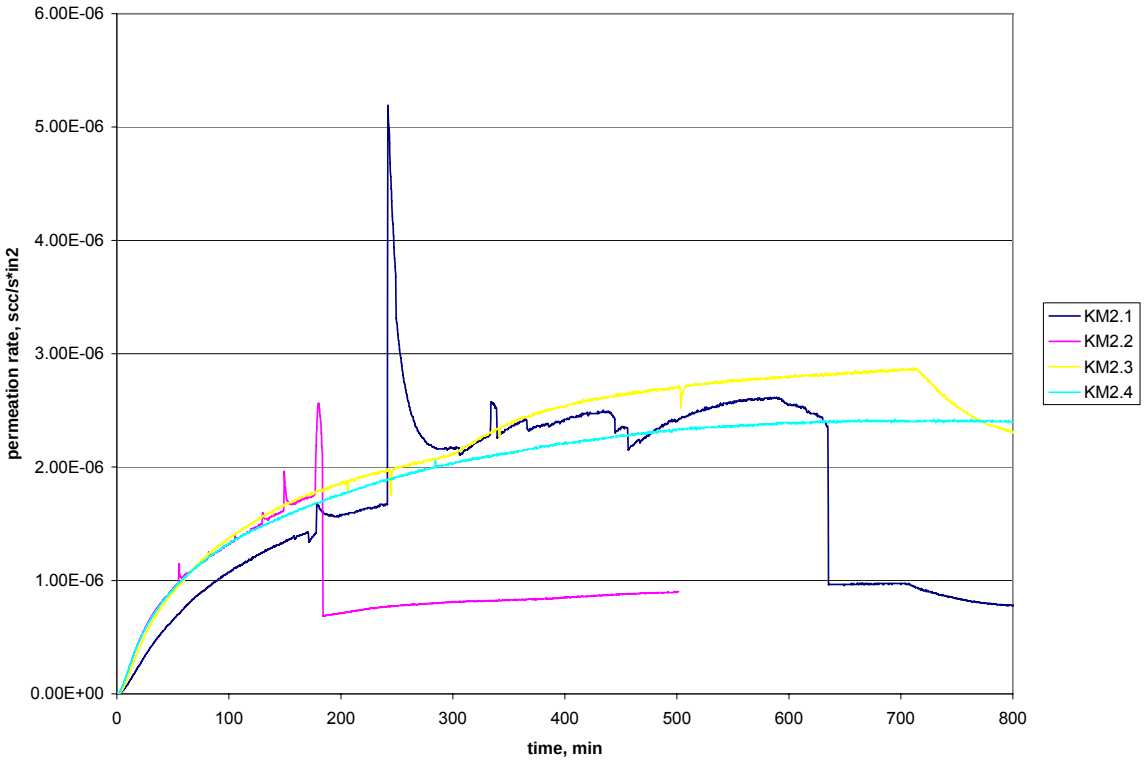

Fig. 5.1.23. Permeation rate of Kevlar coated with SilverTip marine epoxy with acetone

5.1.7. Nomex 2T412 and Kevlar 3.9N636 papers from DuPont coated with med-low viscosity SilverTip Marine Epoxy laminating resin mixed with fast hardener in 2:1 proportion, with 2%, 4%, 6% of Bentolite L-10 and acetone added, in following procedure:

- nanoclay sonicated in 10 time bigger amount of acetone for 1 hour
- resin added and mixed with stirring sticks for few minutes
- left in the oven at 60ºC for few hours to evaporate acetone
- resin mixed with hardener with stirring sticks for few minutes
- mixture poured on both sides of papers
- placed between metal plates
- left to dry in room temperature overnight
- final cure in oven at 40ºC for few hours

Samples of epoxy films were mostly impossible to test due to existence of through thickness air bubbles formed during mixing and curing process and as a result of adding acetone to the mixture. Samples of epoxy mixed with 2% of Bentolite had too many bubbles and holes to be tested. Only two samples of epoxy mixed with 4% of Bentolite and two samples of epoxy mixed with 6% of the same nanoclay sustained vacuum pressure. Samples of epoxy with 4% have better permeability properties than those with 6% of Bentolite.

Graphs of permeation rate for samples of Nomex papers coated with epoxy mixed with Bentolite show different performance than those for Kevlar paper coated with the same epoxy systems. The curves show very unstable behavior, especially for samples with 2% and 6% of Bentolite, see Fig. 5.1.26 and 5.1.28. Samples of coated Kevlar gave comparable results except for Kevlar samples with epoxy and 2% of Bentolite whose graphs illustrate existence of peaks on permeation rate curves, see Fig. 5.1.29. That probably was caused by existence of not entirely evaporated acetone in the coating mixture and it seems to be true for the full set of samples of epoxy mixed with 2% of nanoclay. That was a first and pioneer set of samples with nanoclay and manufacturing procedure could have been faulty and given defective samples and results.

Table 5.1.7. Sample documentation for aramid papers coated with SilverTip epoxy and Bentolite

Paper	Remarks Thickness T [in; mm]	Sample Nr	Sample thickness [in]
None	2% of Bentolite Big bubbles, all the way through		
	4% of Bentolite Inlet pressure, 5psi 0.0126; 0.32	MB4.1	0.0133
		MB4.2	0.0094
		MB4.3	0.0096
		MB4.4	0.0062
	6% of Bentolite Inlet pressure, 5psi 0.0093; 0.2362	MB6.1	0.0062
		MB6.2	0.0073
		MB6.3	0.0074
		MB6.4	0.0068
Nomex 2T412	2% of Bentolite Inlet pressure, 5psi 0.0238; 0.6045	NMB2.1	0.0224
		NMB2.2	0.0198
		NMB2.3	0.0259
		NMB2.4	0.0181
	4% of Bentolite Inlet pressure, 5psi 0.0158; 0.4013	NMB4.1	0.015
		NMB4.2	0.0112
		NMB4.3	0.0163
		NMB4.4	0.01
	6% of Bentolite Inlet pressure, 5psi 0.0094; 0.2388	NMB6.1	0.0073
		NMB6.2	0.0054
		NMB6.3	0.0086
		NMB6.4	0.0079
Kevlar 3.9N636	2% of Bentolite Inlet pressure, 5psi 0.0214; 0.5436	KMB2.1	0.0225
		KMB2.2	0.0224
		KMB2.3	0.0222
		KMB2.4	0.0224
	4% of Bentolite Inlet pressure, 5psi 0.0147; 0.3734	KMB4.1	0.016
		KMB4.2	0.0125
		KMB4.3	0.011
		KMB4.4	0.011
	6% of Bentolite Inlet pressure, 5psi 0.0099; 0.2515	KMB6.1	0.0098
		KMB6.2	0.0084
		KMB6.3	0.0095
		KMB6.4	0.0091

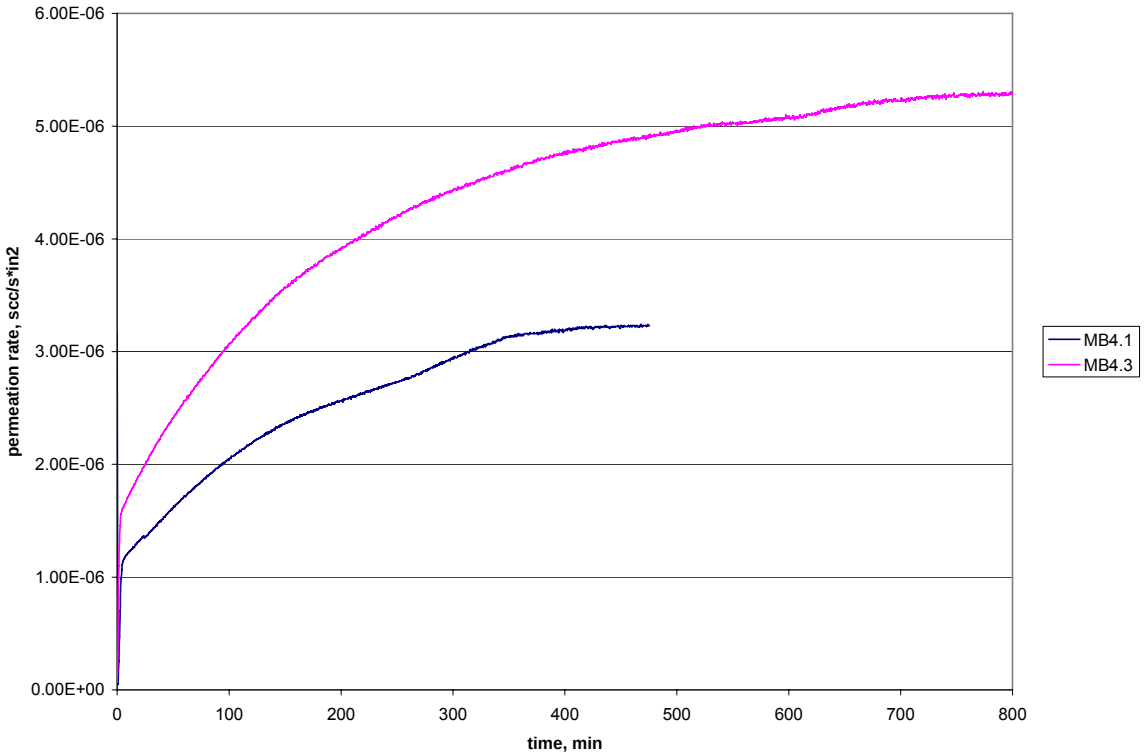

Fig. 5.1.24. Permeation rate of SilverTip marine epoxy with 4% of Bentolite

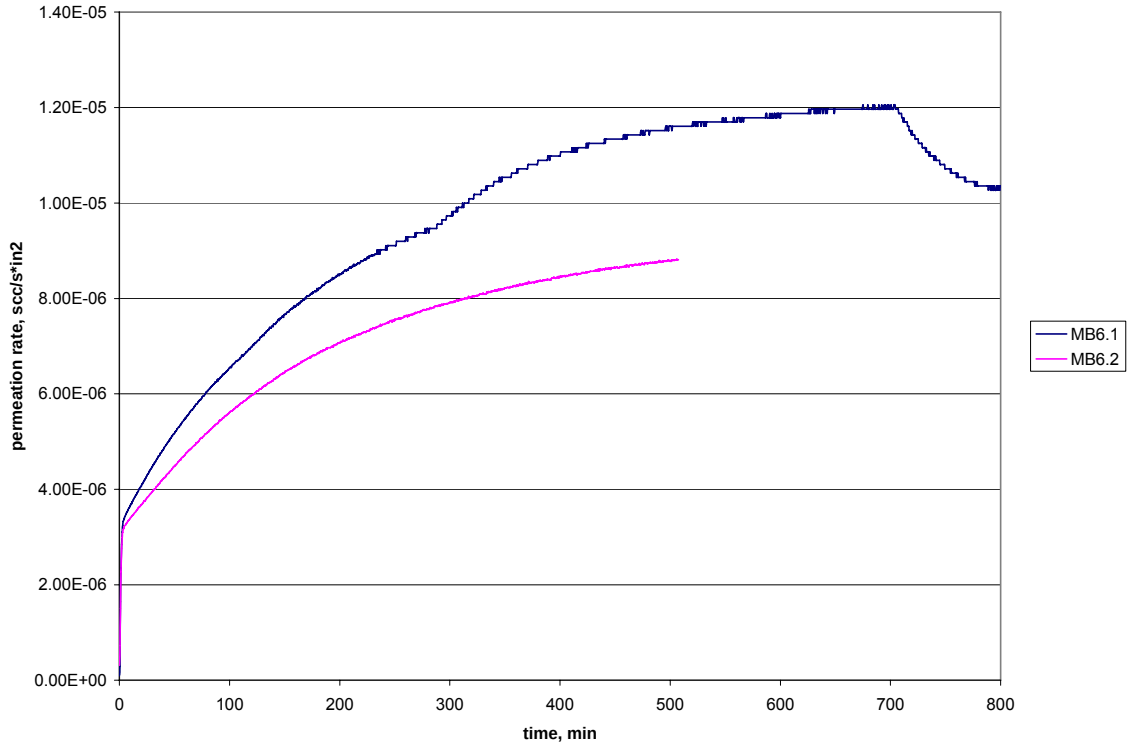

Fig. 5.1.25. Permeation rate of SilverTip marine epoxy with 6% of Bentolite

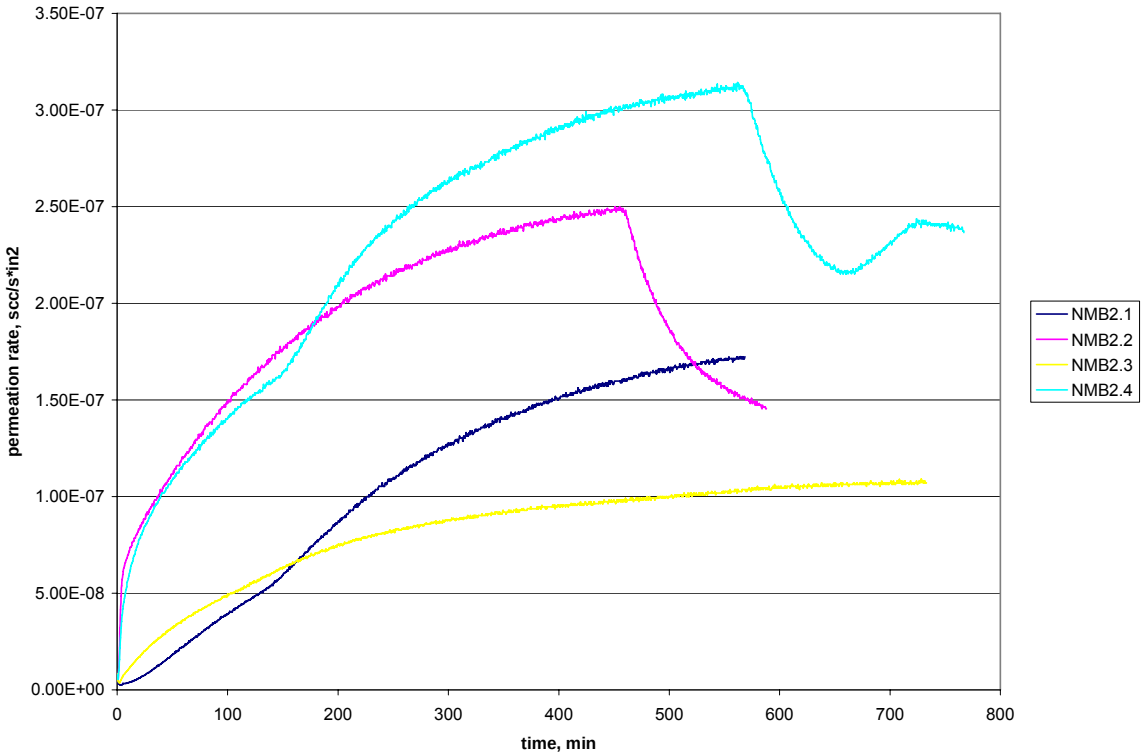

Fig. 5.1.26. Permeation rate of Nomex coated with SilverTip marine epoxy with 2% of Bentolite

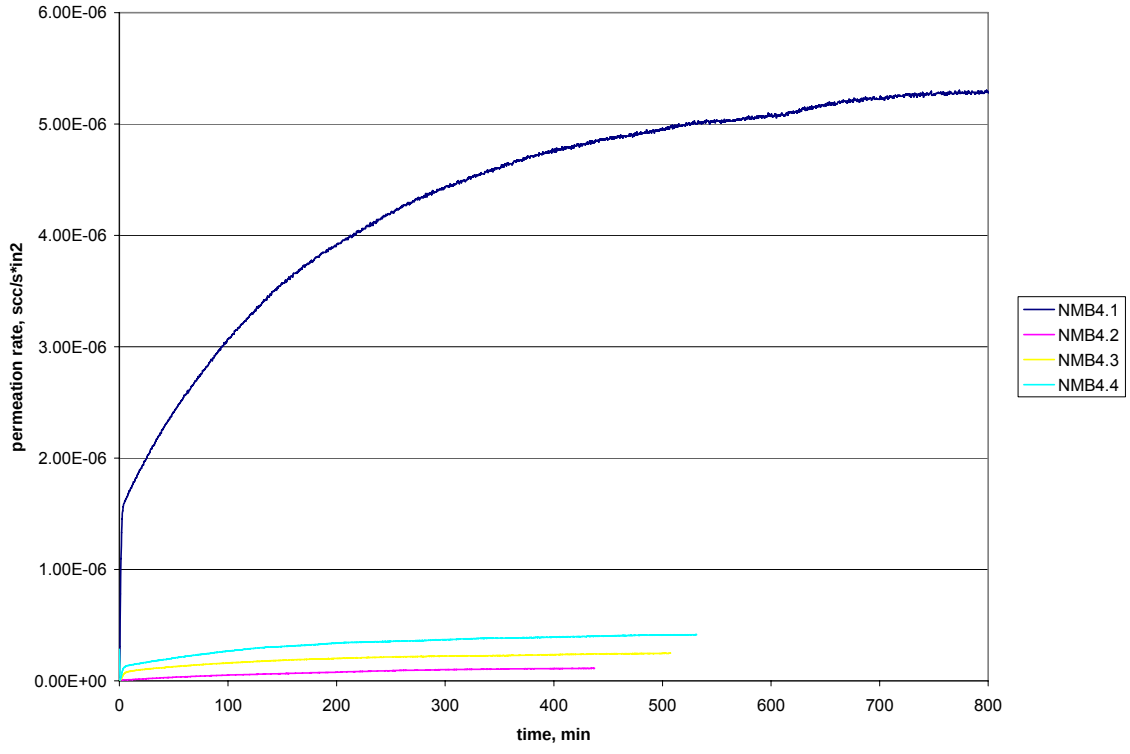

Fig. 5.1.27. Permeation rate of Nomex coated with SilverTip marine epoxy with 4% of Bentolite

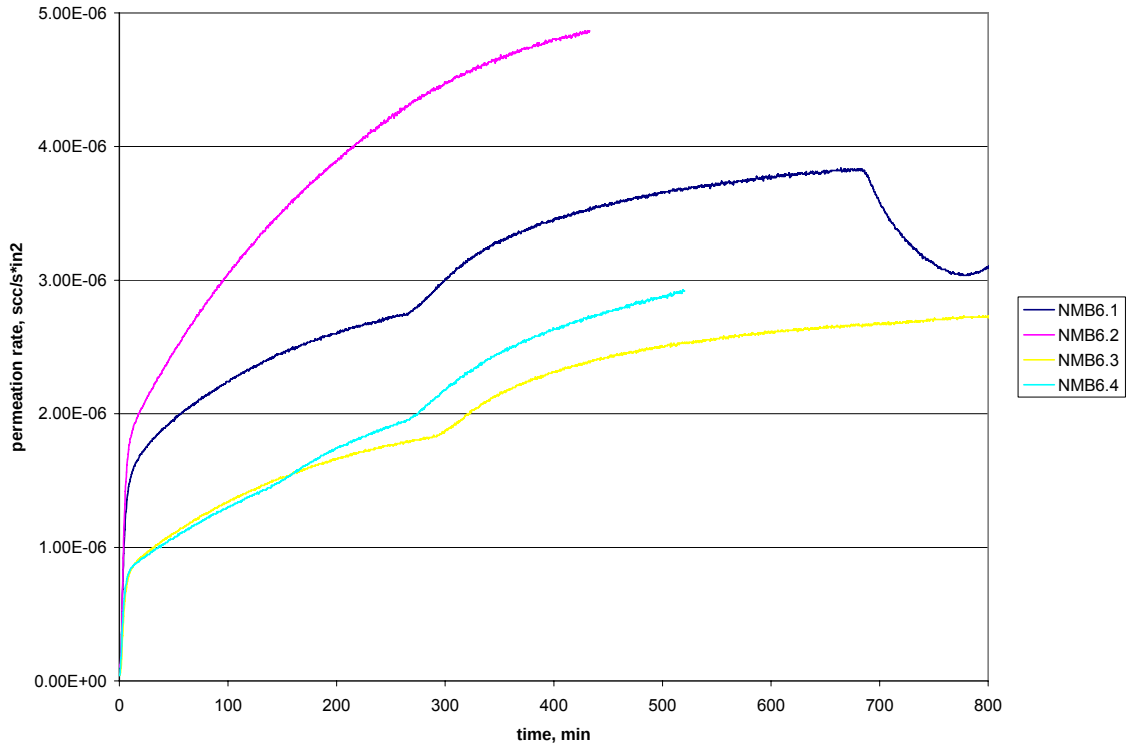

Fig. 5.1.28. Permeation rate of Nomex coated with SilverTip marine epoxy with 6% of Bentolite

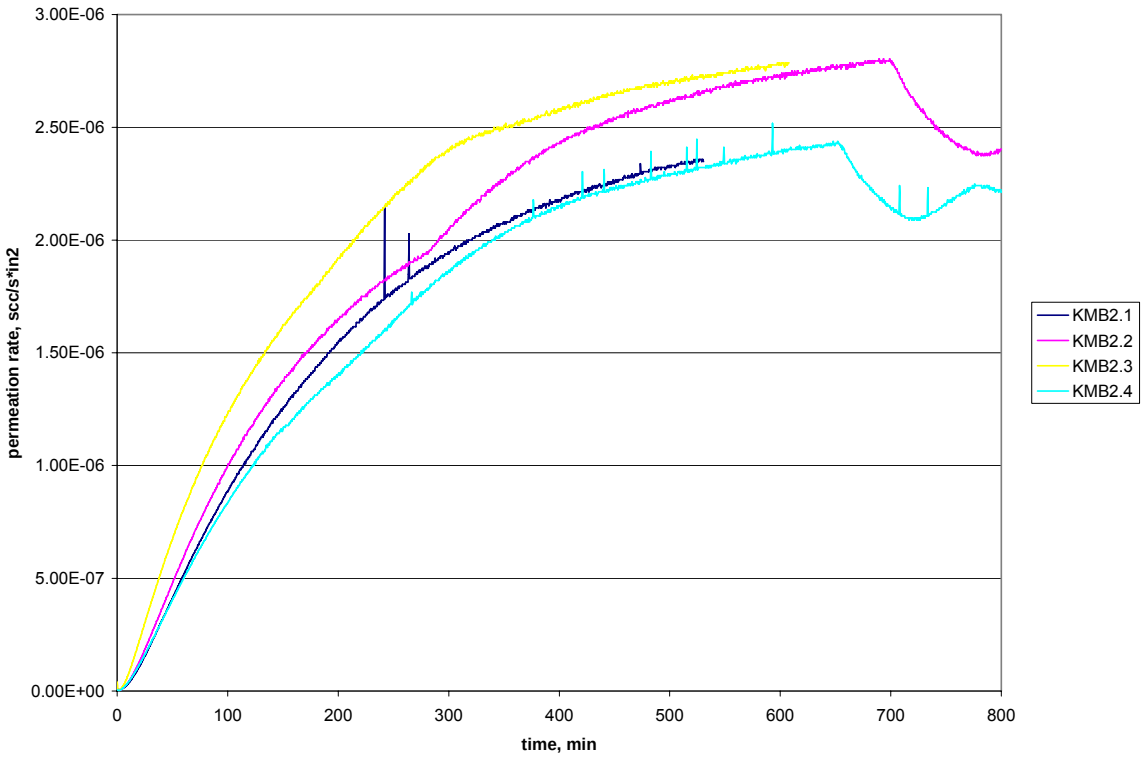

Fig. 5.1.29. Permeation rate of Kevlar coated with SilverTip marine epoxy with 2% of Bentolite

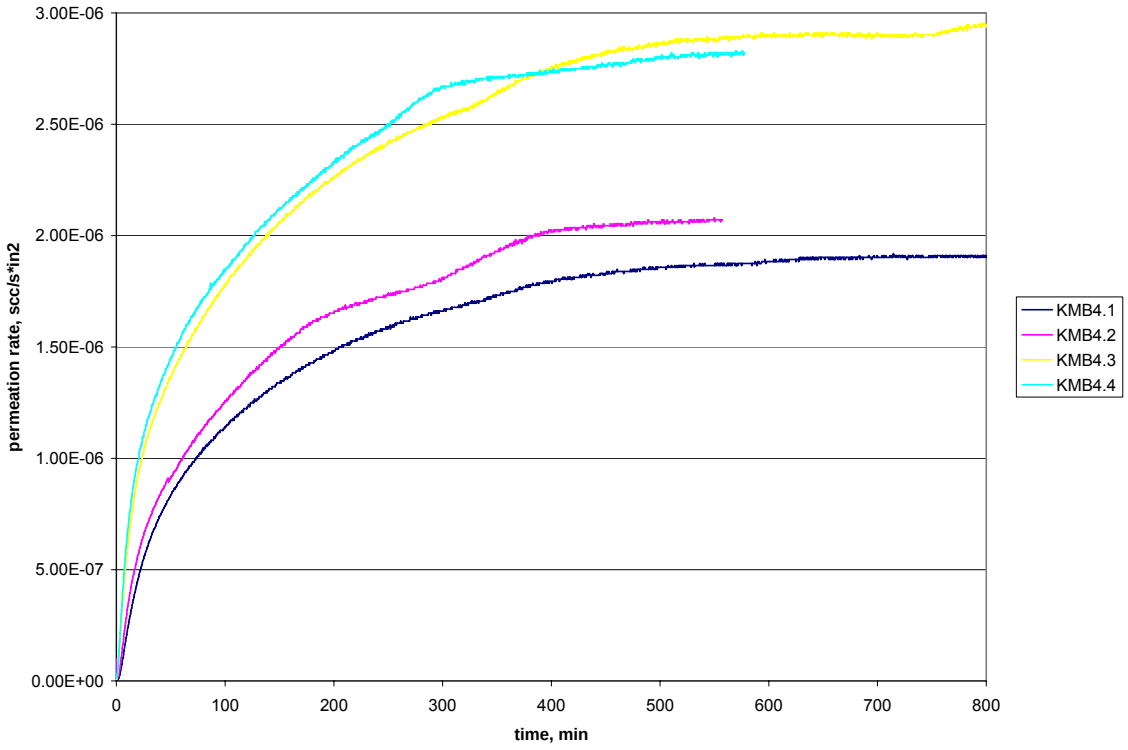

Fig. 5.1.30. Permeation rate of Kevlar coated with SilverTip marine epoxy with 4% of Bentolite

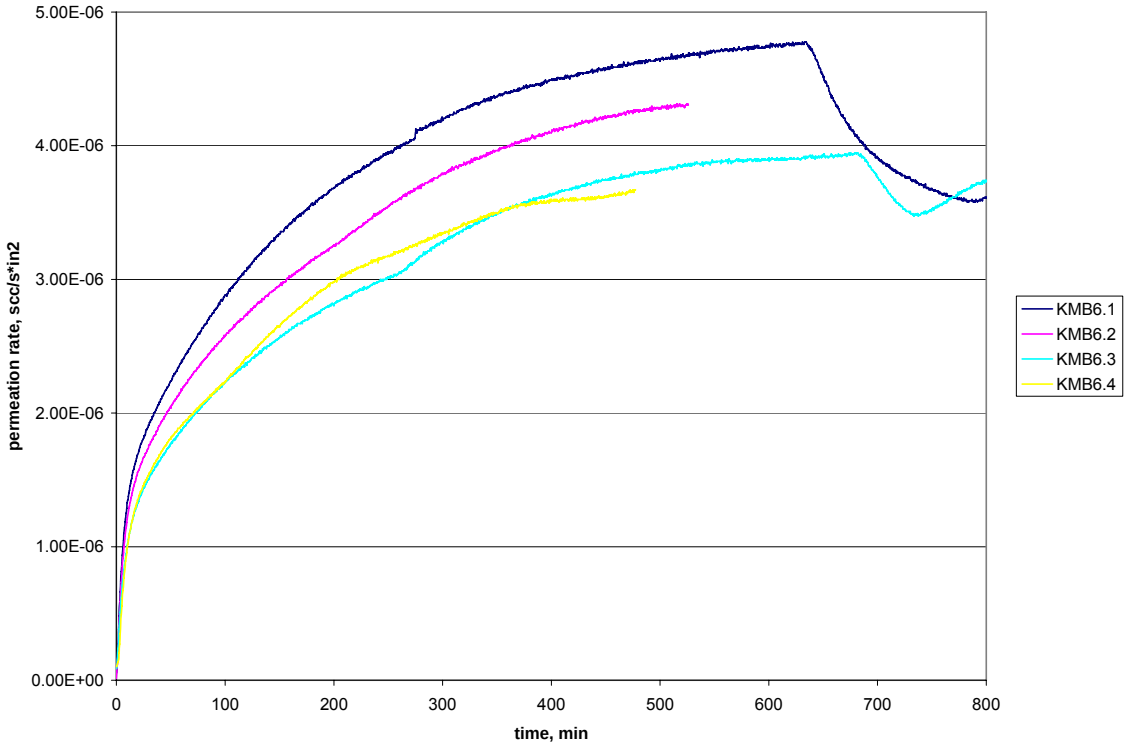

Fig. 5.1.31. Permeation rate of Kevlar coated with SilverTip marine epoxy with 6% of Bentolite

Samples of Nomex and Kevlar coated with 2% and 6% and epoxy film with 6% of nanoclay show different behavior of permeation rate curve. At some point the rate increases slightly more and after some time drops significantly. That could be explained by some possible changes in sample structures under pressure, e.g. dislocation of nanoclays causing opening and closing of leak paths. Samples with epoxy mixed with acetone are softer than those without diluent and membrane bending is bigger, what creates extra stresses and changes in size and shape of possible defects inside structure.

5.1.8. Nomex 2T412 and Kevlar 3.9N636 papers from DuPont coated with med-low viscosity SilverTip Marine Epoxy laminating resin mixed with fast hardener in 2:1 proportion, with 2%, 4%, 6% of Nanocor I.30E and acetone added, in following procedure:

- nanoclay sonicated in 10 time bigger amount of acetone for 2 minutes
- resin added and mixed with stirring sticks for few minutes
- left in the oven at 60ºC for few hours to evaporate acetone
- epoxy cooled and high speed mixed for 2 minutes,
- resin mixed with hardener with stirring sticks for few minutes
- mixture poured on both sides of papers
- placed between metal plates
- left to dry in room temperature overnight
- final cure in oven at 40ºC for few hours

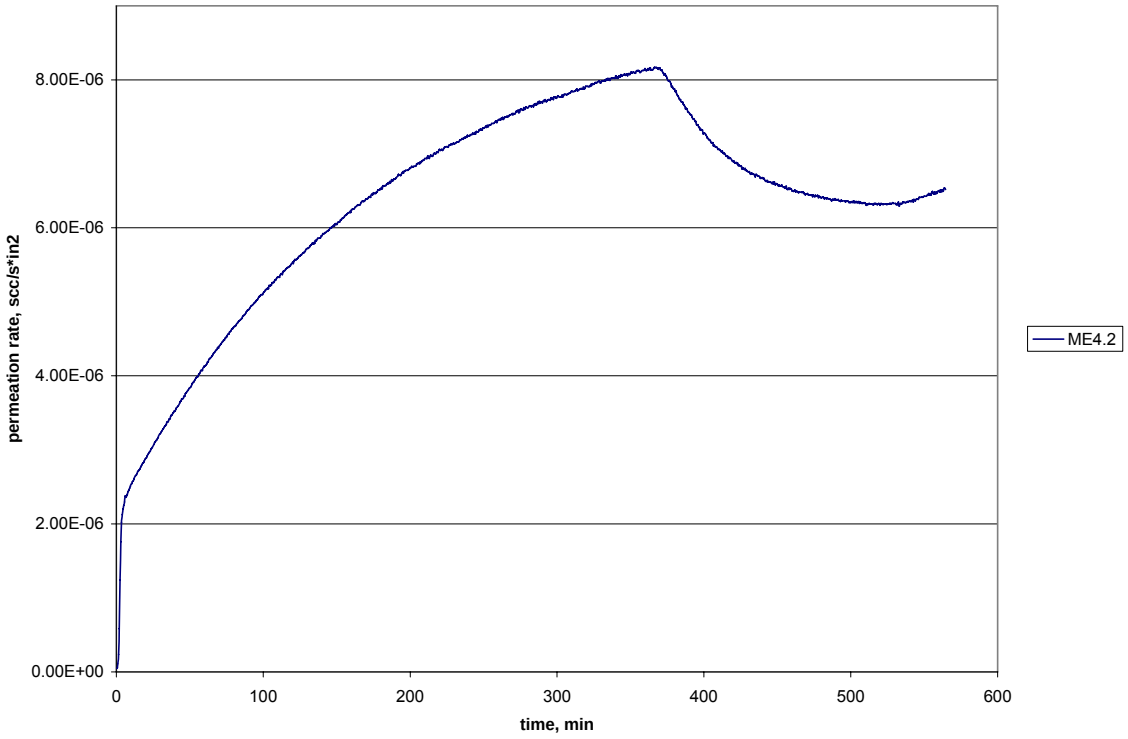

Fig. 5.1.32. Permeation rate of SilverTip marine epoxy with 4% of Nanocor

Nanoclay Nanocor is specially pretreated clay for easy industrial use. The I.30E grade has a protonated octadecyl amine on the clay surface. Surface treatment helps to better exfoliate nanoclay in the medium and sonication is not needed. First attempt to combine this nanoclay was to mechanically mix it with drill but that created air bubbles and first samples of epoxy mixed with 2 and 4% of nanoclay had through holes. Only one sample of 4% of nanoclay had intact structure and was able to be tested. The rest of samples were prepared through fast sonication and mixing with stirring sticks. In case of fast mechanical mixing it is advised to degas the mixture before adding hardener.

Table 5.1.8. Sample documentation for aramid papers coated with SilverTip epoxy and Nanocor

Paper	Remarks Thickness T [in; mm]	Sample Nr	Sample thickness [in]
None	2% of Nanocor Vacuum leak 0.0054; 0.1372	ME2.1	0.0037
		ME2.2	0.0024
		ME2.3	0.0069
		ME2.4	0.006
	4% of Nanocor Inlet pressure, 5psi Vacuum leak 0.0069; 0.1753	ME4.1	0.0039
		ME4.2	0.0093
		ME4.3	0.0062
		ME4.4	0.006
		ME4.5	0.0071
		ME4.6	0.0077
	6% of Nanocor Inlet pressure, 5psi 0.0103; 0.2616	ME6.1	0.0062
		ME6.2	0.0107
		ME6.3	0.0083
		ME6.4	0.0162
Nomex 2T412	2% of Nanocor Inlet pressure, 5psi 0.008; 0.2032	NME2.1	0.0097
		NME2.2	0.0083
		NME2.3	0.0064
		NME2.4	0.0092
	4% of Nanocor Inlet pressure, 5psi 0.0244; 0.6198	NME4.1	0.0233
		NME4.2	0.0161
		NME4.3	0.0263
		NME4.4	0.0194
	6% of Nanocor Inlet pressure, 5psi 0.0095; 0.2413	NME6.1	0.0085
		NME6.2	0.0102
		NME6.3	0.0059
		NME6.4	0.006
Kevlar 3.9N636	2% of Nanocor Inlet pressure, 5psi 0.0077; 0.1956	KME2.1	0.0081
		KME2.2	0.0105
		KME2.3	0.0121
		KME2.4	0.0082
	4% of Nanocor Inlet pressure, 5psi 0.0087; 0.221	KME4.1	0.0094
		KME4.2	0.008
		KME4.3	0.0088
		KME4.4	0.0088
	6% of Nanocor Inlet pressure, 5psi 0.0093; 0.2362	KME6.1	0.0079
		KME6.2	0.0106
		KME6.3	0.0096
		KME6.4	0.0097

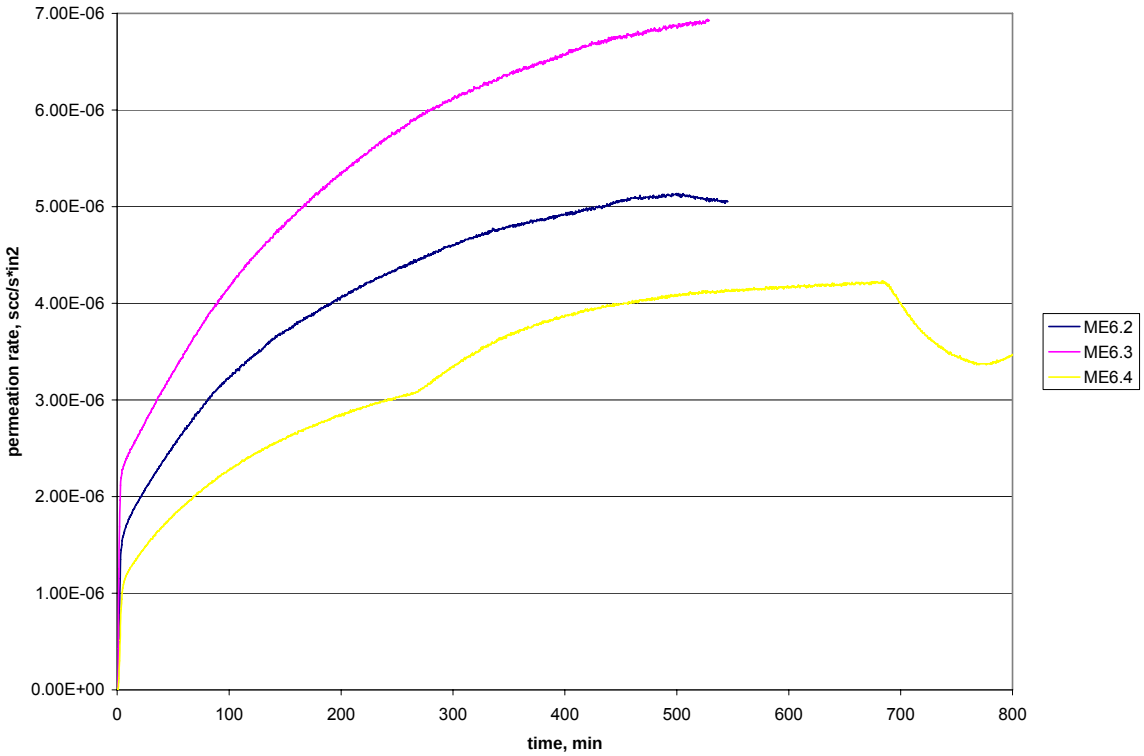

Fig. 5.1.33. Permeation rate of SilverTip marine epoxy with 6% of Nanocor

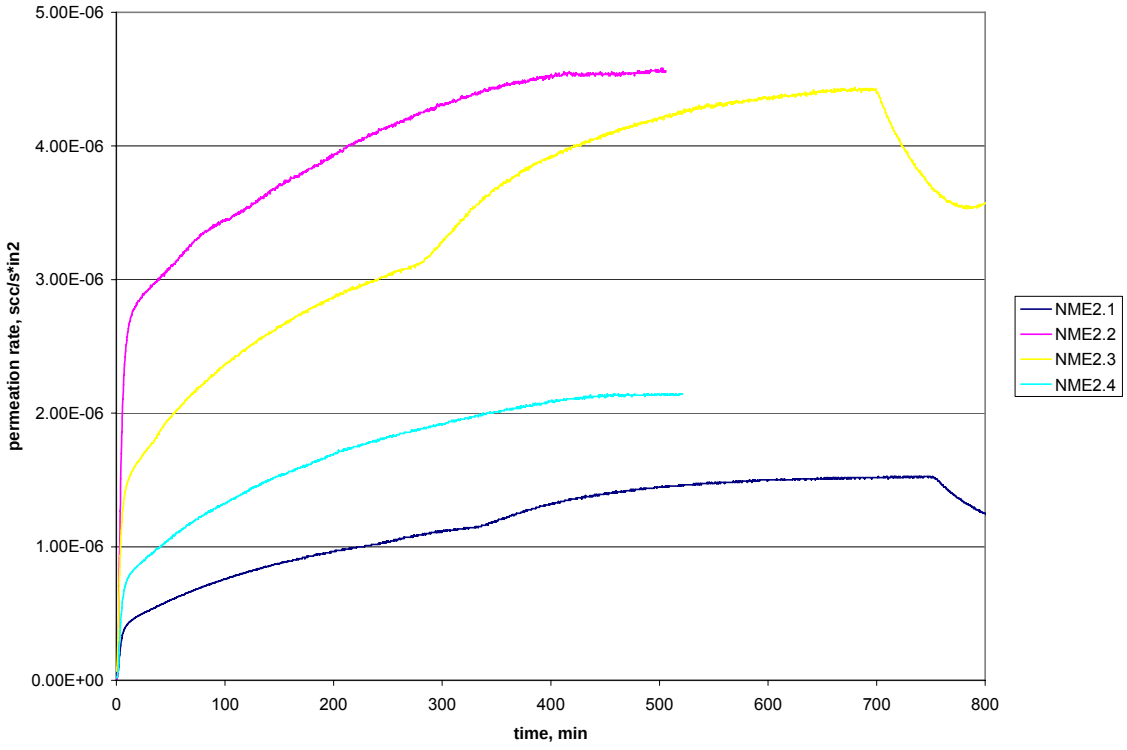

Fig. 5.1.34. Permeation rate of Nomex coated with SilverTip marine epoxy with 2% of Nanocor

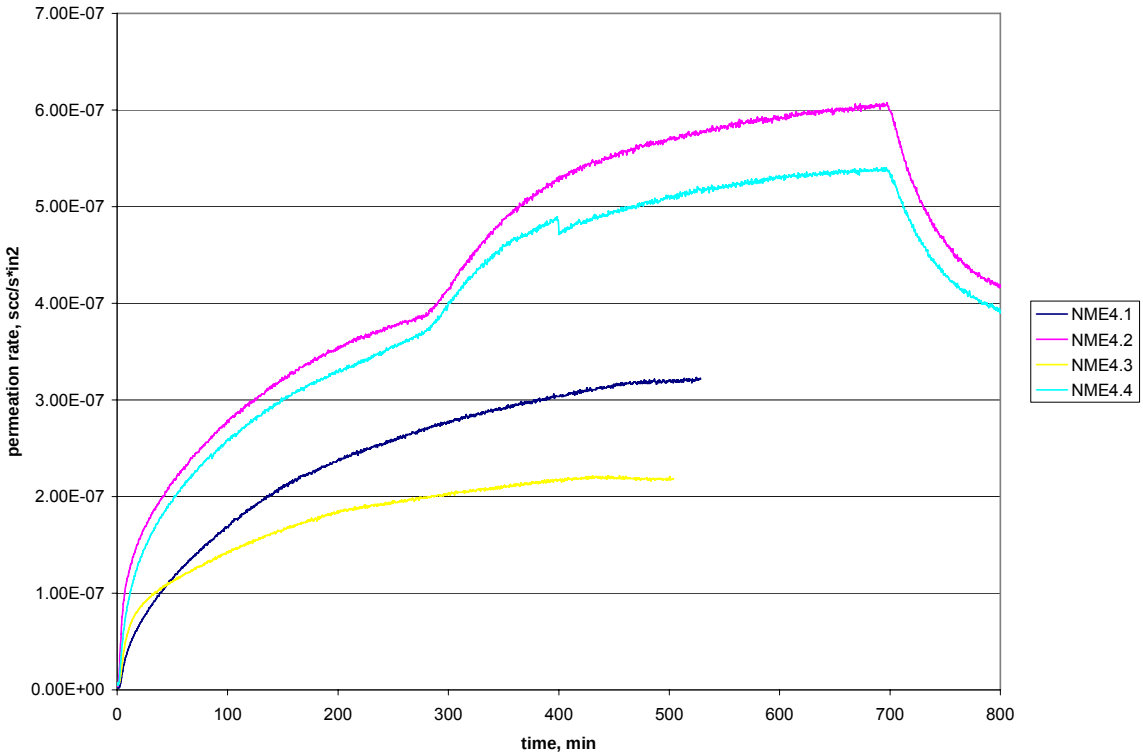

Fig. 5.1.35. Permeation rate of Nomex coated with SilverTip marine epoxy with 4% of Nanocor

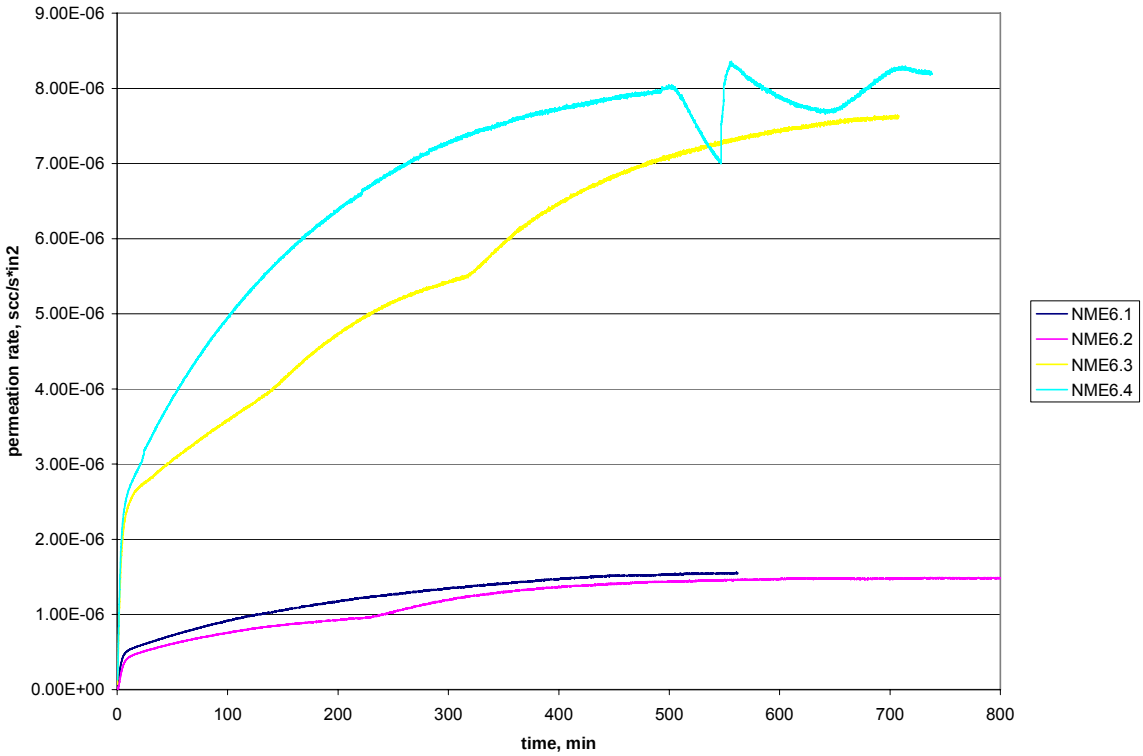

Fig. 5.1.36. Permeation rate of Nomex coated with SilverTip marine epoxy with 6% of Nanocor

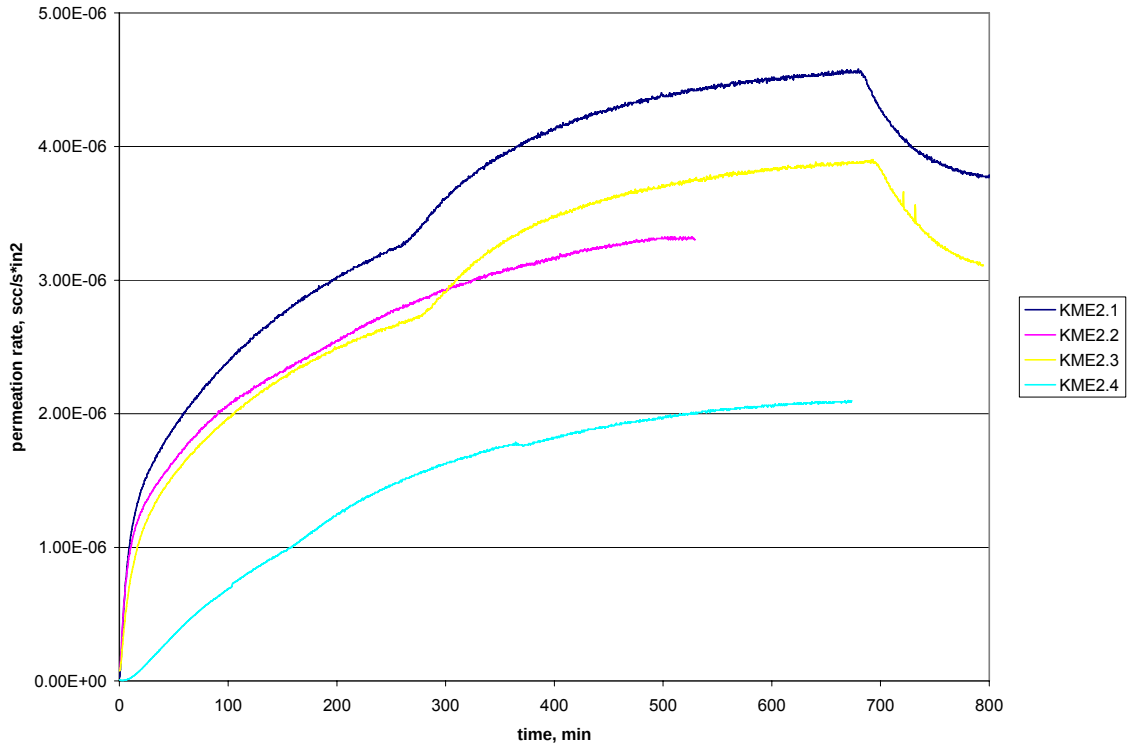

Fig. 5.1.37. Permeation rate of Kevlar coated with SilverTip marine epoxy with 2% of Nanocor

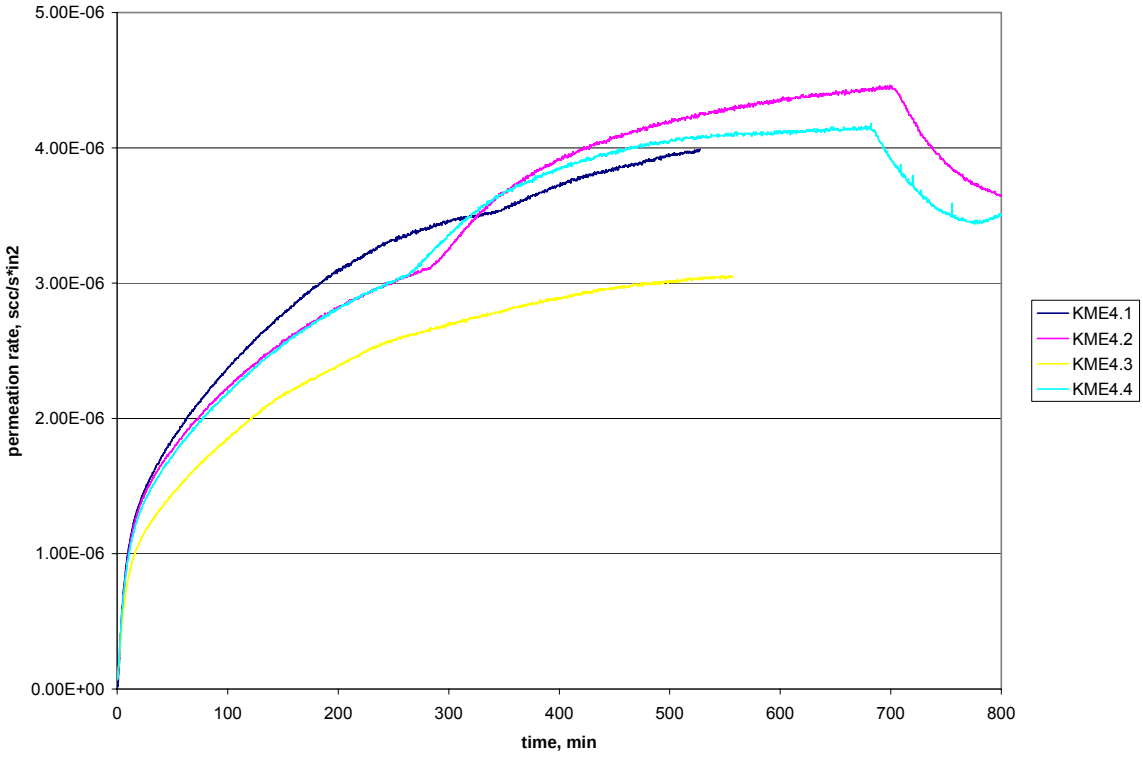

Fig. 5.1.38. Permeation rate of Kevlar coated with SilverTip marine epoxy with 4% of Nanocor

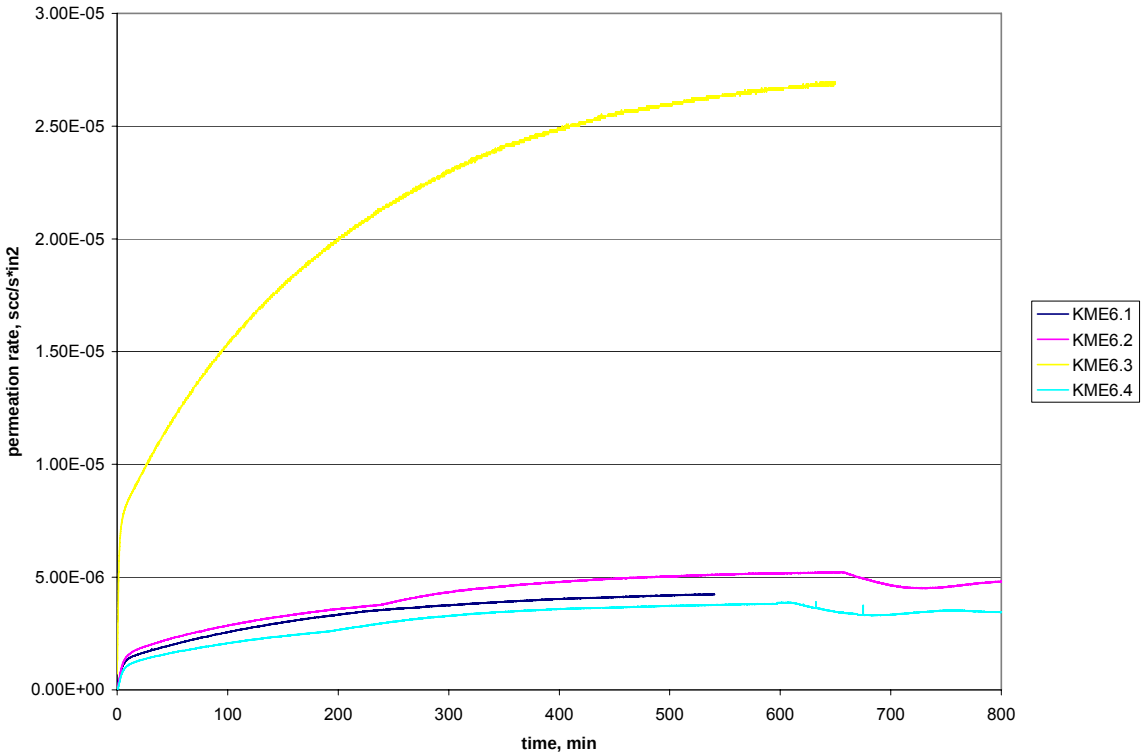

Fig. 5.1.39. Permeation rate of Kevlar coated with SilverTip marine epoxy with 6% of Nanocor

Results of permeability tests of samples with Nanocor show similar behavior as for samples with Bentolite. Majority of permeability rate curves are bent after about 300 minutes. That could be caused by mentioned before effects of membrane bending of samples softened with acetone or creep over long time: change of size and shape of sample structure defects. Samples of both papers coated with epoxy mixed with 6% of Nanocor have the biggest result discrepancy, what could be caused by bad dispersion of too big quantity of nanoclay.

5.1.9. Nomex 2T412 and Kevlar 3.9N636 papers from DuPont coated with med-low viscosity SilverTip Marine Epoxy laminating resin mixed with fast hardener in 2:1 proportion, with 2%, 4%, 6% of Pyrograf III carbon fibers HT grade and acetone added, in following procedure:

- nanoclay sonicated in 10 time bigger amount of acetone for 1 hour
- resin added and mixed with stirring sticks for few minutes
- left in the oven at 60ºC for few hours to evaporate acetone
- resin mixed with hardener with stirring sticks for few minutes
- mixture poured on both sides of papers
- placed between metal plates
- left to dry in room temperature overnight
- final cure in oven at 40ºC for few hours

Table 5.1.9. Sample documentation for aramid papers coated with SilverTip epoxy and Pyrograf

Paper	Remarks Thickness T [in; mm]	Sample Nr	Sample thickness [in]
None	2% of Pyrograf Inlet pressure, 5psi 0.0179; 0.4547	MC2.1	0.0205
		MC2.2	0.017
		MC2.3	0.0161
		MC2.4	0.0194
	4% of Pyrograf Inlet pressure, 5psi 0.0096; 0.2438	MC4.1	0.0084
		MC4.2	0.0106
		MC4.3	0.0103
		MC4.4	0.0097
	6% of Pyrograf Inlet pressure, 5psi 0.0178; 0.4521	MC6.1	0.0193
		MC6.2	0.0179
		MC6.3	0.0182
		MC6.4	0.0174
Nomex 2T412	2% of Pyrograf Inlet pressure, 5psi 0.0147; 0.3734	NMC2.1	0.0149
		NMC2.2	0.01556
		NMC2.3	0.0145
		NMC2.4	0.0133
	4% of Pyrograf Inlet pressure, 5psi 0.0182; 0.4623	NMC4.1	0.0208
		NMC4.2	0.0223
		NMC4.3	0.019
		NMC4.4	0.0155
Kevlar 3.9N636	4% of Pyrograf Inlet pressure, 5psi 0.0356; 0.9042	KMC4.1	0.0406
		KMC4.2	0.0415
		KMC4.3	0.0297
		KMC4.4	0.0415

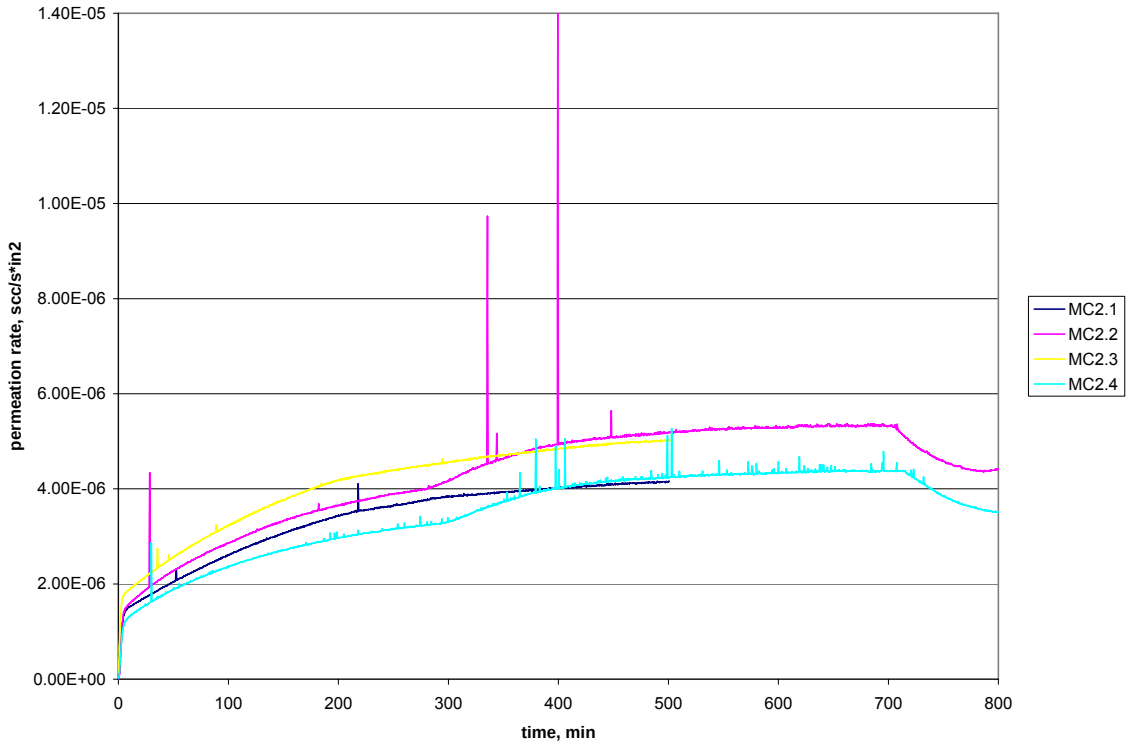

Fig. 5.1.40. Permeation rate of SilverTip marine epoxy with 2% of Pyrograf

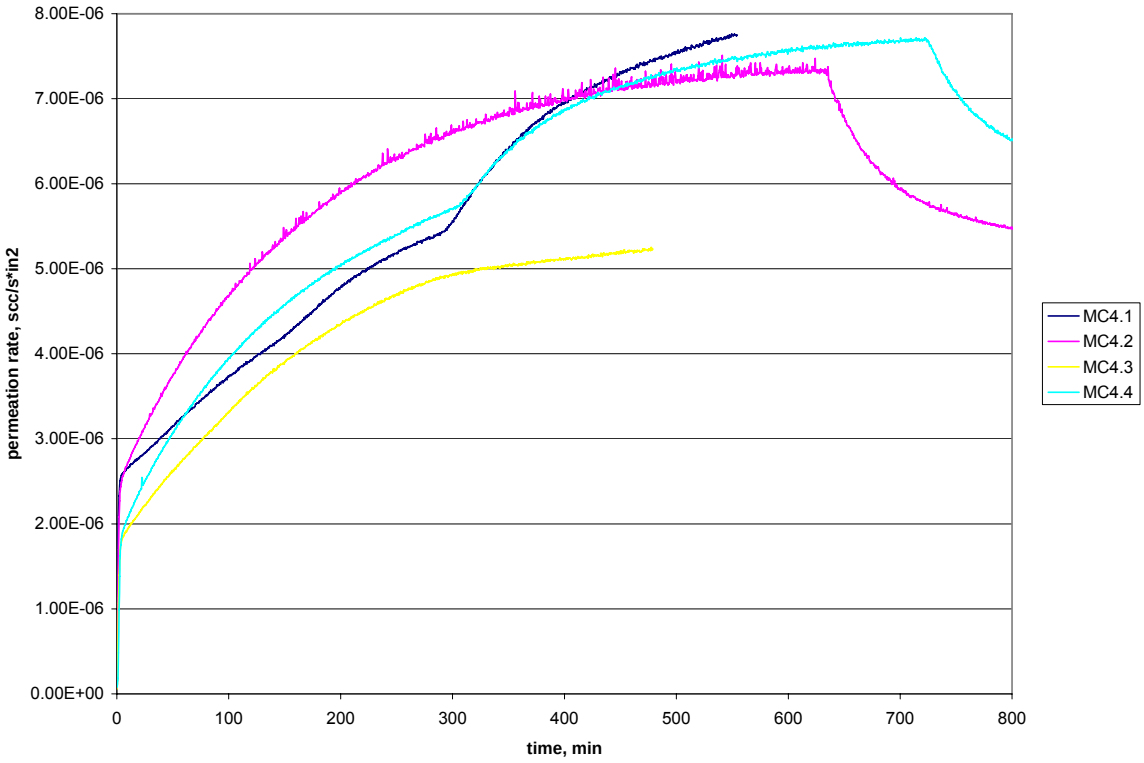

Fig. 5.1.41. Permeation rate of SilverTip marine epoxy with 4% of Pyrograf

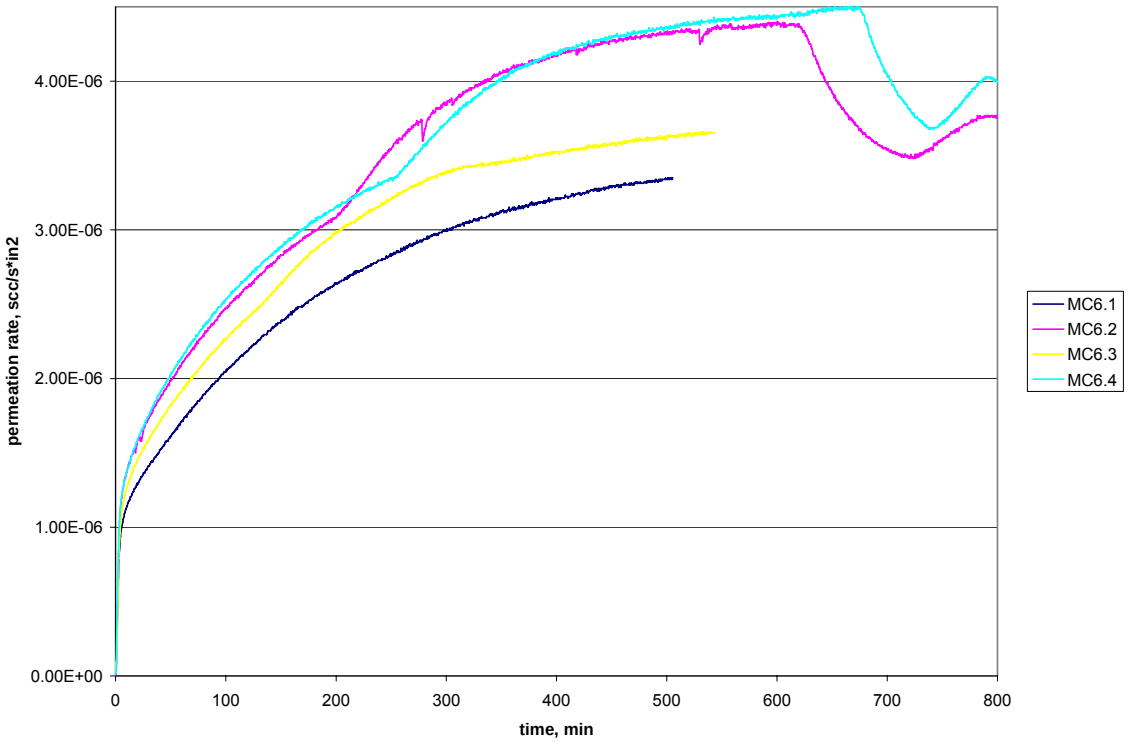

Fig. 5.1.42. Permeation rate of SilverTip marine epoxy with 6% of Pyrograf

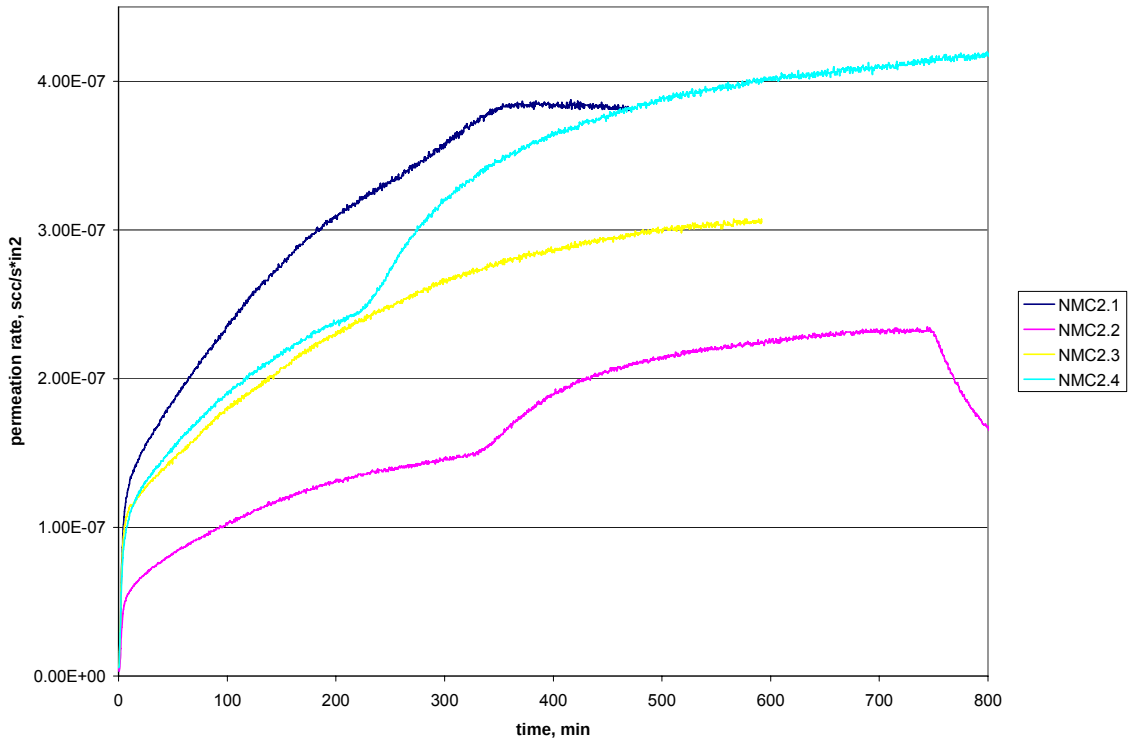

Fig. 5.1.43. Permeation rate of Nomex coated with SilverTip marine epoxy with 2% of Pyrograf

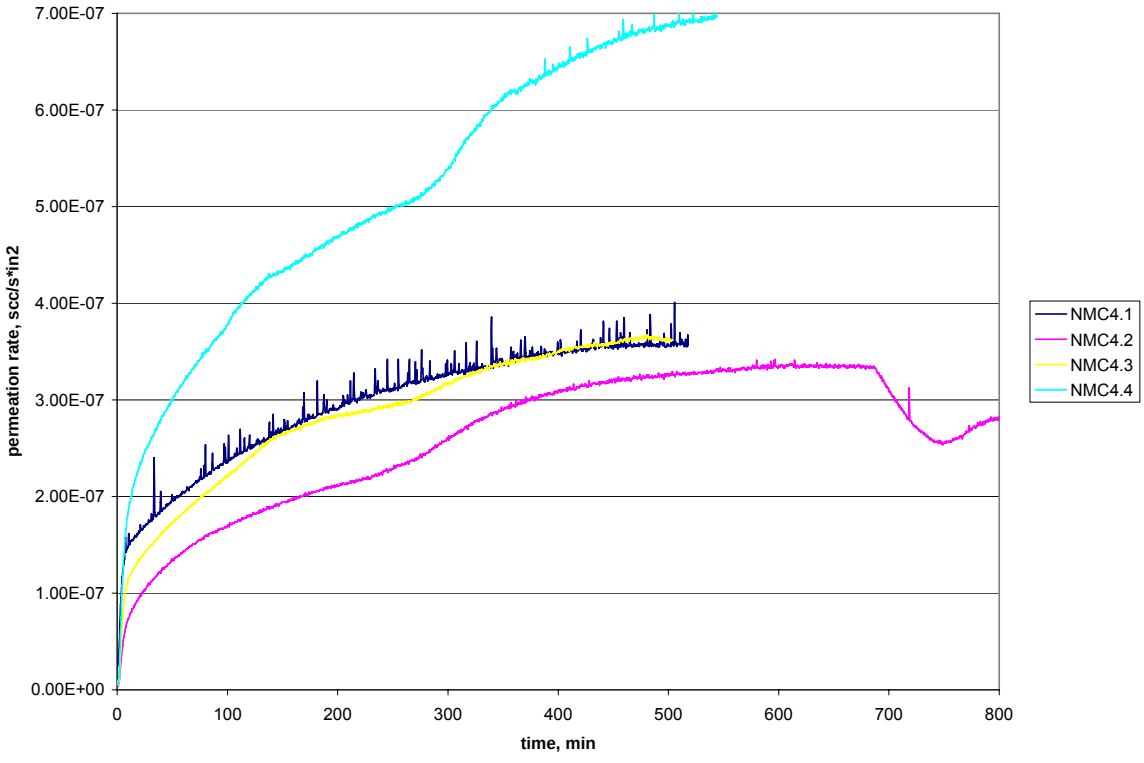

Fig. 5.1.44. Permeation rate of Nomex coated with SilverTip marine epoxy with 4% of Pyrograf

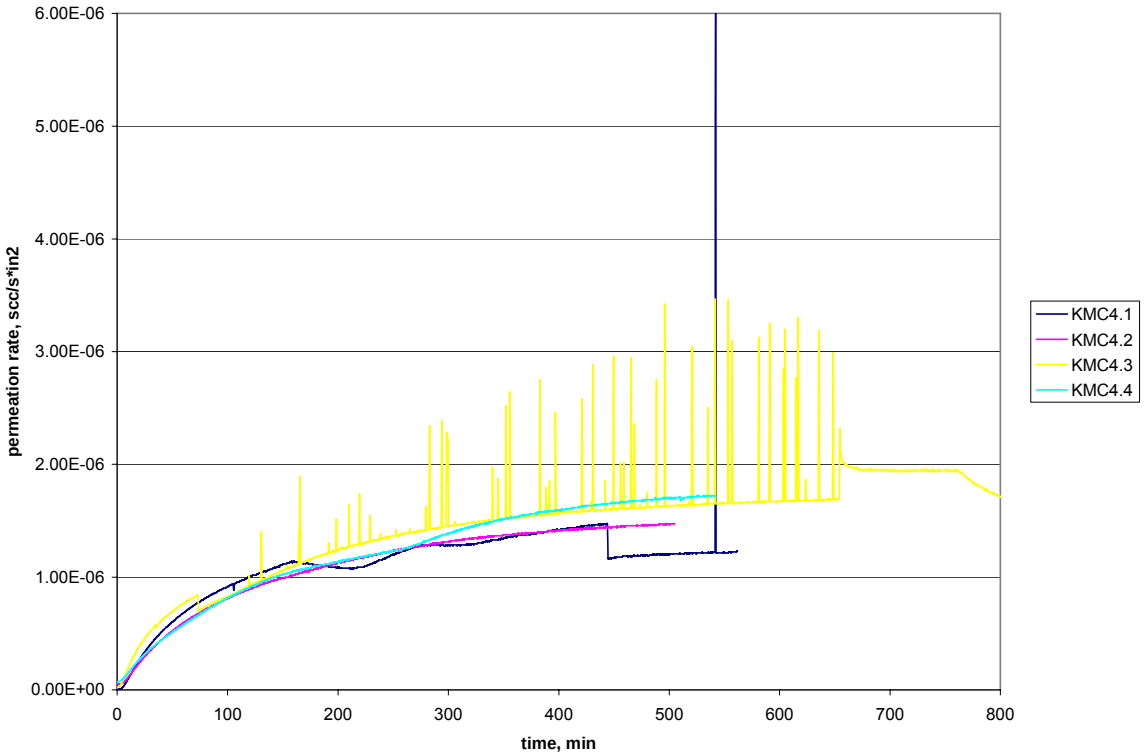

Fig. 5.1.45. Permeation rate of Kevlar coated with SilverTip marine epoxy with 4% of Pyrograf

In case of this grade of carbon nanofibers it was difficult to completely evaporate acetone due to their hygroscopic nature. Some samples air dried during couple of days and became wrinkled. It is advised to totally evaporate the acetone in the oven before mixing resin with hardener to keep the primary shape of final product. Majority of the samples had good nanoparticles dispersion and no visible bubbles. Similarly to permeability rate graphs of samples with Bentolite and Nanocor, curves for samples with Pyrograf are bent, which is typical for samples of epoxy mixed with acetone. Graphs for samples of resin films show good repeatability of curves and only small imperfections, especially for samples of epoxy mixed with 2% of Pyrograf, see Fig. 5.1.40. Also results for both papers coated with 4% of nanofibers show unusual behavior probably caused by existence of air bubbles or pockets in the mixture. According to mixing procedure samples with 4% of nanofibers were manufactured through sonication in twice as big amount of acetone as for samples with 2%, what probably caused existence of bigger surplus of acetone in final product.

5.1.10. Permeability tests results comparison

In the case of current permeability measurements, value obtained from helium leak detector is a flow rate or leak rate Q, and after taking into consideration area of flow, this value is recalculated to presented above permeation rate, which characterizes flow rate density q_{pV} and is pV flow per unit area. From equation 4.16 permeability coefficient, called simply permeability, K_{pV} can be obtained:

$$K_{pV} = q_{pV}\frac{h}{\Delta p} = \frac{Q_{pV}}{A}\frac{h}{\Delta p} \tag{5.1}$$

There are different flow rates used in literature: mass flow rate Q_M, volume flow rate Q_V, molar flow rate Q_N, and pressure-volume product flow rate Q_{pV}. They are used in the same formulae as described above, only the physical meaning and dimensions of corresponding permeability coefficients are different. SI units for the coefficients are:

$$[K_V] = \frac{m^2}{Pa \cdot s}; \quad [K_M] = \frac{kg}{m \cdot Pa \cdot s} = s; \quad [K_{pV}] = \frac{m^2}{s}; \quad [K_N] = \frac{mol}{m \cdot Pa \cdot s} \tag{5.2}$$

The links between different coefficients are:

$$K_M = \rho K_V; \quad K_M = \mu K_N; \quad K_M = \frac{\mu}{RT}K_{pV} \tag{5.3}$$

where ρ, μ are density and molecular mass of penetrating medium. Here T is absolute temperature in K, and R is universal gas constant (R=8.3144 J*mol^{-1}*K^{-1}).

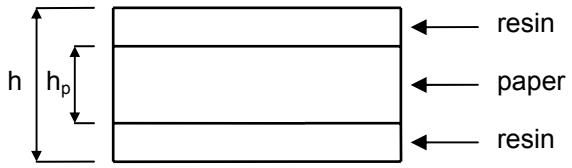

Fig. 5.1.46. Coated paper structure

Assuming that coated paper is a simple laminate structure consisting of layer of aramid paper between two layers of resin as it is showed in Fig. 5.1.46 permeability coefficient and thickness relation can be calculated from equation 4.9. Calculation of that relationship based on permeability coefficients obtained from tests for Nomex coated with epoxy SilverTip shows that:

$$\frac{h_p}{K_p} + \frac{h_r}{K_r} \neq \frac{h}{K}; \qquad h_r = h - h_p \tag{5.4}$$

where superscripts p and r stand for paper and resin respectively. That inequality shows that one of the parameters on the left side of the expression changed during process of coating. Since thickness of the paper and permeability coefficient of resin should not be influenced by manufacturing process the most probable to change is permeability of paper after coating. That agrees with assumption that paper is porous and has been impregnated with resin and changes properties. Based on equation 4.9 permeability coefficient and the accuracy (error) of impregnated paper can be calculated from:

$$K_{ip} = \frac{KK_r h_p}{K_r h - K h_r} = \frac{KK_r h_p}{K_r h + K(h_p - h)} \tag{5.5}$$

$$\Delta K_{ip} = \frac{KK_r h_p (K - K_r)\Delta h + K_r^2 h h_p \Delta K + KK_r h (K_r - K)\Delta h_p + K^2 h_p (h_p - h)\Delta K_r}{\left[K_r h + K(h_p - h)\right]^2} \tag{5.6}$$

The results of calculations of permeability coefficient of impregnated Nomex for different samples can be found in Table 5.1.10 and in Fig. 5.1.47. It is easy to observe that impregnated papers have the best leak resistance properties in the whole structure. The best results were achieved for paper impregnated with epoxy without acetone and mixed with 4% of either nanoparticle. Samples with 2% of carbon nanofibers gave good results as well, while 6% of either Bentolite or Nanocor gave the worst outcome.

Table 5.1.10. Calculated permeability coefficient of impregnated papers

Sample	Thickness h [m]	Standard deviation Δh [m]	Sample perm. K [m^2/s]	Standard deviation ΔK [m^2/s]	Perm. of resin K_r [m^2/s]	Standard deviation ΔK_r [m^2/s]	Perm. of impreg. paper K_{ip} [m^2/s]	Error ΔK_{ip} [m^2/s]
NM1	0.00042	0.00002	$9.46*10^{-14}$	$3.52*10^{-14}$	$1.68*10^{-12}$	$3.31*10^{-13}$	$1.2*10^{-14}$	$6.06*10^{-15}$
NM1a	0.000375	0.000072	$2.53*10^{-13}$	$8.75*10^{-14}$	$1.68*10^{-12}$	$3.31*10^{-13}$	$3.94*10^{-14}$	$2.61*10^{-14}$
NM2	0.000164	0.000036	$3.99*10^{-13}$	$2.83*10^{-13}$	$1.84*10^{-12}$	$3.48*10^{-13}$	$1.45*10^{-13}$	$9.36*10^{-14}$
NMB4	0.000318	0.000085	$9.25*10^{-14}$	$4.82*10^{-14}$	$1.37*10^{-12}$	$1.65*10^{-13}$	$1.57*10^{-14}$	$1.37*10^{-14}$
NMB6	0.000185	0.000035	$7.51*10^{-13}$	$6.48*10^{-14}$	$2.07*10^{-12}$	$1.94*10^{-13}$	$2.79*10^{-13}$	$9.97*10^{-14}$
NME4	0.00054	0.000113	$2.46*10^{-13}$	$6.28*10^{-14}$	$2.23*10^{-12}$	-	$2.57*10^{-14}$	$1.39*10^{-14}$
NME6	0.000194	0.000053	$9.01*10^{-13}$	$5.61*10^{-14}$	$1.4*10^{-12}$	$3.62*10^{-13}$	$4.48*10^{-13}$	$3.59*10^{-13}$
NMC2	0.000361	0.000017	$1.41*10^{-13}$	$3.38*10^{-14}$	$2.51*10^{-12}$	$1.25*10^{-13}$	$2.08*10^{-14}$	$5.24*10^{-15}$
NMC4	0.000493	0.000074	$2.44*10^{-13}$	$5.13*10^{-14}$	$2*10^{-12}$	$3.22*10^{-13}$	$2.82*10^{-14}$	$3.31*10^{-15}$

Thickness of paper h_p=0.0000508m, accuracy Δh_p=0.00000254 m

Addition of acetone caused increase in both permeation rate and permeability coefficient. It can be observed for samples of papers coated with unsaturated polyester: Nomex when comparing NP2 to NP4, Kevlar when comparing KP1 to KP3 and KP4, see Fig. 5.1.48 and 5.1.49. It is strongly visible for samples of marine epoxy SilverTip and papers coated with it, see following Tables and Figures. Since acetone was used for sonication of nanoparticles, effect of addition of nanoparticles can only be evaluated based on results of permeation tests of samples with acetone which are worse than results for samples without any additives. That is why substitution of this diluent by some other or eliminating it can further improve barrier properties of nanocomposites. Especially for samples with Nanocor sonication process could be substituted by mechanical mixing and degassing, what is recommended for future research.

Addition of alcohol gave opposite outcome: decrease of permeation. It can be observed for samples of Nomex coated with fiberglass polyester when comparing NF1 to NF2 and for Kevlar coated with epoxy MAS when KE2 with bigger amount of alcohol has smaller permeability coefficient than KE1.

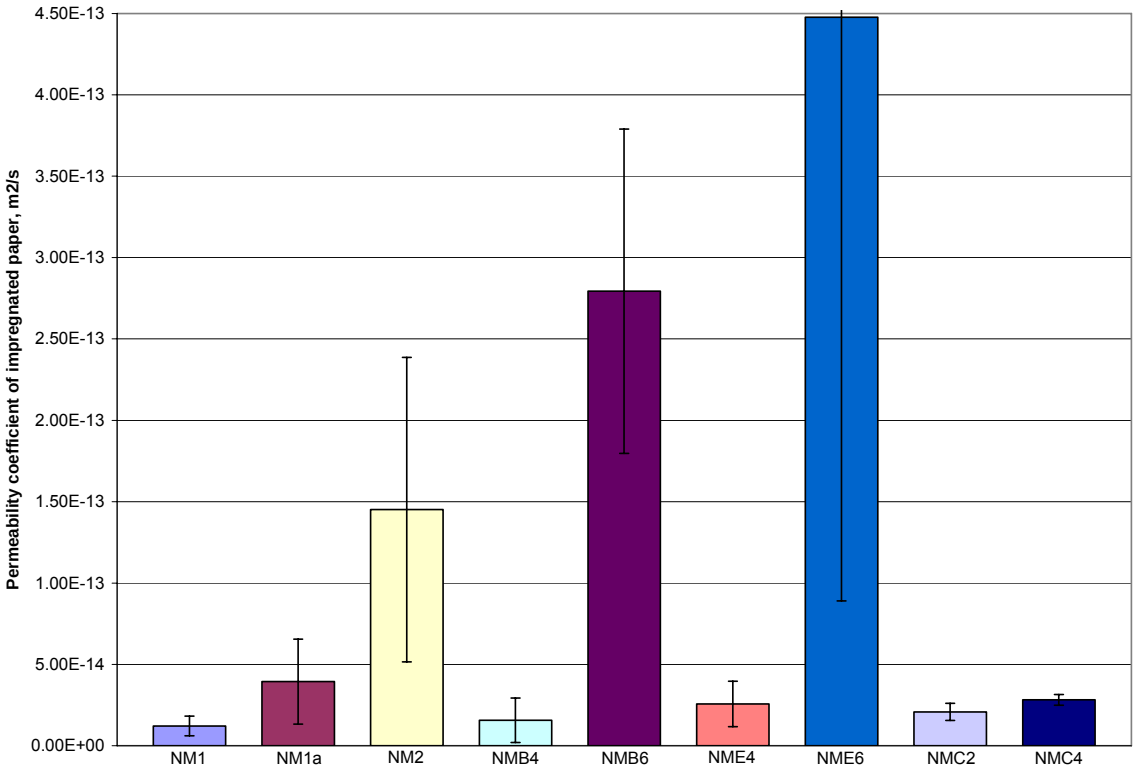

Fig. 5.1.47. Comparison of calculated permeability coefficient of impregnated papers

Fig. 5.1.51 depicts comparison of permeability coefficients of Kapton films and epoxy systems. Kapton films tested at 5psi have similar permeability coefficients depending slightly on film thickness; the thicker the film is the smaller the coefficient. It can be explained through membrane bending analysis. Deflection of circular membrane clamped at the edges is inversely proportional to the thickness squared, and the bigger the deflection the bigger stretching it causes and more gas leaks through. However, permeability coefficient of the thickest film tested at 10psi has bigger coefficient than any other Kapton sample. It also can be explained through membrane bending. Bigger pressures cause bigger deflection and bigger stretching of the film what causes increase in leak path size and quantity; twice as much pressure causes twice as much deflection. Also creep influence is bigger for bigger pressures.

Addition of 4% of Bentolite and 6% of Nanocor to epoxy resin gave improved properties when compared to results of epoxy mixed with acetone as well as epoxy without acetone.

Coated Nomex paper in general gives better barrier properties since it is less permeable to gases itself. When comparing particular paper coated with epoxy mixed with different percentages of particular nanoclay usually 4% of inclusions gives the best results. Only Nomex coated with 2% of Pyrograf showed better barrier properties than for 4% and Kevlar coated with 2% of Nanocor gave permeability coefficient similar to that of Kevlar coated with 4% of the same nanoclay. In general Bentolite gave the biggest improvement of helium barrier properties.

Table 5.1.11. Sample nomenclature and helium permeability test results

Sample	Explanation of sample symbol	Flow rate density (permeation rate) q [Pa*m/s]	Permeability coefficient K [m^2/s]
NP2	Nomex 3T412 coated with unsaturated polyester Bondo, 1psi	$(2.43\pm1.44)*10^{-1}$	$(1.8\pm0.9)*10^{-10}$
NP3	Nomex 3T412 coated with unsaturated polyester Bondo, acetone added	$(2.26\pm2.15)*10^{-4}$	$(5.45\pm5.1)*10^{-13}$
NP4	Nomex 3T412 coated with unsaturated polyester Bondo, acetone added, 1psi	$(2.59\pm0.56)*10^{-1}$	$(1.82\pm0.39)*10^{-10}$
KP1	Kevlar 2.8N636 coated with unsaturated polyester Bondo	$(4.62\pm2.19)*10^{-4}$	$(1.04\pm0.57)*10^{-12}$
KP3	Kevlar 2.8N636 coated with unsaturated polyester Bondo, acetone added	$(9.42\pm1.1)*10^{-4}$	$(1.68\pm0.76)*10^{-12}$
KP4	Kevlar 2.8N636 coated with unsaturated polyester Bondo, acetone added	$(5.89\pm1.67)*10^{-4}$	$(1.67\pm0.52)*10^{-12}$
NF1	Nomex 3T412 coated with fiberglass polyester resin NAPA	$(8.22\pm1.54)*10^{-4}$	$(9.79\pm2.38)*10^{-13}$
NF2	Nomex 3T412 coated with fiberglass polyester resin NAPA, alcohol added	$(7.96\pm3.31)*10^{-5}$	$(1.16\pm0.24)*10^{-13}$
KF1	Kevlar 2.8N636 coated with fiberglass polyester resin NAPA, alcohol added	$(9.03\pm0.87)*10^{-4}$	$(1.06\pm0.23)*10^{-12}$
NE1	Nomex 3T412 coated with low viscosity epoxy MAS	$(5.13\pm1.99)*10^{-4}$	$(3.38\pm1.41)*10^{-13}$
KE1	Kevlar 2.8N636 coated with low viscosity epoxy MAS, alcohol added	$(10.68\pm1.34)*10^{-4}$	$(1.89\pm0.21)*10^{-12}$
KE2	Kevlar 2.8N636 coated with low viscosity epoxy MAS, alcohol added	$(11.73\pm4.82)*10^{-4}$	$(1.04\pm0.36)*10^{-12}$
K50	Kapton 50HN film	$(21.63\pm4.93)*10^{-1}$	$(2.02\pm0.46)*10^{-12}$
K100	Kapton 100HN film	$(10.44\pm0.83)*10^{-1}$	$(1.95\pm0.15)*10^{-12}$
K500 at 5 psi	Kapton 500HN film at 5psi	$(1.81\pm0.62)*10^{-3}$	$(1.69\pm0.58)*10^{-12}$
K500 at 10 psi	Kapton 500HN film at 10psi	$(3.65\pm0.11)*10^{-3}$	$(2.72\pm0.08)*10^{-12}$
N2	Nomex paper 2T412 at 1psi	17.68 ± 2.99	$(8.3\pm1.4)*10^{-9}$
M1	SilverTip Marine Epoxy laminating resin	$(6.9\pm1.39)*10^{-4}$	$(1.68\pm0.33)*10^{-12}$
M2	Marine epoxy, acetone added	$(1.31\pm1.01)*10^{-3}$	$(1.84\pm0.35)*10^{-12}$
NM1	Nomex 2T412 coated with marine epoxy	$(3.09\pm1.19)*10^{-5}$	$(9.46\pm3.52)*10^{-14}$
NM1a	Nomex 2T412 coated with marine epoxy, different sample	$(9.02\pm1.68)*10^{-5}$	$(2.53\pm0.87)*10^{-13}$
NM2	Nomex 2T412 coated with marine epoxy, acetone added	$(3.46\pm2.73)*10^{-4}$	$(3.99\pm2.83)*10^{-13}$
KM1	Kevlar 3.9N636 coated with marine epoxy	$(2.61\pm0.36)*10^{-4}$	$(8.7\pm0.88)*10^{-13}$
KM2	Kevlar 3.9N636 coated with marine epoxy, acetone added	$(2.8\pm1.56)*10^{-4}$	$(9.91\pm5.28)*10^{-13}$

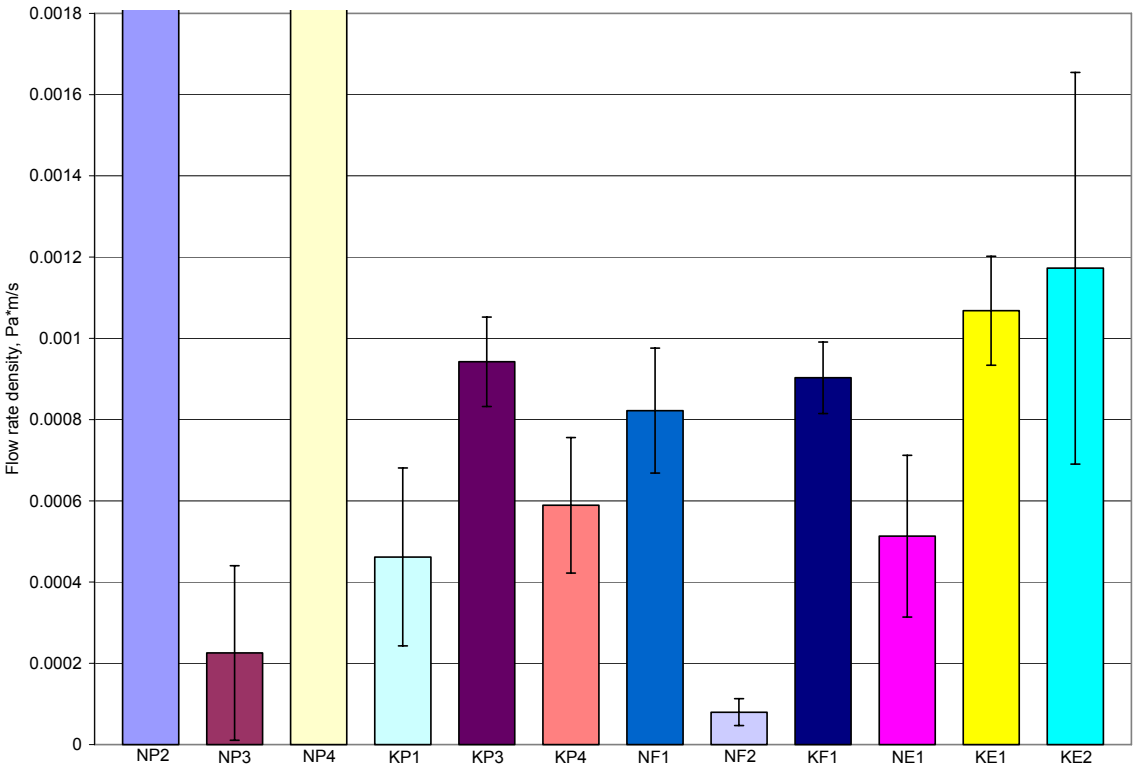

Fig. 5.1.48. Comparison of permeation rate for papers coated with different resins

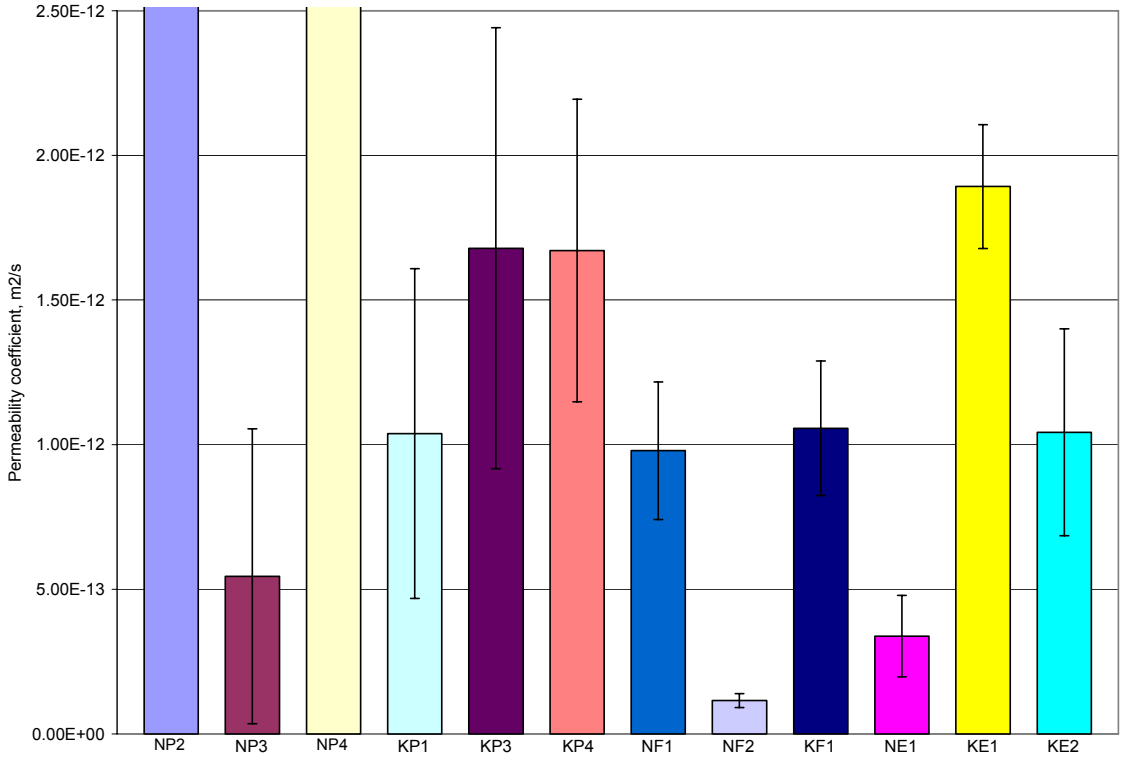

Fig. 5.1.49. Comparison of permeability coefficient for coated aramid papers

Table 5.1.12. Sample nomenclature and helium permeability test results for samples with nanoparticles

Sample	Explanation of sample symbol	Flow rate density (permeation rate) q [Pa*m/s]	Permeability coefficient K [m^2/s]
MB4	Marine epoxy, 4% of Bentoline added	$(6.68\pm2.3)*10^{-4}$	$(1.37\pm0.17)*10^{-12}$
MB6	Marine epoxy, 6% of Bentoline added	$(1.66\pm0.34)*10^{-3}$	$(2.07\pm0.19)*10^{-12}$
NMB2	Nomex 2T412 coated with marine epoxy, acetone, 2% of Bentoline added	$(3.29\pm1.41)*10^{-5}$	$(1.26\pm0.37)*10^{-13}$
NMB4	Nomex 2T412 coated with marine epoxy, acetone, 4% of Bentoline added	$(4.06\pm2.38)*10^{-5}$	$(9.25\pm4.82)*10^{-14}$
NMB6	Nomex 2T412 coated with marine epoxy, acetone, 6% of Bentoline added	$(5.72\pm1.59)*10^{-4}$	$(7.51\pm0.65)*10^{-13}$
KMB2	Kevlar 3.9N636 coated with marine epoxy, acetone, 2% of Bentoline added	$(4.06\pm0.37)*10^{-4}$	$(1.7\pm0.15)*10^{-12}$
KMB4	Kevlar 3.9N636 coated with marine epoxy, acetone, 4% of Bentoline added	$(3.84\pm0.83)*10^{-4}$	$(8.82\pm0.86)*10^{-13}$
KMB6	Kevlar 3.9N636 coated with marine epoxy, acetone, 6% of Bentoline added	$(6.65\pm0.7)*10^{-4}$	$(1.14\pm0.16)*10^{-12}$
ME4	Marine epoxy, 4% of Nanocor added	$1.28*10^{-3}$	$2.23*10^{-12}$
ME6	Marine epoxy, 6% of Nanocor added	$(8.52\pm2.2)*10^{-4}$	$(1.4\pm0.36)*10^{-12}$
NME2	Nomex 2T412 coated with marine epoxy, acetone, 2% of Nanocor added	$(4.98\pm2.45)*10^{-4}$	$(7.41\pm2.99)*10^{-13}$
NME4	Nomex 2T412 coated with marine epoxy, acetone, 4% of Nanocor added	$(6.62\pm2.85)*10^{-5}$	$(2.46\pm0.63)*10^{-13}$
NME6	Nomex 2T412 coated with marine epoxy, acetone, 6% of Nanocor added	$(7.41\pm5.81)*10^{-4}$	$(9.01\pm5.61)*10^{-13}$
KME2	Kevlar 3.9N636 coated with marine epoxy, acetone, 2% of Nanocor added	$(5.45\pm1.65)*10^{-4}$	$(1\pm0.36)*10^{-12}$
KME4	Kevlar 3.9N636 coated with marine epoxy, acetone, 4% of Nanocor added	$(6.15\pm0.95)*10^{-4}$	$(1\pm0.15)*10^{-12}$
KME6	Kevlar 3.9N636 coated with marine epoxy, acetone, 6% of Nanocor added	$(6.29\pm1.65)*10^{-4}$	$(1.12\pm0.37)*10^{-12}$
MC2	Marine epoxy, 2% of Pyrograf added	$(7.42\pm0.88)*10^{-4}$	$(2.51\pm0.12)*10^{-12}$
MC4	Marine epoxy, 4% of Pyrograf added	$(1.1\pm0.19)*10^{-3}$	$(2\pm0.32)*10^{-12}$
MC6	Marine epoxy, 6% of Pyrograf added	$(6.25\pm0.89)*10^{-4}$	$(2.12\pm0.23)*10^{-12}$
NMC2	Nomex 2T412 coated with marine epoxy, acetone, 2% of Pyrograf added	$(5.31\pm1.33)*10^{-5}$	$(1.41\pm0.34)*10^{-13}$
NMC4	Nomex 2T412 coated with marine epoxy, acetone, 4% of Pyrograf added	$(6.99\pm2.68)*10^{-5}$	$(2.44\pm0.51)*10^{-13}$
KMC4	Kevlar 3.9N636 coated with marine epoxy, acetone, 4% of Pyrograf added	$(2.61\pm0.4)*10^{-4}$	$(1.85\pm0.17)*10^{-12}$

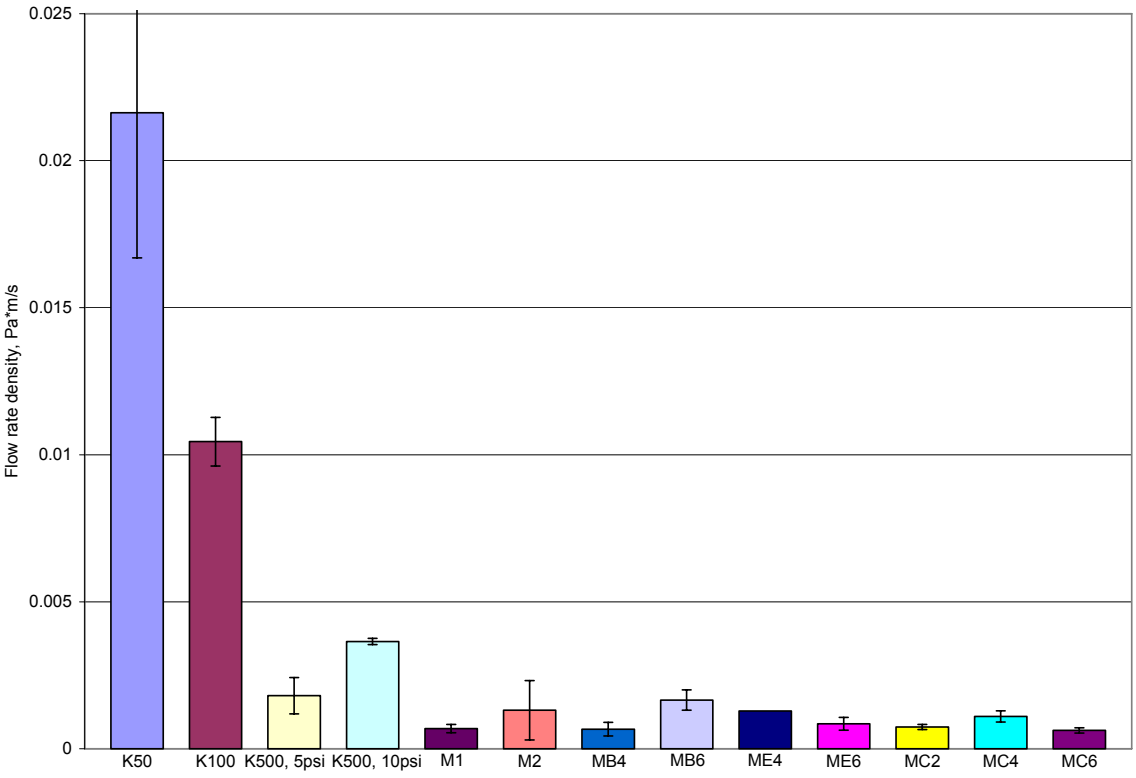

Fig. 5.1.50. Comparison of permeation rate for epoxy resin systems and Kapton films

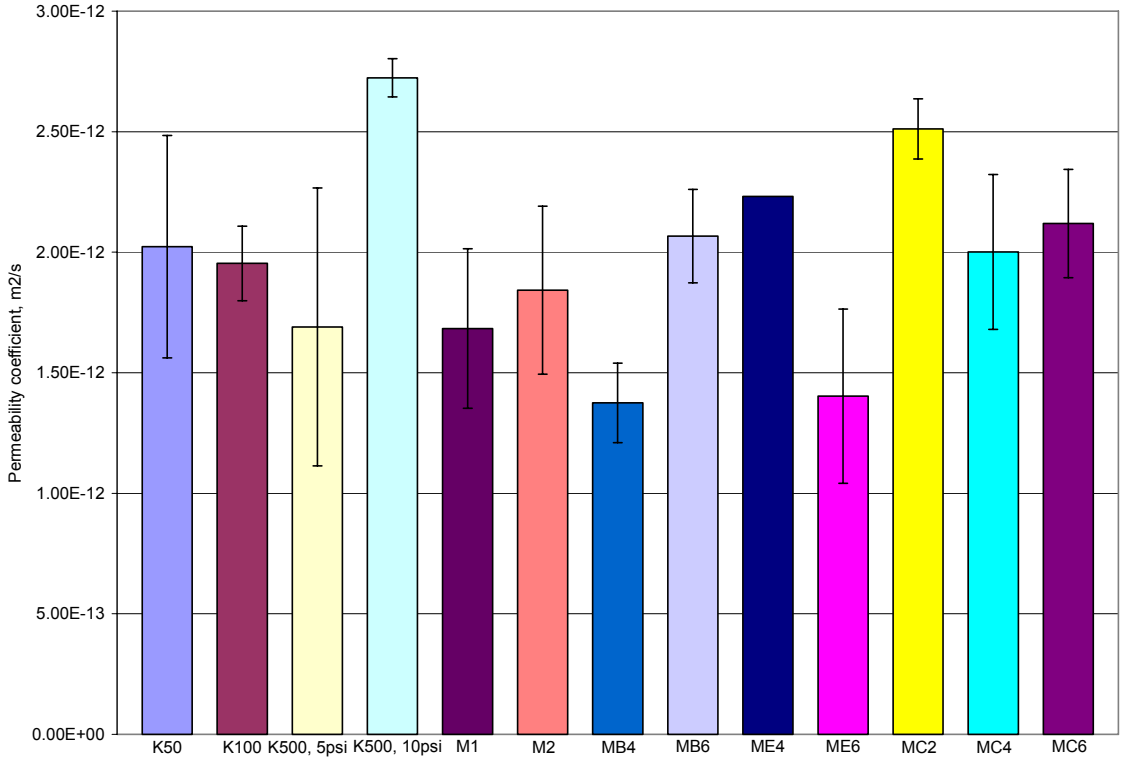

Fig. 5.1.51. Comparison of permeability coefficient for epoxy resin systems and Kapton films

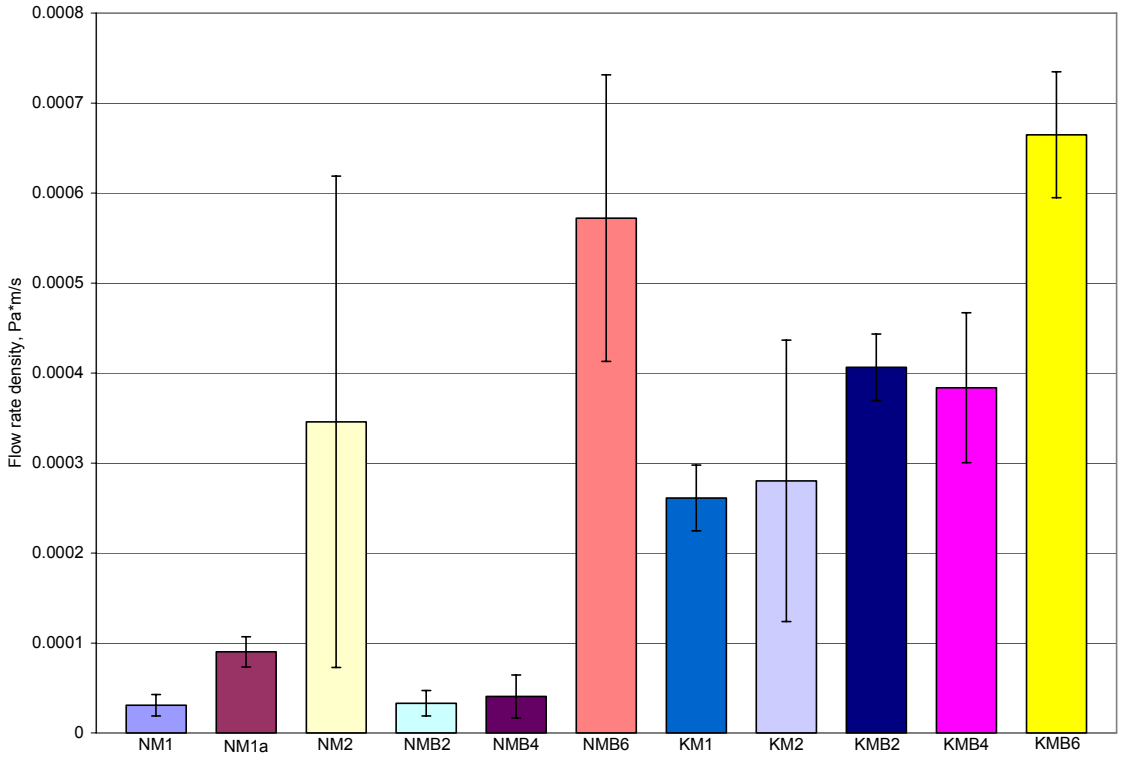

Fig. 5.1.52. Comparison of permeation rate for papers coated with epoxy and Bentolite

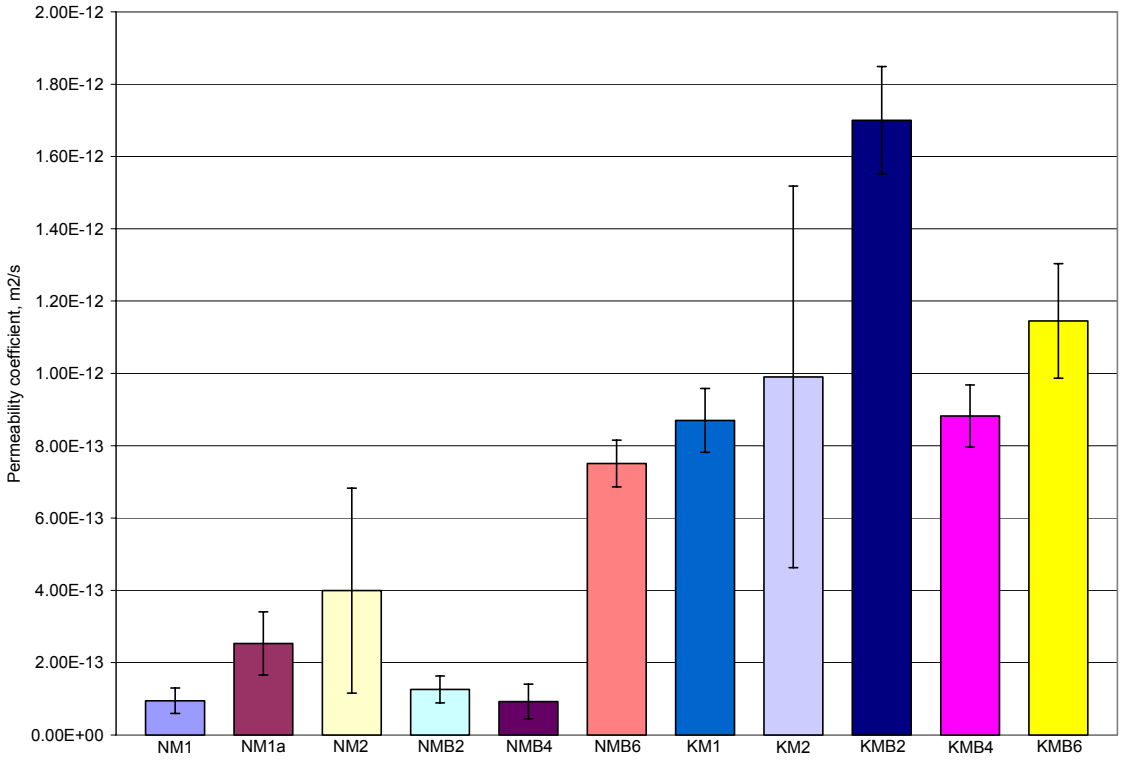

Fig. 5.1.53. Comparison of permeability coefficient for papers coated with epoxy and Bentolite

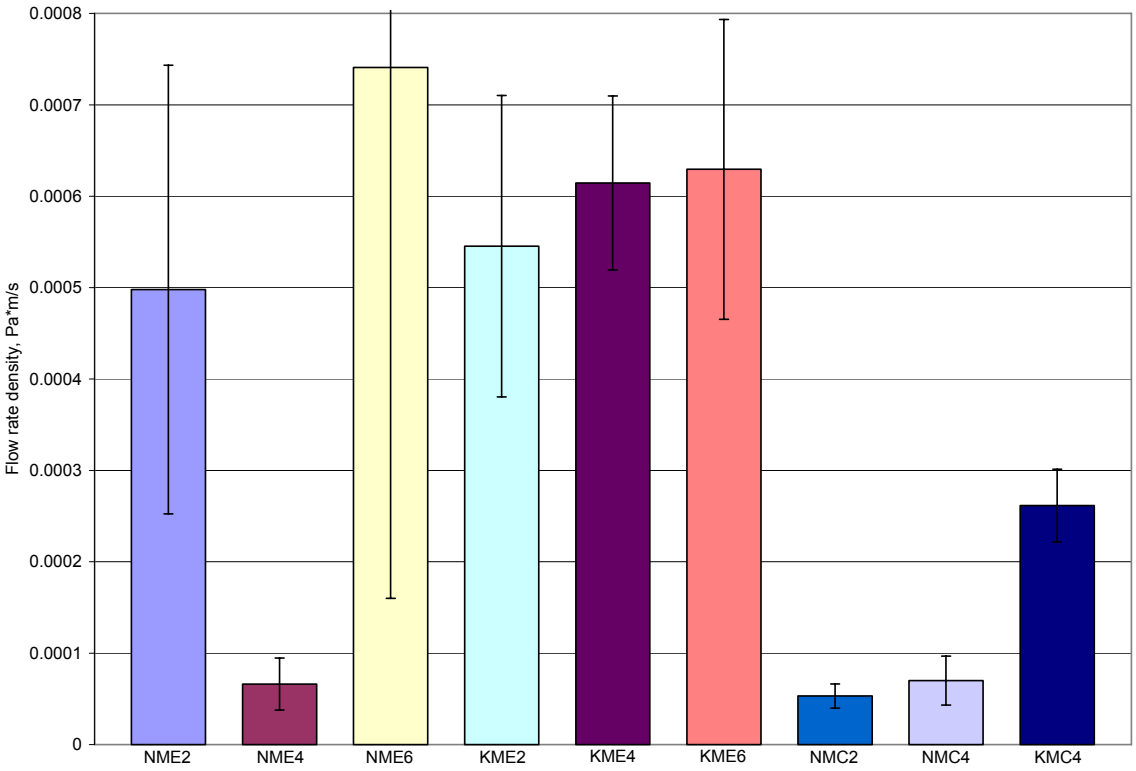

Fig. 5.1.54. Comparison of permeation rate for papers with epoxy, Nanocor, and Pyrograf

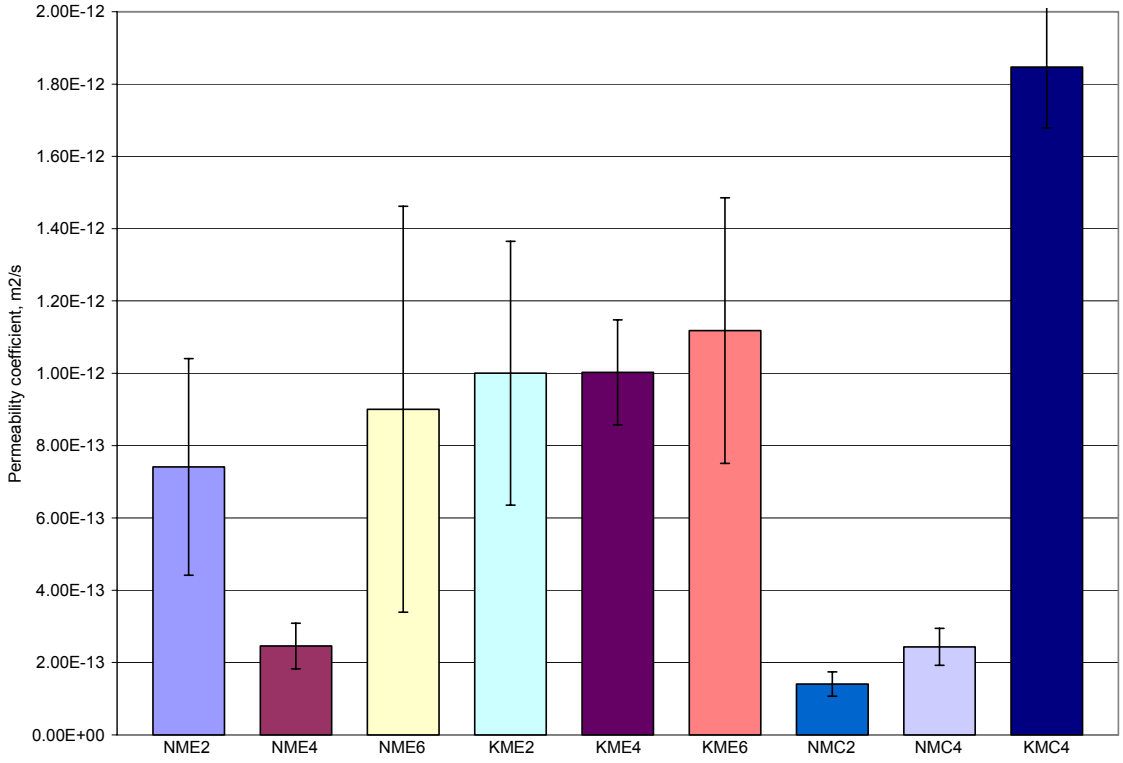

Fig. 5.1.55. Comparison of permeability coefficient for papers with Nanocor and Pyrograf

Table 5.1.13 shows comparison of permeability coefficient obtained from steady state part of leak rate curves and calculations based on derivatives and integrals of these curves. *K(L)*, *K(t*)*, *K(Z')*, and *K(t^)* were calculated using equations 4.30, 4.31, 4.38, and 4.36 respectively. The closest values of *K* were obtained from calculations based on *L*, which is the maximal value of the derivative, obtained from the beginning of the process. But it is still not as precise as traditional method and long-term testing procedure should not be neglected. Calculation of *K(Z')* and *K(t^)* gave much bigger values and should not be considered as a trustful method for calculating permeability coefficient.

All methods used for determination of permeability coefficients have their own negative sides and the results do not match well. It is necessary to mention that determination of low permeability is not easy: difference in few defects or their configurations among parallel samples can change the value of permeability coefficient by several decimal orders. The main method used in this work was based on achieving steady state of permeation; however, this state is reached usually after several hours. Polymer membrane under even small difference of pressures can have significant creep during this time, which causes change of structure of membrane material, and change in defect configuration can significantly affect the results of permeability test. Methods based on differentiation of experimental kinetic curve usually have very low repeatability and small deviation of experimental results can give significant change in the slope of experimental curve. Methods based on using the specific time are also not good because the start time of the process is determined with some error related to the manual procedure. Time *t^* is determined from extrapolation and depends on the slope of the curve. Time *t** is determined from the maximum of the slope, which is very sensitive to experimental errors. Comparison of results shows difference from few percents to change in decimal order. However, because the physical meaning of permeability coefficients found by different methods can be different (characteristic of initial structure of membrane, characteristic of structure after creep, characteristic of dynamics of structural change, etc.), the information obtained from different methods can be useful for analysis and for quantitative comparison of different materials.

Table 5.1.13. Comparison of permeability coefficients obtained from different sources

Sample	K	L	K(L)	t*	K(t*)	Z'	K(Z')	t^	K(t^)
NP4.1	$1.55*10^{-10}$	$2*10^{-6}$	$1.46*10^{-11}$	75	$7.1*10^{-12}$	$6.95*10^{-3}$	$4.9*10^{-12}$	7680	$1.26*10^{-13}$
NP4.2	$2.1*10^{-10}$	$5.17*10^{-6}$	$2.35*10^{-11}$	210	$2.54*10^{-12}$	$1*10^{-2}$	$7.05*10^{-12}$	4830	$2*10^{-13}$
KF1.1	$1.34*10^{-12}$	$8.33*10^{-9}$	$3*10^{-12}$	150	$1.93*10^{-11}$	$3.36*10^{-5}$	$4.4*10^{-14}$	6420	$8.21*10^{-13}$
KF1.2	$1.15*10^{-12}$	$7.1*10^{-9}$	$3.08*10^{-12}$	90	$3.7*10^{-11}$	$2.71*10^{-5}$	$3.8*10^{-14}$	5430	$1.11*10^{-12}$
KF1.3	$8.08*10^{-13}$	$8.67*10^{-9}$	$1.85*10^{-12}$	60	$2.47*10^{-11}$	$2.78*10^{-5}$	$2.6*10^{-14}$	5670	$4.74*10^{-13}$
KF1.4	$9.37*10^{-13}$	$8.87*10^{-9}$	$2.16*10^{-12}$	105	$1.71*10^{-11}$	$2.95*10^{-5}$	$3.03*10^{-14}$	6300	$5.16*10^{-13}$
KE2.1	$1.45*10^{-12}$	$1.62*10^{-8}$	$2.16*10^{-12}$	135	$8.88*10^{-12}$	$5.97*10^{-5}$	$5.02*10^{-14}$	5580	$3.9*10^{-13}$
KE2.3	$8.67*10^{-13}$	$8.33*10^{-9}$	$1.81*10^{-12}$	105	$1.41*10^{-11}$	$3.07*10^{-5}$	$2.87*10^{-14}$	7596	$3.54*10^{-13}$
KE2.4	$8.08*10^{-13}$	$6.63*10^{-9}$	$1.62*10^{-12}$	105	$1.41*10^{-11}$	$2.92*10^{-5}$	$2.73*10^{-14}$	9120	$2.95*10^{-13}$
K50.1	$2.67*10^{-12}$	$5*10^{-7}$	$4.44*10^{-13}$	60	$2.47*10^{-13}$	$9.58*10^{-4}$	$8.96*10^{-14}$	5304	$5.07*10^{-15}$
K50.2	$2.03*10^{-12}$	$4.67*10^{-7}$	$4.29*10^{-13}$	90	$1.64*10^{-13}$	$7.04*10^{-4}$	$6.59*10^{-14}$	6060	$4.44*10^{-15}$
K50.3	$1.73*10^{-12}$	$3.33*10^{-9}$	$3.63*10^{-14}$	75	$1.97*10^{-13}$	$5.98*10^{-4}$	$5.6*10^{-14}$	6252	$4.3*10^{-15}$
K50.4	$1.66*10^{-12}$	$3*10^{-9}$	$3.44*10^{-14}$	60	$2.47*10^{-13}$	$5.86*10^{-4}$	$5.48*10^{-14}$	7578	$3.55*10^{-15}$
K500.5	$2.71*10^{-12}$	$5.83*10^{-8}$	$4.28*10^{-12}$	120	$1.23*10^{-11}$	$1.18*10^{-4}$	$8.82*10^{-14}$	6984	$3.85*10^{-13}$
K500.6	$2.75*10^{-12}$	$7*10^{-8}$	$4.69*10^{-12}$	105	$1.41*10^{-11}$	$1.17*10^{-4}$	$8.73*10^{-14}$	4824	$5.57*10^{-13}$
K500.7	$2.62*10^{-12}$	$7.3*10^{-8}$	$4.79*10^{-12}$	90	$1.64*10^{-11}$	$1.14*10^{-4}$	$8.52*10^{-14}$	5442	$4.94*10^{-13}$
K500.8	$2.81*10^{-12}$	$7.33*10^{-8}$	$4.8*10^{-12}$	75	$1.97*10^{-11}$	$1.17*10^{-4}$	$8.71*10^{-14}$	3420	$7.86*10^{-13}$
NME6.1	$3.85*10^{-13}$	$1.6*10^{-9}$	$1.76*10^{-12}$	120	$3.56*10^{-11}$	$4.87*10^{-3}$	$7.75*10^{-12}$	6960	$1.12*10^{-12}$
NME6.2	$4.49*10^{-13}$	$1.47*10^{-9}$	$2.22*10^{-12}$	132	$4.67*10^{-11}$	$4.67*10^{-3}$	$8.91*10^{-12}$	9420	$1.19*10^{-12}$
NME6.3	$1.32*10^{-12}$	$1.01*10^{-8}$	$2.56*10^{-12}$	60	$3.44*10^{-11}$	$2.35*10^{-3}$	$2.59*10^{-12}$	9936	$3.77*10^{-13}$
NME6.4	$1.45*10^{-12}$	$1.18*10^{-8}$	$2.84*10^{-12}$	78	$2.73*10^{-11}$	$2.48*10^{-3}$	$2.78*10^{-12}$	6194	$6.25*10^{-13}$
KME6.1	$9.84*10^{-13}$	$5.2*10^{-9}$	$2.85*10^{-12}$	96	$3.85*10^{-11}$	$1.31*10^{-2}$	$1.94*10^{-11}$	6409	$1.05*10^{-12}$
KME6.2	$1.63*10^{-12}$	$5*10^{-9}$	$4.34*10^{-12}$	96	$6.93*10^{-11}$	$1.56*10^{-2}$	$3.09*10^{-11}$	7227	$1.67*10^{-12}$
KMB6.4	$1.1*10^{-12}$	$4.2*10^{-9}$	$3.48*10^{-12}$	114	$4.88*10^{-11}$	$1.13*10^{-2}$	$2.05*10^{-11}$	6546	$1.54*10^{-12}$

Units: K [m^2/s], t [sec], L [$Pa*m/s^2$], Z' [Pa*m/s]

5.2. Flammability Tests

Cone calorimeter allows to test materials and to receive complete information about burning process. All the samples tested earlier for gas permeability, together with Kevlar fabric, were tested here and most of the results are presented in Tables and Figures. Documentation of Kevlar fabric samples, uncoated and coated with epoxy resin, can be found in Table 5.2.1. Resin films, uncoated and coated papers and fabric were cut into squares and stuck together in few layers depending on thickness. Number of layers, thickness, weight, resin content and mass loss can be found in Table 5.2.2. Table 5.2.3 and following Figures show quantitative comparison of results characteristic for flammability test.

Burning time depends on sample size and is shorter for small samples. It is easier to compare burning time per unit mass, see Fig. 5.2.3 and 5.2.4 showing that uncoated papers and fabric, and Kapton film need more time to burn out. Addition of nanoparticles makes burning faster probably because there is less resin in the system, however addition of 6% of nanoclay gives longer burning time then 4% probably because such amount of clay starts to act as flame retardant material or separates masses of resin. Ignition time for uncoated papers and fabric, and Kapton film is much bigger when compared to all other samples, see Fig. 5.2.5. It is difficult to detect any influence of addition of nanoparticles on ignition time. Comparisons of total heat release (THR) and THR per unit mass show small values for uncoated papers, fabric, pure resins, and Kapton film. Summarizing of results for papers and resins alone in Fig. 5.2.9 does not give values for coated papers, which means that impregnated papers burn easier and faster. Addition of nanoclays reduced THR, especially for samples with 4 and 6% of both Bentolite and Nanocor with exception of epoxy film with 6% of Bentolite, see Fig. 5.2.10. Comparisons of heat release rate (HRR) and peak of HRR (PHRR) depict small values for papers, fabric, and Kapton, and big ones for pure polyester resin and Kevlar fabric coated with epoxy. Influence of addition of nanoparticles on PHRR values can be found in Fig. 5.2.14, where nanoclays Bentolite and Nanocor reduce the values with exception of epoxy film with 6% of Bentolite, while nanofibers Pyrograf increase them. Graphs of effective heat of combustion (EHC) and peak of EHC (PEHC) show that unmixed materials (papers, fabric, and resins separately) give smaller values with exception for PEHC value for pure epoxy, see Fig. 5.2.17. Influence of addition of nanoparticles on values of EHC and PEHC is difficult to be evaluated and discussed.

Table 5.2.1. Sample documentation for Kevlar fabric

Material		Remarks Thickness T [in, mm]	Sample number	Sample thickness [in]
Fabric	Resin			
Kevlar fabric	None	Yellow	Kf	0.016
	Epoxy SilverTip	Yellow fabric in transparent epoxy 0.017; 0. 4318	KfM.1	0.017
			KfM.2	0.016

Table 5.2.2. Flammability test sample dimensions

Symbol	# of layers	Mass [g]	Mass loss [%]	Thickness [mm]	Resin content by thickness [%]	Resin content by mass [%]
N2	6	3	42	0.33	0	0
	6	3	10	0.34	0	0
K2	6	5	11	0.56	0	0
	6	5	16	0.58	0	0
NP3	3	9	80	0.88	74	82
KP1	3	6	92	0.53	57	68
	3	7	100	0.67	66	72
KP3	3	6	77	0.61	63	68
	3	4	70	0.51	55	51
KP4	3	11	75	1.3	82	82
	3	13	73	1.13	80	85
F1	3	5	-	0.39	100	100
	3	5	62	0.41	100	100
NF1	3	4	63	0.5	54	59
NF2	3	11	78	0.96	76	85
KF1	3	6	71	0.45	49	68
	3	7	61	0.57	60	72
E1	3	3	57	0.27	100	100
NE1	3	4	50	0.35	35	59
KE1	3	6	72	0.77	70	68
	3	6	63	0.76	70	68
KE2	3	4	53	0.42	46	51
	3	4	60	0.37	38	51
Kf	1	4	23	0.4	0	0
KfM	1	5	72	0.44	9	8
	1	5	48	0.44	9	8
K500	3	5	10	0.38	100	100
	3	5	4	0.38	100	100
M2	4	11	100	1.12	100	100
	4	11	95	1.22	100	100
KM1	3	11	100	1.22	77	77
	3	11	100	1.19	76	77
NM2	3	11	100	1.11	85	86
	3	11	-	1.17	86	86
MB4	3	8	-	0.86	100	100
MB6	3	9	99	0.81	100	100
NMB6	2	7	75	0.75	85	86
	2	8	94	0.76	86	88
KMB6	2	5	88	0.54	65	67
	2	5	90	0.53	64	67
NME2	3	5	84	0.56	71	70
	3	7	75	0.63	74	79
KME2	3	10	81	0.89	68	75
KME4	3	8	55	0.65	56	69
KME6	3	8.5	56	0.66	57	71
MC4	2	8	90	0.78	100	100
MC6	2	8	100	0.72	100	100
	2	9	-	0.74	100	100

Table 5.2.3. Flammability test results for aramid papers coated with different resins

Symbol	Burning time [s]	Ignition time [s]	THR [MJ/m^2]	HRR [kW/m^2]	PHRR [kW/m^2]	at time [s]	EHC [MJ/kg]	PEHC [MJ/kg]	at time [s]
N2	50	11	1.03	40.59	83.81	30	8.89	40.96	30
	109	47	0.04	0.33	2.89	75	1.21	0.09	85
K2	120	74	0.62	17.43	47.06	110	10.36	34.39	105
	115	72	1.07	35.72	72.41	105	-	-	-
NP3	146	4	16.8	124.17	399.64	40	21.15	77.30	65
KP1	123	5	11.39	94.85	328.83	40	18.62	77.22	60
	134	5	15.15	121.18	310.49	35	18.53	64.85	35
KP3	84	5	10.16	135.45	306.36	25	18.94	53.28	65
	70	3	6.4	106.55	252.12	25	21.69	70.76	45
KP4	109	4	17.71	177.07	418.2	30	18.84	64.85	90
	129	7	21.18	184.13	366.94	30	19.54	71.7	90
F1	42	2	6.82	227.33	520.05	25	12.38	58.15	25
	35	3	3.43	171.66	481.3	25	9.46	35.88	20
NF1	50	2	6.4	158.71	315.48	25	19.19	76.78	35
NF2	111	5	19.8	197.81	440.59	45	21.35	63.96	80
KF1	66	5	8.78	159.6	286.84	40	17.54	50.52	45
	72	5	9.22	153.62	301.42	25	19.46	70.37	50
E1	23	2	0.96	95.51	368.86	15	4.11	61.42	15
NE1	35	2	2.5	127.19	305.98	25	10.29	15.04	20
KE1	58	4	10.67	236.9	430.75	35	23.52	53.61	40
	62	3	11.22	224.15	418.98	35	24.02	57.36	40
KE2	50	8	5.06	168.21	323.32	30	22.47	66.95	35
	57	5	5.9	147.41	306.85	30	21.85	68.72	35
Kf	96	43	1.4	35.53	74.88	70	13.95	30.46	75
KfM	49	2	9.75	278.21	730.4	25	27.71	57.03	35
	46	2	7.38	245.69	571.45	30	19.81	65.35	25
K500	175	123	0.12	2.92	9.31	165	2.13	4.62	165
	106	64	0.09	2.52	4.58	80	3.33	38.49	85
M2	339	2	31.33	105.14	1135	38	22.73	77	80
	139	3	27.42	219.29	988.17	40	23.45	73.47	50
KM1	247	3	31.34	265.51	1191.7	28	26.19	56.6	38
	119	4	28.35	253.09	680.55	22	22.76	71.14	70
NM2	370	3	27.25	83.05	927.96	34	22.49	72.51	40
	382	3	28.14	75.22	769.54	36	-	-	-
MB4	93	4	19.5	218.57	796.82	29	-	-	-
MB6	164	1	24.8	152.18	1198.1	31	23.87	75.49	35
NMB6	59	2	14.28	250.46	713.75	26	24.03	76.49	33
	207	4	20.26	99.78	866.68	31	24.32	77.97	54
KMB6	58	1	10.38	178.92	453.44	20	20.8	72.46	31
	62	4	11.04	190.22	452.14	28	21.54	76.6	29
NME2	42	1	10.59	258.11	653.08	23	19.86	78.72	27
	47	2	13.59	301.82	690.94	28	20.93	77.03	33
KME2	162	4	20.2	128.05	419.33	35	22.68	71.18	45
KME4	61	3	10.3	176.9	343.95	21	20.20	75.56	29
KME6	70	1	11.8	170.28	346.5	34	21.96	74.08	60
MC4	97	3	22	234.07	1276.2	28	28.31	75.57	65
MC6	122	4	22.62	200.12	1073.9	30	17.3	58.13	25
	69	3	20.81	315.21	1095.6	29	-	-	-

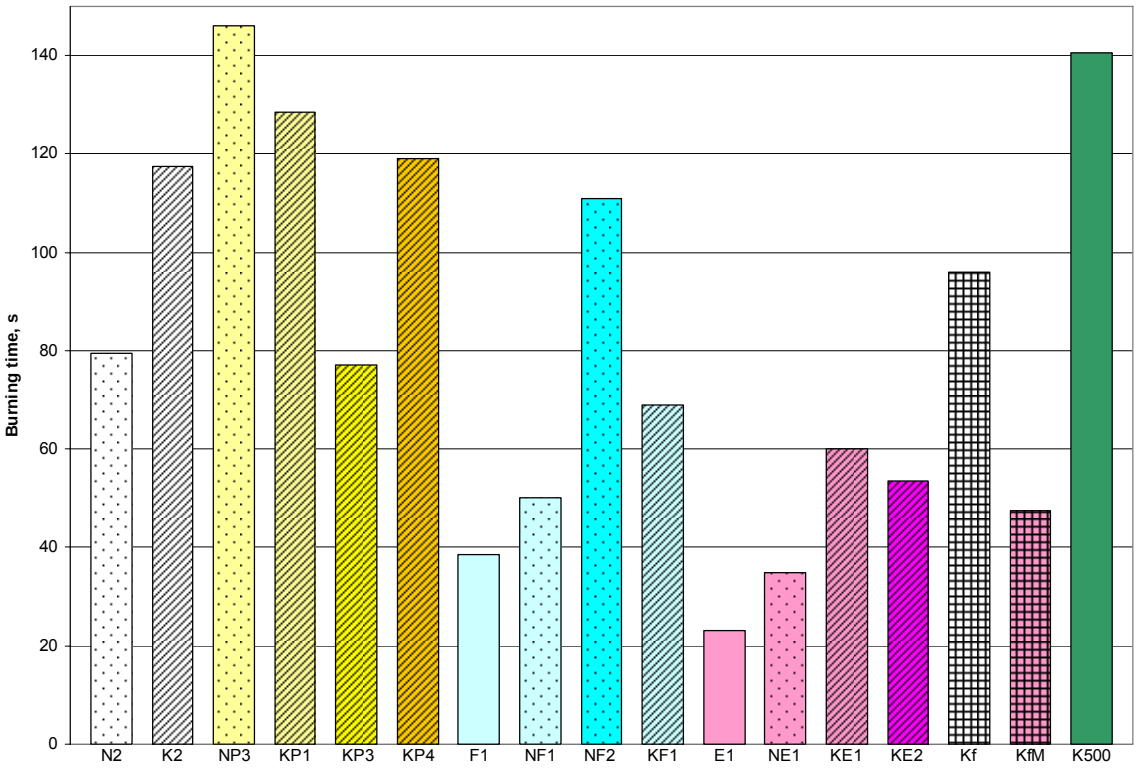

Fig. 5.2.1. Comparison of burning time of aramid papers coated with different resins

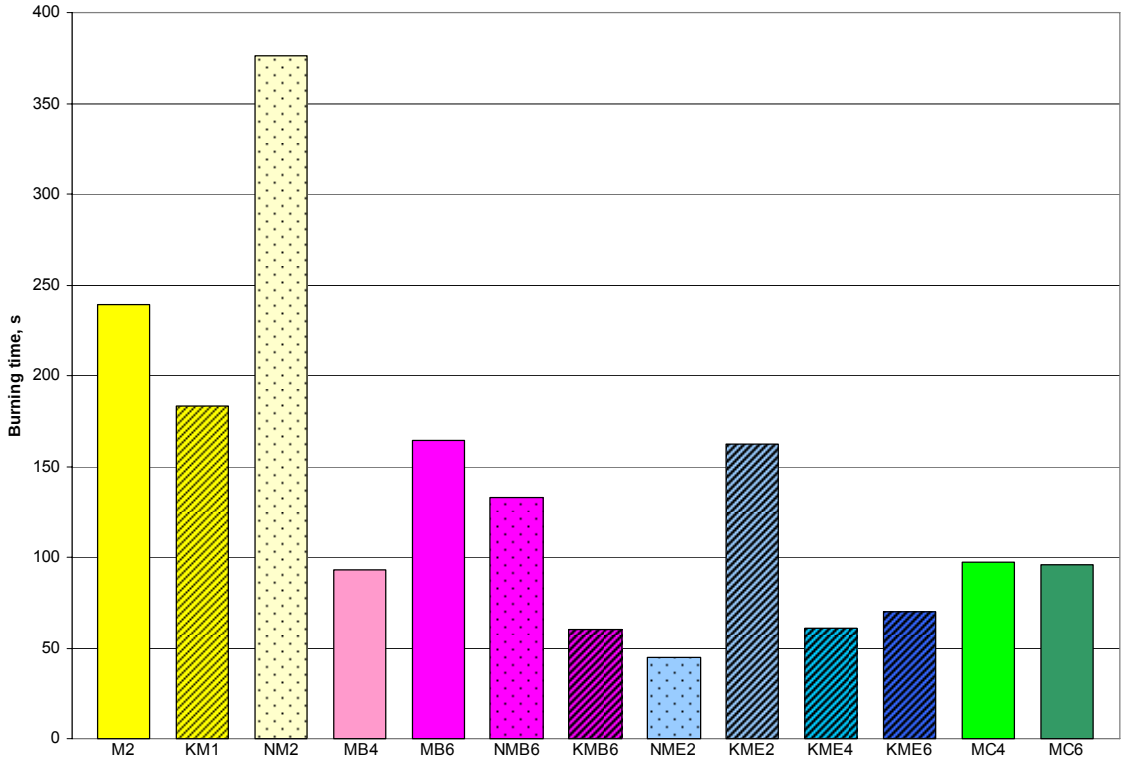

Fig. 5.2.2. Comparison of burning time of epoxy systems with nanoparticles

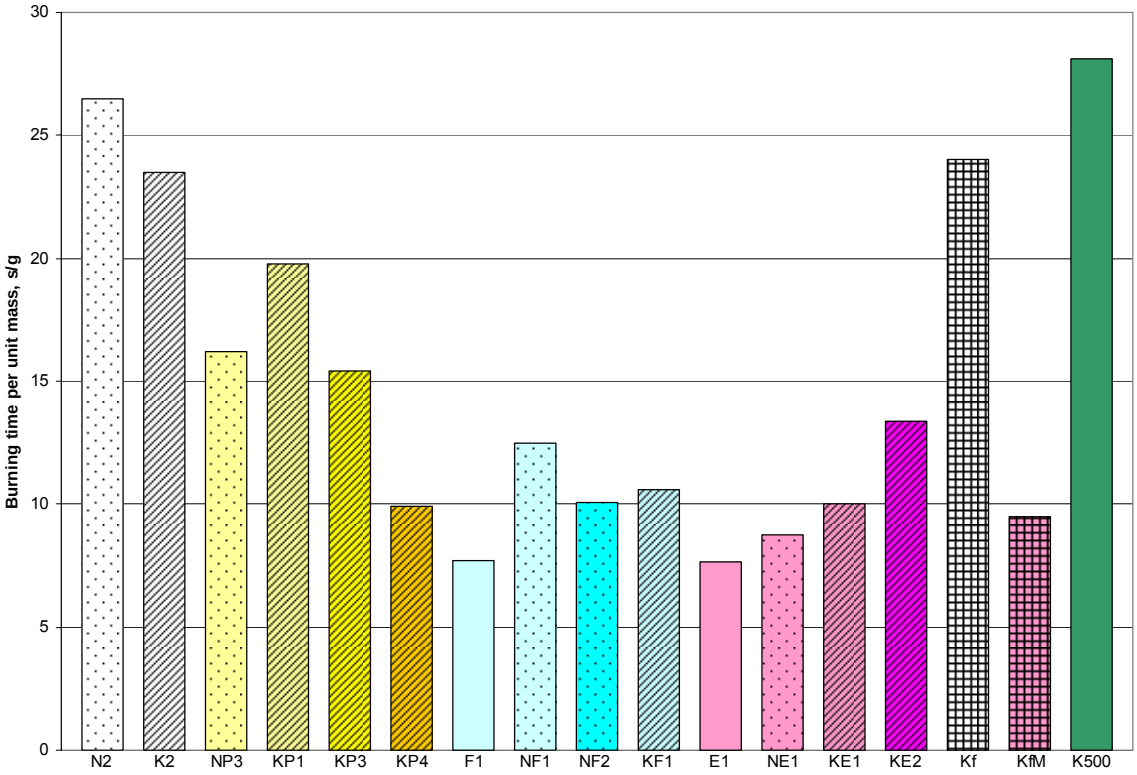

Fig. 5.2.3. Comparison of burning time per unit mass for coated aramid papers

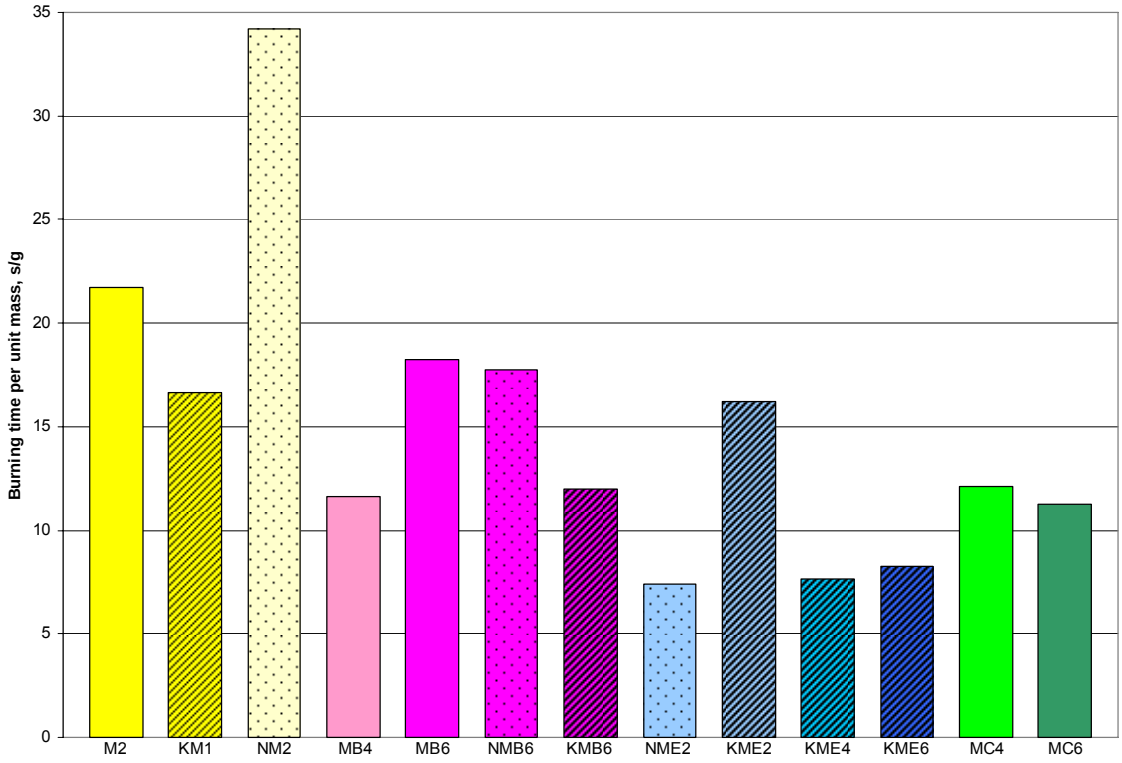

Fig. 5.2.4. Comparison of burning time per unit mass for epoxy systems with nanoparticles

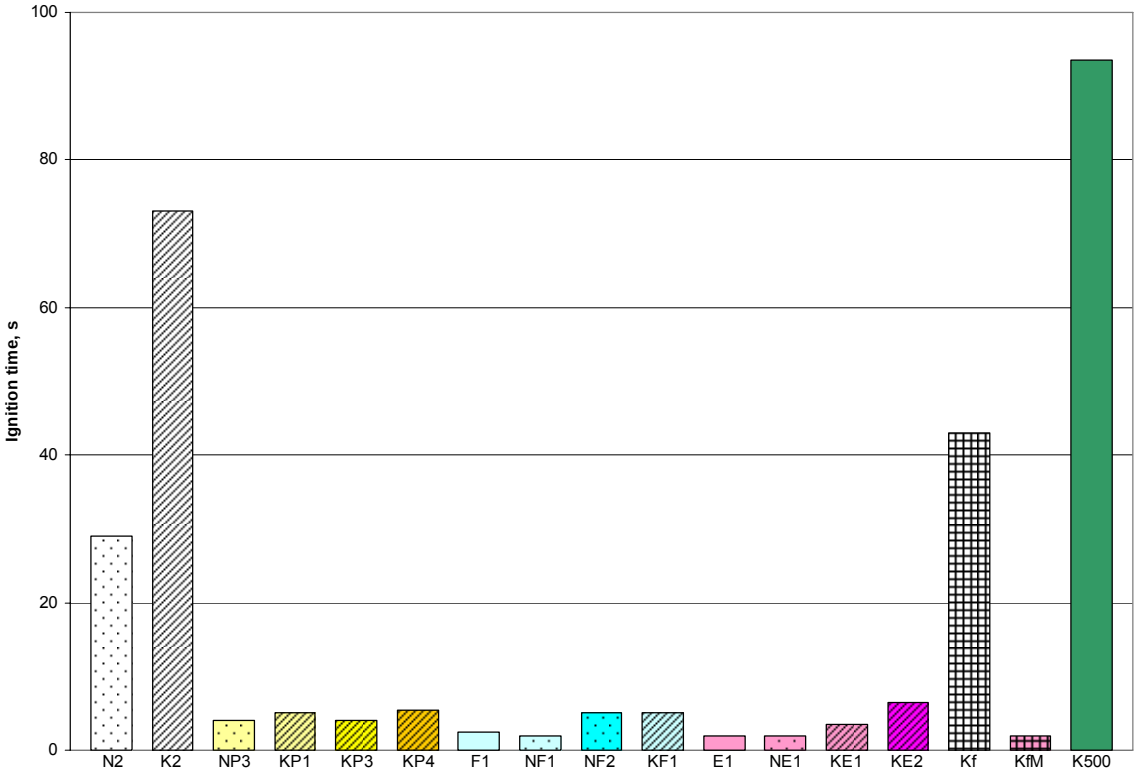

Fig. 5.2.5. Comparison of ignition time of aramid papers coated with different resins

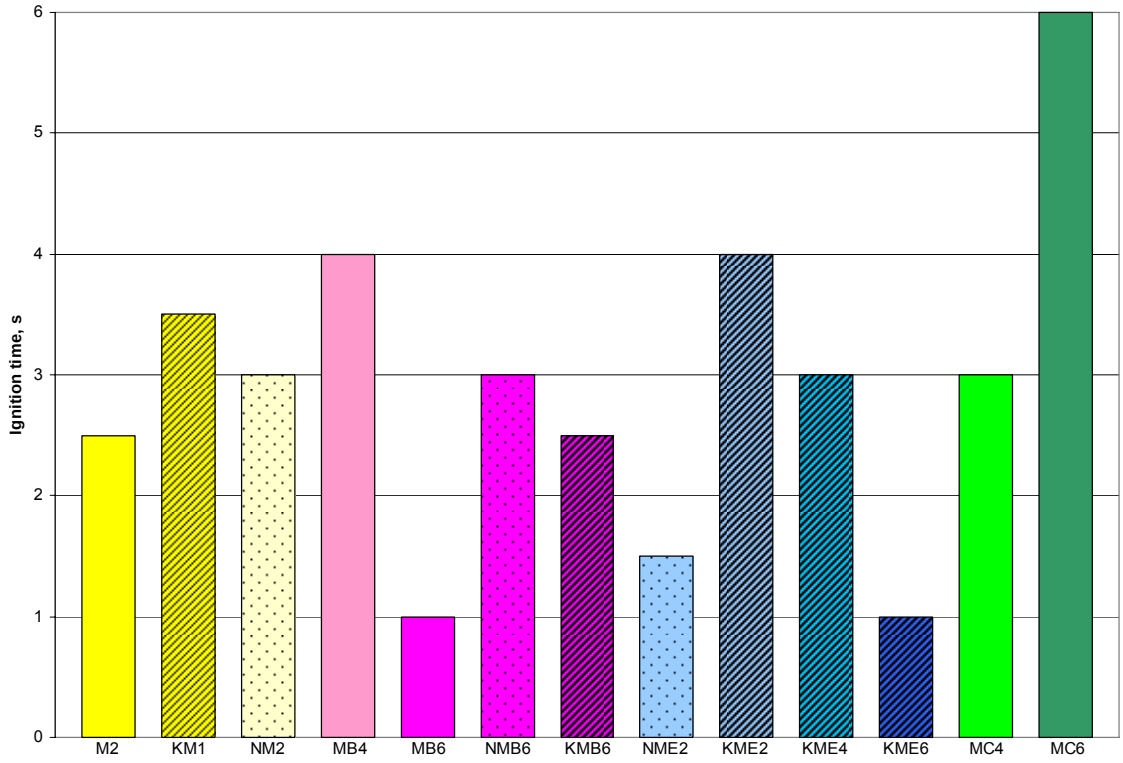

Fig. 5.2.6. Comparison of ignition time of epoxy systems with nanoparticles

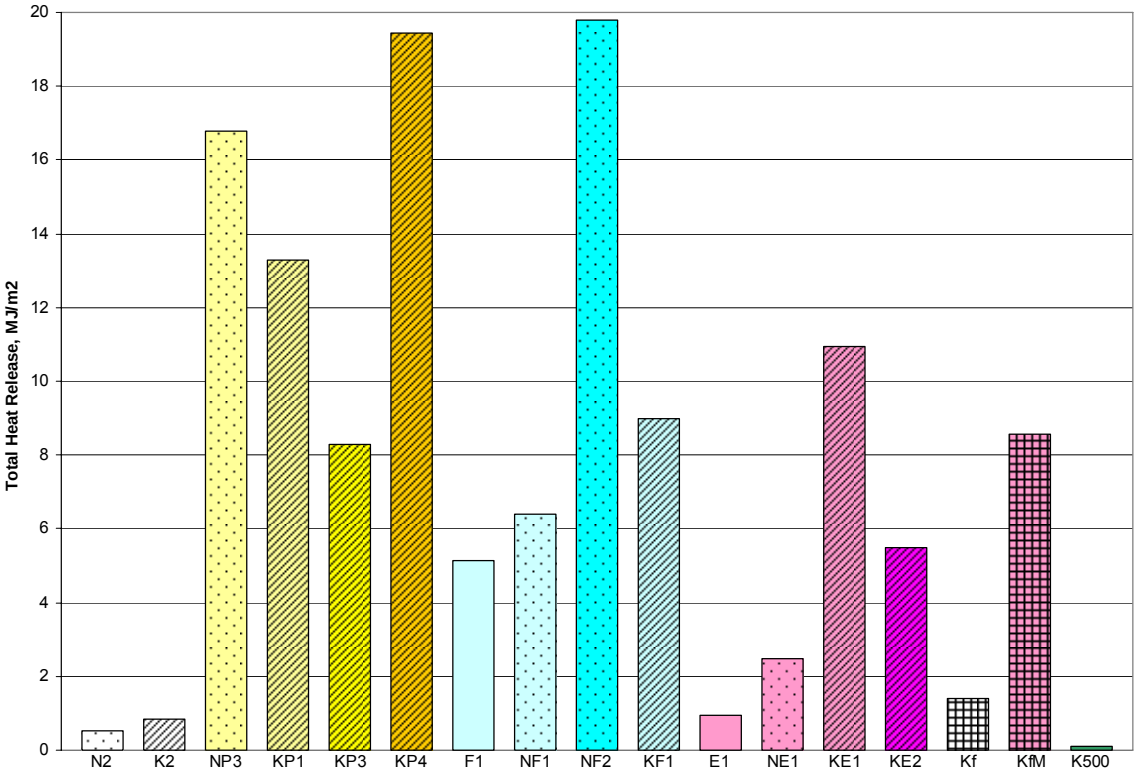

Fig. 5.2.7. Comparison of total heat release values for coated aramid papers

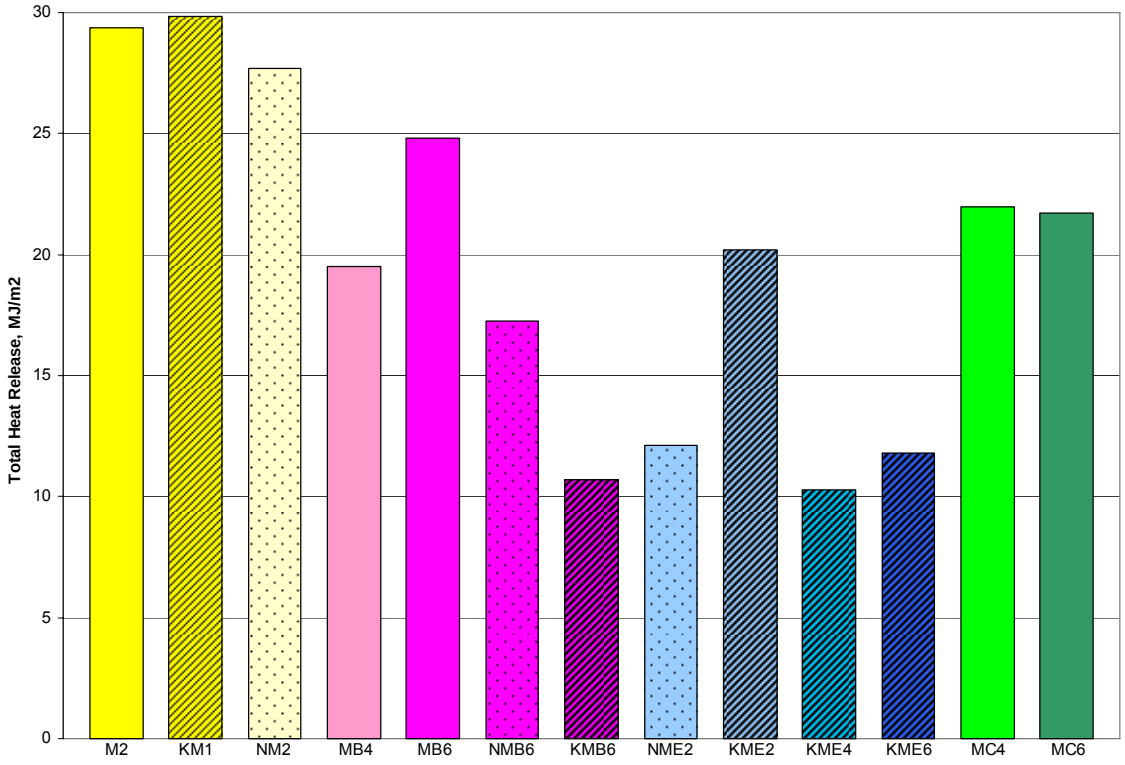

Fig. 5.2.8. Comparison of total heat release values for epoxy systems with nanoparticles

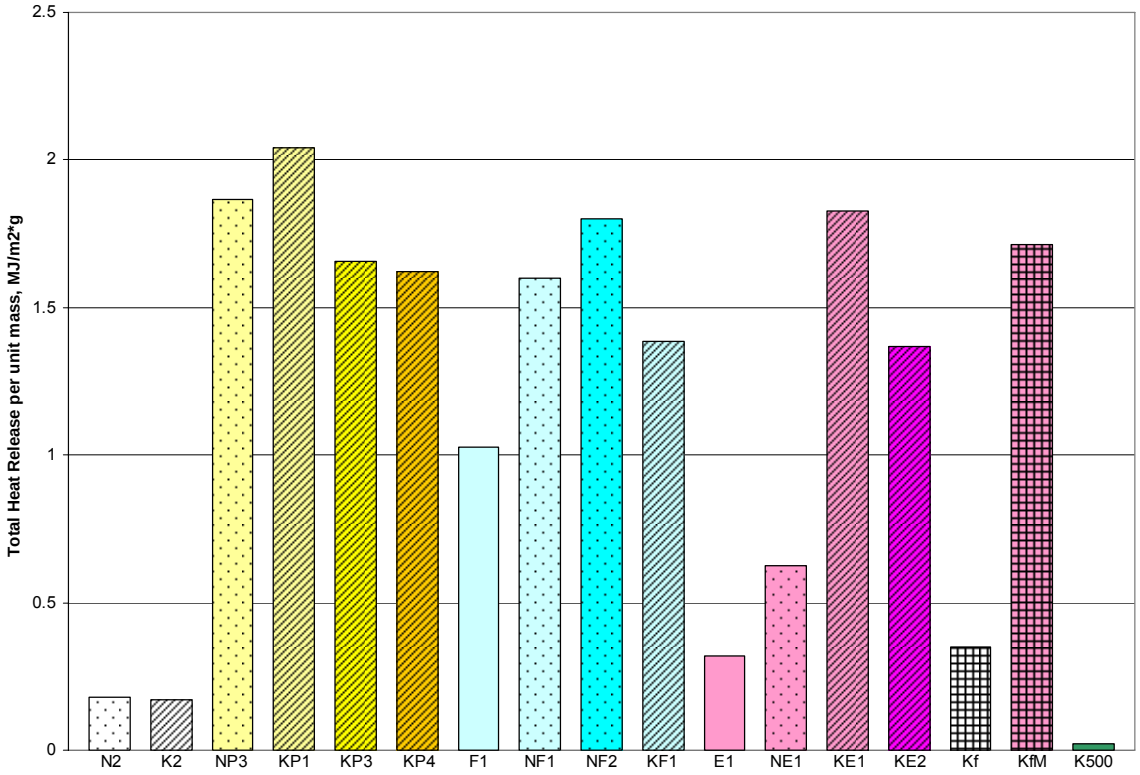

Fig. 5.2.9. Comparison of total heat release per unit mass for coated aramid papers

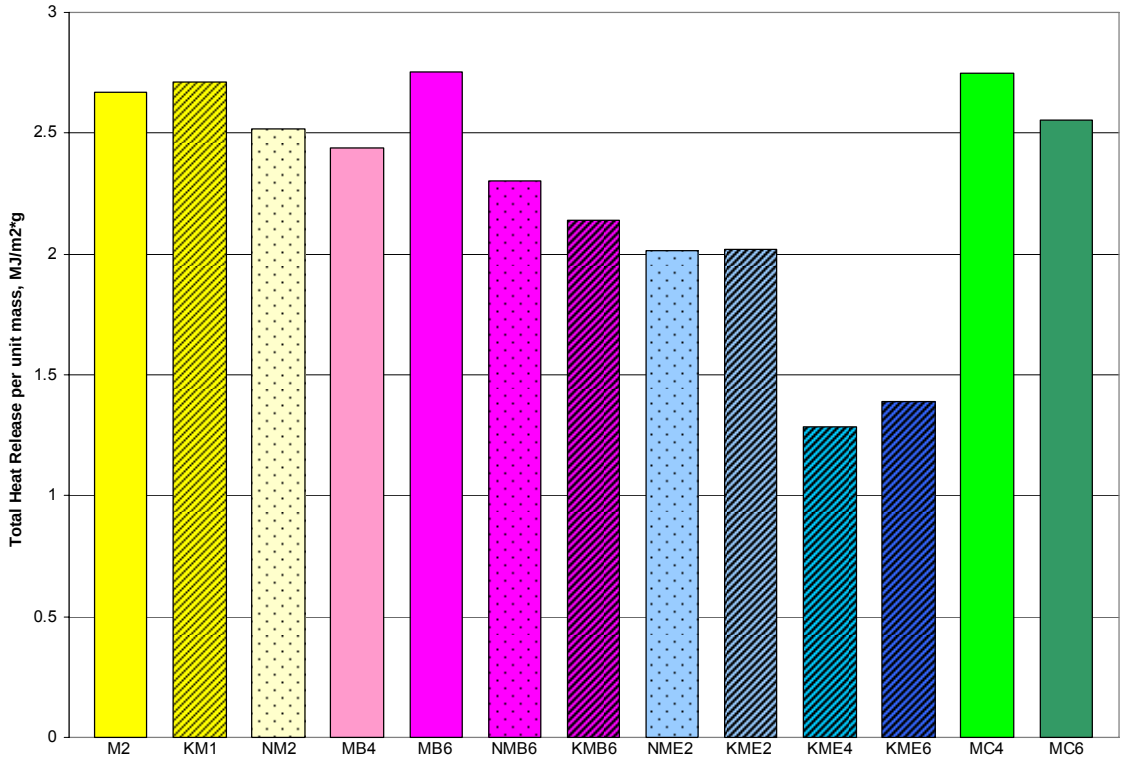

Fig. 5.2.10. Comparison of total heat release per unit mass for epoxy systems with nanoparticles

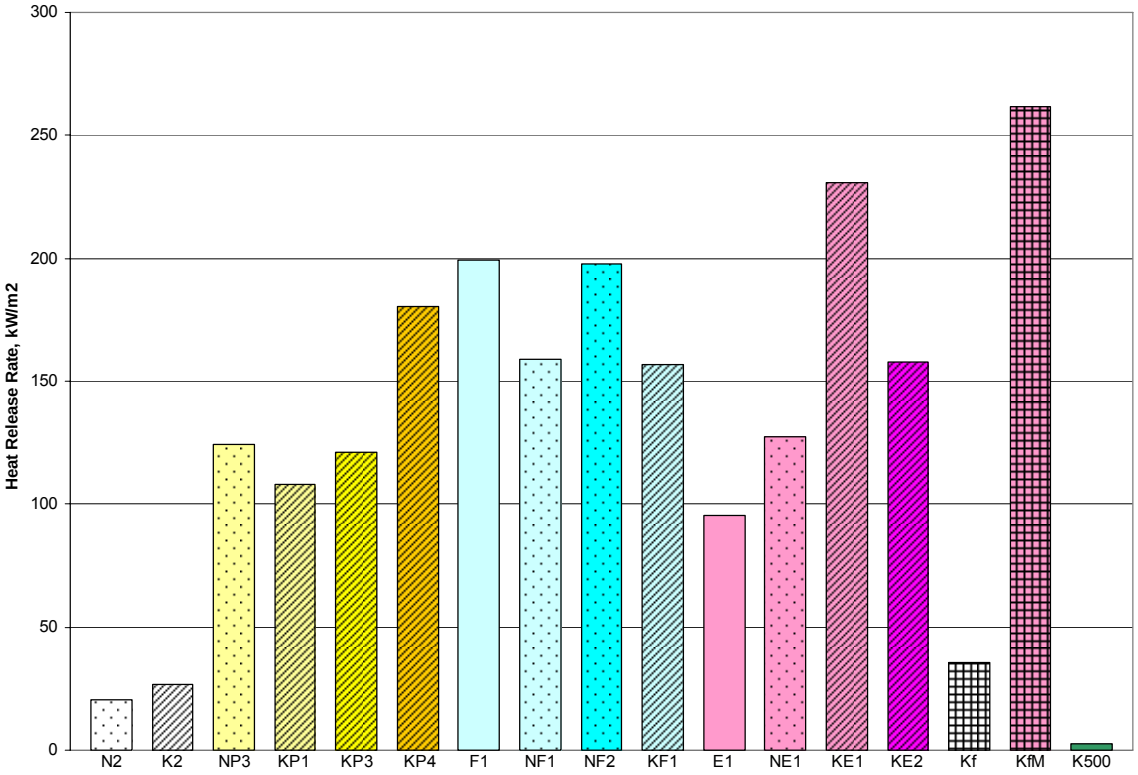

Fig. 5.2.11. Comparison of heat release rates for coated aramid papers

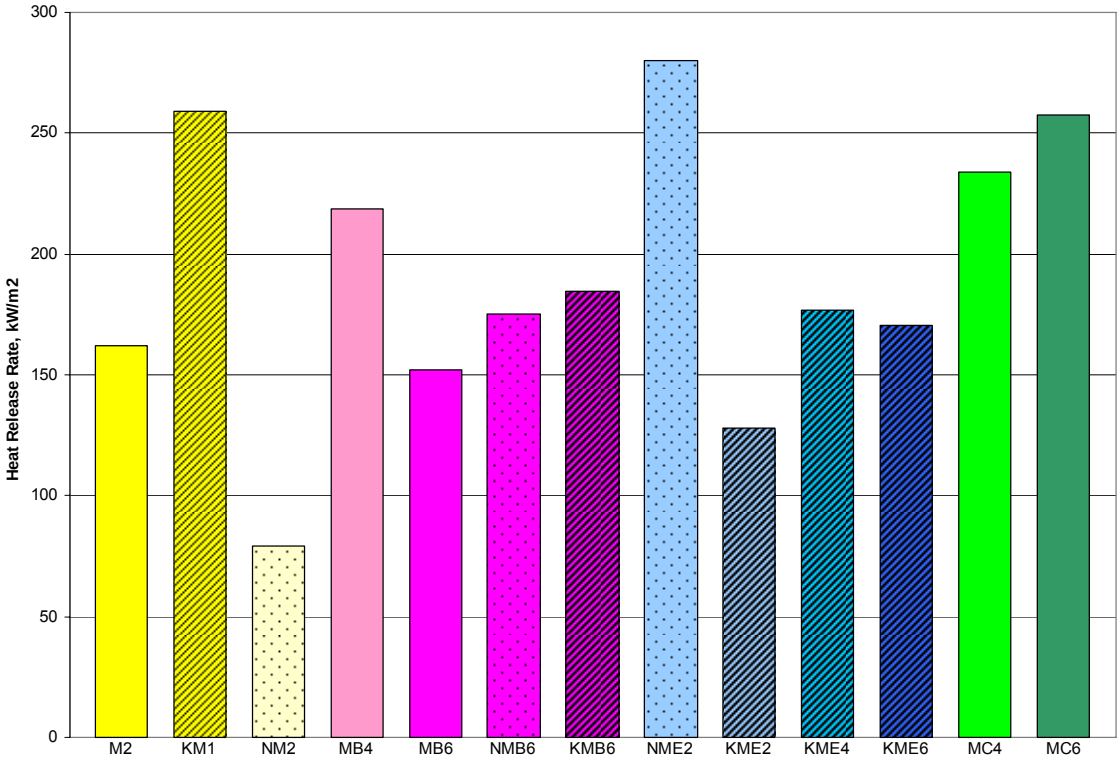

Fig. 5.2.12. Comparison of heat release rates for epoxy systems with nanoparticles

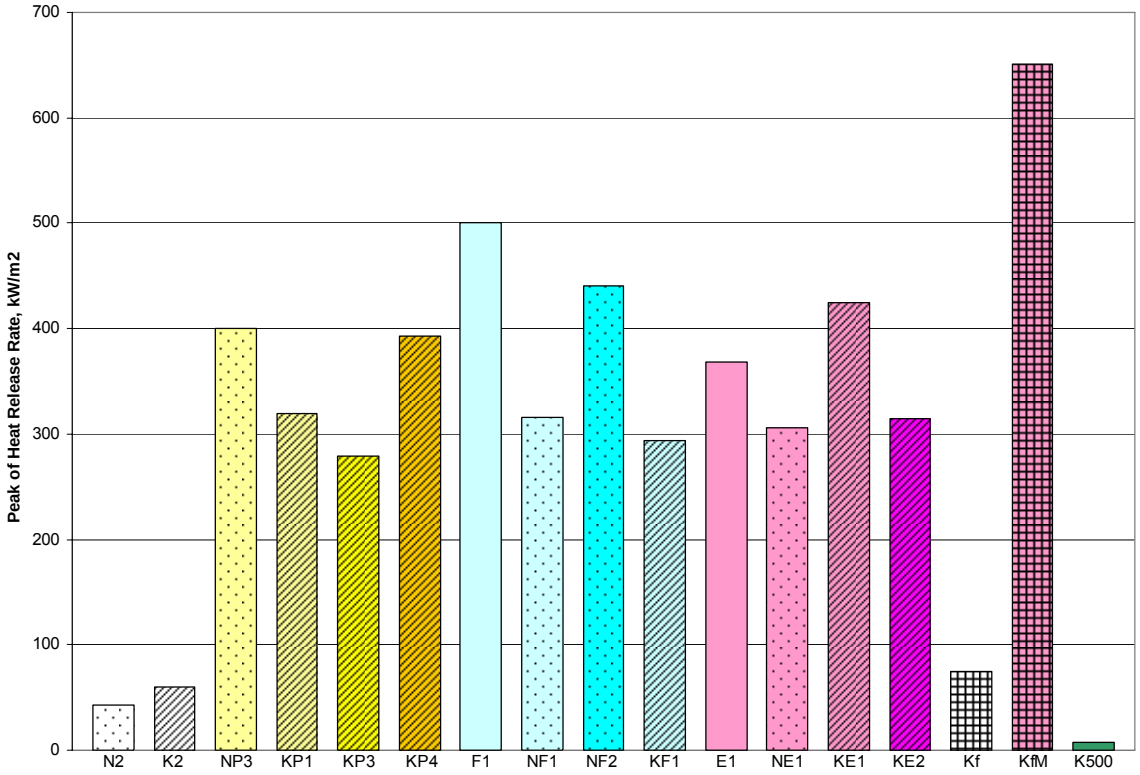

Fig. 5.2.13. Comparison of peak values of heat release rate for coated aramid papers

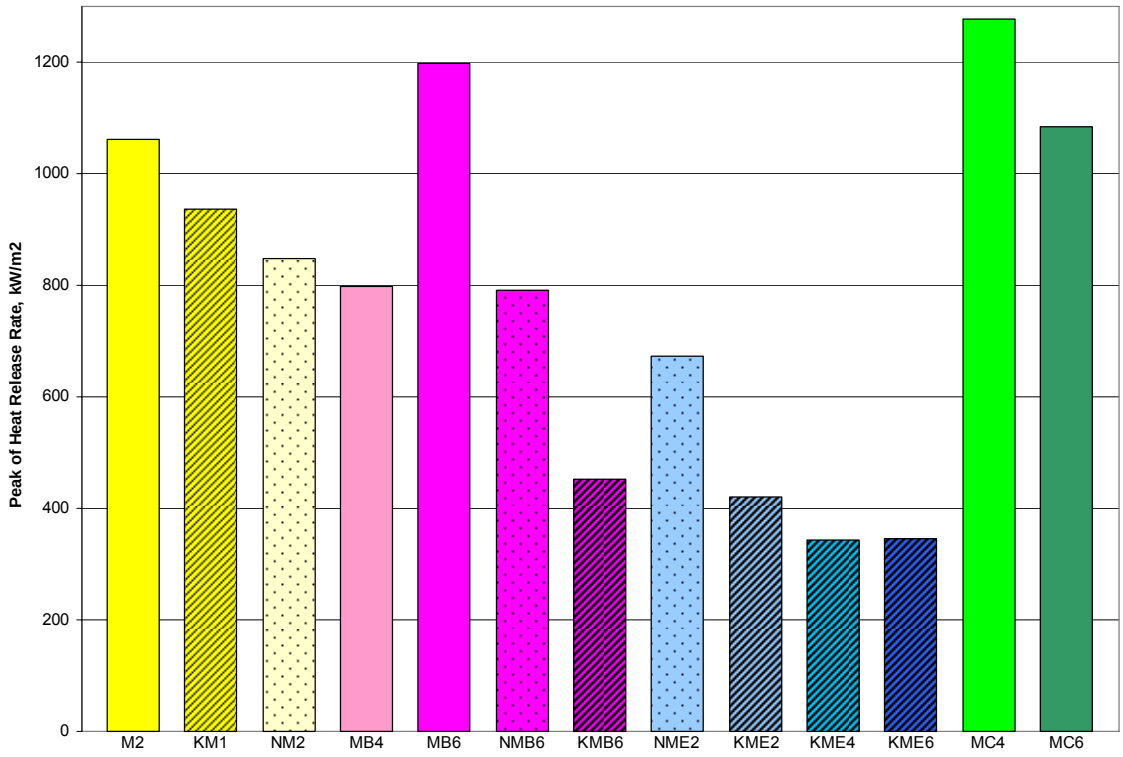

Fig. 5.2.14. Comparison of peak values of heat release rate for epoxy systems with nanoparticles

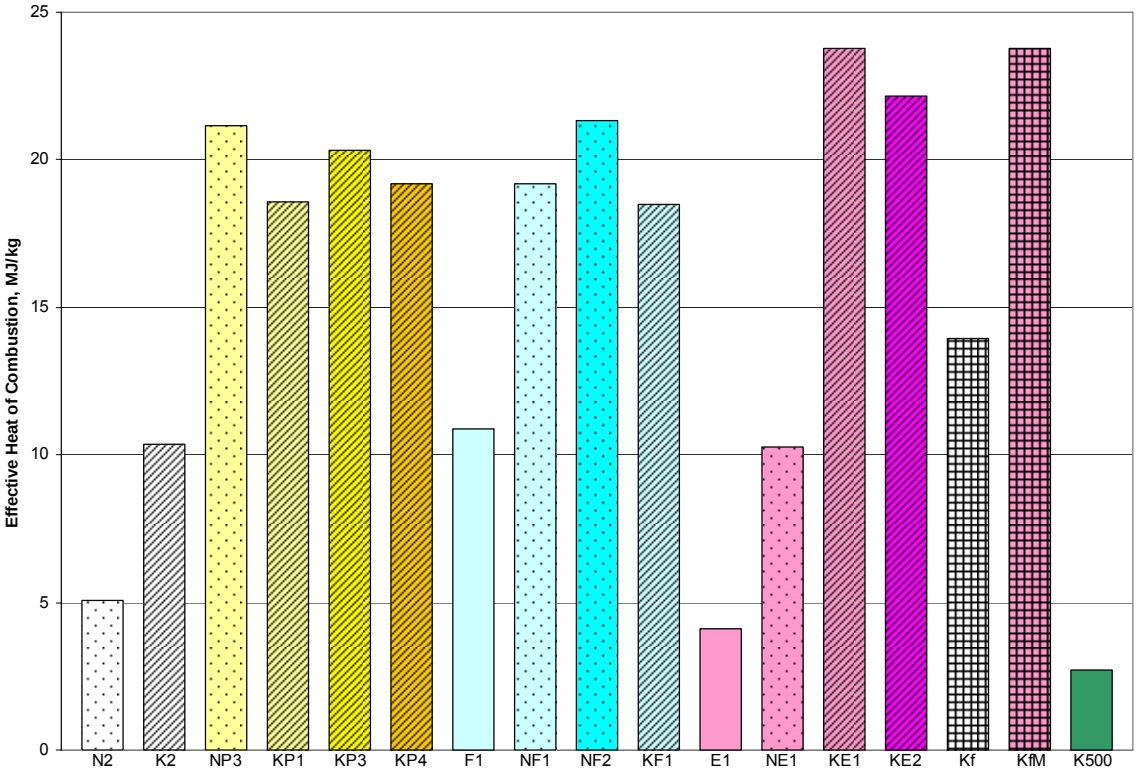

Fig. 5.2.15. Comparison of effective heat of combustion for coated aramid papers

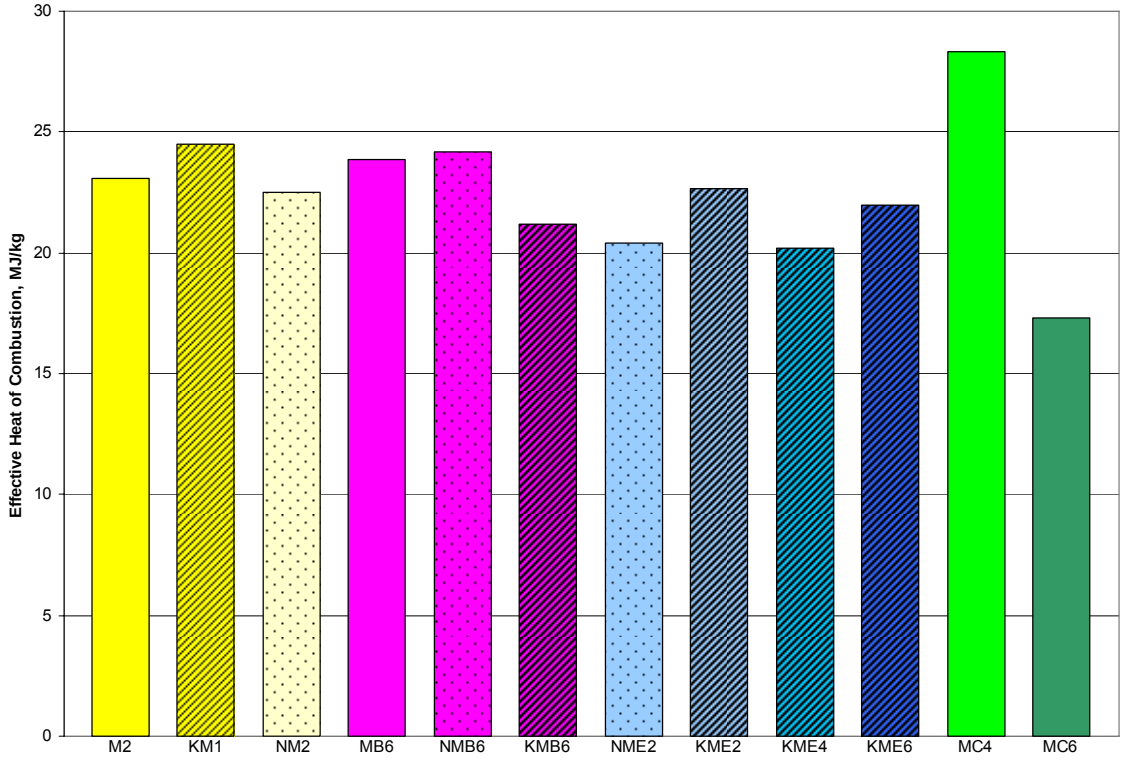

Fig. 5.2.16. Comparison of effective heat of combustion for epoxy systems with nanoparticles

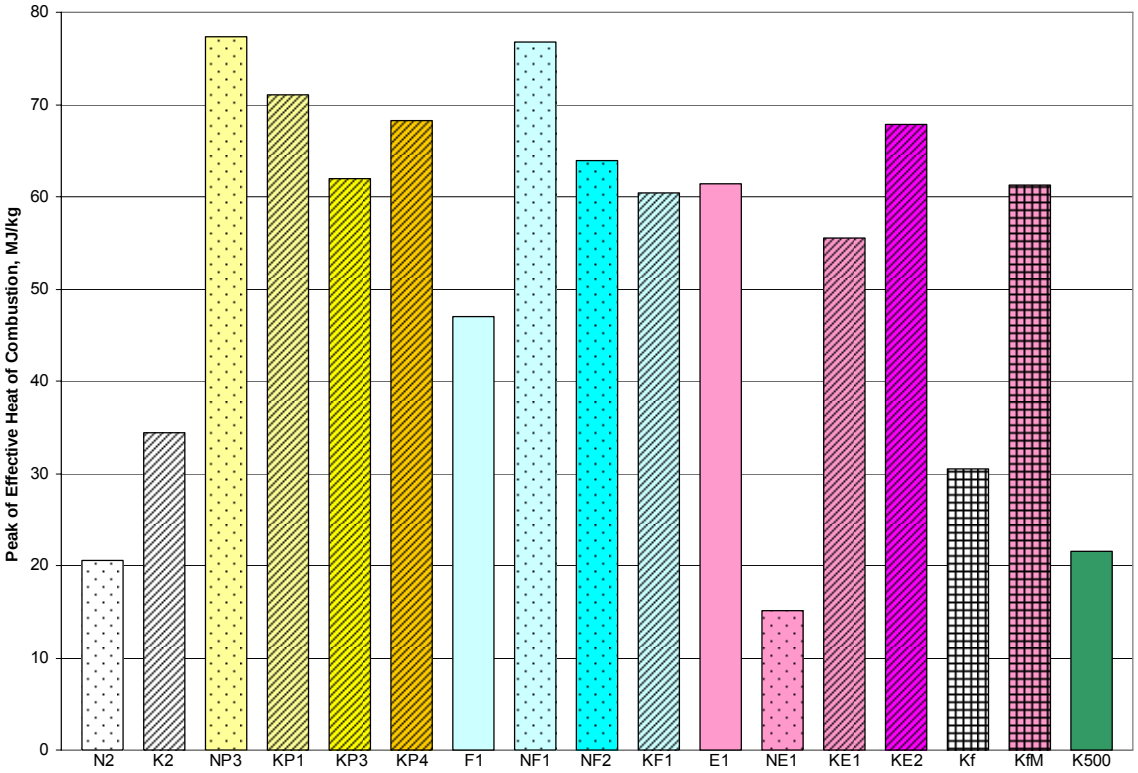

Fig. 5.2.17. Comparison of peak values of effective heat of combustion for different resins

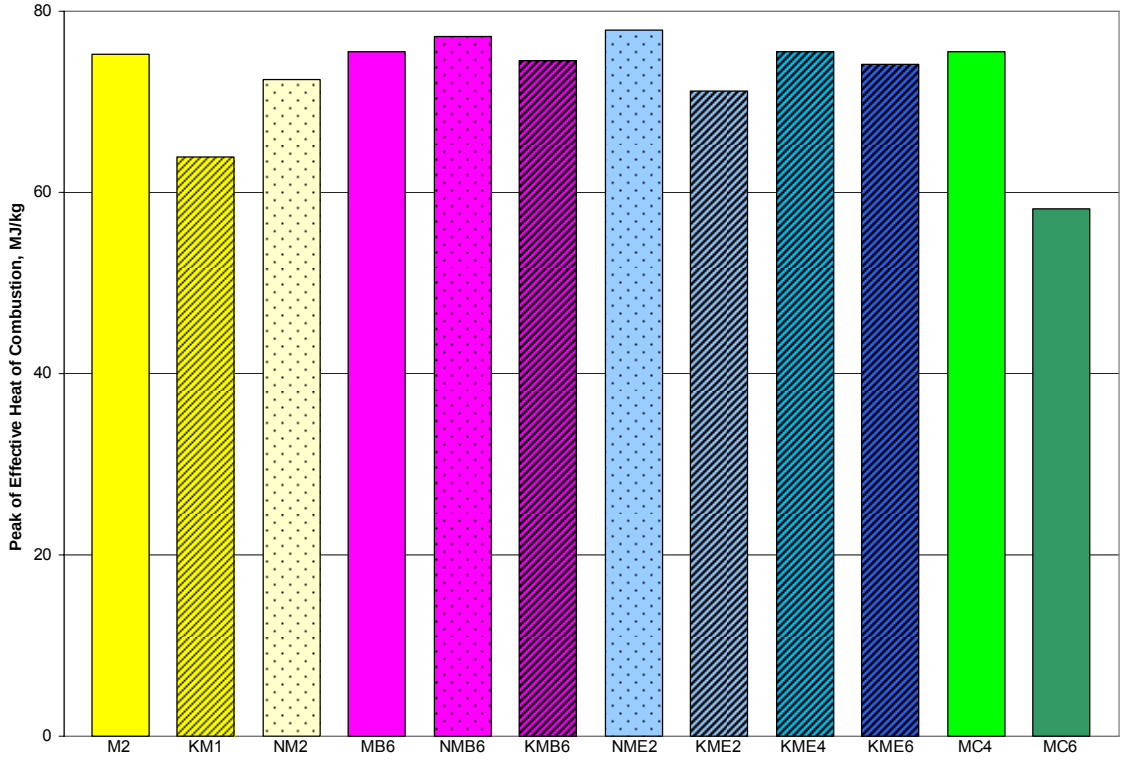

Fig. 5.2.18. Comparison of peak values of effective heat of combustion for epoxy systems

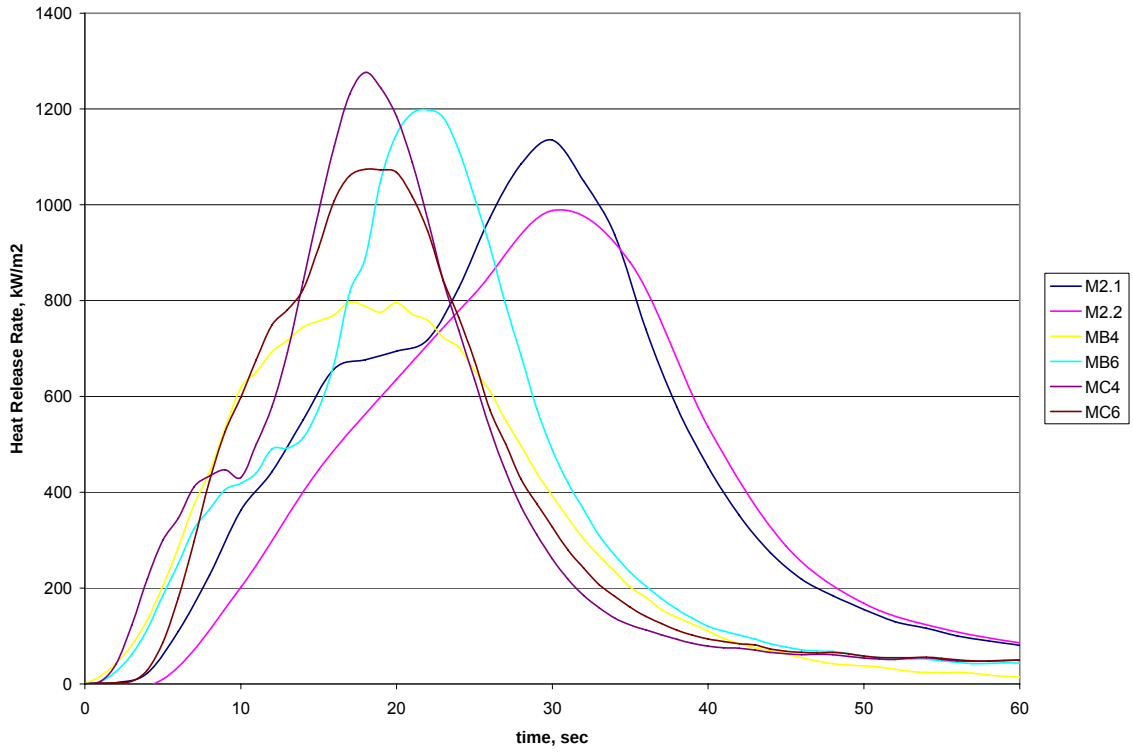

Fig. 5.2.19. Heat release rate kinetics of epoxy systems with nanoparticles

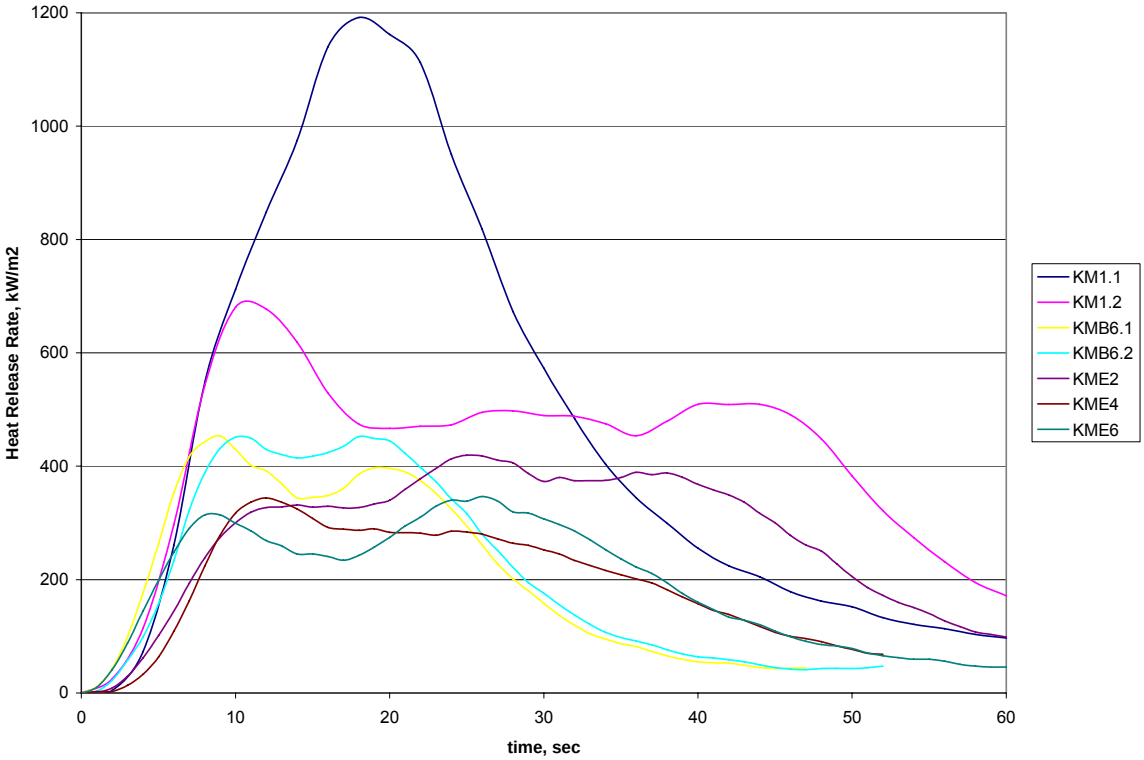

Fig. 5.2.20. Heat release rate kinetics of Kevlar coated with epoxy systems

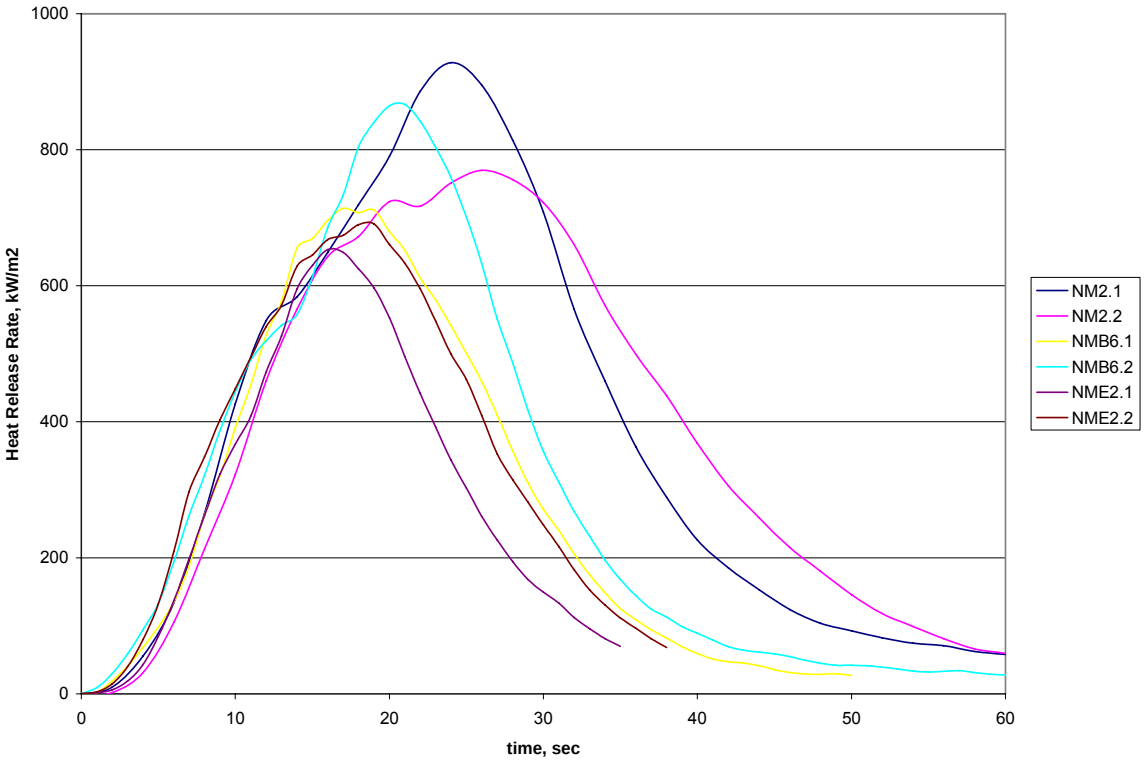

Fig. 5.2.21. Heat release rate kinetics of Nomex coated with epoxy systems

Comparison of influence of nanoparticles on material flammability is easier to study on graphs of dynamic changes of heat release rate over the time. Based on literature review and publications mentioned before material has better burning resistance properties when values of HRR are smaller and the curve of HRR is flatter and stretched in time. Peak of heat release rate, which is a major parameter in controlling flame propagation in fires, should be reduces. Fig. 5.2.19 through 5.2.21 show influence of different nanoparticles on HRR kinetics for resin, coated Kevlar, and coated Nomex respectively. The best results gave addition of 4% of nanoclay, either Bentolite or Nanocor, while the worst outcome gave Pyrograf. Nanoclay samples have significantly reduced PHRR when compared to pure resin ones and exhibit two typical stages: one is a rapid increase stage and another is a plateau stage. The first stage behavior could be explained by catalysis effect of organoclay at the beginning of burning process due to decomposition of clay following some chemical reaction which product can catalyze the degradation of polymer matrix. The second stage exists due to enhancement of flame resistance by addition of inclusions and creating barrier effect. Incorporation of the clay into resin matrix induces formation of clay-enriched protective chars at the sample surface during the combustion. These chars retard the heat and mass transfer and result in improvement of flammability properties of nanocomposites.

5.3. NASTRAN Modeling Results

The sample was modeled as a cylinder with the same thickness but smaller diameter since only 1D flow (through the thickness) is considered. Sample size has been rescaled to bigger range (1,000,000 times) for easier meshing and pressures recalculated to be adequate to the rescaled dimensions. Nanoclays were modeled as small cylinders with aspect ratio of 10 and 20. For transient analysis initial pressure was assumed to be atmospheric one. Since density of nanoclay, for example montmorillonite, is similar to that of epoxy, inclusion percentage by weight is the same as percentage by volume, which is used in the modeling. Numbers of nanoclay models in two sizes were calculated to receive 2 and 4% of inclusion, see Table 5.3.1. Permeability coefficient of epoxy was taken from results of helium permeability tests and that of nanoclay was assumed to be close to zero.

Table 5.3.1. Dimensions of modeled samples with 2 and 4% of inclusions

Aspect ratio	Inclusion radius	Inclusion height	Percentage	Numbers of inclusions
10	100	20	2	7
10	100	20	4	15
20	100	10	2	15
20	100	10	4	30

Sample radius: 500, sample height: 300

First, a cylinder of epoxy without inclusions was modeled and analysis ran for steady state and transient mass flux. A model of the sample is depicted in Fig. 5.3.1, results of transient flux over the time for three different elements in Fig. 5.3.2 (green line for the surface on the side of vacuum, blue one for face at high pressure, and red one for circumference), and over the thickness after stabilization in Fig. 5.3.3. Transient flux stabilized after about three hundred time steps and reached value calculated from steady state model.

Secondary, one model of nanoclay was added and steady state analysis ran, chosen as faster and still adequate, see Fig. 5.3.4 and 5.3.5. After that, models of epoxy samples with 2 and 4% of inclusions were prepared, analyzed, remeshed to smaller size of elements, and analyzed again. Results of mass flux or permeation rate calculation can be found in Table 5.3.2 even though it was difficult to find correct values of mass flux for samples with many inclusions.

Percentage loss of permeability rate for samples with inclusions can be also used as percentage loss of permeability coefficient, which is independent of sample thickness, for investigating correlation between modeling and helium permeability test results for samples with nanoclays. The test results are not expected to perfectly match modeling results because influence of pores on gas barrier properties is bigger then influence of inclusions.

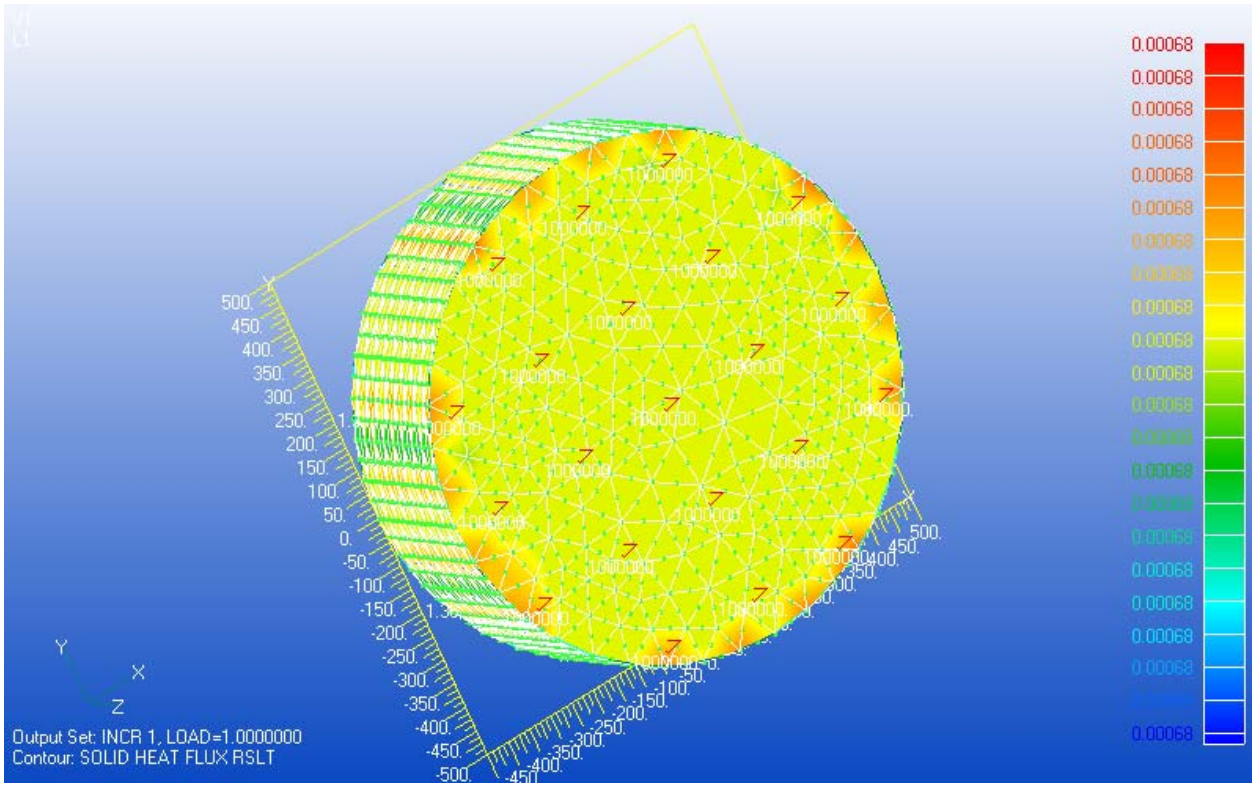

Fig. 5.3.1. Model of flux through sample of epoxy

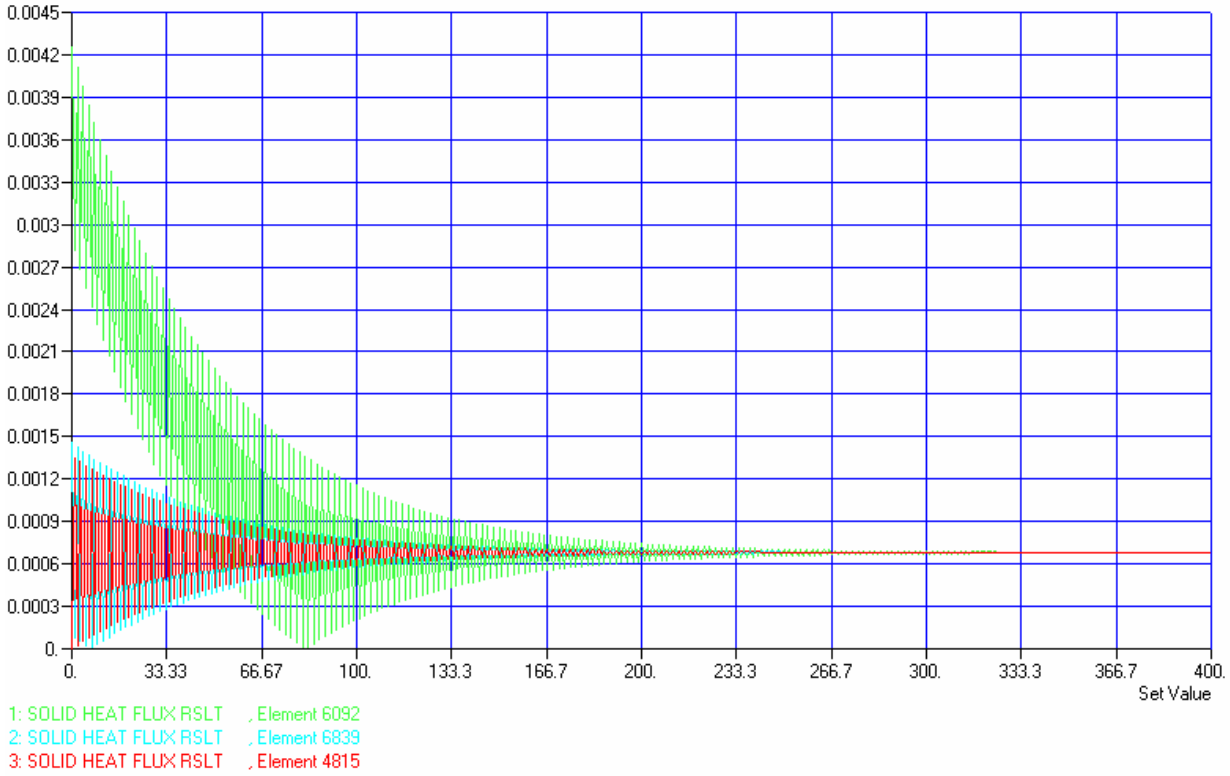

Fig. 5.3.2. Transient flux results for different elements of epoxy sample

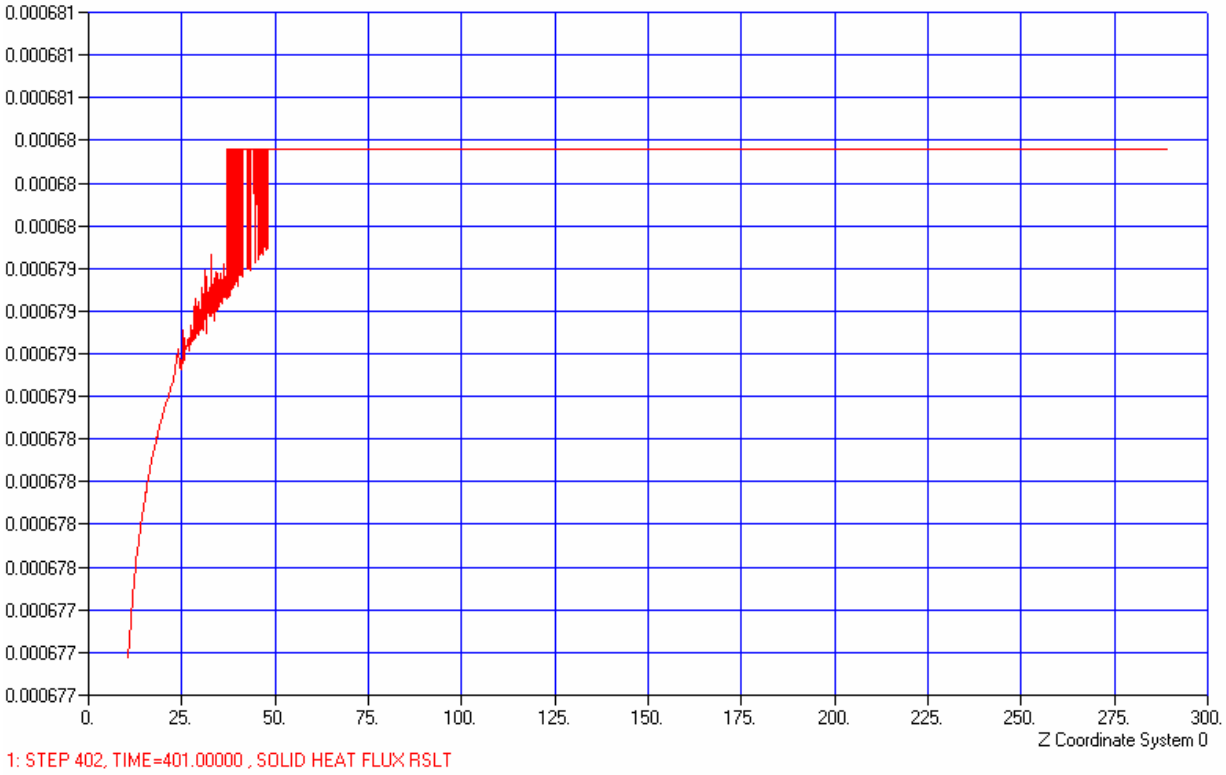

Fig. 5.3.3. Transient flux through the thickness result for epoxy sample

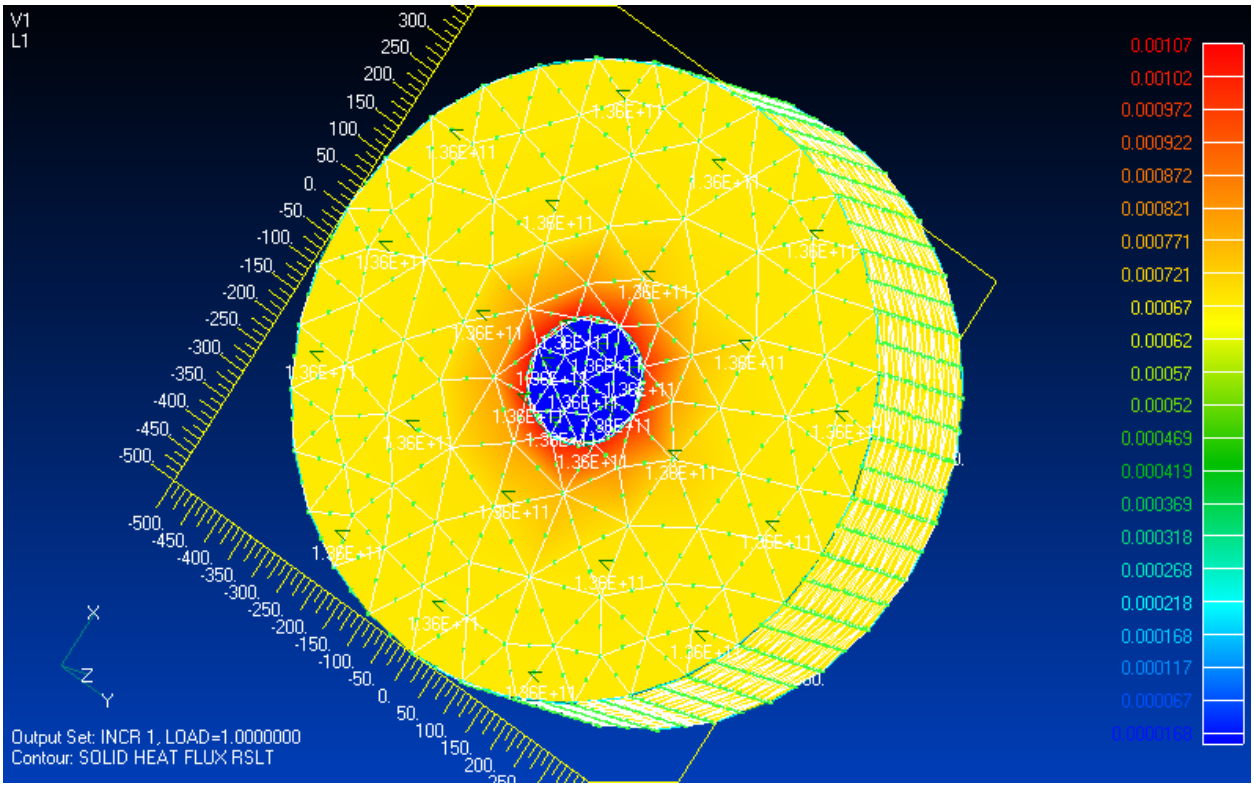

Fig. 5.3.4. Model of flux through sample of epoxy with one clay on the surface

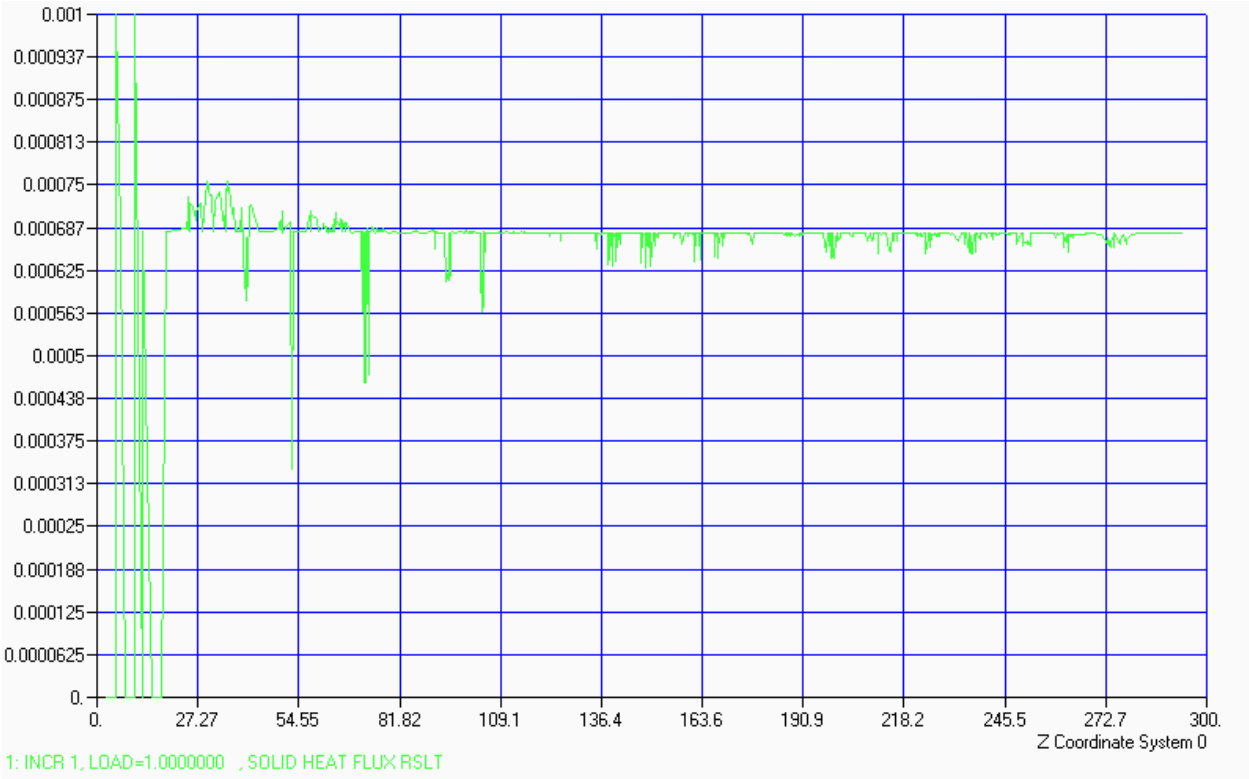

Fig. 5.3.5. Flux through the thickness result for epoxy sample with one clay

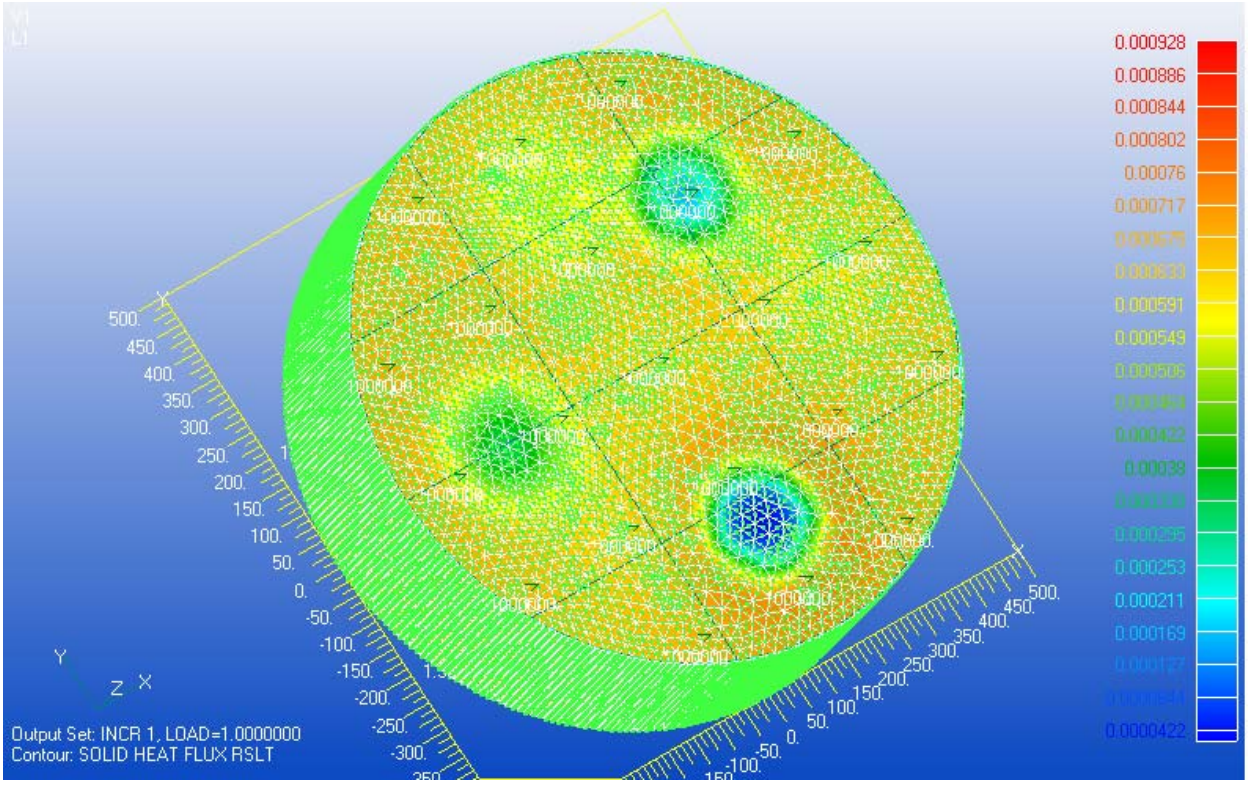

Fig. 5.3.6. Model of flux through sample of epoxy with seven clays as 2%

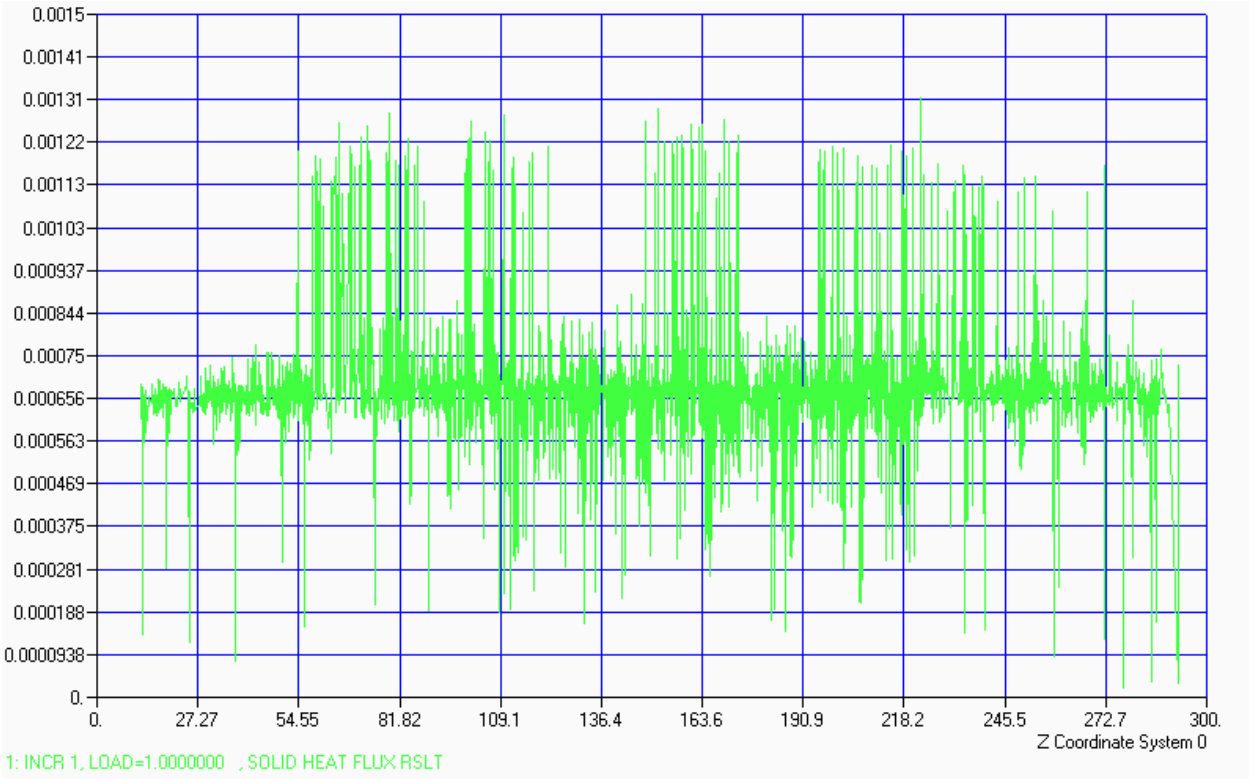

Fig. 5.3.7. Flux through the thickness result for epoxy sample with seven clays as 2%

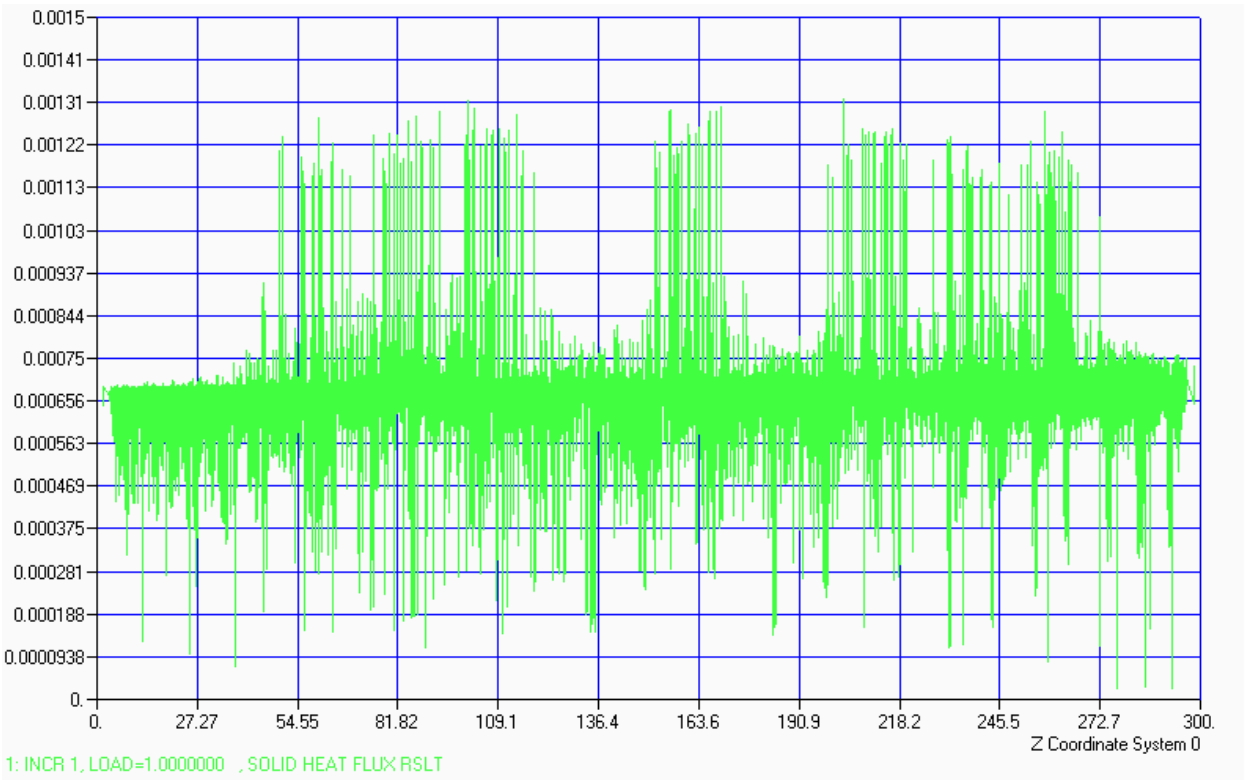

Fig. 5.3.8. Flux through the thickness for sample with seven clays as 2% after refining mesh

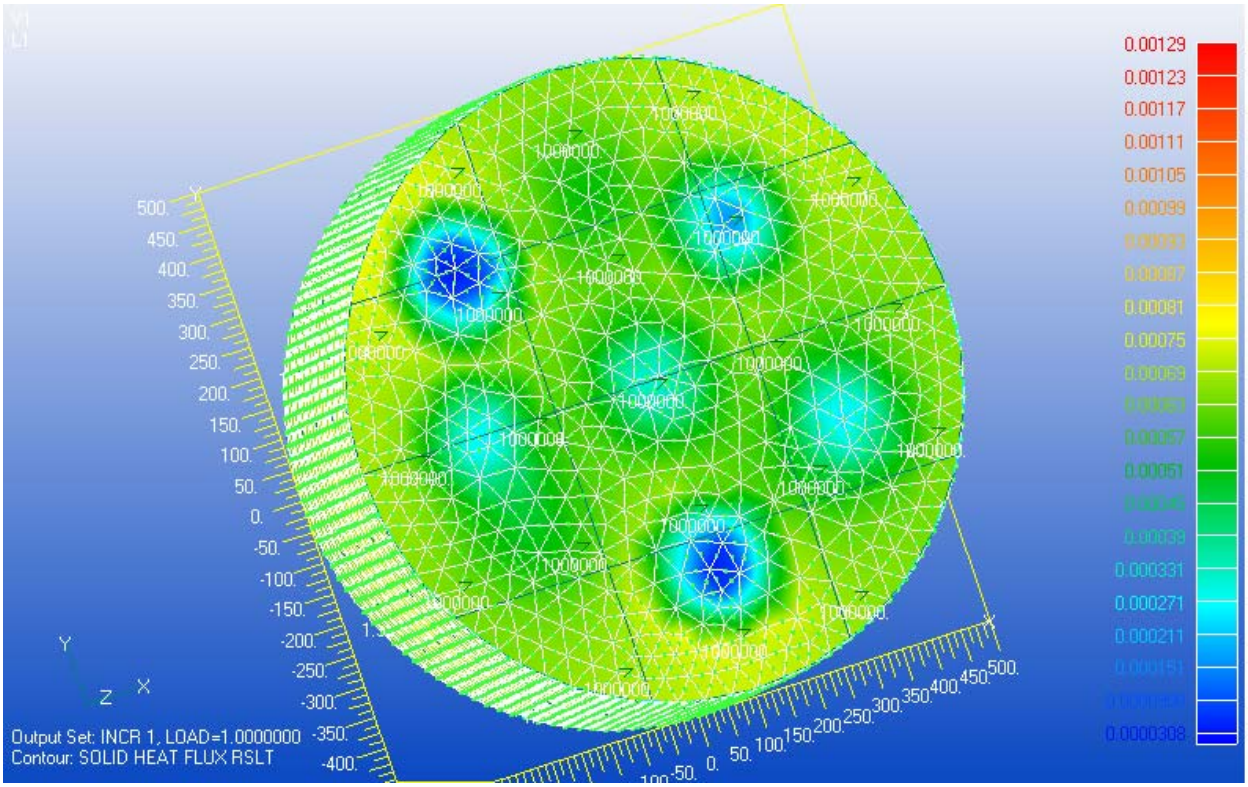

Fig. 5.3.9. Model of flux through sample of epoxy with fifteen clays as 4%

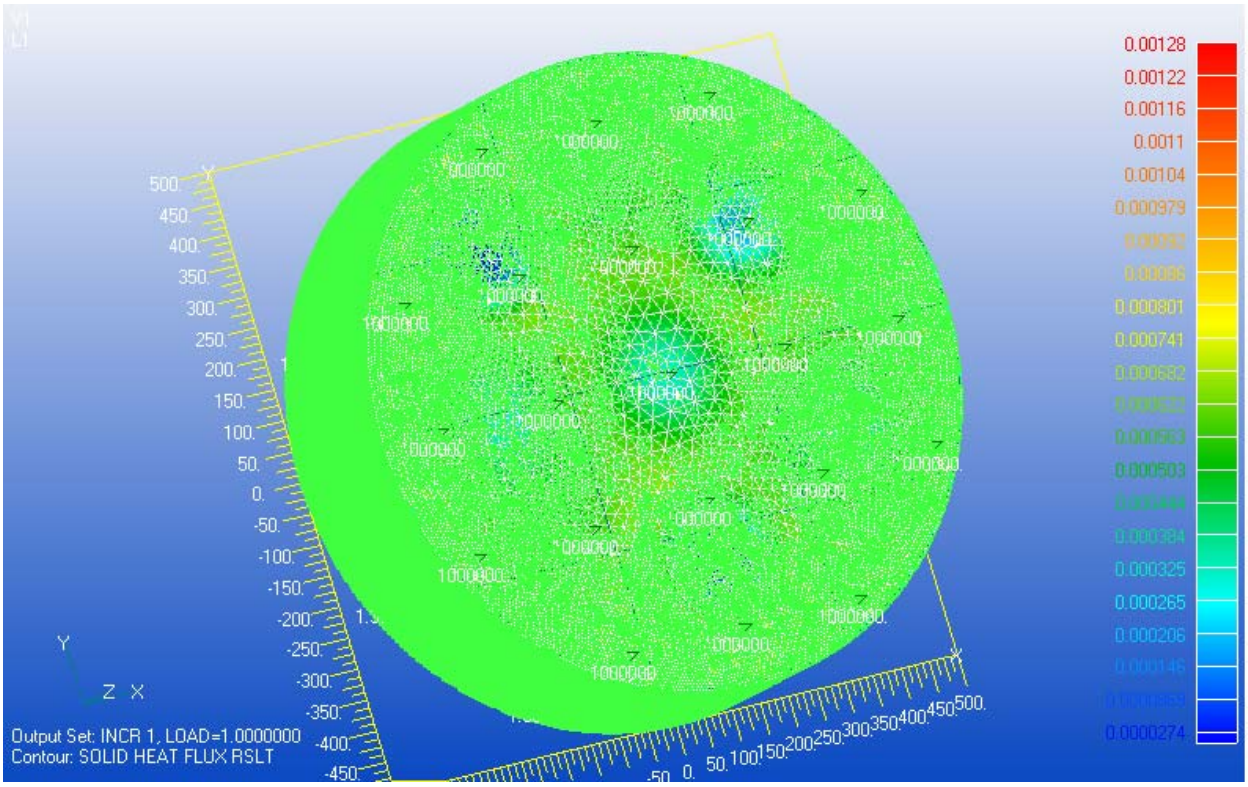

Fig. 5.3.10. Model of flux through sample of epoxy with fifteen clays as 4% after remeshing

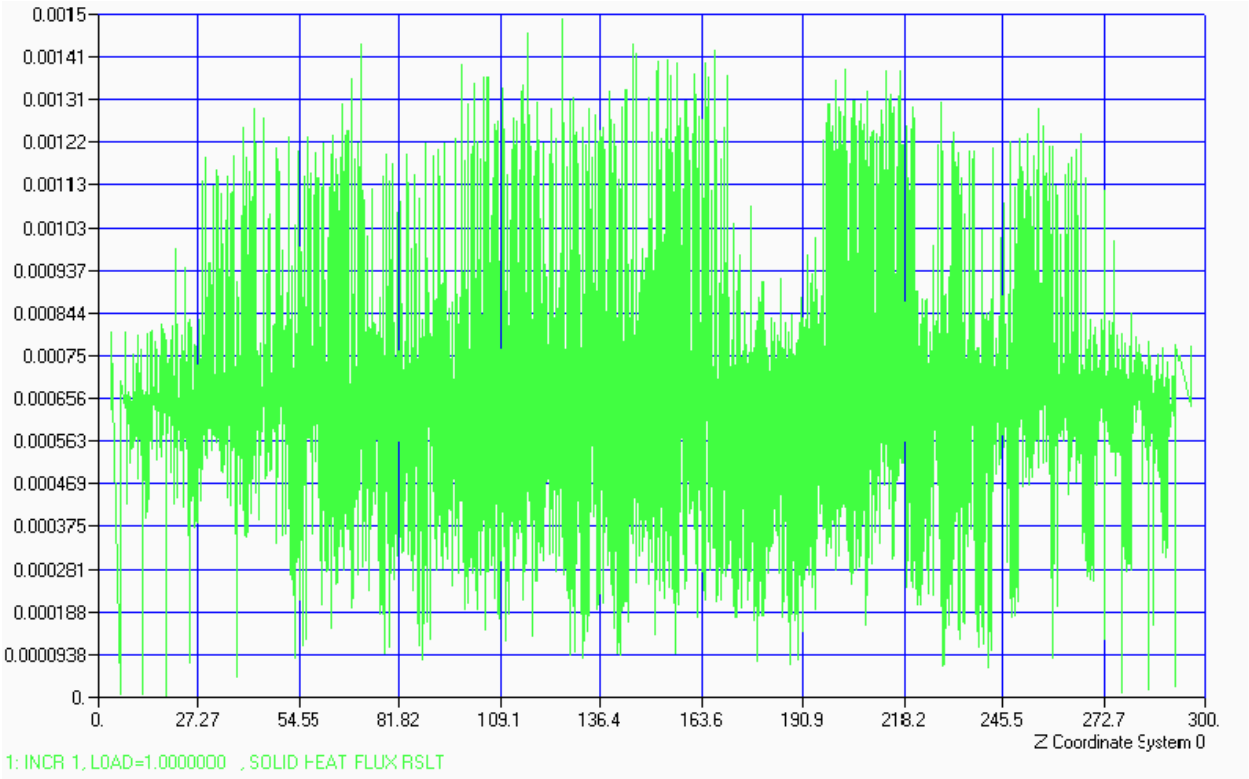

Fig. 5.3.11. Flux through the thickness for sample with fifteen clays as 4%

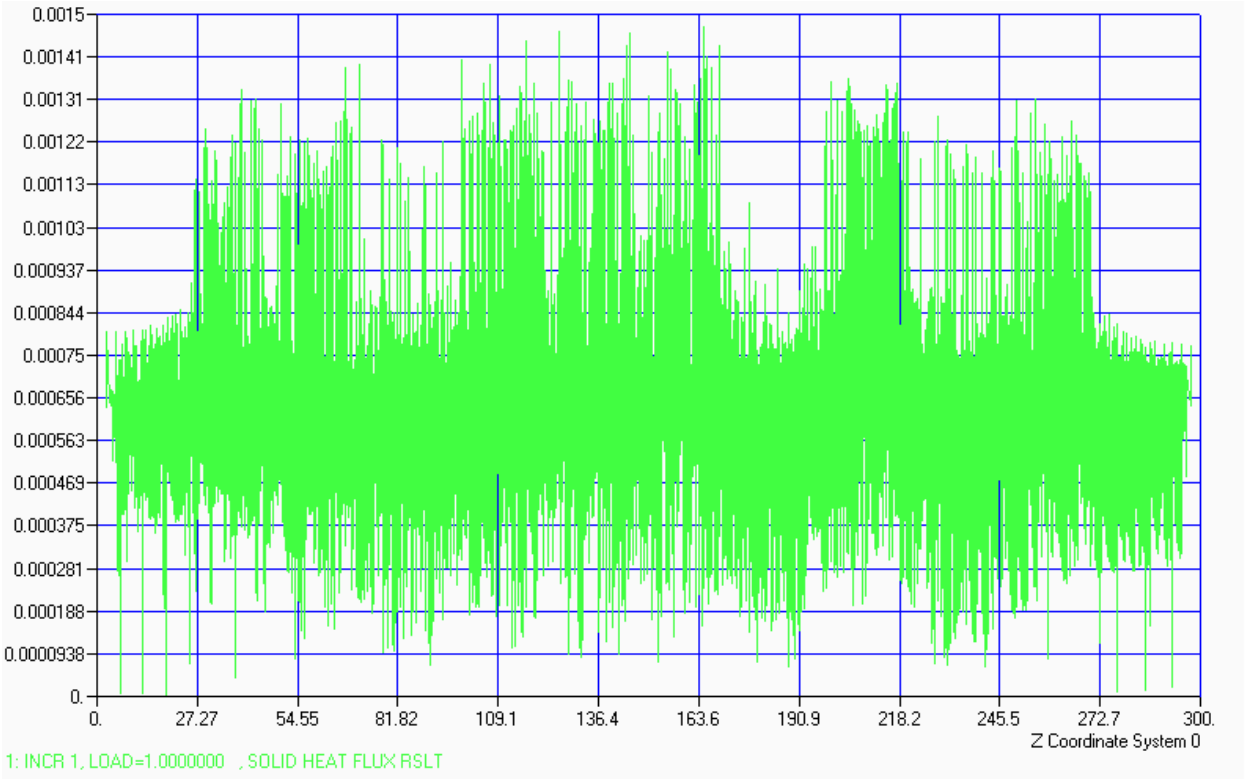

Fig. 5.3.12. Flux through the thickness for sample with fifteen clays as 4% after remeshing

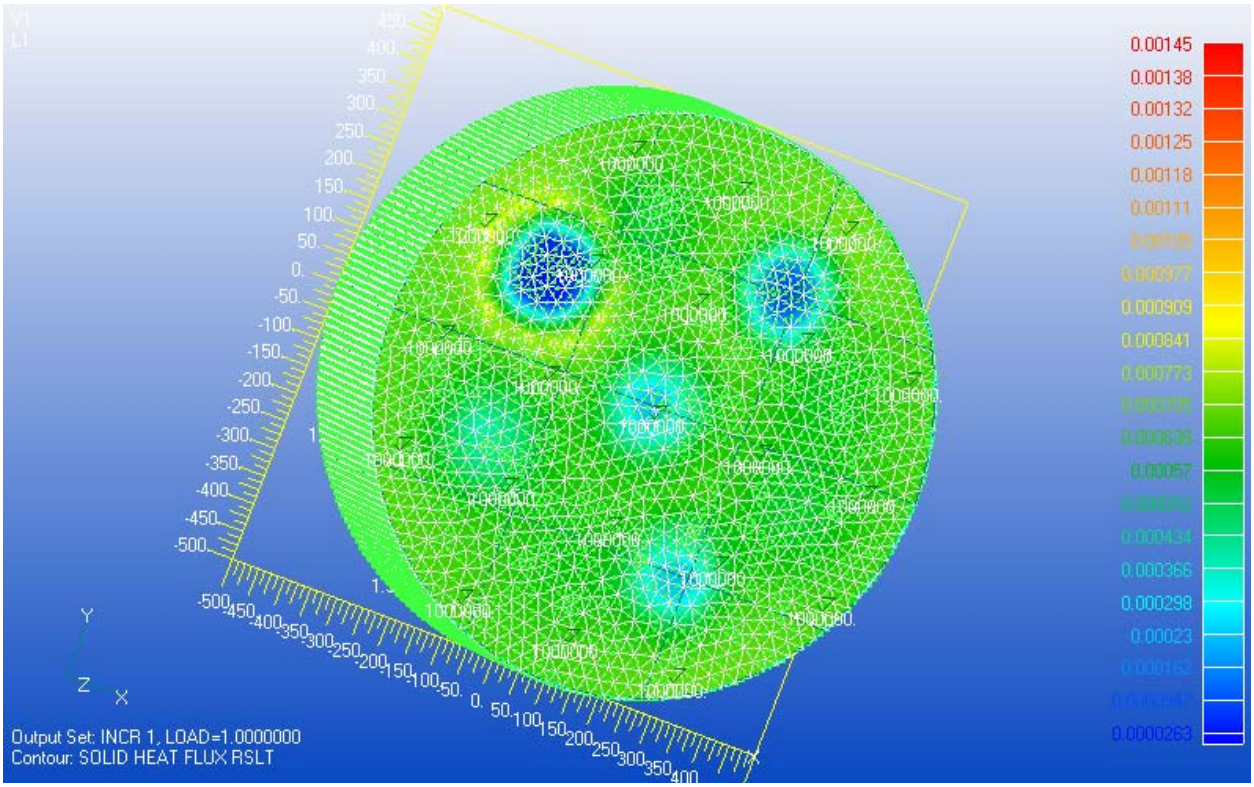

Fig. 5.3.13. Model of flux through sample of epoxy with fifteen clays as 2%

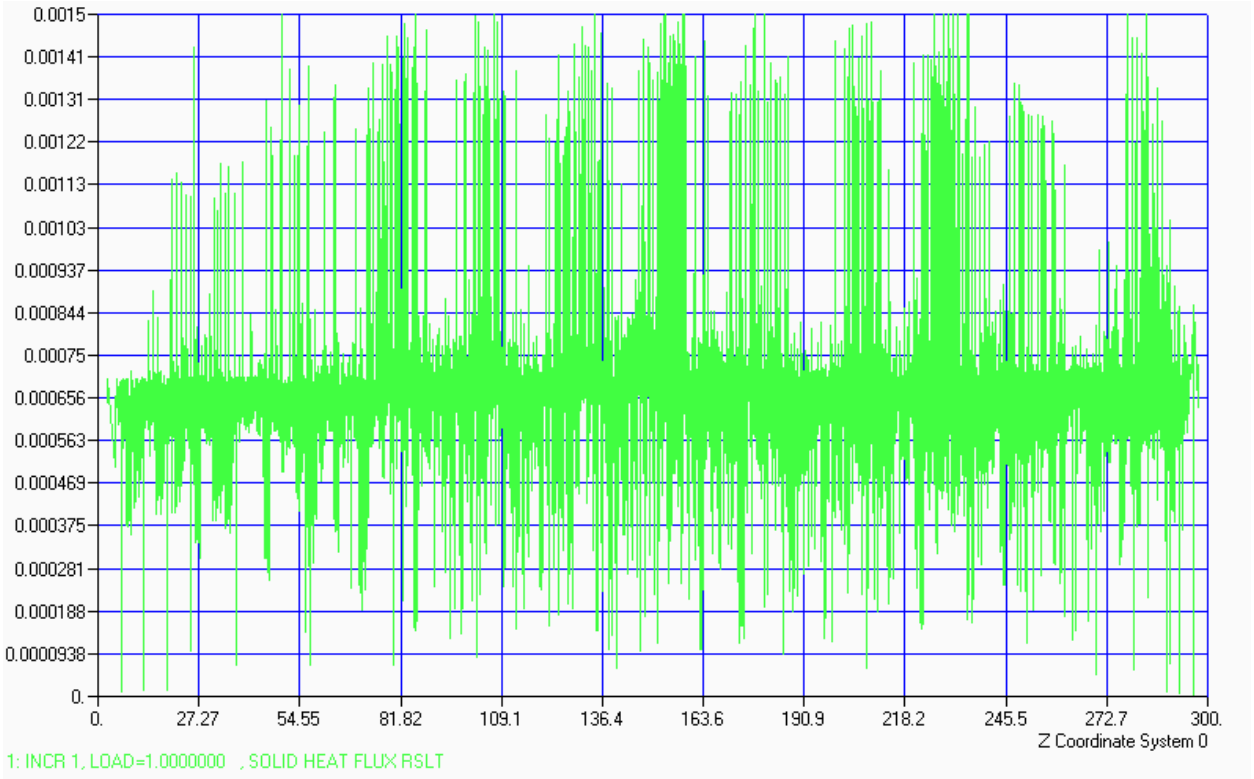

Fig. 5.3.14. Flux through the thickness for sample with fifteen clays as 2%

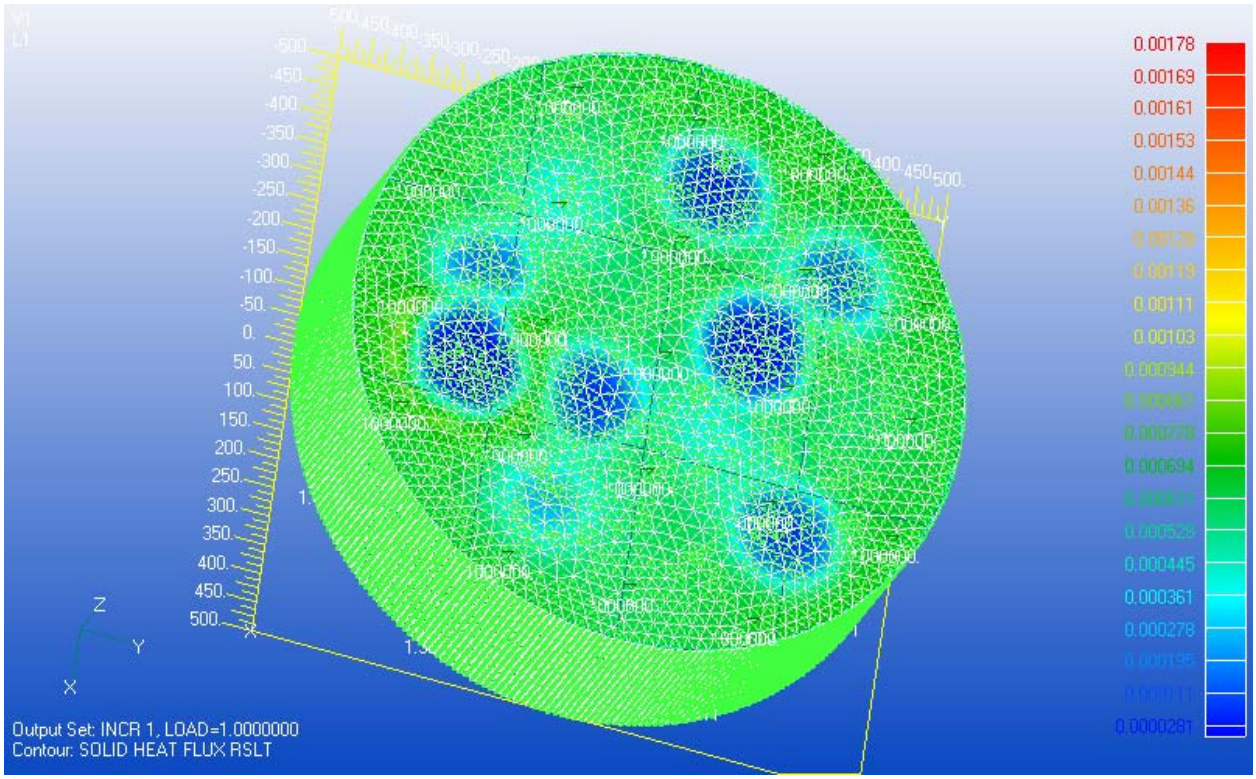

Fig. 5.3.15. Model of flux through sample of epoxy with thirty clays as 4%

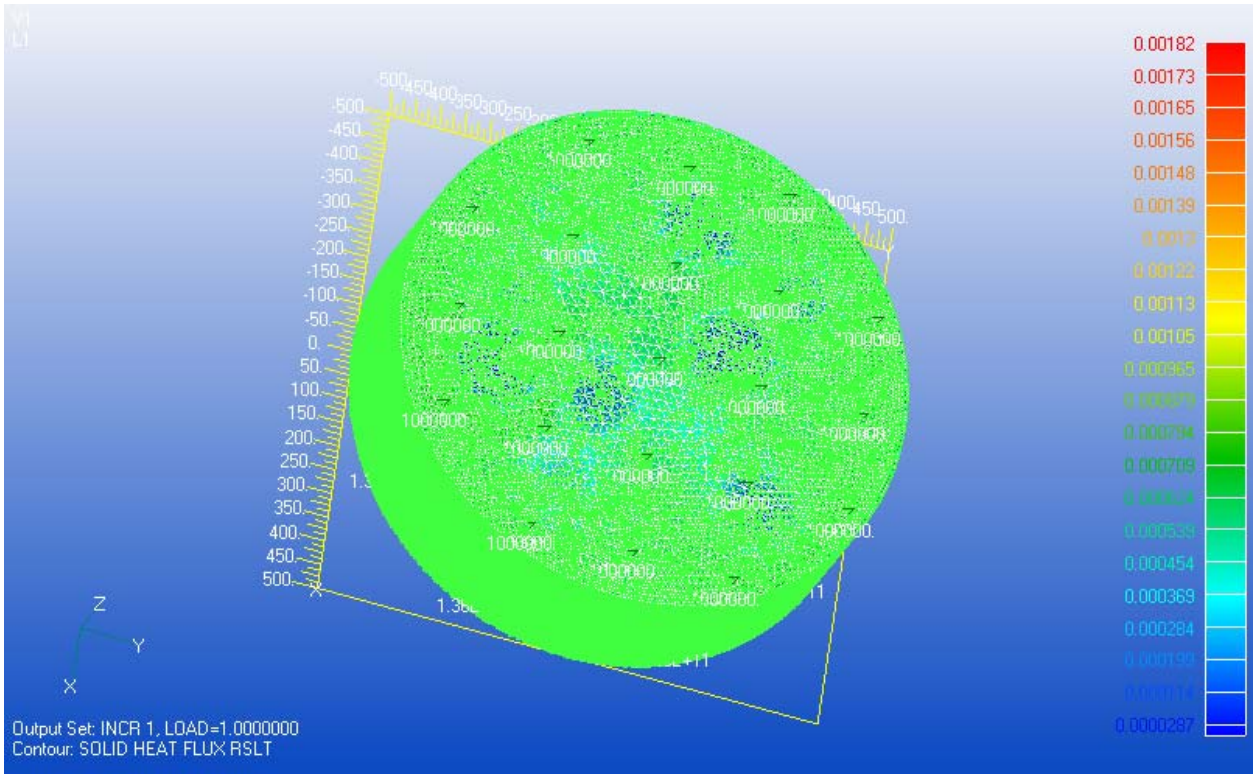

Fig. 5.3.16. Model of flux through sample of epoxy with thirty clays as 4% after remeshing

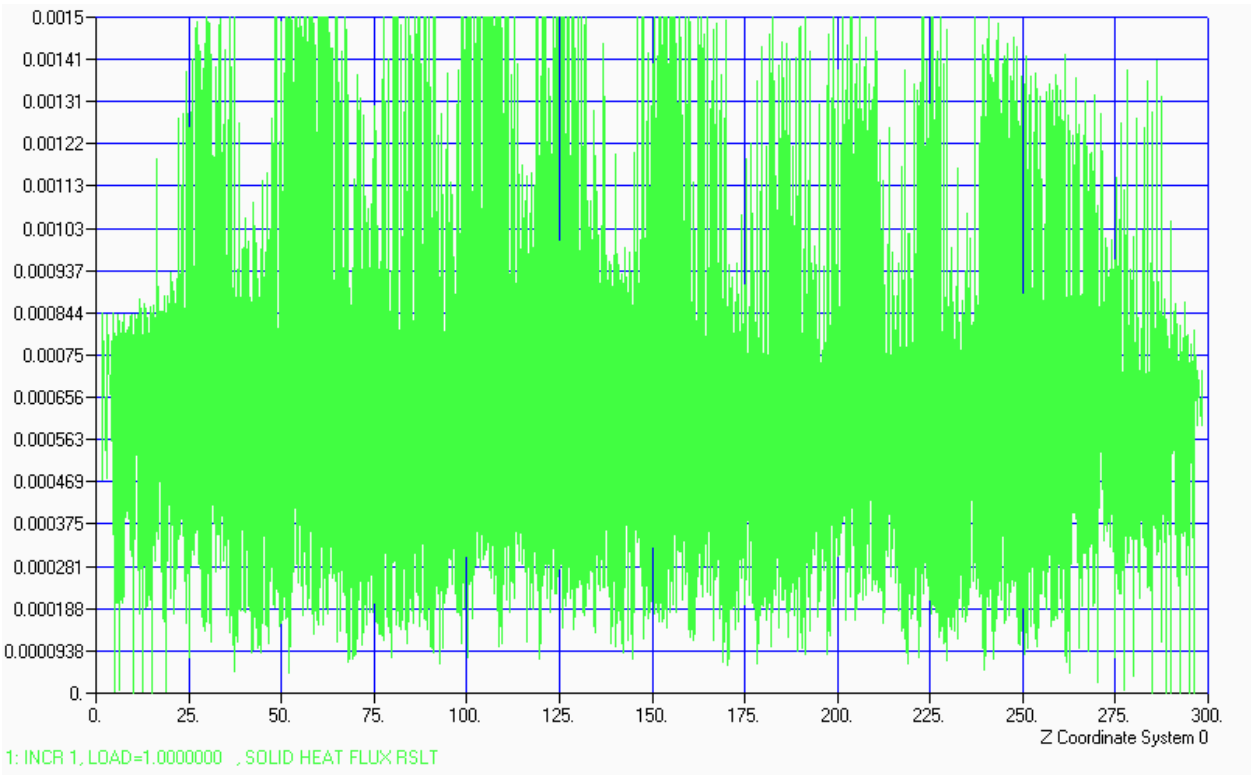

Fig. 5.3.17. Flux through the thickness for sample with thirty clays as 4%

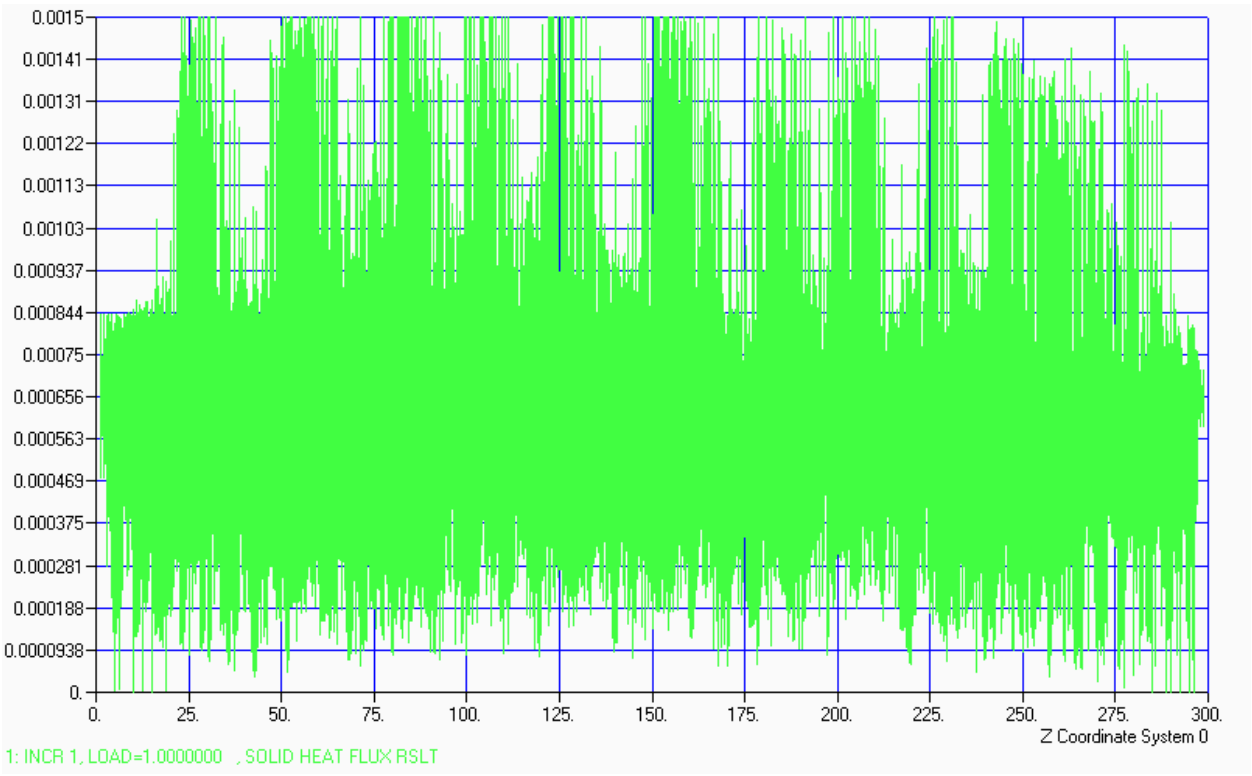

Fig. 5.3.18. Flux through the thickness for sample with thirty clays as 4% after remeshing

Table 5.3.2. Results of computer modeling of permeation rate *q*

Inclusion percentage	Inclusion aspect ratio	Modeled permeability rate	Percentage loss of permeability rate
0	-	$6.8*10^{-4}$	-
2	20	$6.56*10^{-4}$	3.5
2	10	$6.56*10^{-4}$	
4	20	$6.1*10^{-4}$	10.3
4	10	$6.1*10^{-4}$	

Table 5.3.3. Comparison of permeability test results and computer modeling

Sample	Permeability coefficient	Comment
M2	$(18.4\pm3.5)*10^{-13}$	Referral material
MB4	$(13.7\pm1.7)*10^{-13}$	Agrees within error limits
ME4	$22.3*10^{-13}$	Does not agree
NM2	$(3.99\pm2.83)*10^{-13}$	Referral material
NMB2	$(1.26\pm0.37)*10^{-13}$	Agrees within error limits
NMB4	$(0.925\pm0.482)*10^{-13}$	Agrees for upper error limit
NME2	$(7.41\pm2.99)*10^{-13}$	Agrees for lower error limit
NME4	$(2.46\pm0.63)*10^{-13}$	Agrees within error limits
KM2	$(9.91\pm5.28)*10^{-13}$	Referral material
KMB2	$(17\pm1.5)*10^{-13}$	Does not agree
KMB4	$(8.82\pm0.86)*10^{-13}$	Agrees within error limits, perfect match for average values
KME2	$(10\pm3.6)*10^{-13}$	Agrees within error limits
KME4	$(10\pm1.5)*10^{-13}$	Agrees within error limits

As discussed before samples with nanoclays contain many pores and air bubbles caused by addition of acetone and mixing procedures. Also aramid papers are porous materials and may contain some air bubbles on the surface and inside its structure. That is why results of gas permeability tests for particular material give average permeability coefficient with very big standard deviation and comparison

of such a result to mathematical or computer modeling is complicated. Agreement of test results with modeling is presented in Table 5.3.3. In general for test results with such big standard deviations it is not difficult to find suitable values to prove computer modeling results. Only samples of epoxy film mixed with 4% of Nanocor and Kevlar coated with epoxy mixed with 2% of Bentolite have result much above modeled values although result of epoxy film with Nanocor should not be taken into consideration since only one sample was tested. Discrepancy of results of permeability tests of Kevlar coated with 2% of Bentolite is difficult to explain since the same paper coated with 4% of the same nanoclay gives almost perfect match with computer modeling. To improve consistency of tests results and computer modeling better quality samples, which give more reliable results, should be prepared and tested again.

References:

[1] Baer E., Hu Y.S., Liu R.Y.F., Schiraldi D.A., Hiltner A. Polymeric Materials: Science and Engineering 89 (2003) 19-20

Chapter 6

CONCLUSIONS

The research described above proves that coated aramid papers are excellent candidates for barrier materials. Addition of nanoparticles improves their gas barrier behavior and enhances flame resistance. Gas permeability has been tested through long-term leak rate control process and calculated using mathematical approach and computer modeling. Flammability behavior was investigated through burning process using high-class flame testing equipment.

During sample preparation and permeability testing influence of sample manufacturing procedure on various properties was strongly visible. Especially addition of nanoparticles should be of great concern and performed with big care. Diluents should be chosen to enhance resin properties; tests showed that acetone increases permeability coefficient while alcohol gives opposite effect. Also, mixing procedure should not harm nanoparticle structure and good particles exfoliation must be of the greatest importance.

Acetone was used for sonication of nanoparticles and effect of addition of nanoparticles can only be evaluated based on results of permeation tests of samples with acetone. That is why substitution of this diluent by some other or eliminating it can further improve barrier properties of nanocomposites. Especially for samples with Nanocor sonication process could be substituted by mechanical mixing and degassing what is recommended for future research.

Addition of 4% of Bentolite and 6% of Nanocor to epoxy resin gave improved properties when compared to results of epoxy mixed with acetone as well as epoxy without acetone. When comparing particular paper coated with epoxy mixed with different percentages of particular nanoclay usually 4% of inclusions gives the best results. Only Nomex coated with 2% of Pyrograf showed better barrier properties than that with 4% and Kevlar coated with 2% of Nanocor gave permeability coefficient similar to that with 4%. In general Bentolite gave the biggest improvement of helium barrier properties.

All mathematical methods used for determination of permeability coefficient have their own negative effects and the results do not match well. However, even if the most trustful method is the long-term gas leak testing procedure, the information obtained from different mathematical methods can be used for comparison of different materials. Computer modeling showed reduced permeability rate with increased amount of nanoparticles what agrees with gas leak tests results.

Influence of nanoparticles on material flammability is proven in graphs of heat release rate change in time. Peak of heat release rate, which is a major parameter in controlling flame propagation in fires, is reduces. The best results gave addition of 4% of nanoclay to epoxy resin as both, a film and a paper coating, either Bentolite or Nanocor, while the worst outcome gave Pyrograf.

Coming with the advent of popularity of nanotechnology is concern about the environmental, health and safety impact of the technology. At the nanometer level not only do the laws of physics, biology, and chemistry merge but the behavior of these small particles change, including their mobility in the environment, reactivity, toxicity, and ability to enter the human body. Because of the large surface area and small size of nanoparticles, nanotubes, buckyballs, and quantum dots it would be expected that inhalation could be a primary exposure route. As particles become smaller their likelihood of causing harm to the lung increases. It has been reported that direct penetration of the skin has been observed for particles with a diameter of 1000 nm, which is much larger than nanoparticles. Exposure via the digestive route is possible but has not been demonstrated. There has been speculation that carbon nanotubes, being of size similar to asbestos fibers, may have health effects similar to asbestos. It is also clearly evident that nanoparticles may impact living organisms in their natural environment. It is entirely possible that microorganisms in soil or water could bioaccumulate nanoparticles within their cells. Potential impacts could be persistence, bioaccumulation, and toxicity. Because of the quantum properties of nanoparticles and especially the large surface area effect, it is suspected that nanomaterials could be potential catalysts for reactions that would otherwise proceed slowly. The National Institute of Environmental Health Sciences has also stated that generally, the smaller the particles, the more reactive and toxic are their effects. Nanoparticles may, under certain conditions, pose a fire or explosion hazard. That is why the use of nanoparticles should be of great concern to industry. In case of mass production workers exposure to nanoparticles may be reduced by using nanoclays or nanofibers already dispersed in resins or solvents what makes them easy and safe to use. In case of industrial use of nanoparticles the safety engineer is strongly encouraged to perform detailed risk assessments and utilize a hierarchy of engineering controls and personal protective equipment to minimize risk to workers. Strongly recommended is the use of adequate local exhaust ventilation with a dust collector to minimize worker exposure.

Results of current and previous research were published as follows:

1. Bubacz M., Beyle A., Hui D., Ibeh C. “Helium permeability of coated aramid papers,” *Composites B*, (submitted for publication)
2. Bubacz M., Bietto S., Ibeh C., Hui D. “Flammability of Polymer Nanocomposite Systems,” 6th AIAA Aviation Technology, Integration and Operations Conference, 2006, Wichita, KS, (abstract submitted)
3. Bubacz M., Hui D., Beyle A., Ibeh C. “Gas Permeability Properties of Aramid Papers Coated with Epoxy Resin Systems,” ICCE-14 2006, Boulder, CO
4. Bubacz M., Hui D., Beyle A., Santibhasker P., Ibeh C. “Aramid Papers Coated with Different Resin Systems as Excellent Gas Permeability Barrier” 47th AIAA/ASME/ASCE/AHS/ASC Structures, Structural Dynamics & Materials Conference, 2006, Newport, RI

5. Bubacz M., Hui D., Daniel L., Beyle A., Ibeh C., Susnik R. “Different approaches to sandwich structure permeability problem using coated aramid papers,” SAMPE 37th International Technical Conference, 2005, Seattle, WA
6. Bubacz M., Hui D., Leo D. “Permeability of helium through aramid fiber papers coated with unsaturated polyester,” ICCE-12 2005, Tenerife, Spain
7. Bubacz M., Martinez-Vilarino S., Hui D., Daniel L. “Problem of corrosion in spacecrafts,” ICCE-12 2005, Tenerife, Spain
8. Martinez-Vilarino S., Bubacz M., Hui D., Daniel L. “Overview of corrosion issues in ships,” ICCE-12 2005, Tenerife, Spain
9. Bubacz M., Chipara M. “Temperature dependence of magnetization in magnetic nanocomposites,” ICCE-10 2003, New Orleans, LA

VITA

Monika Bubacz was born in Inowroclaw, Poland, on August 2, 1974, the daughter of Ewa and Andrzej Bubacz. After finishing Jan Kasprowicz High School in Inowroclaw in 1993, she attended Poznan University of Technology in Poland and received the degree of Master of Science in Mechanical Engineering and Management in 1998. Between 1997 and 2001 she worked in Metal Forming Institute, Poznan, Poland on Research position in Metal Powder Forming Department and Assistant position in Marketing Department. She then entered the University of New Orleans, LA in the spring of 2002 and worked as a Graduate Research Assistant for Mechanical Engineering Department. She currently works for the Center of NanoComposites and Multifunctional Materials at Pittsburg State University, KS on Research Associate position.